Microwave Optomechanics with a Carbon Nanotube Quantum Dot

DISSERTATION

ZUR ERLANGUNG DES DOKTORGRADES DER NATURWISSENSCHAFTEN
(DR. RER. NAT.)
DER FAKULTÄT FÜR PHYSIK
DER UNIVERSITÄT REGENSBURG
VORGELEGT VON

STEFAN BLIEN
AUS STRAUBING

IM JAHR 2020

Das Promotionsgesuch wurde am 13.05.2020 eingereicht.

Das Kolloquium fand am 09.10.2020 statt.

Die Arbeit wurde von Dr. Andreas K. Hüttel betreut.

Prüfungsausschuss	Vorsitzende	Prof. Dr. Milena Grifoni
	1. Gutachter	PD Dr. Andreas K. Hüttel
	2. Gutachter	Prof. Dr. Jascha Repp
	weiterer Prüfer	PD Dr. Alfred Weymouth

Contents

List of Abbreviations and Symbols

ac	Alternating Current
ALD	Atomic Layer Deposition
CNT	Carbon Nanotube
CPW	Coplanar Waveguide
CVD	Chemical Vapour Deposition
dc	Direct Current
DUT	Device Under Test
EBL	Electron Beam Lithography
eV	Electronvolt
FIB	Focused Ion Beam
Fig.	Figure
HEMT	High-Electron-Mobility Transistor
hf	High Frequency
MKID	Microwave Kinetic Inductance Detector
mw	Microwave
NEMS	Nanoelectromechanical System
OMIT	Optomechanically Induced Transparency
PCB	Printed Circuit Board
PMMA	Polymethylmethacrylat
QD	Quantum Dot
QED	Quantum Electrodynamics
rf	Radio Frequency
rms	Root Mean Square
RRR	Residual Resistance Ratio
RWA	Rotating Wave Approximation
Sect.	Section
SEM	Scanning Electron Microscope
SET	Single Electron Tunneling
SWCNT	Single Wall Carbon Nanotube
TEM	Transverse Electromagnetic
TLS	Two-Level Systems
UHV	Ultra-High Vacuum
VNA	Vector Network Analyser
XPS	X-ray Photoelectron Spectroscopy
zpf	Zero-Point Fluctuations

c	Speed of light in vacuum ($c = 2.9979 \cdot 10^8\,\mathrm{m/s}$)
e	Elementary Charge ($e = 1.6022 \cdot 10^{-19}\,\mathrm{C}$)
ϵ_0	Vacuum Permittivity ($\epsilon_0 = 8.8542 \cdot 10^{-12}\,\mathrm{A\,s/V\,m}$)
h	Planck constant ($h = 6.6261 \cdot 10^{-34}\,\mathrm{J\,s}$)
k_B	Boltzmann constant ($k_\mathrm{B} = 1.3806 \cdot 10^{-23}\mathrm{J/K}$)
μ_0	Vacuum permeability ($\mu_0 = 1.2566 \cdot 10^{-6}\,\mathrm{N/A^2}$)

1

Introduction

The assumption that light exerts a pressure on an object when shining on it was first suggested by Johannes Kepler in the 17th century. With this concept he explained why the tail of a comet always points away from the sun [Kepler, 1619]. Later, the quantitative prediction of this radiation pressure force was put forth by James Clerk Maxwell. Experimental proof was impeded by dominating thermal effects for a long time. However, Pjotr Lebedew [Lebedew, 1901] and independently Ernest Fox Nichols and Gordon Ferrie Hull [Nichols and Hull, 1903] successfully demonstrated radiation pressure using light mill experiments.

In the rapidly growing research field of optomechanics, this force is exploited to investigate the interaction between electromagnetic radiation and mechanical oscillators. The coupling is mediated via the momentum transfer of photons to the mechanical system. Usually, this effect is of small nature. However, it can be rigorously enhanced with the implementation of an optical cavity, with one "mirror" being the mechanical resonator; this is the paradigmatic optomechanical system. The photons (injected by, e.g., a laser) then scatter multiple times on the mirrors. With each reflection they transfer a momentum onto the mechanical oscillator. However, when this mirror is displaced (the mechanical resonator starts vibrating), the optical cavity resonance frequency shifts as the cavity length is modified. Due to this shift, the light amplitude in the cavity is decreased as the laser frequency is unchanged. Being controlled by the light amplitude, i.e. the number of photons in the cavity, the radiation pressure force is thus dependent on the mechanical oscillator position.

The same physics as for optical cavities applies for superconducting resonators in the microwave regime, e.g. coplanar waveguides or LC circuits, however in a different parameter range. Here, the mechanical resonator is formed by a mechanically compliant capacitance. Examples are capacitively coupled nanobeams [Regal et al., 2008] or two-dimensional, membrane-like materials [Singh et al., 2014a]. Independent of the system, the optomechanical interaction can be described via the cavity resonance frequency shift as a function of mechanical displacement. This is called *dispersive coupling* [Aspelmeyer et al., 2014].

Braginsky *et al.* have studied the role of the radiation pressure in optical interferometers [Braginsky and Manukin, 1967]. They were able to experimentally demonstrate mechanical motion manipulation in pioneering experiments and later also investigated the role of quantum fluctuations of radiation pressure and the limit in displacement sensing that these fluctuations cause [Vladimir B. Braginsky, 1995]. A resulting effect important in the context of gravitational wave detectors, such as LIGO and VIRGO, is the *standard quantum limit* of continuous position detection.

More recent experiments focus on the optomechanical coupling of micro- or nanomechanical resonators to optical or microwave radiation. Here, interferometric displacement detection with precision beyond the standard quantum limit [Regal et al., 2008, Teufel et al., 2009], the creation and measurement of non-classical states (squeezed states, Fock states, entangled states) [Clerk and Marquardt, 2014], and mechanical motion manipulation on the quantum scale are of particular interest. The latter field involves quantum ground state cooling of mesoscopic objects [Teufel et al., 2011], enabling the study of decoherence, and the coherent driving of mechanical modes, leading to parametric amplification [Braginsky et al., 2001] and self-induced oscillations [Singh et al., 2014a]. Further technological applications include the development of high precision sensors [Krause et al., 2012], quantum memory for novel computers [Fiore et al., 2011], and quantum transducers between optical and microwave domain [Fan et al., 2018].

In 1953, multiwall carbon nanotubes were first discovered in TEM images [Radushkevich and Lukyanovich, 1952]. Later, Iijima and Ichihashi [Iijima and Ichihashi, 1993] and independently Bethune [Bethune et al., 1993] found single wall carbon nanotubes in the products of arc discharge experiments. This was followed by a hype in the scientific community and an increase in publications. In 1997, Tans *et al.* [Tans et al., 1997] electrically contacted individual carbon nanotubes carrying out low temperature measurements. These experimentally confirmed the quantum dot nature of such devices.

Suspended carbon nanotubes can act as *nano-electromechanical systems* (NEMS) exhibiting transversal vibrational modes as their lowest energetic excitation. These show both large mechanical quality factors at cryogenic temperatures [Moser et al., 2014] and strong coupling between the vibrational mode and single electron tunneling [Lassagne et al., 2009]. While for large-scale technological applications, the production methods for defect-free suspended nanotubes with predictable characteristics still have to be refined, mainly two techniques have been followed for research purposes. In the *overgrowth method* [Cao et al., 2005], the carbon nanotubes are grown over a pre-defined electrode structure in a last fabrication step. Herein, the metals used on the chip have to withstand a detrimental atmosphere of hot temperatures and corrosive gases; extensive material studies have been performed [Hüttel et al., 2009, Singh et al., 2014b, Götz et al., 2016, Blien et al., 2016]. In *transfer methods* [Gramich et al., 2015, Blien et al., 2018], the nanotubes are grown on a separate chip and then transferred to the electrode chip.

Because of their small physical size, however, the application of carbon nanotubes in the field of optomechanics has been scarce. Specifically, an optical implementation at room temperature [Tavernarakis et al., 2018] and the utilisation of resonant coupling to a microwave cavity [Ares et al., 2016] have been shown so far. In this thesis, an alternative method for optomechanical coupling was benefited from, namely, the coupling enhancement mediated by the quantum capacitance of the carbon nanotube. Advantages over other strategies are the ability to cool the carbon nanotube to cryogenic temperatures, enabling high mechanical quality factors and the simultaneous study of single electron effects, and the possibility to distinguish motional sidebands from the cavity resonance (the so called *resolved sideband regime*), which is a necessary condition for ground state cooling.

After this introduction, the properties of carbon nanotubes are presented in chapter 2: a summary over the theory of their electronic structure, fabrication techniques, electronic transport and quantum dot as well as nanomechanical resonator behaviour are given. This is followed by chapter 3 which explains the cryogenic setup and important measurement devices. After that, there are two chapters concentrating on coplanar waveguide resonators. The first one (chapter 4) presents the theoretical background, the second one (chapter 5) shows material characteristics of a molybdenum/rhenium alloy amongst other things obtained from resonator measurements. The final two chapters focus on a device where the coupling of carbon nanotube to a superconducting coplanar waveguide resonator could be accomplished. Chapter 6 explains the fabrication routine and demonstrates basic experiments that account for electronic coupling. Chapter 7 first introduces the most important theoretical aspects of optomechanics and then illustrates optomechanical experiments on said device at millikelvin temperatures. A quantitative analysis as well as a theoretical model for the enhancement of optomechanical coupling due to the quantum capacitance of the carbon nanotube are included. Finally, the thesis is concluded by a short roundup on important outcomes and an outlook on how to further improve the coupling strength, allowing for more advanced experiments. Additional measurements and details can be found in the appendix.

2

Properties of carbon nanotubes

Single wall carbon nanotubes (SWCNTs) are cylindrical macromolecules composed of a single rolled up graphene layer. Hence, they are counted among the allotropes of carbon, like diamond, graphite (graphene), and buckminsterfullerene. Their discovery [Iijima and Ichihashi, 1993, Bethune et al., 1993] lead to a multitude of possible scientific and technical applications. This is in particular ascribed to their high mechanical, thermal, and chemical stability, as well as electronic, mechanical, and thermal characteristics.

At room temperature, they show excellent transistor attributes. Their high tensile strength and elastic modulus as well thermal conductivity make them interesting in applications of material science [Bandaru, 2007]. When suspended, they display at low temperatures high mechanical quality factors, making their implementation as nano-electromechanical systems appealing [Sazonova et al., 2004].

At cryogenic temperatures, carbon nanotubes (CNTs) act as quasi-one dimensional conductors due to their large aspect ratio. The low defect structure leads to highly regular systems: CNTs possess the ability to form quantum dots, or "artificial atoms", together with the lead electrodes. Mechanical quality factors are very much enhanced at low temperatures [Hüttel et al., 2009].

2.1. Fundamentals

Describing carbon nanotubes as rolled up graphene sheets gives a basic understanding and leads to approximate physical properties [Saito et al., 1998]. Graphene is a one-atomic layer of graphite, constructed of sp^2-hybridised carbon atoms in a hexagonal honeycomb structure (see Fig. 2.1 (a)) with a bond length of $1.42\,\text{Å}$. The remaining electron in the p_z-orbital builds a delocalised π-band (bonding and antibonding) with the p_z-electrons of neighbouring atoms.

Each elementary cell of the graphene lattice contains two carbon atoms. This is why the lattice can be described as consisting of two inequivalent sublattices, labelled A and B. These are themselves hexagonal Bravais lattices. The unit cell is spanned by two basis vectors $\vec{a}_1$ and $\vec{a}_2$ with a lattice constant of $a = 2.46\,\text{Å}$. The reciprocal lattice is spanned by vectors $\vec{b}_1$ and $\vec{b}_2$ fulfilling the orthogonality condition $\vec{a}_i \cdot \vec{b}_j = 2\pi\delta_{ij}$. The inequality of the real space sublattices leads to inequivalent points K and K' (called *Dirac points*) in the six corners of the first Brillouin zone; see Fig. 2.1 (b). This adds an additional valley degree of freedom [Laird et al., 2015].

In the nearest neighbour approximation, the dispersion relation of the π-band can be calcu-

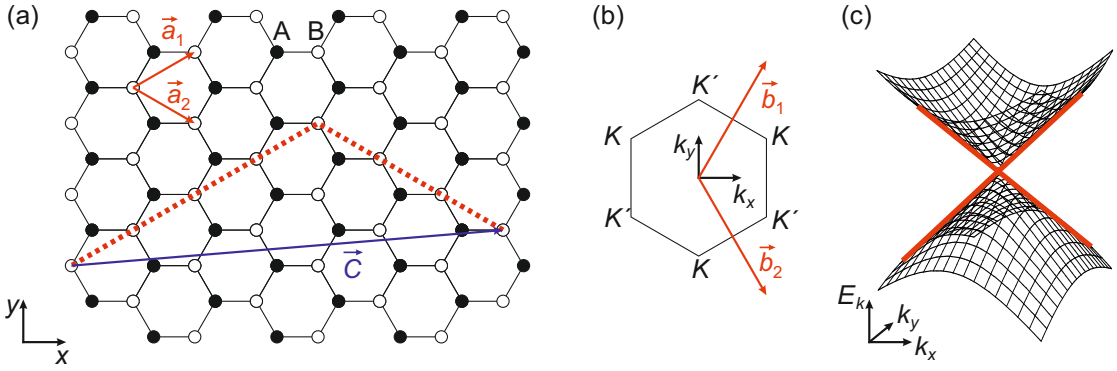

Figure 2.1.: Graphene real-space (a) and reciprocal (b) lattice and dispersion relation (c). (a) The two sublattices A and B along with their basis vectors $\vec{a}_1$ and $\vec{a}_2$ (red). A chiral vector of the configuration $(5, 3)$ is displayed in blue. (b) First Brillouin zone with its reciprocal vectors $\vec{b}_1$ and $\vec{b}_2$ (red). In its corners, two inequivalent points K and K' are situated. (c) There, the dispersion relation is linear in k. It has been calculated using Eq. 2.1. Adapted from [Charlier et al., 2007].

lated analytically in the tight binding model [Saito et al., 1998] as

$$E(k_x, k_y) = \pm\gamma_0 \left\{ 1 + 4\cos\left(\frac{\sqrt{3}k_x a}{2}\right)\cos\left(\frac{k_y a}{2}\right) + 4\cos^2\left(\frac{k_y a}{2}\right) \right\}^{1/2}, \tag{2.1}$$

where k_x, k_y are the electron momenta in x-/y-direction and γ_0 is the transfer integral between nearest neighbour π-orbitals (typically $\gamma_0 = 2.9\,\mathrm{eV}$). From this relation it follows that the conduction and valence band touch in the Dirac points. Around these, the dispersion relation is linear in the low energy limit and they define the plane of the Fermi surface. These characteristics lead to quasi-metallic behaviour of graphene.

For CNTs a chiral vector $\vec{C}$ can be defined. It uniquely determines a parameter set (n, m) that characterises the roll-up of the CNT from a graphene sheet. The chiral vector is given by

$$\vec{C} = n\vec{a}_1 + m\vec{a}_2 = (n, m) \tag{2.2}$$

and can be seen in Fig. 2.1 (a). From the chiral vector, three different types of nanotubes can be determined:

- *zigzag nanotubes* $(n, 0)$
- *armchair nanotubes* $(n, m = n)$
- *chiral nanotubes* $(n, m \neq n \neq 0)$

The denotations *zigzag* and *armchair* emerge from the atomic pattern along the circumference of the CNT, i.e. along the direction of the chiral vector.

The roll-up of the graphene sheet into a nanotube leads to periodic boundary conditions and thus to a quantisation of the wave vector $k_\perp$ perpendicular to the tube axis (along the circumference). At the same time, the component parallel to the axis, $k_\parallel$, remains continuous (as far as infinitely long CNTs are assumed). In this way, the dispersion relation of graphene collapses into one-dimensional subbands. These are evenly spaced by

$$\Delta k_\perp = \frac{2\pi}{|\vec{C}|}\,. \tag{2.3}$$

The *zone-folding approximation* now combines the restriction of perpendicular wave vectors to discrete values with the dispersion relation of graphene in order to obtain the dispersion relation of a carbon nanotube.

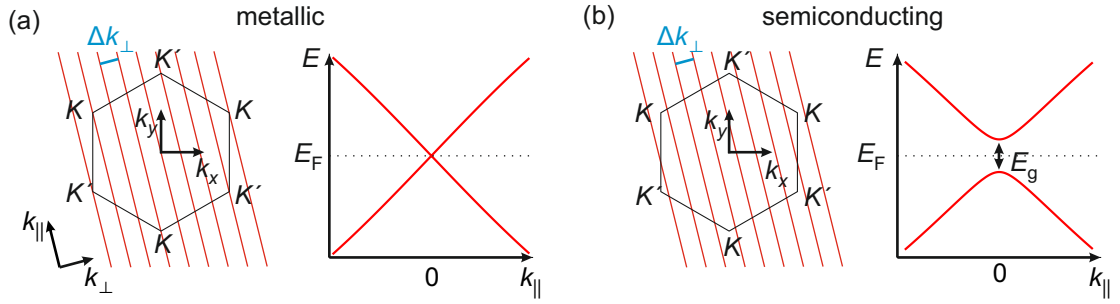

Figure 2.2.: Zone-folding approximation for a metallic (a) and semiconducting (b) nanotube. (a) The intersection of the K and K' points by the allowed $k_\perp$ leads to a linear dispersion without bandgap. (b) The allowed $k_\perp$ do not intersect the K and K' points. A bandgap arises in the dispersion relation. Adapted from [Laird et al., 2015].

In the Brillouin zone, the zone-folding approximation leads to a set of parallel lines spaced by $\Delta k_\perp$. From this, two situations can be distinguished:

- *metallic nanotubes*: Here, $n - m = 3l$ with l being an integer. The allowed wave vector lines intersect the Dirac points at K and K'. In the band structure, states arbitrarily close to the Fermi energy can be found. Armchair nanotubes and zigzag nanotubes of the form $(3l, 0)$ are metallic in the zone-folding approximation.

- *semiconducting nanotubes*: Here, the condition $n-m = 3l\pm1$ is fulfilled. This is true for chiral CNTs and zigzag CNTs of the form $(3l \pm 1, 0)$. In the one-dimensional dispersion relation, conductance and valence band are approximately parabolic and are separated by an energy gap.

The zone-folding approximation does not account for effects arising due to the curvature of the CNTs [Charlier et al., 2007]. Among these are changing bond lengths, modification of the hybridisation, and an induced spin-orbit coupling (which is intrinsically low in graphene). This leads to the fact that only armchair nanotubes are truly metallic, while for zigzag nanotubes of the form $(3l, 0)$, a small bandgap opens.

These different types of CNTs can readily be identified in room temperature measurements. A gate potential shifts the position of the chemical potential and thus the bandgap (if existing) relative to the Fermi energy [Laird et al., 2015]. Measuring the conductance of the nanotube in dependence of an applied gate voltage generates situations like in Fig. 2.3. A metallic CNT shows no dependence of gate voltage, because subbands intersect the KK' points and therefore no bandgap exists. In the case of a semiconducting CNT ($k_\mathrm{B}T \ll E_\mathrm{g}$), the Fermi energy can be tuned into the bandgap, so that current is suppressed over a large gate range. When $k_\mathrm{B}T \sim E_\mathrm{g}$, the current will show a dip, but will not be completely suppressed at room temperature. This is the case for small-bandgap CNTs.

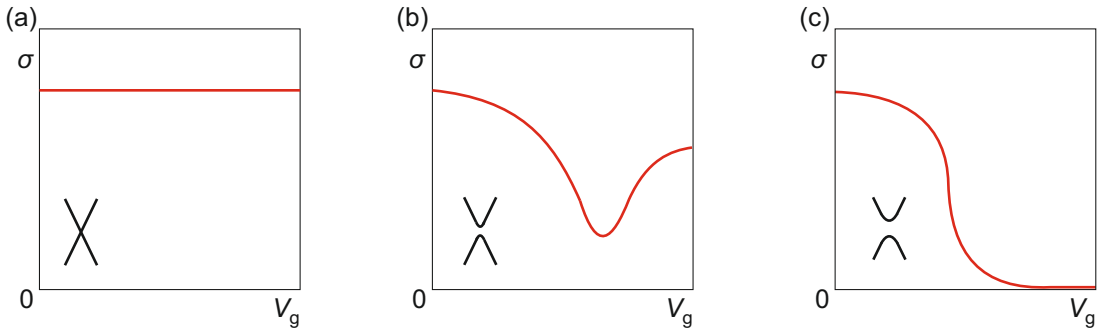

Figure 2.3.: Sketches of room temperature conductance $\sigma(V_\mathrm{g})$ for metallic (a), small-bandgap (b), and semiconducting (c) CNT in dependence of gate voltage. Insets show the respective dispersion relations from which the conductance behaviour can be deduced. Adapted from [Laird et al., 2015].

2.2. Fabrication techniques

In the course of this work, two different techniques for the fabrication of carbon nanotube devices have been used: an *overgrowth technique* [Götz et al., 2016, Blien et al., 2016], growing the CNTs on-chip as a last fabrication step, and a *fork transfer technique* [Blien et al., 2018], where electrode chip fabrication and CNT growth are separated. Both techniques produce suspended, so-called *ultraclean CNTs* with clean electronic spectra and outstanding mechanical properties. While the overgrowth technique is suitable to gain a high yield but random directional growth on simple-structured devices, where the same electrode structure can be multiplexed several times on one substrate chip, the fork technique aims for the directed transfer into more complex devices.

2.2.1. On-chip overgrowth

For earlier results of Sect. 5, an on-chip overgrowth technique following [Cao et al., 2005] was used. It was initially planned to also use this approach for fabricating carbon nanotube-microwave resonator hybrid devices. However, as an alternative fabrication method was accom-

plished, the overgrowth process was abandoned in this context; for the alternative method, the fork transfer process, see the next section.

In the overgrowth method, the CNT is grown in the last fabrication step over the pre-existing electrode structure. As a consequence, the choice of contact material is restricted. The growth process is detrimental to most materials: many metals melt in the high temperature atmosphere and superconductors lose or at least are diminished in their superconducting quality. Still some materials have been reported to survive this processing. Among these are thin films of platinum-tungsten [Hüttel et al., 2009], rhenium [Schmid et al., 2012] and, as used in this thesis, alloys of molybdenum and rhenium [Singh et al., 2014b, Götz et al., 2016, Blien et al., 2016].

The overgrow approach ensures that the CNT is not exposed to chemicals, which minimises the possibility of defects and surface contaminations in the CNT crystal. Furthermore, *scanning electrode microscopy* (SEM) to directly look for nanotubes after growth is avoided. This prevents the deposition of amorphous carbon coming from the residual gases in the SEM chamber. Nanotube growth and electrical connectivity is solely checked by electrical room-temperature characterisation of the samples.

A catalyst suspension is used within this method (see Fig. 2.4 (a)). It contains a transition metal oxide and metal-organic particles suspended in methanol. To "activate" the suspension, the catalyst flask is placed in an ultrasonic bath for at least $20\,\mathrm{min}$. The devices are covered with *Polymethylmethacrylat* (PMMA) and undergo EBL to define the positions where a catalyst dot will be placed. After development, the catalyst is dropcast onto the chip. A bake out follows, where the methanol evaporates. A lift-off process removes the surplus catalyst and leaves only small clusters in the defined areas. For studies of the effect of the growth process on thin films and resonator characteristics (see Sect. 5), no catalyst was used.

For the growth, the devices are placed into the quartz tube of a CVD furnace (see Fig. 2.4 (b)). They are heated up in a mass-flow controller defined gas flow of Ar and $\mathrm{H_2}$ to $850\,^{\circ}\mathrm{C}$. When the temperature is reached, the Ar flow is cut off and a defined $\mathrm{CH_4}$ flow is turned on. The device is kept in this atmosphere for $10 - 30\,\mathrm{min}$. This is when the CNT growth happens: the methane decomposes at the catalyst and the carbon is building the lattice of the nanotube [Kong et al., 1998]. The growth direction is random (see Fig. 2.4 (c)) and the number and length of the CNTs depend on parameters such as growth time, gas flow, and temperature [Götz et al., 2016]. The chips subsequently cool down in an $\mathrm{Ar/H_2}$ atmosphere. Before measurements at low temperatures, individual structures can be pre-examined in room temperature measurements.

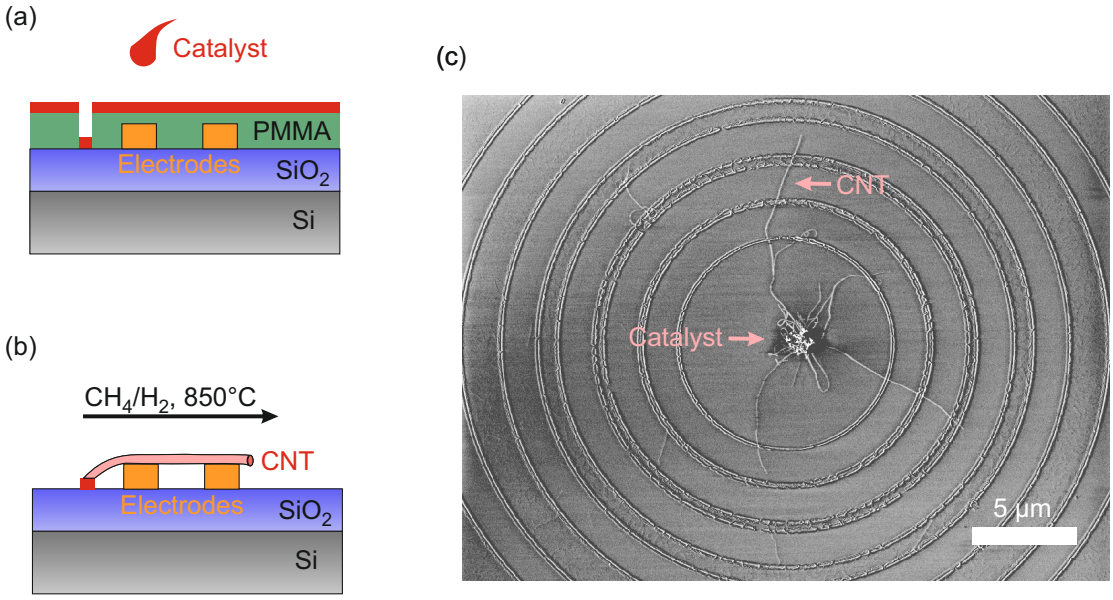

Figure 2.4.: Carbon nanotube overgrowth process. (a) Liquid catalyst is deposited locally by EBL, dropcasting, baking, and lift-off. (b) The samples undergo a CVD process, where the CNTs grow in a methane/hydrogen atmosphere at $850\,°\mathrm{C}$. If CNTs fall over lead electrodes, they are suspended and can be electrically contacted. (c) Exemplary SEM micrograph, where the random growth, with few long tubes $\approx 10\,\mu\mathrm{m}$ and many short ones, can be identified. The concentric ring structure around the catalyst dot is a failed attempt of trench etching.

2.2.2. Fork transfer

The overgrowth process is associated with a low general device yield, as the CNT growth is random regarding number of nanotubes and nanotube growth direction. At the same time, the CNTs are grown in the last fabrication step, which makes sample preparation time consuming. Several groups have found different transfer techniques to overcome this situation. The group of S. Ilani uses scanning probe microscope manipulation of the growth chip to deterministically assemble the CNT on a second chip containing the electrode structure [Waissman et al., 2013]. On the other hand, the groups of Z. Zhong [Wu et al., 2010], L. P. Kouwenhoven [Pei et al., 2012], and C. Schönenberger [Ranjan et al., 2015] implemented a stamping technique, where a growth chip is pressed onto the target chip. The transfer in the stamping technique is still statistical in nature, but electrode and growth structures can in principle be multiplexed on both chips, enhancing the yield.

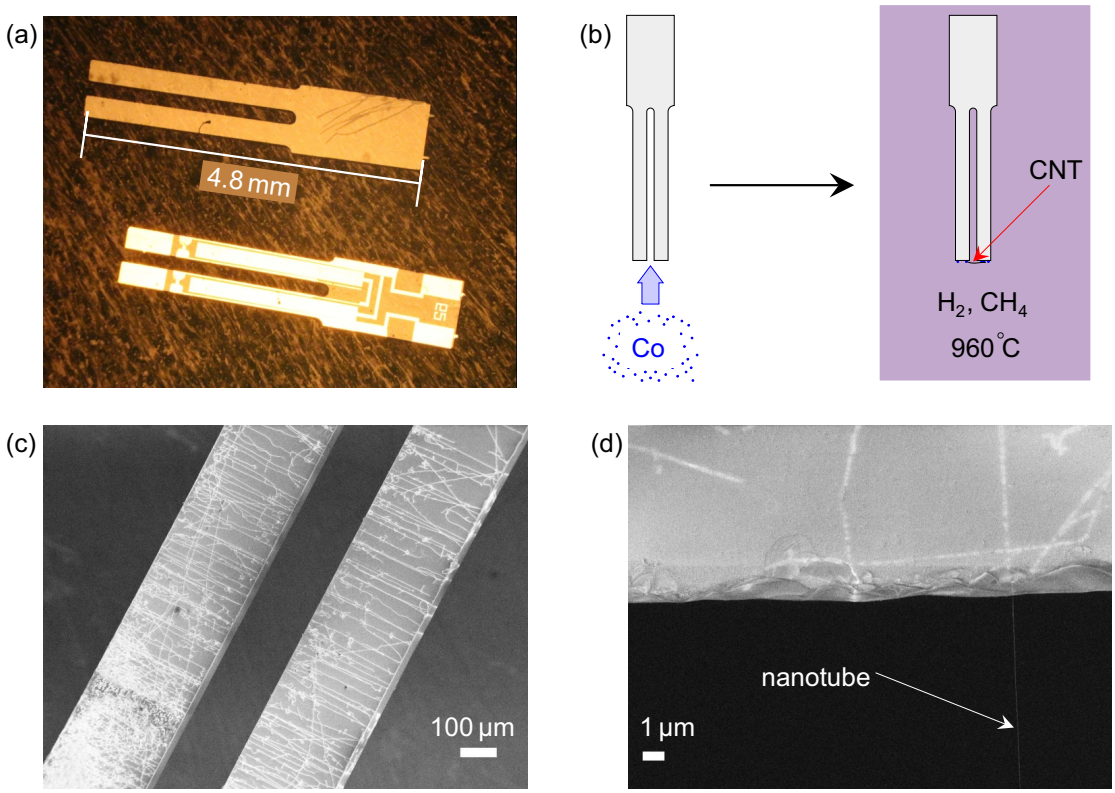

Figure 2.5.: Quartz tuning fork preparation and CNT growth. (a) Forks before and after removal of the metal contacts. (b) As catalyst for the growth process, Co is sputtered onto the fork tips ($\sim$ 1 nm). The nanotube synthesis takes place in a CVD oven in a CH_4/H_2 atmosphere at 960 °C. (c) A SEM micrograph reveals the preferred growth direction. (d) Individual nanotubes crossing the gap can be identified. Adapted from [Blien et al., 2018].

Our fork transfer process [Blien et al., 2018] relies more on Ilani's deterministic approach: we

have adapted the technique described in [Gramich et al., 2015] for macroscopic quartz tuning forks. With this method, the disadvantages of the overgrowth process in regard to the fabrication of complex structures could be much improved: devices are no longer restricted to certain metals that survive the atmosphere of CNT overgrowth, transfer is repeatable as unwanted CNTs can easily be "burned off", and complex structured devices are reusable. Especially with superconducting resonator geometries, advantages are manifold. Devices can be readily bonded, pre-examined, and tested for their resonant behaviour. Only then, a single CNT is transferred directedly into the region, where the coupling to the resonator is large. The fork transfer process as described in this section was established in the master thesis of P. Steger [Steger, 2019].

Starting with commercial-grade quartz tuning forks (Fig. 2.5 (a)), the first step is removal of the metallic contact structure. For this, aqua regia or Lugol's solution as well as hot HCl and hot NaOH baths are used. Cleaning is finished by sonication and plasma ashing. Subsequently, a thin film of nominally $1\,\mathrm{nm}$ of cobalt is sputtered onto the tips of the fork tines (Fig. 2.5 (b)). The forks are placed in a CVD growth oven, where they are heated up perpendicular to a gas flow of Ar and $\mathrm{H_2}$ to $960\,^{\circ}\mathrm{C}$. At this temperature, they remain under a constant flow of $\mathrm{CH_4}$ and $\mathrm{H_2}$ for $30\,\mathrm{min}$. Here, the Co acts as catalyst [Huh et al., 2005] and the CNTs grow from tine to tine, because of the preferential growth direction along the gas flow (Fig. 2.5 (c)). In order to avoid carbon contamination, the forks used for transfer onto actual devices are usually not imaged via SEM. This is done only for testing purpose: bundles, networks, but also single nanotubes crossing the gap of $\sim 144\,\mu\mathrm{m}$ can be identified (Fig. 2.5 (d)).

Photographs of the transfer setup are shown in Fig. 2.6. The forks which have undergone the growth process and possibly carry CNTs are attached on a glass object plate that is mounted to a micromanipulator stage (Fig. 2.6(a), (b)). The setup used here is adapted from [Castellanos-Gomez et al., 2014], where similar components have been used to dry-stamp 2D materials. The transfer can be observed via a camera/optical microscope combination. The target chip is glued onto a *printed circuit board* (PCB) and bonded, so the electrodes can be electrically connected (Fig. 2.6(c)). The contact structure used for the transfer consists of four electrodes of the same height - two for cutting, two as leads - and a lower gate electrode that is electrically isolated by an oxide or cross-linked PMMA layer. On either side of the electrodes is a rectangular area that is locally etched $\sim 12\,\mu\mathrm{m}$ into the substrate by an anisotropic etching process using $\mathrm{SF_6}$ and Ar (see Fig. 2.7) in *reactive ion etching* (RIE).

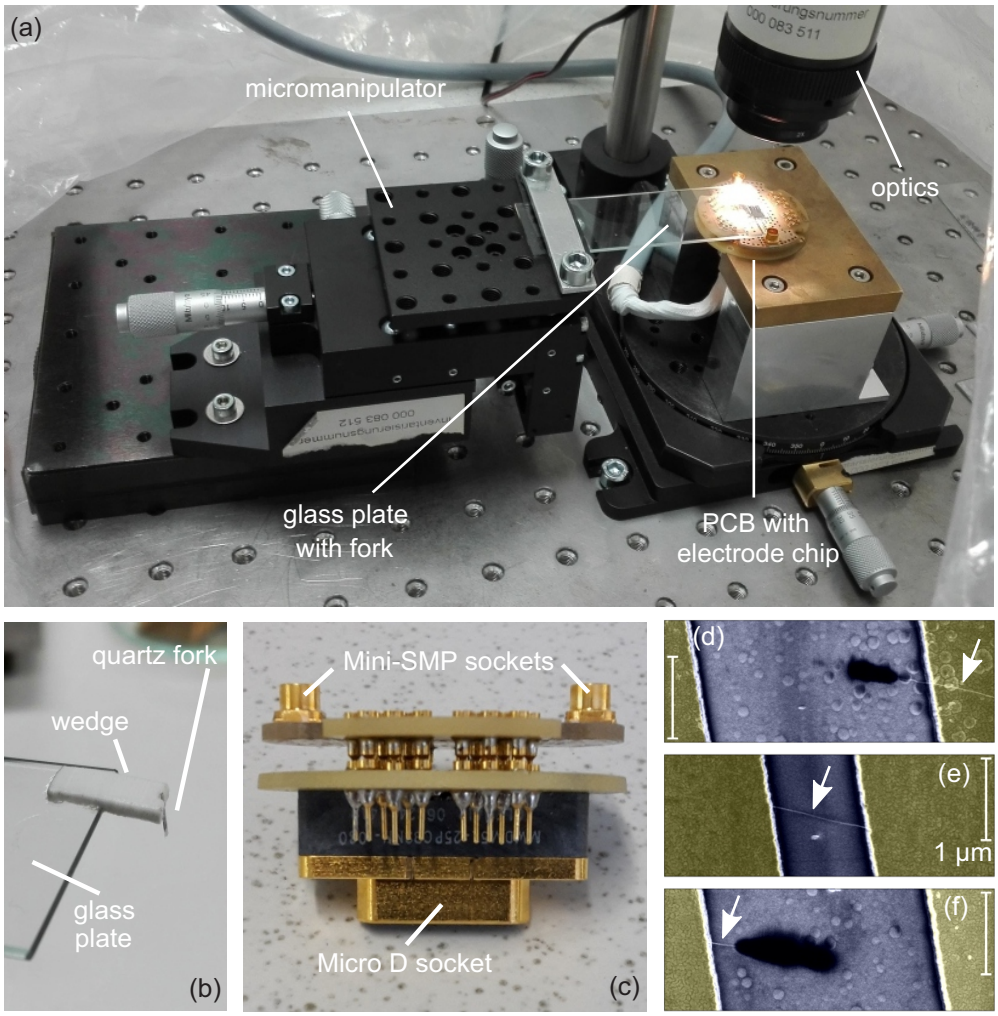

Figure 2.6.: Depiction of the carbon nanotube transfer setup. In (a), an overview of the setup is shown. The glass plate with the fork is mounted on a micromanipulator stage and can be lowered onto the target chip. The chip is glued to a PCB, where it can be electrically connected. The transfer process is monitored via an optical microscope and a camera. (b) A close up of the attached quartz fork and the glass object plate. (c) Side view of the stacked PCB. The lower board contains a Micro D socket for dc connection, the upper one two mini-SMP sockets for microwave experiments. (d-f) shows a SEM of a successfully transferred CNT. The nanotube has been cut between the outer electrode pairs (d, f) and now lies only over the two inner electrodes (e). Adapted from [Blien et al., 2018].

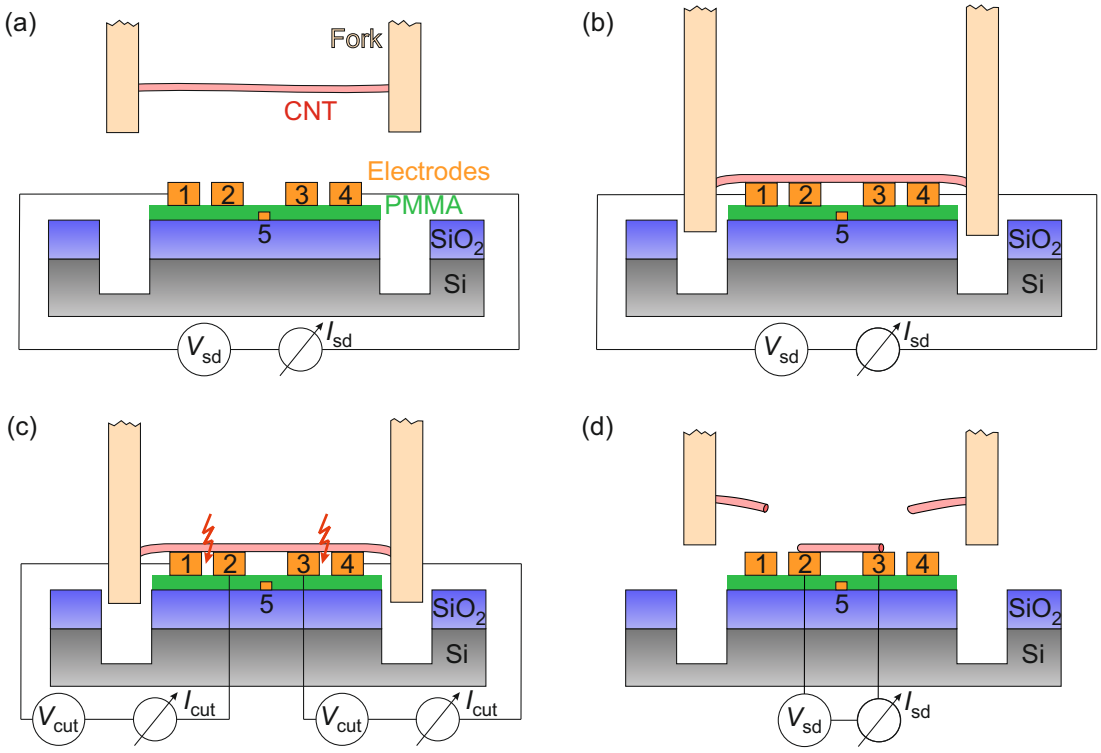

Figure 2.7.: Schematic of the transfer process. (a) A voltage of $V_{\mathrm{sd}} = 100\,\mathrm{mV}$ is applied to the outermost electrodes 1 and 4. (b) The fork is lowered to chip while monitoring the current I_{sd}. The fork tines sink into the deep-etched areas. If a nanotube connects electrodes 1 and 4, a finite current is measured (Fig. 2.8 (a)). (c) After a pre-characterisation by sweeping the gate voltage on electrode 5 (Fig. 2.8 (b)), the CNT can be cut between electrodes 1 - 2 and 3 - 4 by a high current (Fig. 2.8 (c)). (d) The fork can then safely be retracted. The CNT now only connects the inner electrodes 2 and 3 and is suspended over the gap. A final electronic pre-characterisation can be performed.

The transfer process is illustrated in Fig. 2.7 with the resulting electrical characterisation in Fig. 2.8. Initially, the fork is lowered onto the chip using the micromanipulator stage, to sink the tips into the deep-etched areas. Simultaneously, a voltage of $100\,\mathrm{mV}$ is applied to the outer electrodes (1 and 4) and the current is measured. Doing so, the transfer can be monitored electrically and optically (through camera and microscope). As soon as a nanotube touches the outer electrodes, a finite current flows (Fig. 2.8(a)). By sweeping the gate voltage, the type of CNT (see Sect. 2.1 and Fig. 2.8 (b)) can be determined and bundles or single nanotubes can be identified.

To finish the transfer process, the CNT has to be cut between the outer contact pairs. This is done by ramping up the voltage and thus the current between contacts 1 and 2 and contacts 3 and 4, with the device in air; see Fig. 2.7 (c) and Fig.2.8 (c) for this. Consistent with [Waissman et al., 2013], the critical current lies in the range $5 - 30\,\mu\mathrm{A}$. In the case of a single nanotube, the current drops to zero in a single step (Fig. 2.8 (c, left)). If on the other hand a step-like decrease

is observed (Fig. 2.8 (c, right)), this can be ascribed to breaking individual shells in a multiwall nanotube or individual tubes in a bundle. This has been verified in the work of P. Steger by atomic force microscopy [Steger, 2019]. After successful transfer, the carbon nanotube lies only on contact 2 and 3 and is suspended over the trench between them (Fig. 2.6 (d-f) and Fig. 2.7 (d)).

The quartz forks are chemically and mechanically resistant and can be cleaned from remaining nanotube parts and dirt. Plasma ashing removes organic compounds originating from the CVD growth, and a hot nitric acid bath dissolves residues of the catalyst. After another cleaning step using sonication and plasma ashing, the forks can be reintroduced in further fabrication cycles.

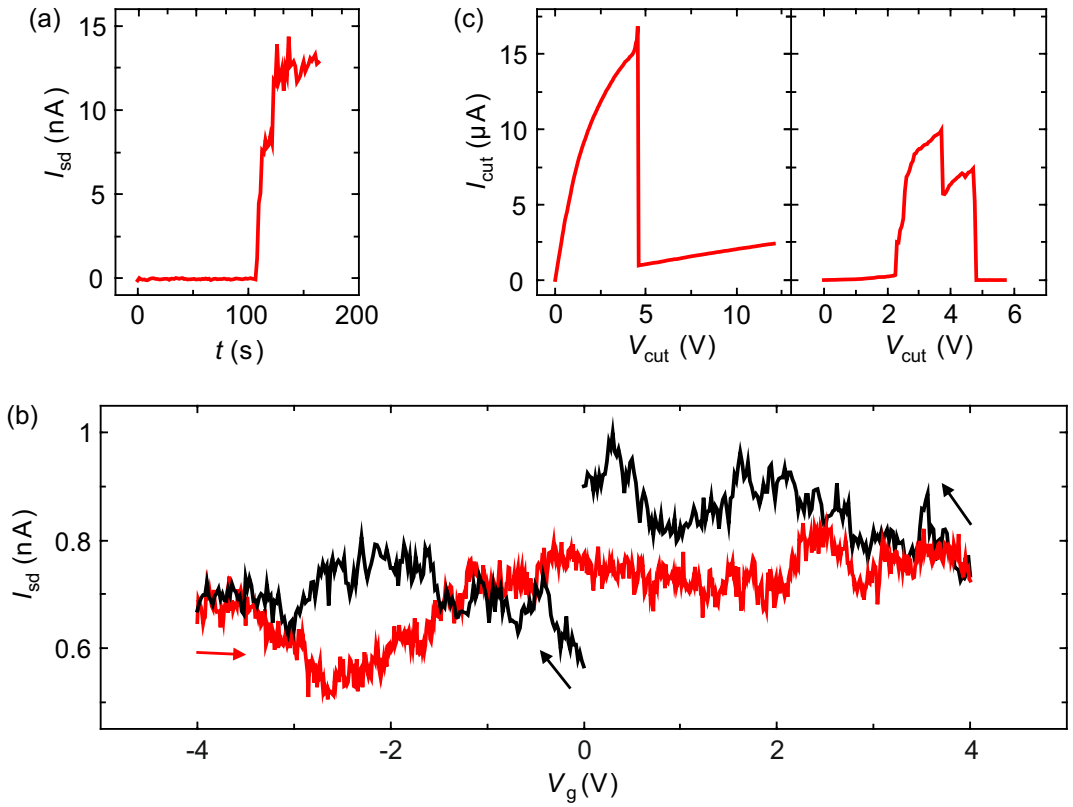

Figure 2.8.: Measurements on a CNT during the transfer process. (a) As soon as a connection to the electrodes is established, the current I_{sd} jumps to a finite value. A first characterisation of the CNT can now be performed. (b) Gate voltage characteristics of a metallic CNT: the current for an applied bias of $V_{\mathrm{sd}} = 3\,\mathrm{mV}$ is independent on the gate voltage. (c) To fix the CNT on the device, the voltages V_{cut} between the outer electrode pairs are ramped. The shape of the current drop allows conclusions on the transferred nanotube; see main text. Adapted from [Blien et al., 2018].

2.3. Electronic transport - Coulomb blockade

When a carbon nanotube is weakly coupled to metallic contacts, the dimensionality of the band structure can be further reduced. The CNT forms a small conducting island that is confined along the tube axis by the formation of tunnel barriers to the source and drain electrodes. Because of its small capacitance, only quantized charging by single electrons is possible. Such a system, combining a discrete number of trapped charges and discrete, well-separated quantum levels, is called *quantum dot* (QD).

2.3.1. Quantum dots in general

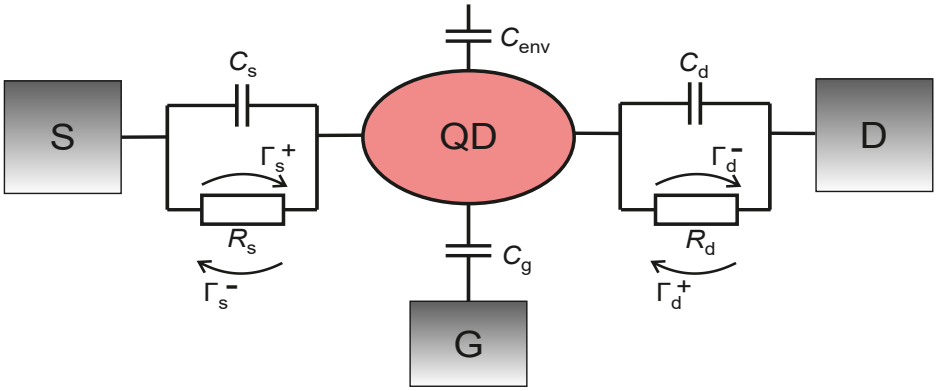

Figure 2.9.: Schematic of a quantum dot. The QD is formed by tunnel barriers with tunnel rates $\Gamma^{\pm}_{\mathrm{s/d}}$. Equivalent capacitances $C_{\mathrm{s/d}}$ and tunnel resistances $R_{\mathrm{s/d}}$ to the source (S) and drain (D) electrodes are shown. A gate electrode (G) is capacitively coupled (C_{g}) to the conducting island. The quantum dot further experiences a parasitic capacitance C_{env} to its surroundings.

Fig. 2.9 displays a schematic equivalent circuit of a quantum dot. It consists of a conductor, that is constrained in every spatial direction and is connected to source and drain electrodes to measure electronic transport. The coupling is given by tunnel barriers that emerge between QD and lead electrodes with tunnel rates to $\Gamma^{+}_{\mathrm{s/d}}$ and from $\Gamma^{-}_{\mathrm{s/d}}$ the dot (see also Sect. 2.3.4). This situation can be modelled by tunnel resistors $R_{\mathrm{s/d}}$ and capacitors $C_{\mathrm{s/d}}$. A gate electrode is capacitively coupled (C_{g}) to the QD to manipulate the electro-chemical potential of the electrons on the dot. A finite capacitance to the surroundings is denoted by C_{env} [Kouwenhoven et al., 1997].

The transport through a quantum dot can be described within the *constant interaction model* [Hanson et al., 2007], which is based on two assumptions:

1. The Coulomb interaction of the electrons on the QD and in close proximity is described by a single parameter C_{Σ} that is the total dot capacitance

$$C_{\Sigma} = C_{\mathrm{s}} + C_{\mathrm{d}} + C_{\mathrm{g}} + C_{\mathrm{env}}\,. \tag{2.4}$$

2. The single particle energy spectrum is independent of these interactions and consequently independent of the number of electrons.

The *Coulomb blockade regime* is now the suppression of electron tunneling due to electrostatic effects, namely Coulomb repulsion. Then, the number of electrons on the quantum dot is fixed. In terms of energy scales, it appears when the thermal energy $k_{\mathrm{B}}T$ is much smaller than the classical electrostatic charging energy[1] E_C [Kouwenhoven et al., 1997, Tans et al., 1997], which is given by

$$E_{\mathrm{C}} = \frac{e^2}{C_\Sigma}\,, \qquad k_{\mathrm{B}}T \ll E_{\mathrm{C}}\,. \tag{2.5}$$

The charging energy depends on the size of the quantum dot and is usually in the range of $\sim \mathrm{meV}$. As thermal energies of electrons are $k_{\mathrm{B}}T \approx 0.34\,\mathrm{meV}$ at liquid helium temperatures $T = 4\,\mathrm{K}$, the quantum dot can enter the Coulomb blockade regime.

A second requirement is a sufficient opaqueness of the tunnel barriers to suppress charge fluctuations on the quantum dot by tunneling [Tans et al., 1997]. This translates, due to the Heisenberg uncertainty principle [Kouwenhoven et al., 1997], to the tunnel resistances $R_{\mathrm{s/d}}$ being much larger than the conductance quantum $h/e^2 \approx 25.8\,\mathrm{k\Omega}$,

$$R_{\mathrm{s/d}} \gg \frac{h}{e^2}\,.$$

In a "classical" quantum dot, the energy required to add an additional electron is given by the charging energy. Thus, the energies are equally spaced by $\Delta E_{\mathrm{add}} = E_{\mathrm{C}}$. Here, the quantum states arising from the spatial confinement of the charge carriers have not been taken into account. In semiconducting QDs, however, where the Fermi wavelength is large, their energy spacing ΔE_N is on the order of the charging energy E_{C} and has to be considered in the energy balance [Kouwenhoven et al., 1997].

The electro-chemical potential (at zero bias voltage $V_{\mathrm{sd}} = 0$) is now defined as

$$\mu(N) = U(N) - U(N-1) = E_{\mathrm{C}}\left(N - \frac{1}{2}\right) - e\alpha_{\mathrm{g}}V_{\mathrm{g}} + E_N\,, \tag{2.6}$$

where $U(N)$ denotes the total energy of the QD with N electrons in the ground state, $\alpha_{\mathrm{g}} = \Delta E/\Delta V_{\mathrm{g}}$ is the gate conversion factor, V_{g} the gate voltage, and E_N the single particle energy level coming from quantum confinement.

For the description of electronic transport in quantum dots, the electro-chemical potential is a convenient parameter; a ladder is formed for all N (see Fig. 2.10). Due to $\mu(N)$ having a linear dependence on V_{g}, the ladder can be shifted up and down by the gate voltage. The distance $\Delta E_{\mathrm{add}}(N)$ between the "rungs" (the potentials) represents the energy that is needed to add a surplus electron. It is given by [Hanson et al., 2007]

$$\Delta E_{\mathrm{add}}(N) = \mu(N+1) - \mu(N) = E_{\mathrm{C}} + \Delta E_N\,, \tag{2.7}$$

[1] The energy of a capacitor charged with a single electron is $E_{\mathrm{C}} = e^2/2C_\Sigma$. Here, however, for convenience the charging energy is defined as twice this value as in [Staring et al., 1991].

and is comprised of the charging energy and the energy distance of the respective quantum levels. ΔE_N can be zero, e.g. when two electrons fill a level that is degenerate.

The transport through a quantum dot now sensitively depends on the alignment of the dot electro-chemical potentials to those of the source and drain electrode μ_s and μ_d. This can be seen in Fig. 2.10 (a-c): when the levels align $\mu_\mathrm{s} = \mu_\mathrm{d} = \mu(N)$, *single electron tunneling* (SET) can occur. In between the tunneling events, levels do not align, and the current is blocked by Coulomb blockade. When additionally a bias voltage $V_\mathrm{sd}$is applied, a bias window of energy $\mu_\mathrm{s} - \mu_\mathrm{d} = -|e|V_\mathrm{sd}$ opens, where tunneling is allowed (see Fig. 2.10 (d)). The current peaks become more and more broadened with increasing V_sd because quantum dot levels responsible for tunneling stay inside the bias window for a larger range of gate voltage. When the current I or differential conductance $\sigma = \mathrm{d}I/\mathrm{d}V_\mathrm{sd}$ in dependence of V_g and V_sd is recorded, stability diagrams are formed. Due to their peculiar shape, they are often called *Coulomb diamonds* [Hanson et al., 2007].

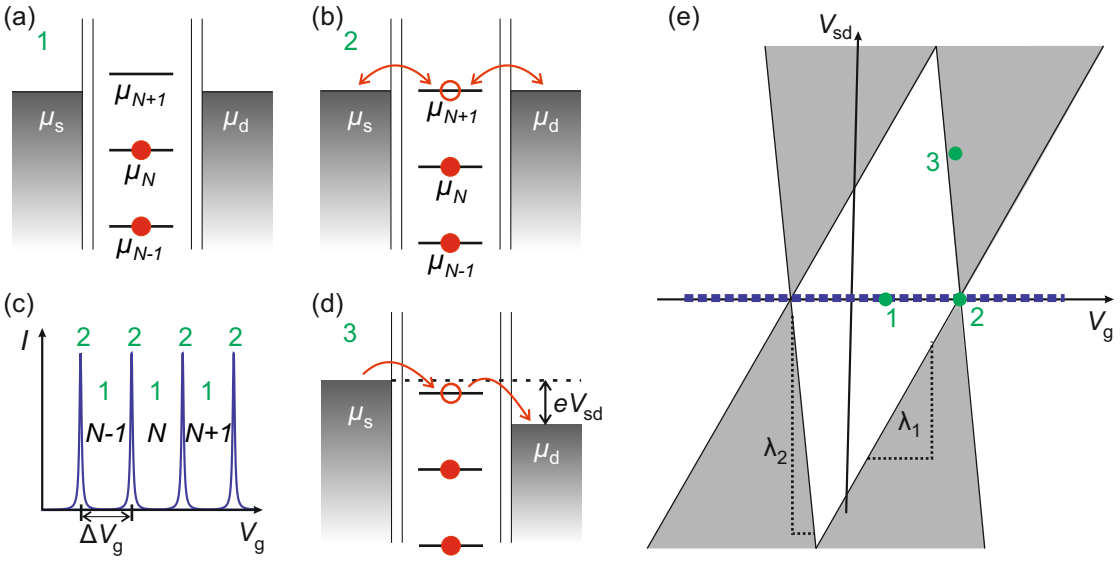

Figure 2.10.: Chemical potential ladder of a quantum dot. In (a) the chemical potentials of the QD do not align with those of the leads. This is called the Coulomb blockade regime. With a gate voltage V_g the dot potentials can be tuned to align with those of the leads (b). Tunneling is then possible. Recording the current while sweeping the gate voltage thus leads to an alternating pattern of no current in the Coulomb blockade regime and SET peaks at distance ΔV_g (c). When a bias voltage V_sd is applied to the leads, a bias window opens (d). Tunneling is possible as long as a potential of the QD is inside the bias window. Sweeping bias and gate voltage while recording the current therefore leads to a diamond shaped pattern (e). This pattern is called a Coulomb diamond. The slopes of the edges of single electron tunneling regions λ_1, λ_2 are given by the capacitances C_Σ, C_g, C_s, and C_d. Taking a line trace at $V_\mathrm{sd} = 0$ (blue dashed line), the zero bias trace of (c) is recovered. Adapted from [Hanson et al., 2007].

The slopes of the Coulomb diamonds give the gate conversion factor or lever arm as [Glazman

and Shekhter, 1989]

$$\alpha_{\mathrm{g}} = \frac{C_{\mathrm{g}}}{C_{\Sigma}} = \left(\frac{1}{|\lambda_1|} + \frac{1}{|\lambda_2|} \right)^{-1} . \tag{2.8}$$

It usually depends on the number of charges N on the dot. From the distance between SET peaks ΔV_{g}, the capacitance between CNT and gate can be estimated as

$$C_{\mathrm{g}}^{\mathrm{CB}} = \frac{e}{\Delta V_{\mathrm{g}}} . \tag{2.9}$$

2.3.2. Carbon nanotube quantum dots

Carbon nanotubes are usually treated as one dimensional objects (see Sect. 2.1). In electronic transport experiments, segments of often $< 1\,\mu\mathrm{m}$ are coupled to lead electrodes. A quantum dot forms in the CNT by the further reduction of the dimensionality by the tunnel barriers at the nanotube-electrode interfaces. The contact separation determines the size of the quantum dot, and thus the energy level spacing ΔE_N [Cao et al., 2005].

Due to the electronic characteristics being based on these of graphene, CNTs exhibit a four-fold degeneracy (spin and valley) in their electronic states. Filling up the CNT quantum dot levels leads thus to the population of the same energetic state for four consecutive electrons. In this case, according to Eq. 2.7, only E_{C} has to be paid. If an electron has to populate a previously unoccupied level, additionally the confinement energy has to be overcome, so that $\Delta E_{\mathrm{add}}(N) = E_{\mathrm{C}} + \Delta E_N$ [Hanson et al., 2007]. Then, there is also a larger distance between the chemical potentials of the quantum dot (see Fig. 2.11 (b)).

In general, it is not easy to estimate the contribution of the confinement energy ΔE_N, because it depends on many different factors, for instance the boundary conditions, contact material and nanotube diameter [Laird et al., 2015]. A simplified model uses hard wall boundary conditions combined with a linear dispersion relation, giving rise to a constant Fermi velocity v_{F}. In the case of hard wall potentials, the longitudinal wavevector separation is given by $\Delta k_{\parallel} = \pi/L$ with the quantum dot length L. A linear dispersion relation is always given in a metallic CNT. In semiconducting nanotubes, this is only true for higher electron states, as then the dispersion relation can be linearly approximated. This takes the applicability of this model away from the bandgap towards the states where many electrons populate the QD. In the case of hard wall potentials and linear dispersion, the confinement levels are equally spaced and depend inversely on the quantum dot length [Tans et al., 1997]

$$\Delta E_N = \frac{h v_{\mathrm{F}}}{2L} . \tag{2.10}$$

Using a Fermi velocity of $v_{\mathrm{F}} \approx 8 \cdot 10^5\,\mathrm{m/s}$ [Laird et al., 2015, Tans et al., 1997], this results in a quite high confinement energy spacing of $\Delta E \approx 1.65 \cdot 10^{-9}\mathrm{eV\,m}/L$. It is for short segments ($L \leq 1\,\mu\mathrm{m}$) in the same range as typical charging energies $E_{\mathrm{C}} = 5 - 20\,\mathrm{meV}$ for CNTs, so that the unequal level spacing of Fig. 2.11 (b) can be experimentally observed.

Interestingly, ΔE is only dependent of the CNT length, not of the number of electrons on the dot (as in other quantum dot systems). As also E_{C} is independent of the charging state, according to the constant interaction model, this makes the CNT energy spectrum simple also in the case of high electron occupation.

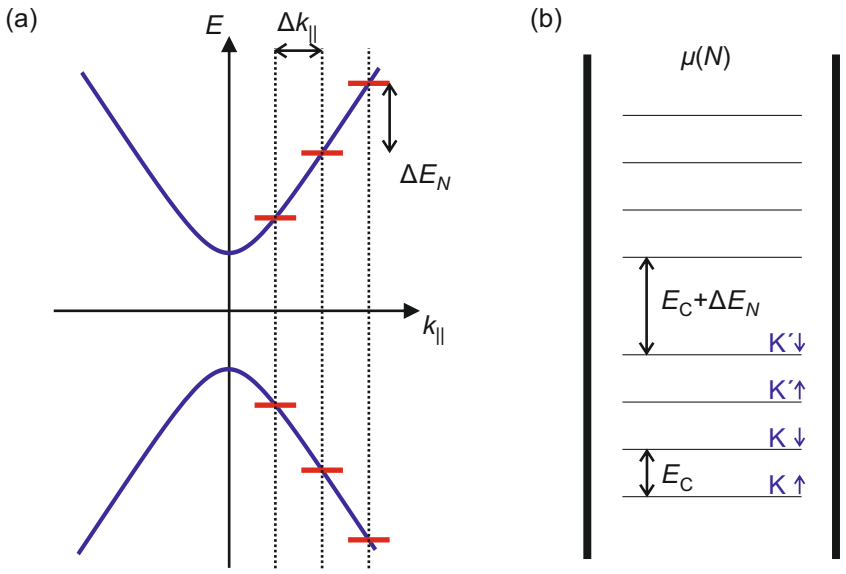

Figure 2.11.: The coupling of the CNT to lead electrodes leads to a longitudinal quantization of the wavevector $k_{||}$ as indicated with vertical dashed lines (a). This results in confinement energies and states (=shells), each fourfold degenerate and with spacing ΔE_N. Adding an electron to a previously unoccupied shell requires this additional energy difference ΔE_N, whereas adding an electron to an already occupied shell only requires E_C (b). The electro-chemical potentials of the QD are then no longer evenly spaced. Adapted from [Cao et al., 2005].

Going beyond above simplifications, the bipartite hexagonal lattice has to be taken into account, leading to more complex boundary and quantisation conditions and thus to unexpected electronic behaviour [Margańska et al., 2019].

2.3.3. Transport spectroscopy of a carbon nanotube quantum dot

In this section, transport spectroscopy results of a CNT quantum dot, on which later all the optomechanical experiments were performed, shall be shown. For this, the CNT was fork transferred (see Sect. 2.2.2) to the coupling region of a half wave resonator (see Sect. 6.1). However, high frequency experiments and setup details shall be ignored for now. Here, an overview of the dc characteristics at low temperatures is given. Some of these are later used to explain the optomechanical coupling enhancement (see Sect. 7.2).

Fig. 2.12 displays schematically the measurement setup used for quantum dot spectroscopy. The device was mounted on the mixing chamber stage of a dilution refrigerator with a nominal bas temperature of $T = 15\,\mathrm{mK}$. The dc wiring is filtered on the still stage by RC filters and again at room temperature by RLC filters. Bias voltages are applied using a Yokogawa GS200 and a voltage divider of ratio 1:1000. A gate voltage was applied using also a Yokogawa GS200 and a $5\,\mathrm{Hz}$ lowpass filter, to reduce ac noise on the gate. With a DL Instruments 1211 current to voltage amplifier, the current through the CNT can be converted to a voltage, which is amplified

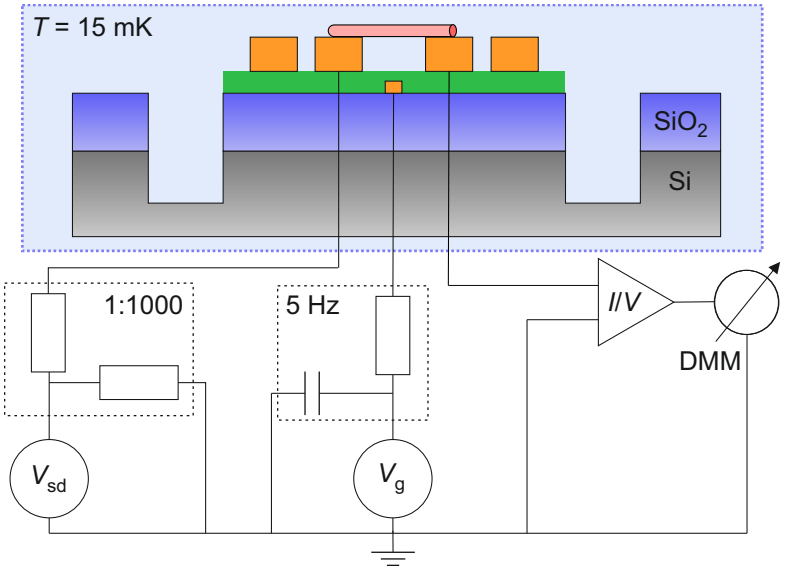

Figure 2.12.: Schematic measurement setup for transport spectroscopy on a CNT quantum dot. The device is mounted on the mixing chamber stage of a dilution refrigerator with a nominal base temperature of $T = 15\,\mathrm{mK}$. A bias voltage V_{sd} is applied over a voltage divider to the source and drain electrode. The current through the CNT is detected at the drain electrode by a current to voltage amplifier and a digital multimeter. The gate voltage V_{g} is applied to the gate electrode after passing a $5\,\mathrm{Hz}$ low-pass filter.

(most of the time by a factor $10^9\,\mathrm{V/A}$) and read out using an Agilent 3458A digital multimeter (DMM). The device temperature can be varied, heating the mixing chamber. In this way, a range from base temperature up to $T = 4\,\mathrm{K}$ can be covered.

Measuring the current I at small bias voltage in dependence of the gate voltage leads to the expected alternating Coulomb blockade current suppressions and SET peaks as explained in Sect. 2.3.1. Fig. 2.13 (a) shows the current for low gate voltages around $V_{\mathrm{g}} = 0$ and higher positiv gate voltages of $5\,\mathrm{V} \leq V_{\mathrm{g}} \leq 10\,\mathrm{V}$. Around $V_{\mathrm{g}} \approx -0.6\,\mathrm{V}$, the bandgap can be observed as a region of suppressed current. There, no QD levels are available to contribute to the electronic transport. Interestingly, this specific CNT shows quantum dot formation on both, the electron and the hole conduction side.

At higher positive gate voltages (= higher electron occupation numbers), a four fold periodicity in the SET peaks can be observed, where every fourth peak takes an additional amount in gate voltage. According to Sect. 2.3.2, this is due to the confinement energy which can then be extracted from this measurement. P. Steger has shown in his master thesis [Steger, 2019] that for this particular CNT, addition energies are $\Delta E_{\mathrm{add}} = (2.9 \pm 0.3)\,\mathrm{meV}$ for $N \neq 4n$, $n = 1, 2, 3, \ldots$, and $\Delta E_{\mathrm{add}} = (4.2 \pm 0.4)\,\mathrm{meV}$ for $N = 4n$, $n = 1, 2, 3, \ldots$. From this, a confinement energy of $\Delta E_N = (1.3 \pm 0.7)\,\mathrm{meV}$ can be calculated. Using Eq. 2.10, this leads to a quantum dot size of $L = (1.3 \pm 0.7)\,\mu\mathrm{m}$, which is not particularly precise, but conforms with the source-drain electrode distance of $1\,\mu\mathrm{m}$.

Fig. 2.13 (b) shows stability diagrams of the same device on the hole conduction side: here, the current was recorded in dependence of both gate and bias voltage, which leads to a highly regular Coulomb diamond pattern. The specific Coulomb oscillation around which all later optomechanical experiments are centred, is the one around $V_\mathrm{g} \approx -1.16\,\mathrm{V}$. From the edges of this Coulomb diamond and Eq. 2.8, a gate lever arm of

$$\alpha_\mathrm{g} = 0.265$$

could be extracted. Taking the zero bias trace, the average distance between two Coulomb oscillations can be stated as $\Delta V_\mathrm{g} = 61.6\,\mathrm{mV}$. Using Eq. 2.9, the gate capacitance can then be calculated as

$$C_\mathrm{g}^\mathrm{CB} = 2.6\,\mathrm{aF}\,.$$

Note that the Coulomb diamonds in Fig. 2.13 (b) do not close. A gap in low bias conduction can be caused by a chain of several quantum dots [Yuli V. Nazarov, 2009]. The high regularity of the diamonds - only one set of delineating slopes occurs - points however to the fact that one QD is dominant. A second potential minimum could be found for example in a trap state at one of the contacts [Blien et al., 2020]. For this reason and for simplification, the system will be treated as a single quantum dot in the rest of this thesis.

Due to a presumable charging of the PMMA isolation layer, a slow drift in the diamond positions emerged over a timespan of six months spent on the experiment. This is why later measurements show these Coulomb oscillations at slightly more negative gate voltages.

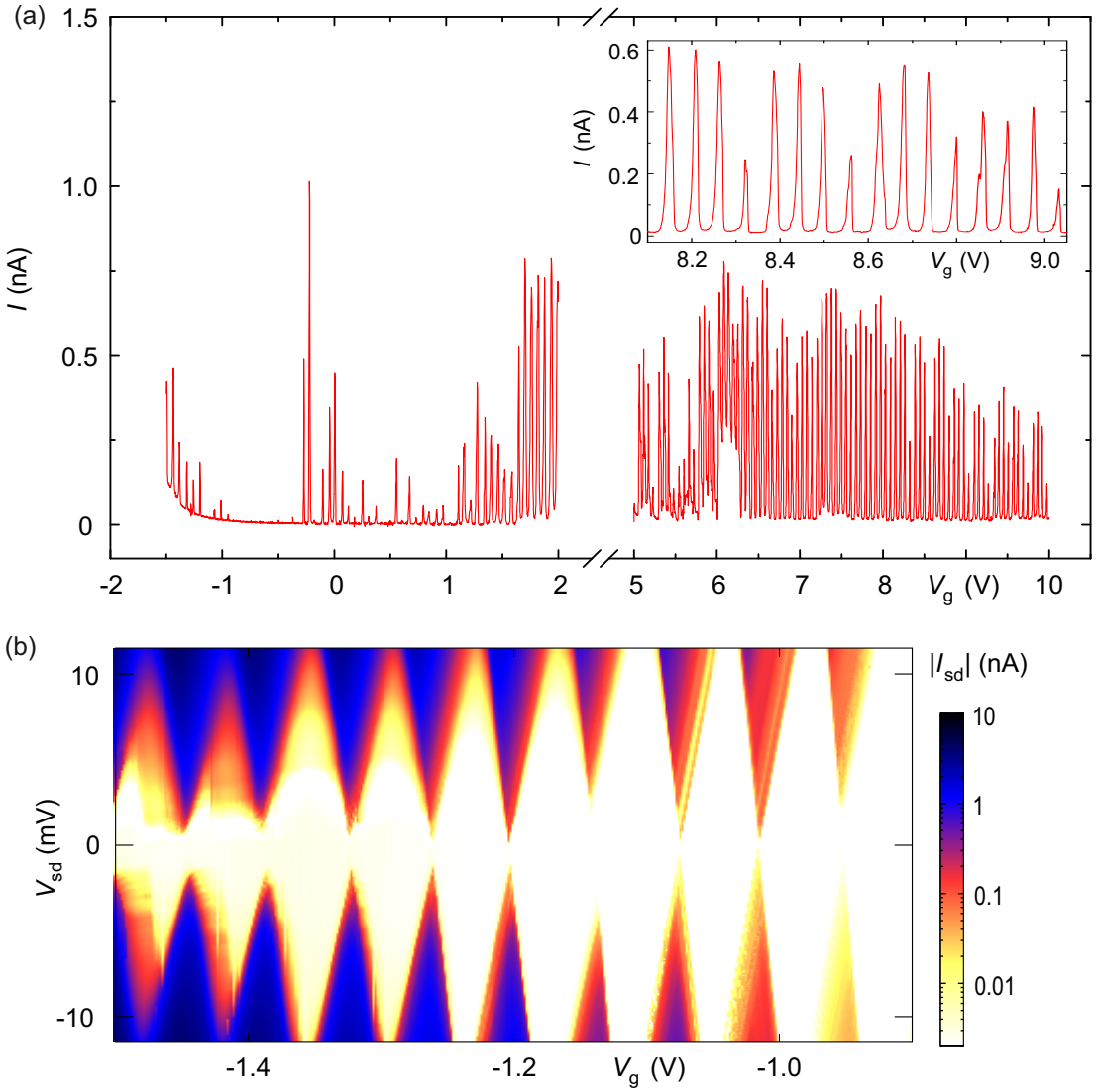

Figure 2.13.: Transport spectroscopy of a (likely small bandgap) CNT quantum dot at $T = 15\,\mathrm{mK}$. (a) displays Coulomb blockade and SET for fixed bias voltages $V_{\mathrm{sd}} = 2\,\mathrm{mV}$ and $V_{\mathrm{sd}} = 1.5\,\mathrm{mV}$ for the low respectively high positive gate voltage range. The bandgap is situated around $V_{\mathrm{g}} = -0.6\,\mathrm{V}$. For higher gate voltage ranges $V_{\mathrm{g}} > 7\,\mathrm{V}$ weak indications of a four fold symmetry unfold; see the inset. (b) shows regular Coulomb diamonds for the hole conduction side. (b) adapted from [Blien et al., 2020].

2.3.4. Modelling conductance and charge evolution

Following [Meerwaldt et al., 2012], a simplified model for the average number of charge carriers on the QD is given in this section. It will be important in Sect. 7.2, where the enhancement of the optomechanical coupling is derived from single electron effects on the quantum dot.

The broadening of a QD level is given by its finite lifetime $\tau = \frac{1}{\Gamma_{\mathrm{broad}}}$ at sufficiently low temperatures (meaning $\hbar\Gamma_{\mathrm{broad}} \gg k_{\mathrm{B}}T$). The density of available states of the QD caused by tunnel coupling to the leads in this regime is described via a Lorentzian shape

$$\mathrm{DOS}(\mu) = \frac{1}{2\pi} \frac{\hbar\Gamma_{\mathrm{broad}}}{(\mu - \mu_{\mathrm{CNT}})^2 + \left(\frac{\hbar\Gamma_{\mathrm{broad}}}{2}\right)^2} \,. \tag{2.11}$$

Here, Γ_{broad} is the full width at half maximum of the lifetime broadened state and μ_{CNT} is the chemical potential of the carbon nanotube corresponding to the specific Coulomb oscillation.

The tunnel rates of Fig. 2.9 can then be calculated as the overlap of the density of states of the QD and the leads times the probability that the state is occupied

$$\int_{-\infty}^{+\infty} \mathrm{DOS}(\mu) \cdot \mathrm{DOS}_{\mathrm{s/d}}(\mu) f_{\mathrm{s/d}}(\mu) \mathrm{d}\mu \,.$$

At low temperatures, the Fermi functions $f_{\mathrm{s,d}}$ can be modelled by step functions

$$f_{\mathrm{s/d}}(E) = \begin{cases} 1, \text{ for } E < \mu_{\mathrm{s/d}} \\ 0, \text{ for } E > \mu_{\mathrm{s/d}} \end{cases} \,, \tag{2.12}$$

and the densities of states of source and drain $\mathrm{DOS}_{\mathrm{s/d}}(\mu)$ are assumed to be constant. Then, for the tunnel rates

$$\Gamma_{\mathrm{s}}^{+} = a_{\mathrm{s}} \int_{-\infty}^{\mu_{\mathrm{s}}} \mathrm{DOS}(\mu)\, \mathrm{d}\mu \quad , \quad \Gamma_{\mathrm{d}}^{+} = a_{\mathrm{d}} \int_{-\infty}^{\mu_{\mathrm{d}}} \mathrm{DOS}(\mu)\, \mathrm{d}\mu \,, \tag{2.13}$$

and

$$\Gamma_{\mathrm{s}}^{-} = a_{\mathrm{s}} \int_{\mu_{\mathrm{s}}}^{\infty} \mathrm{DOS}(\mu)\, \mathrm{d}\mu \quad , \quad \Gamma_{\mathrm{d}}^{-} = a_{\mathrm{d}} \int_{\mu_{\mathrm{d}}}^{\infty} \mathrm{DOS}(\mu)\, \mathrm{d}\mu \tag{2.14}$$

is obtained. Here, constant prefactors a_s, a_d consider the height and width of the tunnel barriers to source and drain electrode. Then, the average charge on the quantum dot is given by

$$\langle N \rangle = N_0 + \frac{\Gamma^{+}}{\Gamma^{+} + \Gamma^{-}} \,, \tag{2.15}$$

where $\Gamma^{\pm} = \Gamma_{\mathrm{s}}^{\pm} + \Gamma_{\mathrm{d}}^{\pm}$.

In the zero-bias regime and assuming similar tunnel rates to both leads $\mu_{\mathrm{s}} = \mu_{\mathrm{d}} = \mu$ and $a_{\mathrm{s}} = a_{\mathrm{d}} = a$ holds. As then $\Gamma^{+} + \Gamma^{-} = a$, Eq. 2.15 reduces to[2]

$$\langle N \rangle = N_0 + \int_{-\infty}^{\mu} \frac{1}{2\pi} \frac{\hbar\Gamma_{\mathrm{broad}}}{(\mu' - \mu_{\mathrm{CNT}})^2 + \left(\frac{\hbar\Gamma_{\mathrm{broad}}}{2}\right)^2} \mathrm{d}\mu' = \frac{1}{2} + \frac{1}{\pi} \cdot \arctan\left(\frac{2(\mu - \mu_{\mathrm{CNT}})}{\hbar\Gamma_{\mathrm{broad}}}\right) \,. \tag{2.16}$$

[2] For a more general discussion using asymmetric tunnel barriers in the finite bias regime, see Sect. C.2.

According to Beenakker [Beenakker, 1991], the conductance is then given by

$$G = \pi G_0 \frac{\hbar\Gamma_{\mathrm{broad}}}{2} \mathrm{DOS}(\mu)\,, \tag{2.17}$$

with the conductance quantum $G_0 = \frac{4e^2}{h}$.

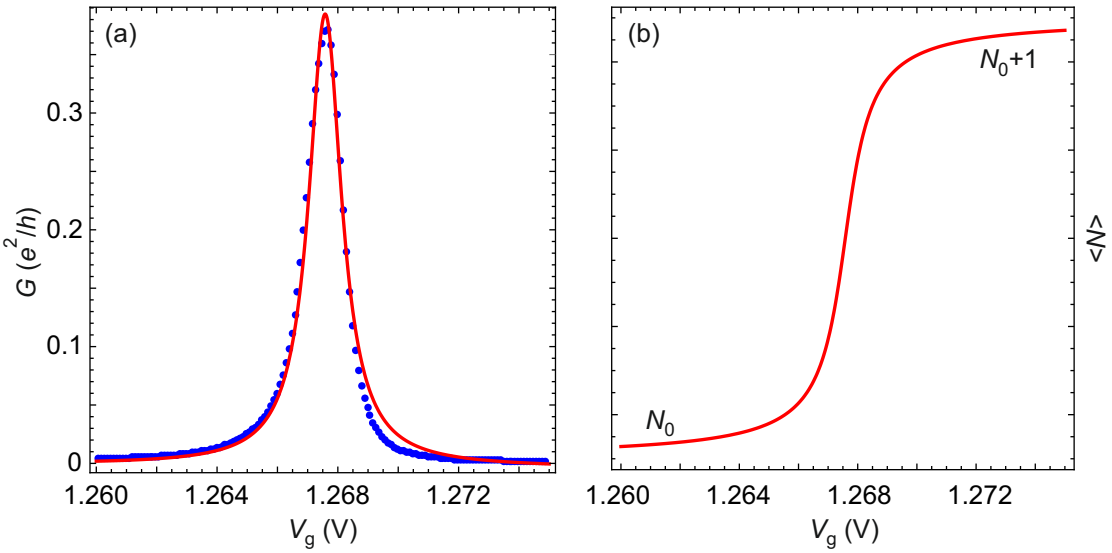

Figure 2.14.: Conductance (a) and number of charge carriers (b) around a single electron tunneling event. (a) shows data of device conductance recorded by D. Schmid and a fit using Eq. 2.17. The fit has been normalized to the data. The number of charge carriers increases stepwise around the SET event (b).

Fig. 2.14 (a) shows data of a conductance peak corresponding to single electron tunneling in dependence of the gate voltage at a bias voltage of $V_{\mathrm{sd}} = 5\,\mu\mathrm{V}$. It that has been fit to Eq. 2.17 with $\mu = e\alpha_{\mathrm{g}} V_{\mathrm{g}}$ and α_{g} being the gate lever arm of Eq. 2.8. As fit parameter, $\Gamma_{\mathrm{broad}} = 0.56\,\mathrm{THz}$ was obtained, which is similar to values obtained in [Meerwaldt et al., 2012]. Translating the broadening Γ_{broad} to a voltage gives $V \approx 370\,\mu\mathrm{V}$; an influence of the bias voltage on the broadening can therefore be excluded. Comparing to a device temperature of $T = 50\,\mathrm{mK}$, the lifetime broadened regime $k_{\mathrm{B}}T \ll \hbar\Gamma_{\mathrm{broad}}$ holds. In Fig. 2.14 (b), the associated charge evolution on the quantum dot according to Eq. 2.16 is plotted. As expected, the number of charge carriers increases stepwise with each individual charge carrier being transferred onto the QD.

2.3.5. Quantum capacitance of a carbon nanotube quantum dot

When charging a classical capacitor, e.g. two parallel plates made of metal, the number of charges on the capacitor increases continuously with applied voltage. This is due to the quasi-infinite density of states in the metal. The total capacitance is then fully determined by the geometry of the capacitor ($C_{\mathrm{tot}} = C_{\mathrm{geo}}$). For quantum mechanical systems, however, low density

of states can emerge, leading to non-linear charging. This effect reduces the total capacitance, acting as another capacitor in series to the geometric one [Ilani et al., 2006]

$$C_{\mathrm{tot}}^{-1} = C_{\mathrm{geo}}^{-1} + C_{\mathrm{Q}}^{-1} \,. \tag{2.18}$$

This term is called *quantum capacitance* and was first defined by S. Luryi [Luryi, 1988].

The quantum capacitance per unit length/area can be derived from the charge carrier density q as [John et al., 2004]

$$c_{\mathrm{Q}} = \frac{\partial q}{\partial V} \,, \tag{2.19}$$

where V is the local electrostatic potential. As carbon nanotubes are one dimensional systems, the total quantum capacitance can be expressed as

$$C_{\mathrm{Q}} = e\frac{\partial \langle N \rangle}{\partial V_{\mathrm{g}}} = e^2 \alpha_{\mathrm{g}} \mathrm{DOS}(V_{\mathrm{g}}) \,, \tag{2.20}$$

where on the right side, Eqs. 2.16 and 2.11 were used. In this way, C_{Q} is proportional to the conductance of the nanotube (see Fig. 2.14 (a)) and has its maximum where $\langle N \rangle$ (V_{g}) is steepest.

Ilani *et al.* [Ilani et al., 2006] have measured the total capacitance of a top gated carbon nanotube device at 77 K with values $\sim 200\,\mathrm{aF}$. They approximate the geometric gate capacitance C_{g} with a wire-over-plane model

$$C_{\mathrm{g}} = \frac{2\pi\epsilon}{\ln(4h/d)} L \,, \tag{2.21}$$

where d and L are the wire (nanotube) diameter and length, and h is its distance to the plane (gate electrode). From this model, they receive $C_{\mathrm{g}} \sim 260\,\mathrm{aF}$, suggesting values for the quantum capacitance of $C_{\mathrm{Q}} \sim 870\,\mathrm{aF}$.

2.4. Nanomechanics of carbon nanotubes

The energetically lowermost vibrational modes of suspended carbon nanotubes [Hüttel et al., 2008] are sketched and characterized in their dependence on the resonator length L in Fig. 2.15. The radial breathing mode (RBM) is only dependent on the nanotube diameter and corresponds to the radial expansion and contraction of the CNT lattice. Typically, its energy lies close to $\hbar\omega_{\mathrm{m}} = 10\,\mathrm{meV}$. Intermediate energies are shown by the longitudinal stretching mode, corresponding to a vibration in axial direction. Usually below the electronic excitations originating form the quantum dot confinement, their resonance frequencies depend on the nanotube length as $\sim 1/L$. The energetically lowest form of mechanical vibration is the guitar string like transversal bending mode. It has first been detected in room temperature measurements in the group of P. McEuen [Sazonova et al., 2004]. With a frequency dependence on the nanotube length as $\sim 1/L^2$, they typically show resonances in the $10 - 1000\,\mathrm{MHz}$ range. Additionally, they depend extensively on the mechanical tension, which can be externally applied by electrostatic forces (as e.g. a gate voltage) [Hüttel et al., 2009] or is intrinsically inherited in the device fabrication process. The rest of the chapter will concentrate on the transversal vibrational mode, its description, actuation and detection, and interaction with SET.

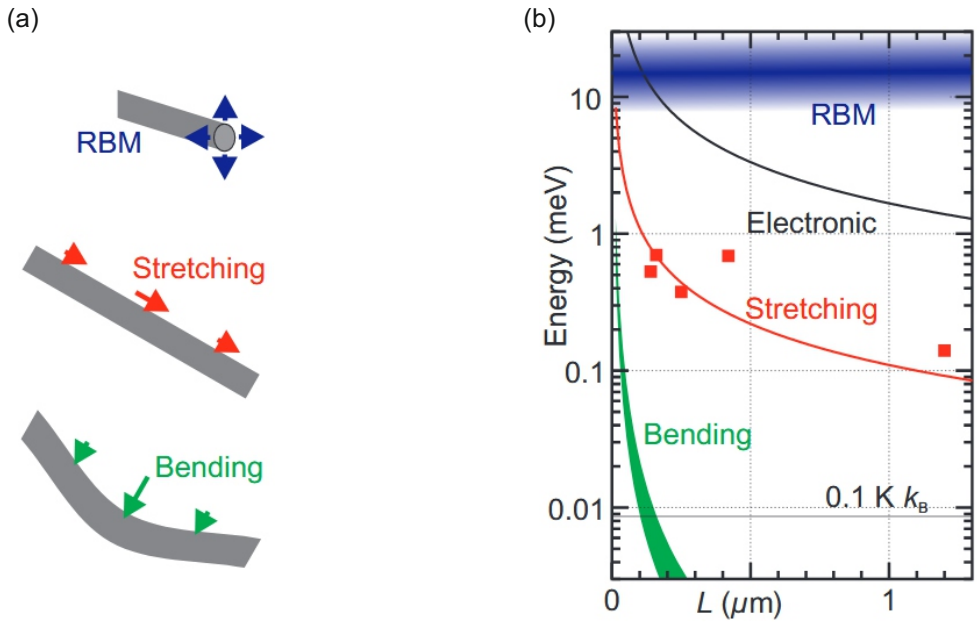

Figure 2.15.: Different mechanical modes that arise in CNTs. Sketches (a) and associated energies (b) of the different forms. In (b), the predicted dependence on the CNT length L is displayed. The widening of the lines of the RBM and the transversal bending mode are due to the additional dependence on the nanotube diameter or (in the case of the transversal mode) the tension. Taken from [Hüttel et al., 2008].

2.4.1. Transversal mode vibrations in carbon nanotube mechanical resonators

Doubly clamped CNTs have shown interesting features of transversal mode vibration [Meerwaldt et al., 2012]. They have at the same time a high Young's modulus of $E \approx 1\,\mathrm{TPa}$ [Lu, 1997], a small diameter, and a low mass density. As a consequence, they can exhibit high mechanical frequencies up to the GHz regime and damping has been shown to be low at cryogenic temperatures [Hüttel et al., 2009]. Thereby, mechanical quality factors of up to 5 million have been experimentally demonstrated [Moser et al., 2014]. These high Q factors allow the observation of interaction between single electron tunneling and motion of the CNT, which can be used as sensitive probe to detect the vibration [Hüttel et al., 2009]. Whereas this electron-phonon interaction leads to additional dissipation and frequency softening [Steele et al., 2009], on the other hand the possibility of sustaining current driven oscillations of the CNT arises [Usmani et al., 2007, Wen et al., 2019]. Originating in the low mass density and high frequency, the zero-point motion amplitude $x_{\mathrm{zpf}} = \sqrt{\hbar/2m\omega_{\mathrm{m}}}$ can achieve values of up to $10\,\mathrm{pm}$ [Poot and van der Zant, 2012].

The starting point for the theoretical description of the bending mode is the Euler-Bernoulli beam equation, where suspended nanotubes are modelled as cylindrical beams [Cleland, 2003, Poot and van der Zant, 2012]. The equation of motion for the displacement $u(x,t)$ in dependence

of time t and position along the beam axis x is

$$\rho A \frac{\partial^2 u}{\partial t^2} + \eta \frac{\partial u}{\partial t} + EI \frac{\partial^4 u}{\partial x^4} - T \frac{\partial^2 u}{\partial x^2} = F_{\text{ext}} \,. \tag{2.22}$$

Here, the first term describes acceleration, where ρA is the product of mass density and cross section area of the beam. The second term describes damping and will be neglected in the following ($\eta = 0$). The restoring force from the bending stiffness (third term) depends on the fourth order derivative of the displacement u with respect to x, with the proportionality factor being the bending rigidity EI (E being the Young's modulus and I being the momentum of inertia). Finally, the fourth term describes the restoring force due to tension T and depends on the second order derivative of the displacement. F_{ext} is an external driving force.

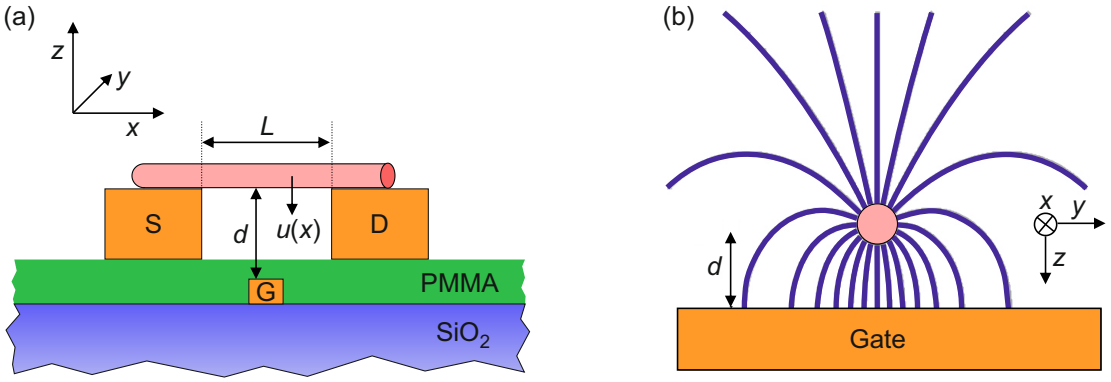

Figure 2.16.: Side (a) and front view (b) of a carbon nanotube mechanical resonator. A segment of length L is suspended between leads above a gate electrode at distance d (a). The CNT can vibrate with position dependent deflection $u(x)$. In (b), the field lines of the electrostatic potential are sketched. (b) adapted from [Poot and van der Zant, 2012].

Now either the third or the fourth term of Eq. 2.22 can dominate the response [Poot and van der Zant, 2012]. In the case where the bending rigidity dominates and the tension term can be neglected, the CNT acts as a *beam resonator*. In the opposite case, where the tension dominates, it behaves as a *string resonator*. For a doubly clamped beam, in both limits

$$u(0,t) = u(L,t) = \frac{\partial u}{\partial x}(0,t) = \frac{\partial u}{\partial x}(L,t) = 0 \tag{2.23}$$

applies. Then, in the case of a beam resonator the eigenfrequencies are given by

$$\omega_n = \sqrt{\frac{EI}{\rho A}} \frac{\beta_n^2}{L^2} \,, \tag{2.24}$$

where β_n has to fulfil $\cos(\beta_n)\cosh(\beta_n) = 1$. In the string resonator case

$$\omega_n = 2\pi \sqrt{\frac{T}{\rho A}} \frac{n+1}{2L} \tag{2.25}$$

is obtained.

In a simplified model, the CNT can be seen as a conductive wire with length L and radius R, that is suspended over an infinite metallic plane (the gate electrode) at distance d (see Fig. 2.16). The deflection dependent capacitance (per unit length) between CNT and gate electrode is then given by

$$C_{\mathrm{g}}(x) = \frac{2\pi\epsilon_0}{\operatorname{arcosh}\left(\frac{d-u(x)}{R}\right)}\,. \tag{2.26}$$

2.4.2. Current-driven oscillations

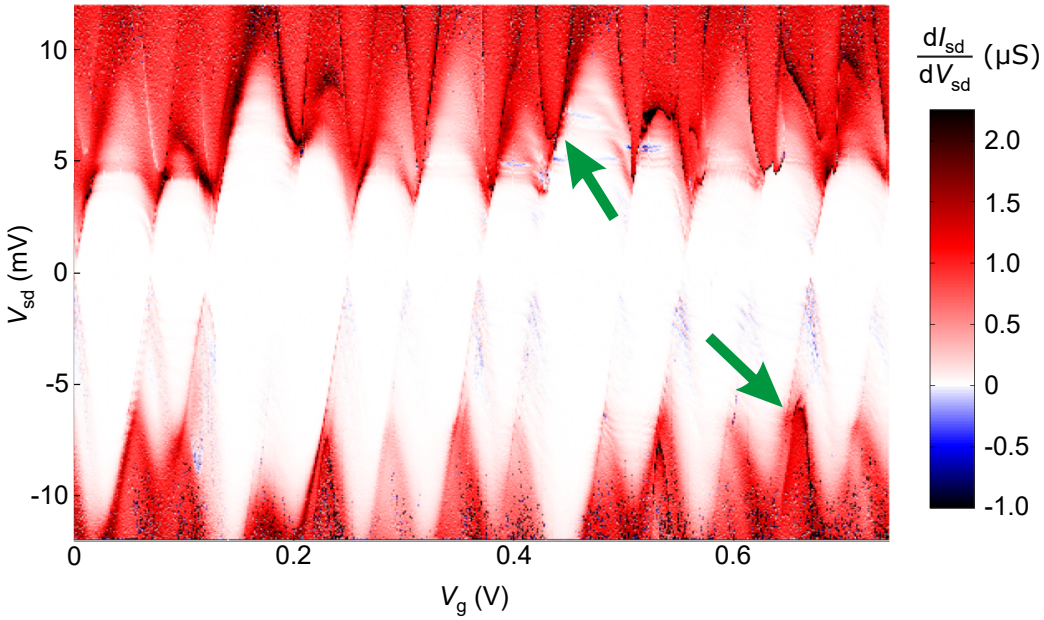

Figure 2.17.: Coulomb diamonds in the positive gate voltage range. Two green arrows mark exemplary sharp ridges in the conductance, that show the onset of current driven mechanical oscillation. The data has been numerically differentiated for better visibility.

The first sign of mechanical activity of the optomechanical CNT device measured in this thesis was observed in the stability diagram of the QD at positive gate voltages. Fig. 2.17 shows the numerically differentiated current in a gate voltage range $0 \leq V_{\mathrm{g}} \leq 0.75\,\mathrm{V}$ and a bias voltage range $-12\,\mathrm{mV} \leq V_{\mathrm{sd}} \leq +12\,\mathrm{mV}$. The onset of mechanical oscillation manifests itself as sharp ridges in the data. This has been previously experimentally observed [Steele et al., 2009, Schmid et al., 2012] and been theoretically described by Usmani *et al.* [Usmani et al., 2007]. They considered a SET device that is weakly coupled to an underdamped mechanical resonator. The motion is generated by strong feedback of the SET events on the resonator. This again strongly modifies the current through the QD, as is explained further in the next section.

2.4.3. Actuation and detection mechanism

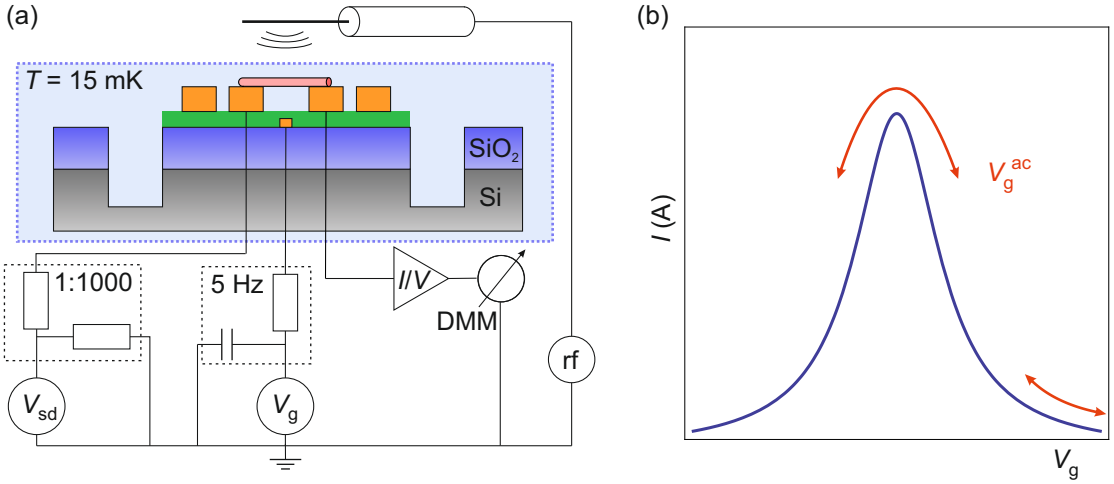

Figure 2.18.: Actuation and detection setup (a) and motion to effective gate voltage conversion mechanism (b). (a) shows the quantum dot spectroscopy setup of Fig. 2.12 where an antenna and a rf generator have been added. (b) The actuation of the vibrational motion of the CNT leads to a time dependent capacitance C_g^{ac}, which can be seen as an effective gate voltage V_g^{ac}. Measuring the time averaged current through the CNT in the vicinity of the SET peak at fixed bias voltage leads to a variation of the current, when the CNT is mechanically active. Adapted from [Hüttel et al., 2009].

For dc characterization of the mechanical mode, another technique is used: the detection principle introduced follows [Hüttel et al., 2009]. For the actuation of mechanical vibration of the CNT, an antenna is placed closely above the device chip (see Fig 2.18 (a)). It consists of a coaxial cable, where the outer conductor and the dielectric have been removed near the end hovering above the chip.

The capacitance between carbon nanotube and gate electrode is given by Eq. 2.26 and can be separated into a static (dc) and a deflection dependent (ac) part $C_g = C_g^{dc} + C_g^{ac}$. When the CNT vibrates on resonance, the amplitude of $C_g^{ac}(t) = (\mathrm{d}C_g/\mathrm{d}u)u_0 \cos(\omega_m t)$ will become large (with the CNT getting closer/further away to/from the gate electrode at frequency ω_m). This will then modulate the current through the CNT quantum dot.

To detect the mechanical resonance, the dc gate voltage is fixed on a SET peak. At small bias voltage, a rf driving signal is applied via the antenna. When the CNT is vibrating, the ac part of the capacitance leads to an effective change in gate voltage $V_g^{ac} = (C_g^{ac}(t)/C_g) \cdot V_g$, shifting the position on the SET peak. A Taylor expansion of the current leads to [Hüttel et al., 2009]

$$I(u_0, V_g) = I(V_g) + \frac{u_0^2}{4}\left(\frac{V_g}{C_g}\frac{\mathrm{d}C_g}{\mathrm{d}u}\right)^2 \frac{\partial^2 I}{\partial V_g^2} + \mathcal{O}(u_0^4)\,. \tag{2.27}$$

As can be seen, the change in current $\Delta I = I(u_0, V_g) - I(V_g)$ is proportional to the curvature of the Coulomb blockade oscillation $\partial^2 I/\partial V_g^2$. It is negative on the oscillation peak giving an

averaged current smaller than the static current. On the flanks, on the other hand, it is positive leading to an averaged current larger than the static current [Hüttel et al., 2009].

As the dc cabling of our measurement setup contains large stray capacitances, the setup behaves as a low-pass filter with a low cut-off frequency. Thus, variations in the current that are situated in the higher MHz range can only be detected as time-averaged currents. This leads to an decrease/increase of dc current at the Coulomb oscillation peak/flanks, when the CNT is vibrating.

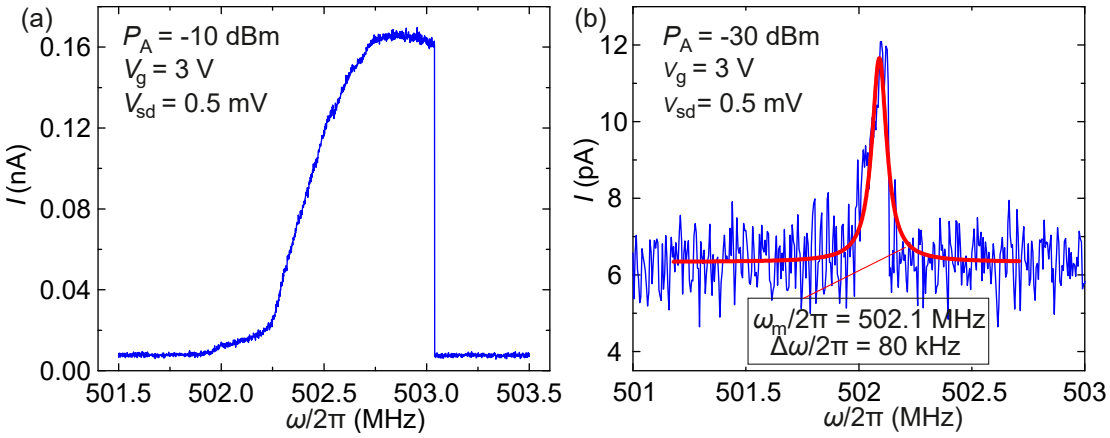

Figure 2.19.: Resonance curves in the high (a) and low power (b) regime. In both measurements, the drive frequency was swept over the mechanical resonance at constant gate and bias voltage, while measuring the dc current. At high drive powers (a), the resonance curve looks highly nonlinear, while at low drive powers (b), a Lorentzian fit can be applied. A quality factor of $Q_\mathrm{m} = 6280$ is obtained.

An exemplary measurement is displayed in Fig. 2.19. The bias voltage was kept constant at a small value $V_\mathrm{sd} = 0.5\,\mathrm{mV}$ and the gate voltage was tuned to the flank of a Coulomb oscillation at $V_\mathrm{g} = 3\,\mathrm{V}$. To detect and characterize the mechanical resonance, the current is now measured continuously, while the antenna frequency is swept (at fixed drive power). When the resonance condition is fulfilled, the aforementioned increase in dc current is observed. For an antenna drive power of $P_\mathrm{A} = -10\,\mathrm{dBm}$ (see Fig. 2.19 (a)), the resonance curve is highly nonlinear. This can be explained by a nonlinear Duffing force term [Hüttel et al., 2009]. At lower drive powers ($P_\mathrm{A} = -30\,\mathrm{dBm}$, see Fig. 2.19 (b)), the peak becomes more linear. A Lorentzian fit results in a mechanical resonance frequency of $\omega_\mathrm{m} = 2\pi \cdot 502.1\,\mathrm{MHz}$, a linewidth of $\kappa_\mathrm{m} = 2\pi \cdot 80\,\mathrm{kHz}$, and thus a quality factor of $Q_\mathrm{m} = \omega_\mathrm{m}/\kappa_\mathrm{m} = 6280$.

2.4.4. Frequency tuning and electromechanical backaction

Applying a dc voltage to the gate electrode, results in an electrostatic force F_el on the carbon nanotube, which is the derivative of the electrostatic energy U

$$F_\mathrm{el} = \frac{\partial U}{\partial z} = \frac{1}{2}\frac{\mathrm{d}C_\mathrm{g}}{\mathrm{d}z}(V_\mathrm{g} - V_\mathrm{CNT})^2\,, \tag{2.28}$$

where V_{CNT} is the voltage on the carbon nanotube. The additional force pulls the CNT closer to the gate electrode and increases its tension, thus leading to *elastic hardening* of the spring constant $k(V_{\mathrm{g}})$, as $k(V_{\mathrm{g}}) = -\partial F_{\mathrm{el}}/\partial z$. In this way, the CNT can be tuned like a guitar string as for a harmonic oscillator $\Delta k \sim \Delta\omega_{\mathrm{m}}$ holds. Increasing the absolute value of the gate voltage leads therefore to an increase in mechanical resonance frequency. Although the relation between ω_{m} and V_{g} is in general more complex [Poot and van der Zant, 2012], the resulting dependency can especially at low gate voltages often be described by a quadratic fit $\omega_{\mathrm{m}}(V_{\mathrm{g}}) \sim \beta V_{\mathrm{g}}^2$ with $\beta > 0$ [Eichler et al., 2013].

Sometimes, however, the gate voltage dependence of the mechanical resonance frequency shows the opposite behaviour: increasing the absolute value of the gate voltage decreases the resonance frequency [Stiller et al., 2013, Wu et al., 2010]. This can be explained by *electrostatic softening*. The charge on the gate electrode and CNT leads to a force that counteracts the restoring force of the mechanical resonator, resulting in a negative contribution to the spring constant. In a simple model, it can be accounted for by $\omega_{\mathrm{m}}(V_{\mathrm{g}}) \sim \beta V_{\mathrm{g}}^2$ with $\beta < 0$

The carbon nanotube investigated in this thesis shows two mechanical modes of similar resonance frequency with peculiar gate voltage behaviour (see Fig.2.20). Both resonances are in the range of $\omega_{\mathrm{m}} \sim 500\,\mathrm{MHz}$ over a large gate voltage range $-10\,\mathrm{volt} \leq V_{\mathrm{g}} \leq +10\,\mathrm{V}$. Lower resonance frequencies have not been observed, leading to the conclusion that these are the fundamental resonances. Given a device length of $L \sim 1\,\mu\mathrm{m}$, this points to the fact that a very high stress has been imprinted onto the CNT during the transfer process. The generally small tuning effect is another indication for high residual tension. Interestingly, when the two modes come close to each other in resonance frequency (at $V_{\mathrm{g}} \approx \pm 8\,\mathrm{V}$), an *avoided crossing* is observed, hinting to a strong coupling between the two modes, which has already been reported in previous publications [Eichler et al., 2012]. The points in Fig 2.20 (b) have been obtained by the trace-wise extraction of the resonance maxima of the data in (a). For the bare modes, a parabolic dispersion ($\omega_{1/2} \sim \beta_{1/2} V_{\mathrm{g}}^2$) has been assumed (green dashed lines). However, one mode shows positive, the other one negative curvature. Both behaviours have been observed in literature as described above. To account for the anticrossings, a coupling parameter W is introduced. The distance in frequency between the two coupled modes is $2W$. The data can then be fitted to

$$\omega_+ = \frac{1}{2}(\omega_1 + \omega_2) + \frac{1}{2}\sqrt{(\omega_1 - \omega_2)^2 + 4|W|^2} \tag{2.29}$$

$$\omega_- = \frac{1}{2}(\omega_1 + \omega_2) - \frac{1}{2}\sqrt{(\omega_1 - \omega_2)^2 + 4|W|^2} \tag{2.30}$$

resulting in the solid lines in Fig. 2.20 (b). Here, ω_+ signifies the upper branch, ω_- the lower one, accordingly. Fitting the data with 2.29 and 2.30, a coupling parameter of $W = 2\pi \cdot 237\,\mathrm{kHz}$ (corresponding to an energy scale of $E \approx 1\,\mathrm{neV}$) is obtained. The appearance of avoided crossings shows that the modes are strongly coupled. This can be also be realised by a comparison between mechanical linewidths and coupling parameter. For the upper branch a decay rate of $\kappa_{\mathrm{m}} \leq 2\pi \cdot 80\,\mathrm{kHz}$ was obtained in the previous section. Assuming the same rate for the lower branch shows both mechanical rates are smaller than the coupling parameter W.

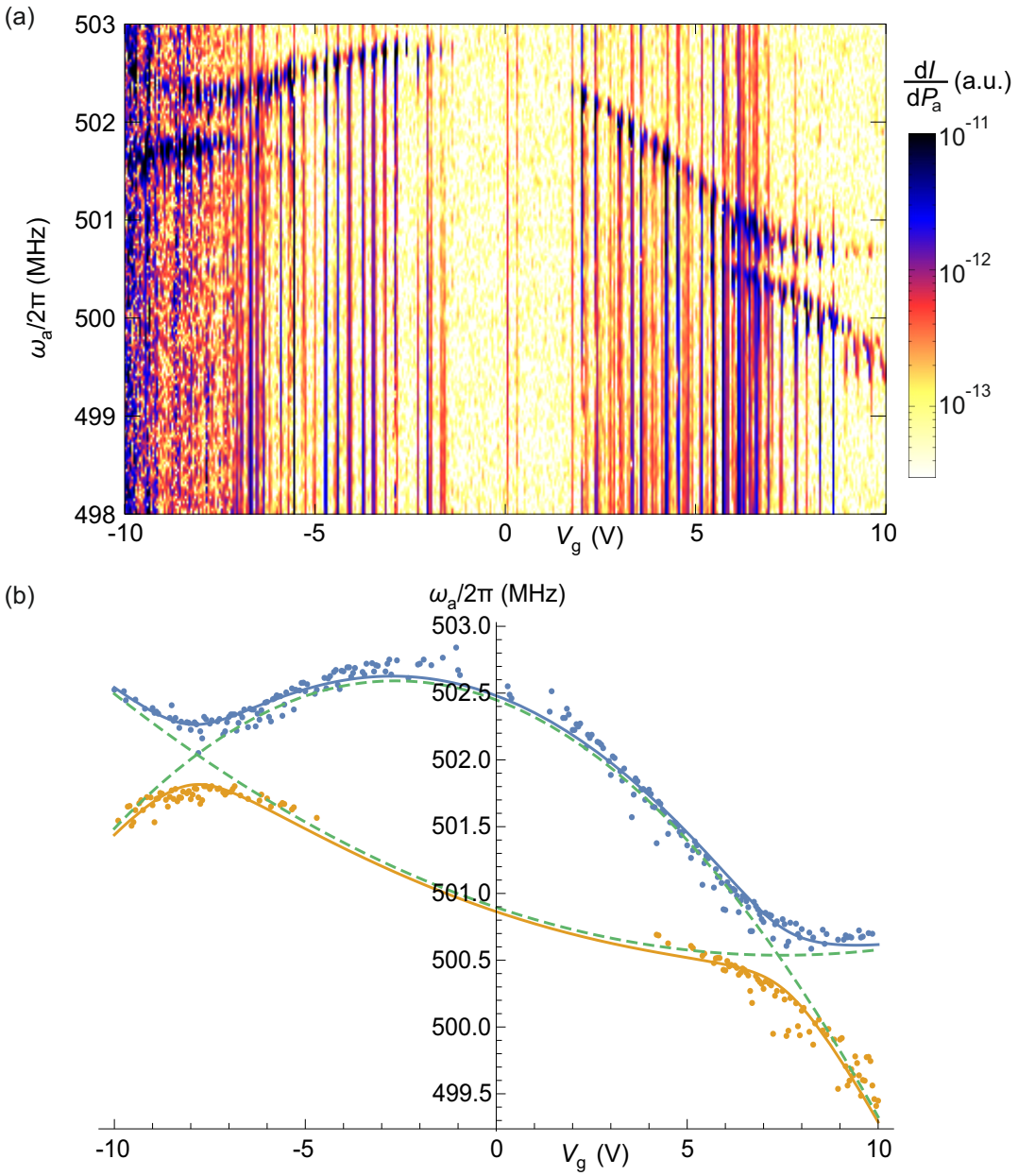

Figure 2.20.: Measurement data (a) and extracted resonance frequencies (b) in dependence of gate voltage. The experimental parameters are $V_{\mathrm{sd}} = 0.5\,\mathrm{mV}$, $P_{\mathrm{A}} = -16\,\mathrm{dBm}$, and $T = 15\,\mathrm{mK}$. The data in (a) is acquired by driving the nanotube with an amplitude modulated drive signal, for details see [Schmid et al., 2012]. In (b), the individual resonance frequencies have been extracted. The CNT shows two gate-dependenent mechanical modes (blue and orange points) that display an avoided crossing at $V_{\mathrm{g}} \approx \pm 8\,\mathrm{V}$. To fit the data, for the bare modes (green dashed lines) a parabolic dispersion has been assumed. Additionally, a coupling parameter common to both anticrossings has been introduced. This results in fit curves (blue and orange solid lines) recreating the gate voltage behaviour of both modes. Adapted from [Blien et al., 2020].

A detailed measurement of the two mechanical modes in a smaller gate voltage range $8.7\,\mathrm{V} \leq V_\mathrm{g} \leq 9.0\,\mathrm{V}$ (see Fig. 2.21) reveals another distinctiveness of CNT mechanical resonators: the coupling of the mechanics to the electronics, called *electromechanical backaction* [Steele et al., 2009, Meerwaldt et al., 2012]. Around the SET peaks, the resonance frequencies drop to lower values. Eq. 2.28 can be used to quantify this spring softening behaviour. The change in spring constant is

$$\Delta k(z, V_\mathrm{g}) = -\frac{\mathrm{d}F_\mathrm{el}}{\mathrm{d}z} = -\frac{1}{2}\frac{\mathrm{d}^2 C_\mathrm{g}}{\mathrm{d}z^2}(V_\mathrm{g} - V_\mathrm{CNT})^2 - \frac{V_\mathrm{g}(V_\mathrm{g} - V_\mathrm{CNT})}{C_\mathrm{g}}\left(\frac{\mathrm{d}C_\mathrm{g}}{\mathrm{d}z}\right)^2 \frac{\partial(V_\mathrm{g} - V_\mathrm{CNT})}{\partial V_\mathrm{g}}\,. \tag{2.31}$$

The first term gives rise to capacitive spring softening and can be neglected for small gate voltage ranges [Meerwaldt et al., 2012]. The voltage on the CNT V_CNT can be expressed by

$$V_\mathrm{CNT} = \frac{q_\mathrm{c} - e\,\langle N\rangle}{C_\Sigma}\,, \tag{2.32}$$

where q_c is called *control charge* and is the charge that would be on the CNT in absence of Coulomb blockade. In the low bias regime and for equal source and drain capacitances $C_\mathrm{s} = C_\mathrm{d}$, it is

$$q_\mathrm{c} = C_\mathrm{g} V_\mathrm{g}\,. \tag{2.33}$$

Then, for the resonance frequency shift $\Delta\omega_\mathrm{m} = \Delta k/2m\omega_\mathrm{m}$ it follows from Eq. 2.31

$$\Delta\omega_\mathrm{m} = \frac{V_\mathrm{g}(V_\mathrm{g} - V_\mathrm{CNT})}{2m\omega_\mathrm{m} C_\Sigma}\left(\frac{\mathrm{d}C_\mathrm{g}}{\mathrm{d}z}\right)^2 \left(1 - \frac{C_\Sigma}{C_\mathrm{g}} - \frac{e}{C_\mathrm{g}}\frac{\partial\,\langle N\rangle}{\partial V_\mathrm{g}}\right)\,. \tag{2.34}$$

The fact that around a Coulomb oscillation $\partial\langle N\rangle/\partial V_\mathrm{g}$ is large, means that here the last term in Eq. 2.34 dominates. Because of the minus sign and $\partial\langle N\rangle/\partial V_\mathrm{g} > 0$, this effect leads to spring softening. A sharper change in charge with gate voltage thus means a larger decrease in mechanical resonance frequency.

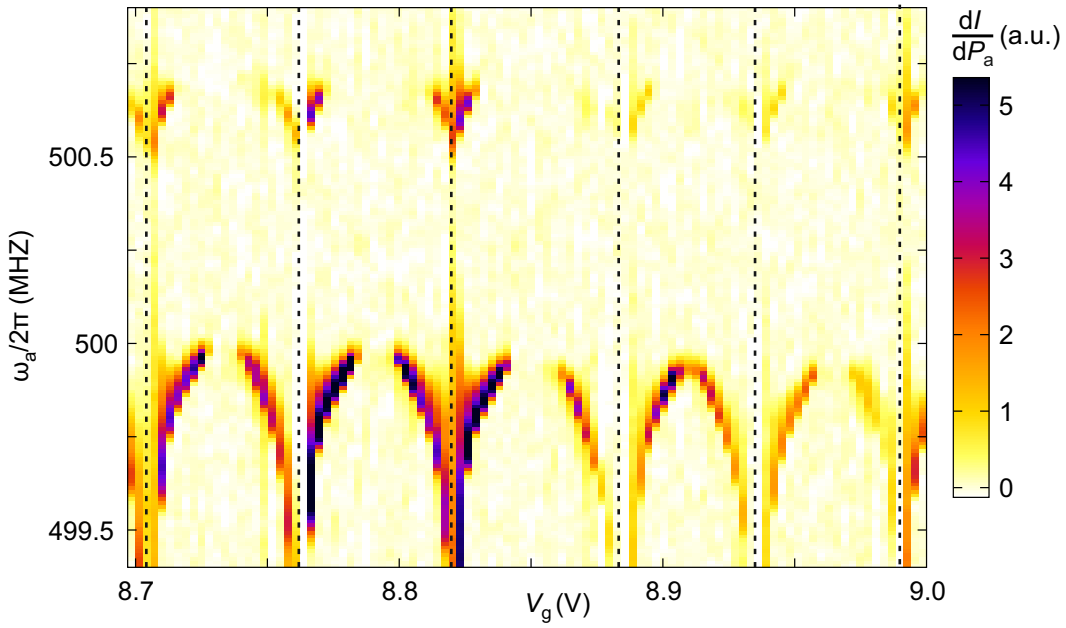

Figure 2.21.: Detailed measurement of the mechanical modes in a smaller gate voltage range covering six Coulomb oscillations (dashed lines). In the vicinity of the Coulomb oscillations, the mechanical frequencies become lower and the Q factor becomes smaller.

3

Cryogenic setup

In this chapter, the measurement apparatus is explained. The main measurements of this work have been recorded in a dilution refrigerator equipped with dc and rf cabling and additional rf components, such as amplifiers, circulators, and attenuators. For rf experiments, a *vector network analyzer* (VNA) is used. Its basic measurement quantities and parameters are explained here.

3.1. Vector Network Analyzer

An important concept in microwave networks is that of the *scattering matrix* $[S]$. It relates the amplitudes of voltages V_j^+ of incident power waves in an n port network to the amplitudes of voltages V_i^- of power waves reflected from this network [Pozar, 2011]. Its elements can be described as

$$S_{ij} = \left.\frac{V_i^-}{V_j^+}\right|_{V_k^+=0 \text{ for } k\neq j} . \tag{3.1}$$

In this thesis, the limitation to a two-port network, where transmission and reflection measurements are carried out, will be sufficient (see Fig. 3.1). Then, S_{11} denotes the reflection coefficient of a wave incident on port 1, whereas S_{21} denotes the transmission coefficient from port 1 to port 2. These generally complex valued scattering coefficients or S-parameters can be measured, using e.g. a VNA.

In the course of this work, a *Rohde&Schwarz (R&S) ZVA24* VNA has been used for high frequency experiments. These devices are equipped with two or more ports that can work both as signal generator and receiver. Since they are based on a heterodyne detection technique they can simultaneously record amplitude and phase of a signal. They are used in transmission and reflection measurements, where the influence of a *device under test* (DUT) in the signal path adds an amplitude and phase shift to the signal. These shifts are obtained by internally comparing the transmitted/reflected signal to the generated one.

VNAs cover a large frequency range, in our case e.g. $10\,\mathrm{MHz} - 24\,\mathrm{GHz}$, where sweeps can be performed. In ordinary experiments, where transmission or reflection of a DUT are tested, the generator frequency is swept over a certain range, while the generator power is fixed. The power level is usually given in dBm, which is the power ratio in dB in reference to $1\,\mathrm{mW}$, i.e. $P_{\mathrm{dBm}} = 10\log_{10}\left(P_{\mathrm{mW}}/1\,\mathrm{mW}\right)$.

A convenient form of representation of the forward transmission is given as $10\log_{10}|S_{21}|^2$ (in dB-scale), directly relating the received signal to the squared amplitude, respectively the power,

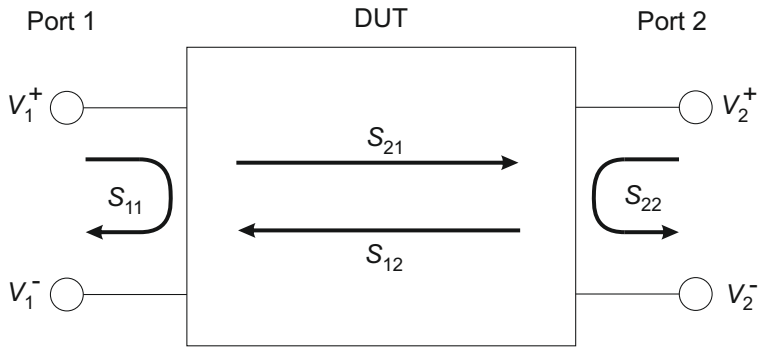

Figure 3.1.: S-parameters of a two port network. Incident voltages are noted as V_i^+, reflected voltages as V_i^- with $i = 1, 2$. S_{11} describes the reflection coefficient on the device back to port 1, S_{21} the transmission coefficient from port 1 to port 2. The same nomenclature holds for port 2.

of the generated signal. Depending on the sign, the power loss/gain imparted by the DUT can directly be read out. The phase is given as $\arg(S_{21})$ in rad.

3.2. 4K Stick

For the pre-characterisation of microwave cavity and carbon nanotube devices, a 4K aluminium dipstick with dc and rf cabling has been used. The device is mounted in an enclosed sample holder with dc and rf connectors. The stick is then pumped, filled with a small amount of helium working as exchange gas, and sunk into a vessel of liquid helium. Within minutes, the cabling, sample holder, and sample have thermalised to roughly $4.2\,\mathrm{K}$ and devices can be pre-examined regarding their dc and rf behaviour.

3.3. Dilution Refrigerator

For the optomechanical experiments, very low temperatures are necessary because of several reasons:

1. In order for the coplanar resonators to obtain very high quality factors, the experiments should take place in environments well below the transition temperature of the superconductor in use. In our case niobium ($T_\mathrm{c} \approx 9\,\mathrm{K}$) or an alloy made of rhenium and molybdenum ($T_\mathrm{c} \approx 5 - 8\,\mathrm{K}$) were used, for which a temperature of $T \approx 2\,\mathrm{K}$ would be low enough to result in high Q factors.

2. Also, the thermal excitation of the coplanar resonator mode plays a role. To minimise the noise of an undriven cavity, e.g. in upconversion experiments (see Sect. 7.3.2), the thermal energy should be smaller than the energy of a microwave quantum at the cavity resonance frequency ω_cav. This means that the temperature should be smaller than $\hbar\omega_\mathrm{cav}/k_\mathrm{B} \approx 280\,\mathrm{mK}$ for $\omega_\mathrm{cav} = 5.8\,\mathrm{GHz}$.

3. The effects that establish a reasonably large optomechanical coupling are mediated by the nonlinear conductance of the carbon nanotube (see Sect. 2.3.4 and 7.2). In order to reach the sharpest possible Coulomb oscillations, the quantum dot behaviour has to be in the lifetime broadened regime, where $T \ll \hbar\Gamma_{\mathrm{broad}}/k_{\mathrm{B}}$. As the tunnel rates are usually in the range of a few hundred GHz, this means that the temperature has to be much lower than a few Kelvin.

4. With the objective of manipulating the motion of the mechanical resonator using radiation pressure forces (see Sect. 7.3), it is convenient to pre-cool it thermally as close as possible to its quantum ground state. For a CNT mechanical resonator with $\omega_{\mathrm{m}} \approx 2\pi \cdot 500\,\mathrm{MHz}$, this means that its ground state is reached below $T = \hbar\omega_{\mathrm{m}}/k_{\mathrm{B}} \approx 25\,\mathrm{mK}$.

All these conditions can be met with our Oxford Instruments Kelvinox 400HA dilution refrigerator, that is shown in an annotated photograph in Fig. 3.2. It has a nominal base temperature of about $T = 7\,\mathrm{mK}$. A *LakeShore 370 AC* resistance bridge and temperature controller reads out thermometers and is capable of adding power to heaters at the sorb, still-, or mixing chamber-stage.

The dc cabling is implemented as twisted pair cables in a loom wire that is thermalised at every temperature stage. High frequency filtering is performed with RC filters at the still stage and an RLC filter box that is at room temperature directly plugged onto the cryostat. The device is mounted in a copper sample holder that is screwed to a sample stage made of silver and stainless steel connected to the mixing chamber stage.

3.4. Buildup of high frequency setup

A wiring diagram that has been used to detect optomechanical induced transparency in our device (see Sect. 7.2.2), is displayed in Fig. 3.3 (a). Taking all rf components into account, the system is capable of processing signals in a frequency range $4 - 8\,\mathrm{GHz}$.

A *R&S SMB 100A* microwave source creates a strong drive tone that is added to a weak probe tone generated by the *R&S ZVA24* VNA. The signal combination takes place in a *Fairview Microwave MC2047-20* directional coupler. This is a device that has two input ports. The mw source is connected to the direct port, which sends the signal to the output port without attenuation; the VNA is connected to the coupled port, which couples the signal with $-20\,\mathrm{dB}$ to the output port. Power that enters the output port is not sent back to the coupled port, but to a fourth, isolated port (terminated with a load) and to the direct port.

The signal transmission happens via UTF85 semirigid coaxial cables. From the 1K stage on, superconducting NbTi cables are used. These offer minimal thermal conductance between the individual temperature stages of the dilution refrigerator. At every one of these stages, thermally anchored attenuators are inserted, leading to a total input attenuation of $-53\,\mathrm{dB}$; see Fig.3.3 (a). These serve to thermalise the inner conductor of the coaxial cables so as not to heat the sample, which shall be cooled to dilution refrigerator base temperature. Additionally, Johnson noise emitted by preceding stages is effectively blocked.

The device chip is glued and bonded to a PCB "sandwich"; see Fig.3.3 (b). It contains two Mini-SMP connectors for high frequency signals and a Micro-D connector for up to 24 dc wires.

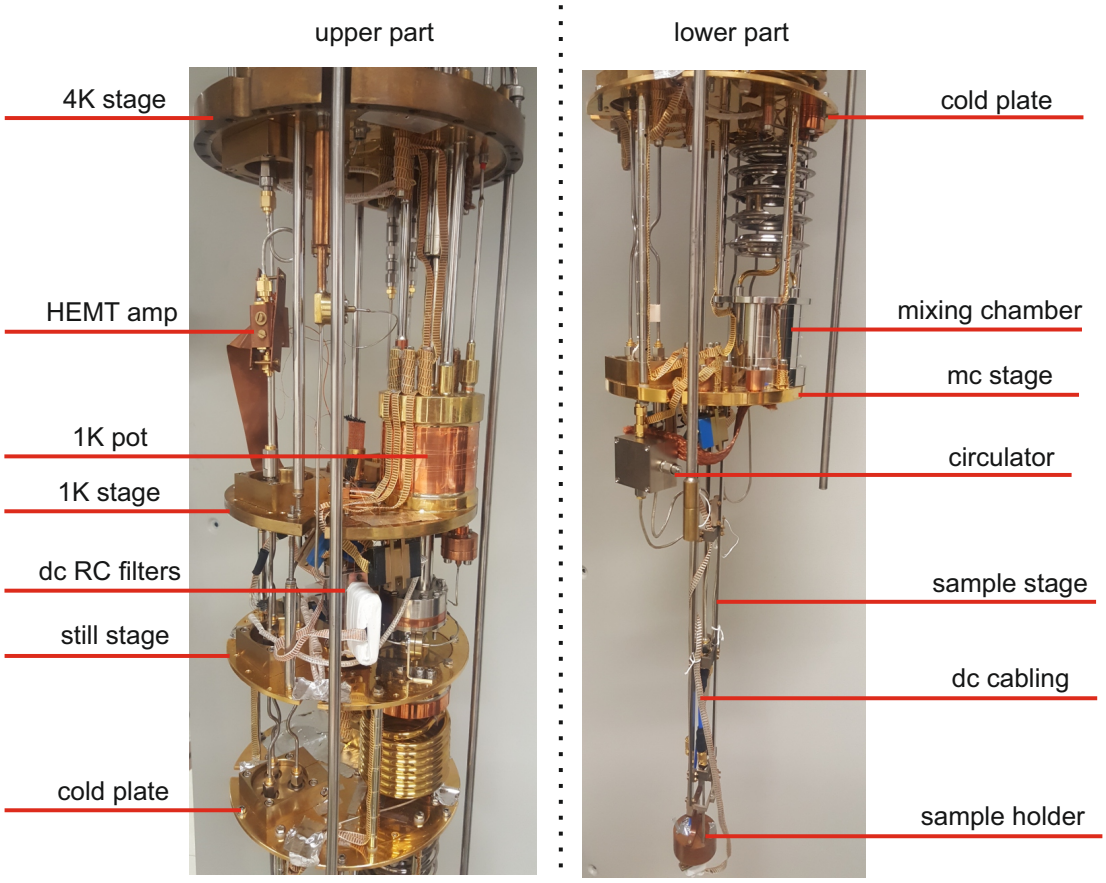

Figure 3.2.: Kelvinox 400HA dilution refrigerator with vacuum and radiation shield removed. Temperature stages and important rf and dc components are marked.

The PCB is enclosed by a copper sample holder with small openings for the coaxial cables.

Directly after having passed through the device, the signal is guided through a *Quinstar CTH0408KCS* circulator mounted at the mixing chamber stage to the hf output line of the cryostat. A terminated third port on the circulator blocks noise from higher temperature stages.

The signal is then passed through a chain of amplifiers. A cryogenic low-noise HEMT amplifier (*Caltech CITCRYO 1-12*) is placed at the 1K stage. In the frequency range eligible for our setup, it has a gain of $\sim 30\,\mathrm{dB}$ and a noise temperature of $\sim 3\,\mathrm{K}$ specified by manufacturer tests. At room temperature, the first amplifier is a narrow-band *Miteq AFS3-04000800-10-10P-4* with a noise temperature of $\leq 75.1\,\mathrm{K}$, followed by a wide band *Miteq AFS3-00101200-35-ULN* with a noise temperature of $\leq 359.2\,\mathrm{K}$. Both room temperature amplifiers have a gain of about $30\,\mathrm{dB}$. The total amplifier chain has thus a noise temperature of $T_{\mathrm{noise}} \sim 3.075\,\mathrm{K}$. Subsequently, the signal is detected by the VNA.

In some experiments an additional antenna was used for rf excitation of the mechanical resonator. Signals in the designated frequency range were applied using a *R&S SMB 100A* mw

source. The rf cabling inside the cryostat is a completely unattenuated coaxial line leading to the sample stage. As described in Sect. 2.4.3, the antenna is a coaxial cable where the outer conductor and the dielectric have been removed near the end. This part is located inside the sample holder, suspended several mm above the chip.

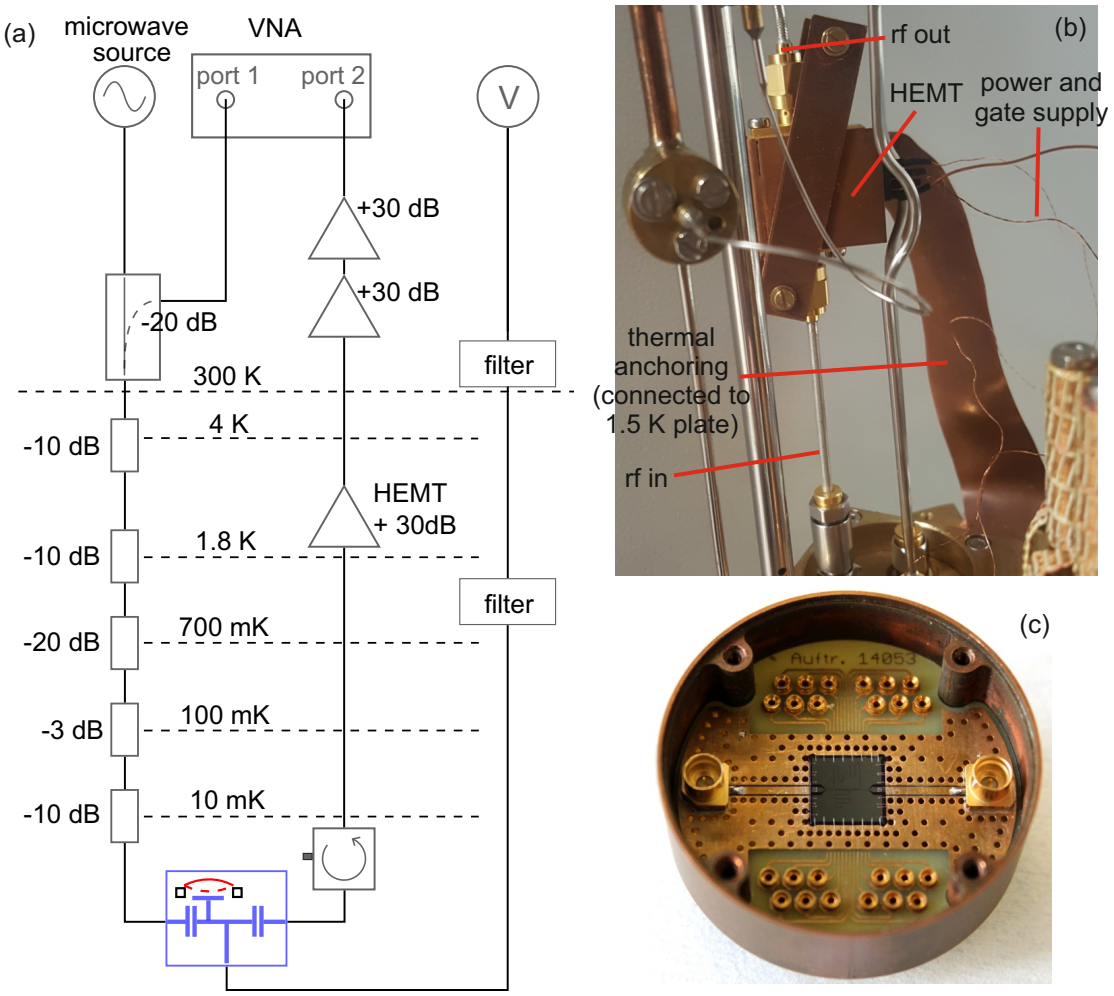

Figure 3.3.: High frequency measurement setup. (a) Schematic of the cryostat with the most important dc and rf components used to detect optomechanical induced transparency. In (b), a close up photograph of the HEMT amplifier, its thermal anchoring, and wiring for the power supply is shown. (c) Top view of sample holder with a device glued and bonded to a PCB. Microwave signals can be applied via the Mini-SMP ports, dc signals via a total of 24 vias that lead to a connector on the bottom side. (a), (c) adapted from [Blien et al., 2020].

4

Coplanar Waveguide Resonators

In this thesis, superconducting half wave resonators were used as photonic resonators in optomechanical experiments and quarter wave resonators have been used to derive high frequency characteristics of a molybdenum/rhenium alloy. This chapter deals with the theoretical description of these resonators. First, the language for describing coplanar waveguides and related parameters is defined. Then, it is investigated how superconductivity changes the waveguide properties. Finally, the working principles, regimes, and parameters of the resonators are presented.

4.1. Introduction to Coplanar Waveguides

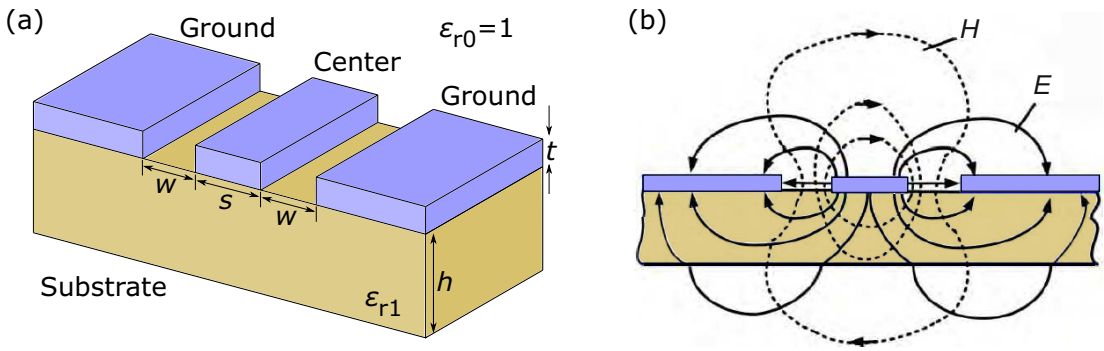

Figure 4.1.: Schematic drawing of a CPW (a) Metal (blue) and substrate (dark yellow) with corresponding dimensions: central conductor width s, metal film thickness t, substrate height h, gap width w, and relative dielectric permittivity of substrate ϵ_{r1} (b) Transversal electric and magnetic field components of a quasi-TEM mode. Adapted from [Chaimool and Akkaraekthali, 2012]

The *coplanar waveguide* (CPW) was invented by Cheng P. Wen in 1969 [Wen, 1969] and is used to convey signals in the microwave frequency domain. This planar form of transmission line consists of a central conductor separated by gaps from two ground planes on the same side of a dielectric substrate. Thus, CPWs can be conveniently fabricated using top-down processes and active and passive elements can be easily integrated. The overall characteristics are governed by mainly three parameters, the effective dielectric constant ϵ_{eff}, the characteristic impedance Z_0, and the attenuation constant α [Simons, 2001]. These parameters are defined by the geometric

dimensions of the waveguide: central conductor width s, metal film thickness t, substrate height h, gap width w, and relative dielectric permittivity of air and substrate $\epsilon_{\mathrm{r}0/1}$; see Fig. 4.1(a).

Crucial for any form of waveguide is the ability to transport energy in *transverse modes*: either one (= transverse electric or TE, transverse magnetic or TM) or both (= transverse electromagnetic or TEM) the electric and magnetic field components in propagation direction vanish. While hollow cavity waveguides only support TE and TM modes, TEM waves can exist when at least two conductors are present [Pozar, 2011], e.g. in coaxial cables. This can be attributed to the boundary conditions the waveguides impose on the waves. Comparable to high pass filters, TE and TM modes possess a non-zero *cutoff frequency* below which propagation can not occur. For TEM modes such as, e.g., plane waves, the cut-off frequency is zero. Modes supported in CPWs are not true TEM. However, their longitudinal field components are small and they are thus referred to as quasi-TEM [Pozar, 2011]. The transverse electric and magnetic field distribution in CPWs is shown in figure 4.1(b).

A disadvantage of coplanar waveguides is the existence of an additional mode, the slotline mode, with also zero cutoff frequency. There is a need to suppress this mode, as the distribution of energy to multiple modes is unwanted. As the slotline mode is an odd mode, this can be achieved by potential equalisation of the two ground planes by, e.g., metallic airbridges or overbonding.

4.2. Important Microwave Parameters

4.2.1. Transmission Line Model

A CPW can be described by a generic two-wire model that is applicable for all kinds of transmission lines. It has to be used when the signal contains large enough frequencies, so that voltage and current significantly vary over cable and device dimensions [1]. Otherwise, there will be substantial radiation power losses and reflections of the signal at discontinuities [Pozar, 2011]. Strictly being a distributed parameter network (voltage and current vary in magnitude and phase over its length), it is represented in this model by lumped element quantities which are defined per unit length.

These quantities are

- *Resistance* R, resulting from the finite conductivity of the wire material,
- *Inductance* L, the series self-inductance of the wires,
- *Shunt conductance* G, originating in dielectric losses in the material between the wires,
- *Capacitance* C, emerging from the adjacent conductors.

Applying Kirchhoff's laws and plane wave solutions for the time evolution of voltage and current, the *telegrapher equations* in the steady-state form can be derived

$$\frac{dV(z)}{dz} = -(R + j\omega L)I(z)\,, \tag{4.1}$$

[1] As a rule of thumb: if the component is larger than 10% of the wavelength, the two-wire model has to be used.

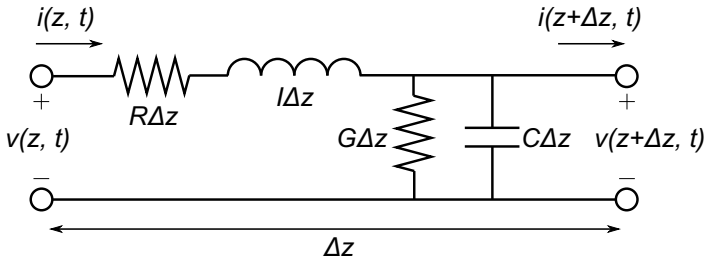

Figure 4.2.: Lumped elements equivalent circuit of a transmission line of length Δz. Resistance R, inductance L, shunt conductance G, and capacitance C of the two wires are defined per unit length. The current is flowing along the wires, while there is a voltage difference between the wires. Adapted from [Pozar, 2011].

$$\frac{dI(z)}{dz} = -(G + j\omega C)V(z)\,. \tag{4.2}$$

These can easily be solved by using travelling wave solutions

$$V(z) = V_0^+ e^{-\gamma z} + V_0^- e^{+\gamma z}\,, \tag{4.3}$$

$$I(z) = I_0^+ e^{-\gamma z} + I_0^- e^{+\gamma z}, \tag{4.4}$$

with the *complex propagation constant*

$$\gamma = \alpha + j\beta = \sqrt{(R + j\omega L)(G + j\omega C)}\,, \tag{4.5}$$

that consists of a real part, the *attenuation constant* α, and an imaginary part, the *phase constant* β. The phase constant is related to the wavelength of the signal as $\beta = 2\pi/\lambda$ and the phase velocity of the waves travelling in the CPW is $v_{\mathrm{ph}} = \omega/\beta$.

As a result, the *characteristic impedance* Z_0 of a transmission line can be defined. It relates the voltage to the current of a single uni-directional propagating wave as

$$Z_0 = \frac{V_0^+}{I_0^+} = \frac{-V_0^-}{I_0^-} = \sqrt{\frac{R + j\omega L}{G + j\omega C}} \tag{4.6}$$

and is only dependent on the transmission line material and geometry but not on its length (for a homogeneous line). This is a very fundamental quantity in microwave physics: the characteristic impedances of individual circuit components have to match (or be matched) in order to avoid signal reflections. Also, a transmission line has to be terminated by an impedance (e.g. the input impedance of a microwave device) equal to the characteristic impedance for the same reason.

The attenuation constant α is in the frequency range of this thesis mainly composed of two contributions [Simons, 2001]

$$\alpha = \alpha_{\mathrm{d}} + \alpha_{\mathrm{c}}\,, \tag{4.7}$$

where α_{d} is the *dielectric loss* and α_{c} is the *conductor loss*. The latter is generally not easy to calculate and depends on frequency, conductivity and field distribution of the waveguide. The

method in use depends on the ratio between skin depth and film thickness (normal conductor) or penetration depth (see Sect. 4.3) and film thickness (superconductor). Other loss mechanisms are self-radiation losses and resistive losses due to finite temperatures or external radiation; for more information, see [Simons, 2001]. The attenuation constant due to dielectric losses is given in Sect. 4.2.2.

In a lossless transmission line [2], where conductor and dielectric losses can be neglected ($R = G = 0$), it is found from equation 4.5 that the attenuation constant is zero $\alpha = 0$ and the phase constant is equal to $\beta = \omega\sqrt{LC}$. The phase velocity is then given by $v_{\mathrm{ph}} = 1/\sqrt{LC}$, while equation 4.6 simplifies to

$$Z_0 \approx \sqrt{\frac{L}{C}} = \frac{1}{C v_{\mathrm{ph}}} \,. \tag{4.8}$$

Note that in the case of a lossless line the propagation constant γ is purely imaginary, whereas the characteristic impedance Z_0 is a real number, typically chosen to be $Z_0 = 50\,\Omega$.

4.2.2. Characteristic Impedance and Effective Permittivity

In the previous chapter, it was stated that for microwave applications, the characteristic impedance of the components has to be taken into consideration. In practical cases, the components can be regarded as lossless, so that equation 4.8 holds. Next, it will be shown how to calculate and determine the characteristic impedance of CPWs. For the definition of geometrical parameters, see figure 4.3.

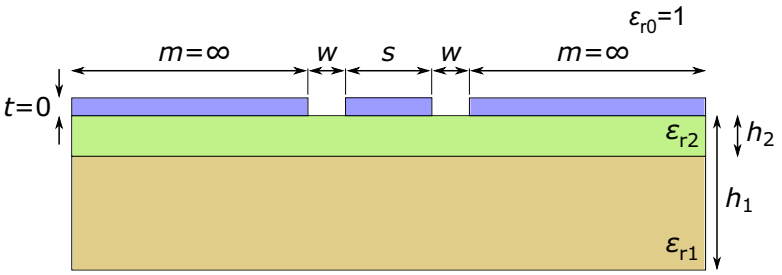

Figure 4.3.: Geometric parameters used in the calculation of C, L, ϵ_{eff}, and Z_0: central conductor width s, gap width w, substrate heights $h_{1/2}$, and dielectric constants $\epsilon_{\mathrm{r}1/2}$. The dielectric constant of vacuum set to unity $\epsilon_{\mathrm{r}0} = 1$, the metal film is presumed as infinitely thin $t = 0$, and the ground planes are presumed as infinitely wide $m = \infty$. Adapted from [Veyres and Hanna, 1980].

All calculations in this chapter are made under the following implicit assumptions:

- The ground planes are much wider than the gap and centerline size, so they can be thought of as infinitely wide ($m \gg s, w \;\Rightarrow\; m \to \infty$).

[2] The assumption of a lossless line in this definition is adequate not only in the case of superconductors but also for normal metals in most practical cases.

- The metal film is much thinner than the gap and centerline size, so it can be thought of as infinitely thin ($t \ll s, w \Rightarrow t \to 0$).
- The CPW is unshielded, i.e., there is no metal plane above or below the CPW in a distance comparable to the gap and centerline size.

Following Simons [Simons, 2001], the capacitance of a CPW per unit length can be subdivided into individual parts

$$C_{\mathrm{CPW}} = C_1 + C_2 + C_{\mathrm{Air}}\,. \tag{4.9}$$

Here, $C_{1/2}$ are the partial waveguide capacitances that account only for substrate layer 1/2 and C_{Air} is the capacitance if no dielectric layers were present.

Single-Layer Substrate

In this limiting case, the substrate height of the second layer is set to zero $h_2 = 0$, so that C_2 must vanish

$$C_{\mathrm{CPW}} = C_1 + C_{\mathrm{Air}}\,. \tag{4.10}$$

Using conformal mapping techniques [Veyres and Hanna, 1980], formulas for these capacitances can be derived

$$C_1 = 2\epsilon_0(\epsilon_{\mathrm{r}1} - 1)\frac{K(k_1)}{K(k_1')}\,, \tag{4.11}$$

$$C_{\mathrm{Air}} = 4\epsilon_0\frac{K(k_0)}{K(k_0')}\,, \tag{4.12}$$

where $K(k)$ is the complete elliptic integral of the first kind

$$K(k) = \int_0^1 \frac{dt}{\sqrt{(1-t^2)(1-k^2t^2)}} \tag{4.13}$$

and

$$k_1 = \frac{\sinh(\pi s/4h_1)}{\sinh(\pi(s+2w)/4h_1)}\,, \tag{4.14}$$

$$k_0 = \frac{s}{s+2w}\,, \tag{4.15}$$

$$k_i' = \sqrt{1-{k_i}^2} \quad \text{with}\, i = 0, 1\,. \tag{4.16}$$

Putting equations 4.11 and 4.12 in equation 4.10 gives the overall waveguide capacitance

$$C_{\mathrm{CPW}} = 2\epsilon_0(\epsilon_{\mathrm{r}1} - 1)\frac{K(k_1)}{K(k_1')} + 4\epsilon_0\frac{K(k_0)}{K(k_0')}\,. \tag{4.17}$$

In a similar way, an expression for the total waveguide inductance per unit length can be derived [Watanabe et al., 1994], if one assumes a film thickness smaller than twice the magnetic penetration depth (see Sect. 4.3) and a uniform current density across the film thickness

$$L_{\mathrm{CPW}} = \frac{\mu_0}{4}\frac{K(k_0')}{K(k_0)}\,. \tag{4.18}$$

Note that non-magnetic substrates have been assumed. In this case, the inductance is not affected by the substrate, because it has the same relative magnetic permittivity as vacuum $\mu_\mathrm{r} = 1$ [Clarke, 2007].

Now, an *effective dielectric permittivity* can be defined as [Collin, 2001]

$$\epsilon_\mathrm{eff} = \frac{C_\mathrm{CPW}}{C_\mathrm{Air}} = 1 + \frac{\epsilon_\mathrm{r1} - 1}{2} \frac{K(k_1)}{K(k_1')} \frac{K(k_0')}{K(k_0)} = 1 + F(\epsilon_\mathrm{r1} - 1)\,, \tag{4.19}$$

where F is the *filling factor*, accounting for the ratio of electric energy in the substrate to total electric energy of the waveguide. The effective dielectric permittivity can be thought of as a relative permittivity of a homogenous medium surrounding the waveguide, because the total waveguide capacitance can then be written as

$$C_\mathrm{CPW} = \epsilon_\mathrm{eff} C_\mathrm{Air} = 4\epsilon_0 \epsilon_\mathrm{eff} \frac{K(k_0)}{K(k_0')}\,. \tag{4.20}$$

A simplification worth mentioning can be given in the limit of thick substrate ($h_1 \to \infty$). Then, $k_1 \to k_0$ and equation 4.19 reduces to

$$\epsilon_\mathrm{eff} = \frac{\epsilon_\mathrm{r1} + 1}{2} \quad \text{with} \quad F = \frac{1}{2}\,. \tag{4.21}$$

This can be interpreted in a way that the electric field of the signal is evenly distributed so that exactly half of it permeates the substrate. As a consequence, the effective permittivity is the mean value of the dielectric constants of substrate and air.

With the help of these parameters, the dielectric loss of Eq. 4.7 can be given by

$$\alpha_\mathrm{d} = \frac{\omega}{2c} \frac{\epsilon_\mathrm{r}}{\sqrt{\epsilon_\mathrm{eff}}} F\vartheta\,. \tag{4.22}$$

Here, ϑ is the *loss tangent* and is usually defined as the ratio of the imaginary to real part of the dielectric constant $\epsilon = \epsilon' - i\epsilon''$ with $\epsilon = \epsilon_\mathrm{r}\epsilon_0$ [Pozar, 2011].

The effective dielectric permittivity affects the phase velocity as

$$v_\mathrm{ph} = \frac{1}{\sqrt{L_\mathrm{CPW} C_\mathrm{CPW}}} = \frac{c}{\sqrt{\epsilon_\mathrm{eff}}}\,, \tag{4.23}$$

c being the speed of light in vacuum.

From equations 4.8, 4.18, 4.20, and 4.23, the characteristic impedance of the CPW can be specified by

$$Z_0 = \frac{1}{4\epsilon_0 c \sqrt{\epsilon_\mathrm{eff}}} \frac{K(k_0')}{K(k_0)} \approx \frac{30\pi}{\sqrt{\epsilon_\mathrm{eff}}} \frac{K(k_0')}{K(k_0)}\,. \tag{4.24}$$

Knowing the effective permittivity of the substrate, the waveguide geometry can be chosen in such a way that the characteristic impedance of the CPW matches that of the surrounding circuitry. The above expressions for Z_0 and ϵ_eff were also derived in the original paper by Wen [Wen, 1969].

Double-Layer Substrate

As many of the devices in this thesis were fabricated on substrates consisting of two dielectric layers of different material, it shall also briefly be shown how the formulas for single-layer substrates have to be altered for this case. For a more detailed derivation see [Simons, 2001, Gevorgian et al., 1995].

The situation of a second layer (sandwiched between the first layer and the metal, see Fig. 4.3) can easily be implemented by modifying the effective permittivity as

$$\epsilon'_{\mathrm{eff}} = \epsilon_{\mathrm{eff}} + \frac{\epsilon_{\mathrm{r}2} - \epsilon_{\mathrm{r}1}}{2} \frac{K(k_2)}{K(k'_2)} \frac{K(k'_0)}{K(k_0)} \,, \tag{4.25}$$

where k_2 and k'_2 are given as in equations 4.14 ad 4.16 with the height of the second layer h_2.

Then, all formulas for the parameters of a single-layer substrate are valid in the case of a double-layer substrate, when using this altered effective permittivity ϵ'_{eff}. Concretely, the characteristic impedance is given by

$$Z_0 = \frac{1}{4\epsilon_0 c \sqrt{\epsilon'_{\mathrm{eff}}}} \frac{K(k'_0)}{K(k_0)} \,. \tag{4.26}$$

For vanishing layer thicknesses ($h_2 \ll s, w$), the second summand in equation 4.25 is close to zero and the effective permittivity regains the expression of the single-layer case (equation 4.19).

4.3. The role of superconductivity

Up until this point the theory on CPWs was not specific to the type of metal. In this section effects originating from superconductivity will be investigated. These play a major role in the field of CPW resonators, as they drastically enhance or influence the resonator characteristics. With this section, a theoretical basis for the description of superconductors used in microwave applications will be formed. This is required in later chapters for the experimental determination of material properties using superconducting resonators.

4.3.1. Two-Fluid Model and Complex Conductivity

In experiments dealing with dc currents, superconductors can be treated as lossless conductors. Additionally, due to the Meißner-Ochsenfeld effect which leads to the spontaneous expulsion of a magnetic field from a superconductor, they are perfectly diamagnetic. Only in the case of large magnetic fields or currents, normal conducting regions, that can contribute to the electric resistance, appear. Yet, electromagnetic fields penetrate into the superconductor with a finite magnetic penetration depth, which can be seen equivalently to the skin depth of normal metals. This behaviour is commonly described by the two phenomenological *London equations* [London and London, 1935]

$$\frac{\partial}{\partial t} \vec{j}_{\mathrm{s}} = \frac{n_{\mathrm{s}} e^2}{m} \vec{E} \,, \tag{4.27}$$

$$\mathrm{rot}\vec{j_\mathrm{s}} = -\frac{n_\mathrm{s}e^2}{m}\vec{B}\,. \tag{4.28}$$

Here, j_s is the supercurrent density and n_s is a phenomenological parameter. Using the Maxwell equation $\mathrm{rot}\vec{B} = \mu_0\vec{j}$ on the second London equation, one obtains

$$\Delta\vec{B} = \frac{1}{\lambda_\mathrm{L}^2}\vec{B}\,, \tag{4.29}$$

which describes the exponentially decaying magnetic field in the superconductor perpendicular to the surface with a temperature dependent characteristic length λ_L. At $T = 0$, the *London penetration depth* λ_L0 is given by

$$\lambda_\mathrm{L0} = \sqrt{\frac{m}{\mu_0 n_\mathrm{s} e^2}}\,. \tag{4.30}$$

In the *two-fluid model*, the phenomenological parameter n_s of the London equations 4.27, 4.28 can be identified with the density of electrons in the superconducting phase. The charge carrier density in the superconductor thus consists of a part n_n describing unpaired electrons (thermal quasiparticle excitations) and a part n_s describing electrons condensed into Cooper pairs [Tinkham, 2004]

$$n = n_\mathrm{n} + n_\mathrm{s}\,. \tag{4.31}$$

The classical equation of motion for charge carriers in the standard Drude model is

$$m\frac{\partial}{\partial t}\vec{v} = e\vec{E} - m\frac{\vec{v}}{\tau}\,, \tag{4.32}$$

with the drift velocity $\vec{v}$ and the scattering time τ. The charge carriers in the two-fluid model then generate two currents

$$\vec{j}_\mathrm{s/n} = n_\mathrm{s/n}e\vec{v} = \sigma_\mathrm{s/n}\vec{E}\,, \tag{4.33}$$

that can be expressed via two conductivities $\sigma_\mathrm{s/n}$. Assuming harmonic regimes for current end electric field ($\vec{j}, \vec{E} \propto \mathrm{e}^{i\omega t}$) in Eqs. 4.32, 4.33, one obtains for the quasiparticles the ac Drude conductivity

$$\sigma_\mathrm{n} = \frac{n_\mathrm{n}e^2}{m}\frac{1}{i\omega + 1/\tau_\mathrm{n}} \tag{4.34}$$

In a coarse approximation, for the superconducting electrons $\tau_\mathrm{s} \to \infty$ holds. Then, the first London equation 4.27 is directly obtained from equations 4.32, 4.33. The conductivity of the superfluid is now

$$\sigma_\mathrm{s} = -i\frac{n_\mathrm{s}e^2}{m\omega} = -\frac{i}{\mu_0\omega\lambda_\mathrm{L}^2} \tag{4.35}$$

The total conductivity is a complex number and can be written as

$$\sigma = \sigma_\mathrm{n} + \sigma_\mathrm{s} = \sigma_1 - i\sigma_2\,. \tag{4.36}$$

This *complex conductivity* was first introduced by Glover and Tinkham [Glover and Tinkham, 1957]. In the limit $\omega\tau_\mathrm{n} \ll 1$ (which is typically valid for microwave frequencies [Tinkham,

2004]), the quasiparticle conductivity in Eq. 4.34 reduces to $\sigma_{\mathrm{n}} = n_{\mathrm{n}} e^2 \tau_{\mathrm{n}}/m = \sigma_1$ (the imaginary part is neglected). From this, it can be seen that the contribution of the quasiparticles to the total conductivity is resistive (as it is a purely real number), while that of the electrons condensed into Cooper pairs is inductive (as it is purely imaginary).

Note that in this chapter it was presumed that the frequencies are below the BCS energy gap of the superconductor. Otherwise, additional loss channels, evoked by pair breaking, would open up. For microwave frequencies, as being dealt with in this thesis, this assumption is fulfilled, as typically, microwave energies are in the μeV-range whereas gap energies are in the meV-range.

4.3.2. Length scales and limits

In the previous chapter, the theory of the two-fluid model was built around the assumption that the current response to the electric field is *local*. This means, that the electric field varies little around a point $\vec{r}$ within a radius of the mean free path $l = v_{\mathrm{F}}\tau$ (v_{F} being the Fermi velocity). However, characteristic penetration depths λ_{eff} were experimentally found that were much larger than the one predicted in equation 4.30 by the London theory[3]. Consequently, Pippard proposed an empirical equation [Pippard, 1953] substituting the London equations in a *non-local* approach. Later, Mattis and Bardeen derived a microscopic non-local theory directly from the BCS theory [Mattis and Bardeen, 1958] (see chapter 4.3.3).

The non-local theories contain the *pure coherence length*[4]

$$\xi_0 = \frac{\hbar v_{\mathrm{F}}}{\pi \Delta_0}\,, \tag{4.37}$$

which is a measure for the minimum size of a Cooper pair given by the Heisenberg uncertainty principle, and the *impure coherence length*

$$\frac{1}{\xi} = \frac{1}{\xi_0} + \frac{1}{\alpha_{\mathrm{p}} l}\,, \tag{4.38}$$

taking scattering into account (α_{p} being a phenomenological constant on the order of unity).

Given these three length scales - λ_{eff}, ξ, and l - several regimes of the electromagnetic response of the superconductor can be distinguished [Tinkham, 2004, Gao, 2008]:

- *clean/dirty regime*: If $l \gg \xi_0$ is fulfilled, then $\xi \approx \xi_0$. This is called the *clean limit*. If, on the other hand, the mean free path limits the coherence length, $l \ll \xi_0$ and $\xi \approx l$ are valid. This is called the *dirty limit*.

- *local/non-local regime*: If $\lambda_{\mathrm{eff}} \gg \xi$ OR $\lambda_{\mathrm{eff}} \gg l$, the response is *local*. In this case, the London equations are recovered from Pippard's equation but with a modified penetration depth λ_{eff}. In the clean limit, this relaxes to the original form with $\lambda_{\mathrm{eff}} = \lambda_{\mathrm{L}}$, while in the dirty limit $\lambda_{\mathrm{eff}} = \lambda_{\mathrm{L}}\sqrt{1 + \xi_0/l}$. In the local limit, the conductivity in classical formulas can be substituted by a complex one $\sigma = \sigma_1 - i\sigma_2$. If $\lambda_{\mathrm{eff}} \ll \xi$ AND $\lambda_{\mathrm{eff}} \ll l$, the response is *non-local*, because the charge carriers "see" a spatially varying field. In this case, the

[3] These are in literature often denoted by just λ, as λ_{eff} is often reserved specifically for the local case.
[4] Eq. 4.37 is here given in the BCS form.

effective penetration depth is $\lambda_{\text{eff}} \approx 0.65 \left(\lambda_{\text{L}}^2 \xi_0\right)^{\frac{1}{3}}$ [Tinkham, 2004]. If additionally the clean limit holds, the regime is called *extreme anomalous*.

- *thick/thin film limit*: If the electron mean free path is limited by the superconducting film thickness t ($l \approx t$), the film is considered *thin*. This means that the response can be made local by making the film thin enough so that $\lambda_{\text{eff}} \gg t$. If l is not limited by the film thickness, the film is called *thick*.

It has to be mentioned that there are no consistent criteria for the distinction between the limits provided in literature. Sometimes, more parameters are introduced [Tinkham, 2004]. The classification that is presented here is relaxed to the point where the above length scales are sufficient for its description, but also rigorous enough to ensure validity [Gao, 2008].

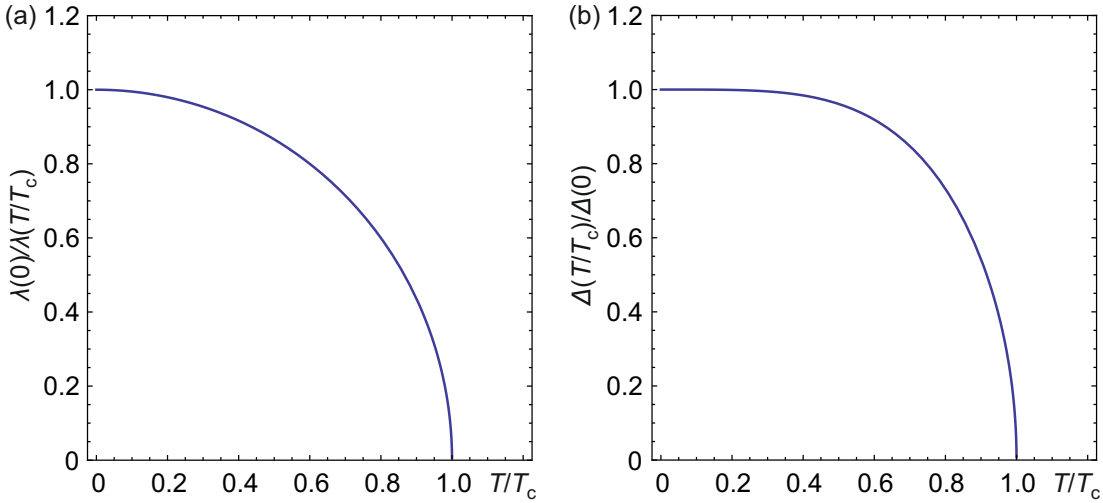

Figure 4.4.: Dependence of $\lambda_{\text{eff}}(0)/\lambda_{\text{eff}}$ (a) and $\Delta/\Delta(0)$ (b) with reduced temperature T/T_{c} according to Eqs. 4.39 and 4.41.

Generally, all of the above length scales are temperature dependent. Of special interest in the further argumentation will, however, only be the temperature dependence of λ_{eff} . There is no universal dependence, but it can to a good degree be approximated in the two-fluid model by [Tinkham, 2004]

$$\frac{\lambda_{\text{eff}}(T)}{\lambda_{\text{eff}}(0)} = \frac{1}{\sqrt{1 - \left(\frac{T}{T_{\text{c}}}\right)^4}} \,. \tag{4.39}$$

The inverse of Eq. 4.39 is plotted in Fig. 4.4 (a), where it can be seen that $\lambda_{\text{eff}}(T)$ diverges at the critical temperature.

An important energy scale of a superconductor is the temperature dependent energy gap parameter $\Delta(T)$. It is predicted by BCS theory as a gap between ground state and excited states in the density of states around the Fermi energy. This means, that a minimum energy $E_{\text{g}} = 2\Delta$ is required to break a Cooper pair [Bardeen et al., 1957].

For $T = 0$, this parameter is maximal and can be approximated by [Bardeen et al., 1957, Tinkham, 2004]

$$E_{\mathrm{g}}(0) = 2\Delta_0 = 3.528 k_{\mathrm{B}} T_{\mathrm{c}}\,, \tag{4.40}$$

where T_{c} is the critical temperature. Above T_{c} the parameter is zero as the gap vanishes.

A useful expression for the temperature dependence of the gap parameter is given by [Pöpel, 1989, Lemberger et al., 2007]

$$\Delta(T) = \Delta_0 \sqrt{\cos\left[\frac{\pi}{2}\left(\frac{T}{T_{\mathrm{c}}}\right)^2\right]}\,. \tag{4.41}$$

This equation is plotted in Fig. 4.4 (b), where it is apparent that the superconducting gap decreases with rising temperature and vanishes at T_{c}.

4.3.3. Mattis-Bardeen theory

Mattis and Bardeen applied the BCS theory of superconductivity to derive a microscopic picture of the electrodynamic response [Bardeen et al., 1957]. Here, only the main outcomes shall be discussed, as the theory is later used to derive the complex conductivity from experimentally accessible parameters. To understand mathematical definitions, the theory of integral transforms shall be shortly introduced.

An integral transform

$$(Tf)(u) = \int_{t_1}^{t_2} f(t) K(t,u) dt \tag{4.42}$$

transforms an input function $f(t)$ into another function $(Tf)(u)$ with the help of a *kernel function* $K(t,u)$. The integral transform is usually used to map an equation from one domain to another, where it can be solved more easily. Then, using an inverse transform with inverse kernel $K^{-1}(u,t)$, the solution is brought back to the original domain. As an example, the kernel of the Fourier transform, mapping from time to frequency domain, is $K(t,\omega) = e^{-i\omega t}/2\pi$.

In the Mattis-Bardeen model, the London equations 4.27, 4.28 are replaced by a total nonlocal current density

$$\vec{j}(\vec{r},\omega) = C \int_V \frac{\vec{R}\left[\vec{R}\cdot\vec{A}(\vec{r}\,',\omega)\right]}{R^4} I(\omega,R,T) e^{-\frac{R}{l}} d\vec{r}\,'\,, \tag{4.43}$$

with $\vec{R} = \vec{r} - \vec{r}\,'$, a constant C, the vector potential $\vec{A}$, the mean free path l, and the Mattis-Bardeen kernel $I(\omega,R,T)e^{-R/l}$, which is the extension of the BCS kernel to nonzero frequencies [Turneaure et al., 1991].

The kernel function is usually a lengthy expression [Bardeen et al., 1957], but can be simplified in the clean (extreme anomalous), as well as dirty (or local) limit [Gao, 2008]. Then again, it is convenient to introduce a complex conductivity as in equation 4.36. It can generally be

defined as

$$\begin{aligned}\frac{\sigma_1}{\sigma_\mathrm{n}} = &\frac{2}{\hbar\omega}\int_{\Delta}^{\infty}\frac{\left[f(E)-f(E+\hbar\omega)\right]\left(E^2+\Delta^2+\hbar\omega E\right)}{\sqrt{E^2-\Delta^2}\sqrt{(E^2+\hbar\omega)^2-\Delta^2}}dE \\ &+\frac{1}{\hbar\omega}\int_{\min\{\Delta-\hbar\omega,-\Delta\}}^{-\Delta}\frac{\left[1-2f(E+\hbar\omega)\right]\left(E^2+\Delta^2+\hbar\omega E\right)}{\sqrt{E^2-\Delta^2}\sqrt{(E^2+\hbar\omega)^2-\Delta^2}}dE\,,\end{aligned} \tag{4.44}$$

$$\frac{\sigma_2}{\sigma_\mathrm{n}} = \frac{1}{\hbar\omega}\int_{\max\{\Delta-\hbar\omega,-\Delta\}}^{\Delta}\frac{\left[1-2f(E+\hbar\omega)\right]\left(E^2+\Delta^2+\hbar\omega E\right)}{\sqrt{\Delta^2-E^2}\sqrt{(E^2+\hbar\omega)^2-\Delta^2}}dE\,, \tag{4.45}$$

with the BCS energy gap Δ and the Fermi-Dirac distribution $f(E) = 1/\left(1+e^{E/k_\mathrm{B}T}\right)$. The first integral in Eq. 4.44 represents conduction by thermally excited quasiparticles, while the second integral (which is zero for $\hbar\omega < 2\Delta$) represents quasiparticle generation through Cooper pair breaking by photons of energy $\hbar\omega$. Eq. 4.45 describes the response of the superconducting condensate on the conductivity, where the integral becomes zero [Kautz, 1978] and the complete expression approaches infinity for $\hbar\omega \to 0$.

For a thermal quasiparticle distribution, the integrals in equations 4.44, 4.45 can be simplified to analytical expressions for $\hbar\omega, k_\mathrm{B}T < 2\Delta$ [Gao, 2008]

$$\frac{\sigma_1}{\sigma_\mathrm{n}} = \frac{4\Delta}{\hbar\omega}e^{-\frac{\Delta}{k_\mathrm{B}T}}\sinh\left(\frac{\hbar\omega}{2k_\mathrm{B}T}\right)K_0\left(\frac{\hbar\omega}{2k_\mathrm{B}T}\right)\,, \tag{4.46}$$

$$\frac{\sigma_2}{\sigma_\mathrm{n}} = \frac{\pi\Delta}{\hbar\omega}\left[1-2e^{-\frac{\Delta}{k_\mathrm{B}T}}e^{-\frac{\hbar\omega}{2k_\mathrm{B}T}}I_0\left(\frac{\hbar\omega}{2k_\mathrm{B}T}\right)\right]\,, \tag{4.47}$$

where I_0 and K_0 are the modified Bessel functions of the first and second kind. In these simplifications, σ_1 and σ_2 can be determined, as T and ω are control parameters, Δ can be approximated by equations 4.40, 4.41, and T_c and σ_n can be measured.

The temperature dependence of σ_1 and σ_2 is shown in Fig. 4.5 for a hypothetical superconductor with $T_\mathrm{c} = 1\,\mathrm{K}$ and an excitation energy of $\hbar\omega = \Delta_0/6$. For the energy gap, relations 4.40, 4.41 are used. It can be seen, that for $T \approx T_\mathrm{c}$, equations 4.46, 4.47 are no longer good approximations: σ_2 should decrease monotonically, until it reaches $\sigma_2 = 0$ at $T = T_\mathrm{c}$, while σ_1 should take on the normal state conductivity σ_n. Due to the decrease of the energy gap, the conditions $\hbar\omega, k_\mathrm{B}T < 2\Delta$ are no longer given in this temperature range. In fact, the above approximations are valid up to a temperature of $T \approx T_\mathrm{c}/2$ [Hein, 1999].

4.3.4. Surface impedance

For any given metal (normal- or superconducting), the *surface impedance* is the observable to determine the electromagnetic response on microwave irradiation. For this, a thin film of thickness t of the metal is placed in a microwave cavity. Changes in quality factor and resonance frequency of the cavity then determine the surface impedance [Turneaure et al., 1991]. It is given by the transverse components of electric and magnetic field,

$$Z_\mathrm{s} = \left.\frac{E_\parallel}{H_\parallel}\right|_{z=0} = \left.\frac{E_\parallel}{\int_0^t j(z)\mathrm{d}z}\right|_{z=0} = R_\mathrm{s} + iX_\mathrm{s} = R_\mathrm{s} + i\omega L_\mathrm{s} = R_\mathrm{s} + i\omega\mu_0\lambda_\mathrm{eff}\,, \tag{4.48}$$

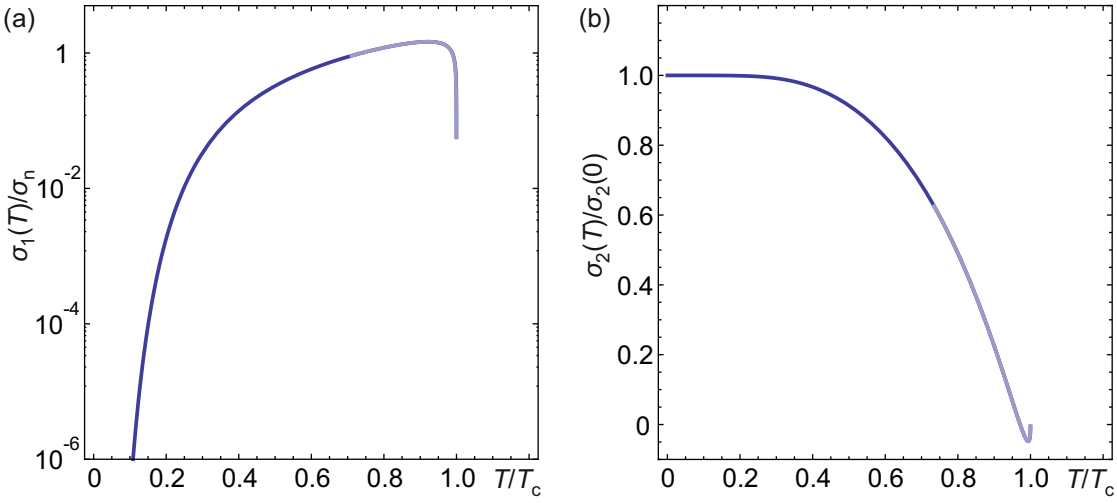

Figure 4.5.: Approximative temperature dependence of σ_1 and σ_2 using equations 4.46, 4.47 for the conductivities and 4.40, 4.41 for the energy gap. For $T < T_c$, the approximations are good. The plots show values for theoretical parameters of $T_c = 1\,\mathrm{K}$ and $\omega = 2\pi \cdot 6\,\mathrm{GHz} \approx \Delta_0/6\hbar$.

and generally consists of a real part, the *surface resistance* R_s, and an imaginary part, the *surface reactance* X_s, which in the case of superconducting films is purely inductive $X_s = \omega L_s$. Accordingly, L_s is called *surface inductance* and can be identified with the effective penetration depth as $L_s = \mu_0 \lambda_{\mathrm{eff}}$ [Gao, 2008, Day et al., 2003]. In the general non-local case, the current density, which determines the magnetic component, requires the Mattis-Bardeen form of equation 4.43 and is difficult to calculate. But there are special cases, in which the surface impedance can be related to the complex conductivity given in equations 4.44, 4.45:

- For thick films in the extreme anomalous limit, the surface impedance can be written as

$$Z_s = \frac{\sqrt{i\omega\mu_0}}{\sqrt[6]{\sigma_n}\sqrt[3]{\sigma_1 - i\sigma_2}} = \frac{i\sqrt{3}\mu_0\omega}{2}\left[\frac{3\pi\mu_0\omega}{4l}\sigma_2 + i\sigma_1\right]^{-\frac{1}{3}}. \tag{4.49}$$

  Here, the first expression was derived from Walsh [Walsh and Tomaselli, 1990] and the original paper of Mattis and Bardeen [Bardeen et al., 1957], and the second expression was given by Gao [Gao, 2008].

- In the local limit $\vec{j} = \sigma\vec{E}$ holds. If additionally the film is thin, the electromagnetic field penetrates the entire film and the current distribution is uniform across the film [Gao, 2008]. Then, the surface impedance can be easily deduced by evaluating the integral over the current, so that

$$Z_s = \frac{1}{(\sigma_1 - i\sigma_2)t} = \frac{\sigma_1}{\left(\sigma_1^2 + \sigma_2^2\right)t} + i\frac{\sigma_2}{\left(\sigma_1^2 + \sigma_2^2\right)t}, \tag{4.50}$$

  where, in this case, $R_s = \sigma_1 / \left(\left(\sigma_1^2 + \sigma_2^2\right)t\right) \approx \sigma_1 / \left(\sigma_2^2 t\right)$ and $L_s = \sigma_2 / \left(\left(\sigma_1^2 + \sigma_2^2\right)\omega t\right) \approx 1/\left(\sigma_2 \omega t\right)$. In the last approximations, it was used that $\sigma_1 \ll \sigma_2$ for $T \ll T_c$. This shows

an important fact, that is independent of the presupposed limit: the inductive response of the film to an external field is determined by the part of the conductivity that describes the superconducting condensate. This will be discussed further in the next section.

- For films of arbitrary thickness in the local limit, Kautz has given a formula [Kautz, 1978]

$$Z_{\mathrm{s}} = \sqrt{\frac{i\mu_0\omega}{\sigma}} \coth\left(\sqrt{i\mu_0\omega\sigma}t\right) , \tag{4.51}$$

that for thin films approaches equation 4.50 and for thick films equals

$$Z_{\mathrm{s}} = \sqrt{\frac{i\mu_0\omega}{\sigma_1 - i\sigma_2}} . \tag{4.52}$$

This result takes the form of the surface impedance of a normal metal but with a complex impedance [Walsh and Tomaselli, 1990].

4.3.5. Waveguide resistance and kinetic inductance

The waveguide resistance per unit length relates to the surface resistance by a purely geometrical factor

$$R_{\mathrm{CPW}} = gR_{\mathrm{s}} . \tag{4.53}$$

In a CPW, this factor is dependent on the waveguide geometry, more precisely s, w, and t as in Fig. 4.1 and is the sum of two contributions

$$g(s,w,t) = g_{\mathrm{ctr}} + g_{\mathrm{gnd}} , \tag{4.54}$$

one for the center conductor and one for the ground planes. Following Collin [Collin, 2001] and using $K(k)$ and k as defined in chapter 4.2.2, these can be written as

$$g_{\mathrm{ctr}} = \frac{1}{4sK^2(k)(1-k^2)} \left[\pi + \ln\left(\frac{4\pi s}{t}\right) - k\,\ln\left(\frac{1+k}{1-k}\right)\right] \tag{4.55}$$

$$g_{\mathrm{gnd}} = \frac{k}{4sK^2(k)(1-k^2)} \left[\pi + \ln\left(\frac{4\pi(s+2w)}{t}\right) - \frac{1}{k}\ln\left(\frac{1+k}{1-k}\right)\right] . \tag{4.56}$$

The total inductance in a *superconducting* CPW consists not only of the geometric inductance of equation 4.18, but has a contribution that can be associated with the characteristics of the superconducting condensate in the metal

$$L_{\mathrm{CPW}} = L_{\mathrm{g}} + L_{\mathrm{k}} = L_{\mathrm{g}} + gL_{\mathrm{s}} , \tag{4.57}$$

where L_{k} is called the *kinetic inductance*, because its origin lies in the inertia of the Cooper pairs. It also relates to the surface inductance by the geometrical factor g.

An important parameter to be considered is the *kinetic inductance fraction* α_{k}, which gives the ratio of kinetic to total inductance

$$\alpha_{\mathrm{k}} = \frac{L_{\mathrm{k}}}{L_{\mathrm{g}} + L_{\mathrm{k}}} = \frac{gL_{\mathrm{s}}}{L_{\mathrm{g}} + gL_{\mathrm{s}}} . \tag{4.58}$$

All of the parameters α_k, L_k, L_s, and R_s are strongly temperature dependent in a superconducting CPW due to the fact that they relate to the Cooper pair and quasiparticle density. For example, $L_\mathrm{s} = \mu_0 \lambda_\mathrm{eff}$ as stated in the previous chapter. The temperature dependence of λ_eff is approximately given by Eq. 4.39 and shown in Fig. 4.4(a).

As shown, in the different limits of the previous section, the surface impedance can be related to the experimentally easier accessible parameters σ_1 and σ_2. In the case of a thin film in the local limit, for example, it has been shown (Eq. 4.50 and the following paragraph) that $R_\mathrm{s} = \sigma_1 / \left(\sigma_2^2 t\right)$ and $L_\mathrm{s} = 1/\left(\sigma_2 \omega t\right)$. Temperature dependences of α_k, L_k, L_s, and R_s can then be calculated in the following manner:

1. Measure σ_n and T_c
2. Calculate the temperature dependency of Δ using Eqs. 4.40 and 4.41
3. Calculate σ_1 and σ_2 using Eqs. 4.44 and 4.45
4. Calculate α_k, L_k, L_s, and R_s by using σ_1 and σ_2 in the appropriate limit

4.4. Quarter wave Resonators

Resonators where standing waves of exactly a quarter of the wavelength appear are called quarter wave resonators. An everyday example is a standing sound wave in pipe that has one open and one closed end. With coplanar waveguides, quarter wave resonators can be defined by choosing and fabricating appropriate boundary conditions [Li et al., 2013]. They have been used in optomechanical experiments [Regal et al., 2008, Singh et al., 2014a] as well as rf characterization of superconductors [Singh et al., 2014b] and substrate [Pappas et al., 2011]. Having the ability to be multiplexed on a single chip, see Fig. 4.6 (b), makes them suitable in applications of astronomical detection for frequencies from far-infrared to X-ray as so-called *microwave kinetic inductance detectors* (MKIDs) [Mazin, 2004].

4.4.1. Transmission line model

A quarter wave resonator in the CPW geometry is a piece of transmission line, that is capacitively coupled to a signal feed line on one end, while its other end is grounded (see Fig. 4.6 (a) and (b)). In the resonant case, energy is coupled out of the feed line by the formation of a standing wave of wavelength $\lambda_n = 4l/n$ ($n \in \{1, 3, 5, \dots\}$) in the resonator. This behaviour is equivalent to a standing sound wave in a pipe with one open and one closed end: due to its boundary conditions, a voltage antinode and current node form in the CPW resonator near the coupling region and vice versa at the grounded end. Its resonance frequencies

$$\omega_n = 2\pi \cdot \frac{v_\mathrm{ph}}{\lambda_n} = 2\pi \cdot \frac{c}{\sqrt{\epsilon_\mathrm{eff}}} \frac{n}{4l} \text{ with } n \in \{1, 3, 5, \dots\} \tag{4.59}$$

are given by the transmission line length l of the resonator and the effective permittivity ϵ_eff. For the phase velocity, $v_\mathrm{ph} = c/\sqrt{\epsilon_\mathrm{eff}}$ as in Eq. 4.23 has been used.

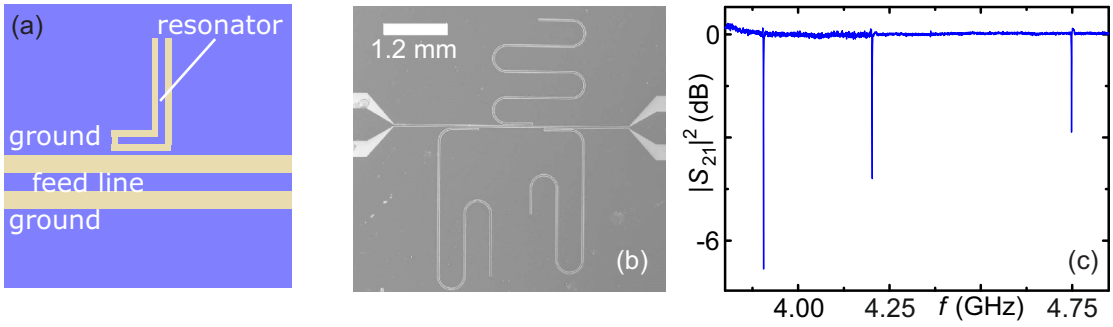

Figure 4.6.: The transmission line model in a schematic drawing (a): a resonator of length l is capacitively coupled to a feed line whose transmission can be probed. The resonance frequency depends on the length of the resonator l and the effective dielectric constant. (b) shows a SEM image of a device consisting of three multiplexed resonators of different length. The corresponding transmitted power of a measurement at $T = 4.2\,\mathrm{K}$ is plotted in (c), showing that the three resonances can clearly be distinguished. The transmission at high power, where superconducting effects in the resonators are suppressed, has been subtracted to normalise the data. (b) and (c) adapted from [Blien et al., 2016].

Alternatively, Eq. 4.23 states $v_{\mathrm{ph}} = 1/\sqrt{L_{\mathrm{CPW}} C_{\mathrm{CPW}}}$. With this, it follows that

$$\omega_n = 2\pi \frac{n}{4l\sqrt{L_{\mathrm{CPW}} C_{\mathrm{CPW}}}} \,. \tag{4.60}$$

The effective permittivity can be calculated from geometric and substrate parameters like it is shown in Sect. 4.2. Using Eq. 4.59, the resonator lengths can be adjusted to give resonance frequencies in the desired frequency range (see Fig. 4.6 (b) and (c)).

4.4.2. Lumped Elements approach

Alternatively, quarter wave resonators can be described as a parallel lumped elements RLC circuit [Li et al., 2013]. The equivalent circuit is shown in Fig. 4.7. Here, R_{RLC}, L_{RLC}, and C_{RLC} represent resistance, capacitance, and inductance equivalents of the CPW resonator. C_{k}, whose influence on the resonance frequency shall be neglected here, is the capacitance of the coupling capacitor.

From transmission line theory, relations between the lumped elements and the waveguide capacitance and inductance can be deduced [Gao, 2008]. It follows that

$$C_{\mathrm{RLC}} = \frac{l}{2} C_{\mathrm{CPW}} \,, \tag{4.61}$$

and

$$L_{\mathrm{RLC}} = \frac{8l}{\pi^2} L_{\mathrm{CPW}} \,. \tag{4.62}$$

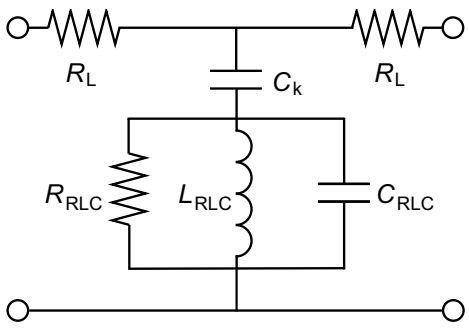

Figure 4.7.: Lumped elements model of a CPW quarter wave resonator. The resistors R_L represent the (real) load impedances of microwave generator and detector. The signal can couple to the resonator by a coupling capacitor C_k. The resonator, in turn, is constructed of lumped elements R_RLC, L_RLC, and C_RLC. The description is valid in the vicinity of the resonance frequency. Adapted from [Li et al., 2013].

With this, the fundamental resonance frequency can be expressed as

$$\omega_\mathrm{r} = \frac{1}{\sqrt{L_\mathrm{RLC} C_\mathrm{RLC}}} = 2\pi \frac{1}{4l\sqrt{L_\mathrm{CPW} C_\mathrm{CPW}}}\,, \tag{4.63}$$

which is consistent with Eq. 4.60.

As explained in Sect. 4.3.5, the inductance of the CPW building the resonator consists of a geometrical and a kinetic part $L_\mathrm{CPW} = L_\mathrm{g} + L_\mathrm{k}$. The latter one, and with it ω_r, is strongly temperature dependent. The resonance frequency changes as

$$\frac{\delta\omega_\mathrm{r}}{\omega_\mathrm{r0}} = \frac{\omega_\mathrm{r}(T) - \omega_\mathrm{r0}}{\omega_\mathrm{r0}} = -\frac{1}{2}\frac{\delta L_\mathrm{CPW}}{L_\mathrm{CPW0}} = -\frac{1}{2}\frac{L_\mathrm{k0}}{L_\mathrm{CPW0}}\frac{\delta(L_\mathrm{g} + L_\mathrm{k})}{L_\mathrm{k0}} = -\frac{\alpha_\mathrm{k}}{2}\frac{\delta L_\mathrm{s}}{L_\mathrm{s0}}\,, \tag{4.64}$$

where 0 as an index refers to a parameter at $T = 0$ and δ indicates a small change from the parameter at $T = 0$. In Eq. 4.64, the definition of the kinetic inductance fraction (Eq. 4.58), $\delta L_\mathrm{g} \approx 0$, and $L_\mathrm{k} = g L_\mathrm{s}$ have been used.

4.4.3. Coupling and loading of resonator

Generally, the quality factor of a resonant circuit can be defined as the ratio of its resonant frequency ω_r and its decay rate κ

$$Q = \frac{\omega_\mathrm{r}}{\kappa}\,. \tag{4.65}$$

The decay rate is given by the full width at half maximum, meaning the frequency bandwidth, over which the power in the resonator is larger than half its maximum value.

The *loaded* or *total* quality factor is given by

$$\frac{1}{Q_\mathrm{L}} = \frac{1}{Q_\mathrm{c}} + \frac{1}{Q_\mathrm{i}} \tag{4.66}$$

and consists of two parts: the *coupling* quality factor Q_c and the *internal* or *unloaded* quality factor Q_i. The coupling quality factor is controlled by the coupling capacitor and in this way dependent on the geometry of the CPW resonator. The internal quality factor, on the other hand, reflects losses in the superconductor and dielectric or by radiation [Gao, 2008] and is consequently a material and temperature dependent quantity. An individual decay rate can be assigned to each quality factor. The internal and coupling decay rate sum up to give the total decay rate $\kappa_\mathrm{L} = \kappa_\mathrm{i} + \kappa_\mathrm{c}$.

The internal quality factor can further be related to the attenuation constant α of Sect. 4.2 [Pozar, 2011], with

$$Q_\mathrm{i} = \frac{\pi}{2\alpha L} \tag{4.67}$$

and L being the resonator length. As α adds up for each loss channel, different Q_i can be assigned to the individual loss mechanisms

$$Q_\mathrm{i}^{-1} = \sum_j Q_{\mathrm{i},j}^{-1} \,. \tag{4.68}$$

Considering only dissipation by the superconductor, Q_i can be expressed by

$$Q_\mathrm{i} = \frac{\omega L_\mathrm{CPW}}{R_\mathrm{CPW}} = \frac{1}{\alpha_\mathrm{k}} \frac{\omega L_\mathrm{s}}{R_\mathrm{s}} \,, \tag{4.69}$$

with α_k being the kinetic inductance fraction. In the same way as for the resonance frequency in Eq. 4.64, a temperature dependence for Q_i can be stated

$$\delta\left(\frac{1}{Q_\mathrm{i}}\right) = \alpha_\mathrm{k} \frac{\delta R_\mathrm{s}}{\omega L_\mathrm{s}} \,, \tag{4.70}$$

where the temperature dependence is expected to be governed by the change in the surface resistance.

With the help of the coupling constant η_c, which is the ratio of the internal to the coupling quality factor,

$$\eta_\mathrm{c} = \frac{Q_\mathrm{i}}{Q_\mathrm{c}} \,, \tag{4.71}$$

three different regimes can be defined:

- *Overcoupled* $Q_\mathrm{c} \ll Q_\mathrm{i} \rightarrow \eta_\mathrm{c} > 1$: Here, the loaded quality factor is governed by the coupling quality factor, so $Q_\mathrm{L} \approx Q_\mathrm{c}$ holds. In this regime, Q_L can be controlled by the choice of coupling capacitance C_k. These strongly coupled resonators usually have small total quality factors combined with a large bandwidth, making them ideal for fast measurements [Göppl et al., 2008].

- *Undercoupled* $Q_\mathrm{c} \gg Q_\mathrm{i} \rightarrow \eta_\mathrm{c} < 1$: Here, $Q_\mathrm{L} \approx Q_\mathrm{i}$, so that the total dissipation is dominated by internal losses of the resonator. As these are small in the case of superconductors, undercoupled resonators can possess large total quality factors. This guarantees a high spectral resolution combined with a long intracavity photon lifetime [Göppl et al., 2008].

- *Critically coupled* $Q_\mathrm{c} \approx Q_\mathrm{i} \approx 2Q_\mathrm{L} \rightarrow \eta_\mathrm{c} \approx 1$: The power that is dissipated in intrinsic processes is equal to the power that leaks through the coupling capacitor. In this regime, the transmitted power at resonance drops to half the transmitted power away from resonance (see Eq. 4.72 for this).

As no specific restrictions on boundary conditions have been given, the results of this section are directly transferable to half wave resonators.

4.4.4. Transmission function

In an experiment, the complex scattering coefficient $S_{21}(\omega)$ of the resonator feed line is measured. It can be quantified by applying Kirchhoff's law on the lumped elements circuit of Fig. 4.7 and making use of its frequency dependent complex impedances [Mazin, 2004, Deng et al., 2013] or by considering a network analysis approach, modelling the transmission line and resonator as a 3-port network [Gao, 2008]. Here, the complete derivation shall be omitted, as only the resulting transmission function is of importance.

In the vicinity of the resonance, the complex transmission can be expressed by

$$S_{21}(\omega) = 1 - \frac{Q_\mathrm{L}/Q_\mathrm{c}}{1 + 2iQ_\mathrm{L}\delta\omega}\,, \tag{4.72}$$

where $\delta\omega = \frac{\omega-\omega_\mathrm{r}}{\omega_\mathrm{r}}$ is the normalized frequency deviation from the resonance frequency. The transmitted power $|S_{21}|^2$ shows an inverted Lorentzian lineshape with a transmission minimum of $|S_{21}(\omega_\mathrm{r})|^2 = ((Q_\mathrm{c} - Q_\mathrm{L})/Q_\mathrm{c})^2$ at $\omega = \omega_\mathrm{r}$, whereas the phase $\arg(S_{21})$ acquires a shift of π and shows a steep slope around the resonance frequency (see Fig. 4.8). In this way, resonance frequencies ω_r and quality factors Q_L, Q_i, and Q_c can be deduced and their temperature dependence can be determined, which allows for the extraction of material dependent parameters (see Sect. 5).

Resonance lineshapes can in reality differ from a perfect Lorentzian due to asymmetric coupling, impedance mismatches, or a complex loading of the resonator [Khalil et al., 2012, Megrant et al., 2012]. Then, a complex-valued *external quality factor* can be introduced as $Q_\mathrm{e} = |Q_\mathrm{e}| \cdot e^{-i\theta}$ and $\mathrm{Re}\left\{Q_\mathrm{e}^{-1}\right\} = Q_\mathrm{c}^{-1}$. Substituting Q_c with Q_e in Eq. 4.72 gives the asymmetric transmission function

$$S_{21}(\omega) = 1 - \frac{(Q_\mathrm{L}/\,|Q_\mathrm{e}|)\,e^{i\theta}}{1 + 2iQ_\mathrm{L}\delta\omega}\,. \tag{4.73}$$

Fig. 4.9 shows such an asymmetric transmission of a quarter wave resonator made of MoRe. Deng *et al.* have argued [Deng et al., 2013] that the bonding wires, that establish the electrical connection between resonator chip and PCB, create large inductances. These serve as reflection points for the microwave, which leads to standing waves on the transmission feed line. When mulitplexed on a chip, different resonators can in this way experience different degrees of asymmetry, which is also observed experimentally (see e.g. Fig. 4.6(c)).

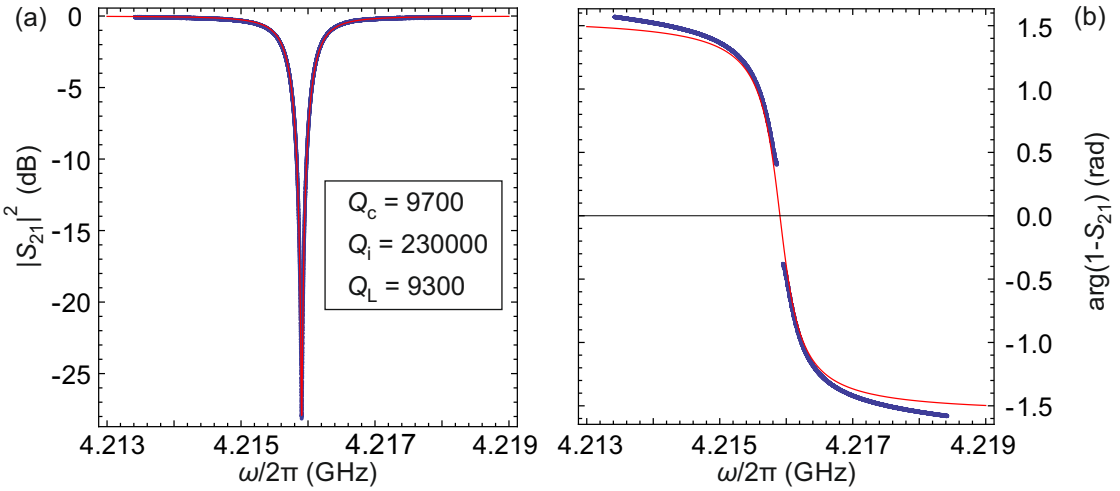

Figure 4.8.: Power transmission (a) and phase (b) of a Nb quarter wave resonator at $T = 15\,\mathrm{mK}$. The data (blue) has been fitted (red) to the response function Eq. 4.72. A linear background has been subtracted and in (b), the phase was set to give the off-resonance value $\pm\pi/2$. Points around the resonance frequency $\omega = \omega_\mathrm{r}$ are missing in (b) due to this normalisation.

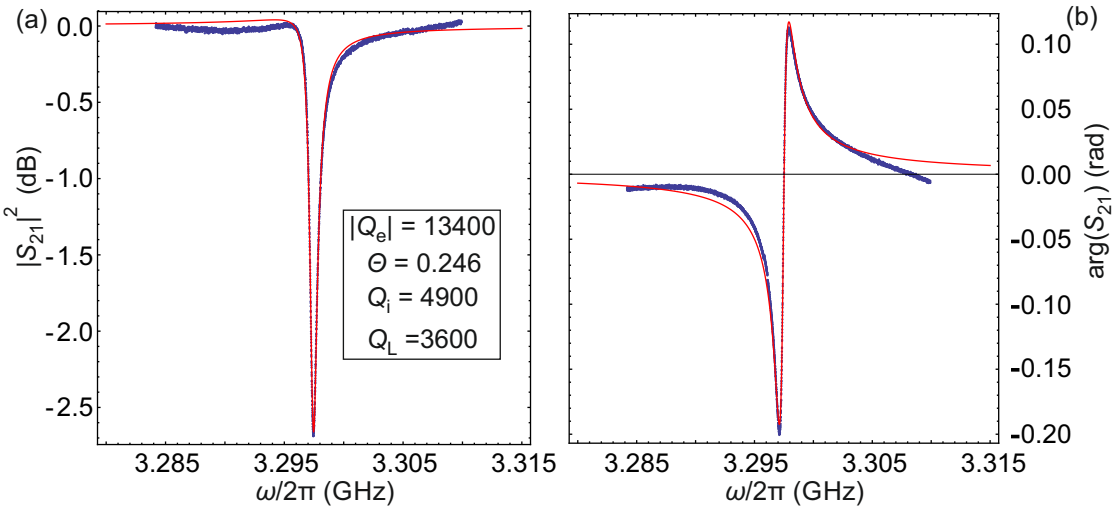

Figure 4.9.: Power transmission (a) and phase (b) of a MoRe quarter wave resonator at $T = 15\,\mathrm{mK}$. The data (blue) has been fitted (red) to the asymmetric response function Eq. 4.73. For normalisation, a linear background has been subtracted.

4.5. Half wave Resonators

Contrary to quarter wave resonators, half wave resonators can sustain a standing wave with exactly half its wavelength. To use the same example, half wave sound resonators are tubes with two open (or closed) ends. Coplanar half wave resonators have first been used in circuit QED experiments [Blais et al., 2004], but also in optomechanics in the microwave domain [Rocheleau et al., 2009].

4.5.1. Transmission line model

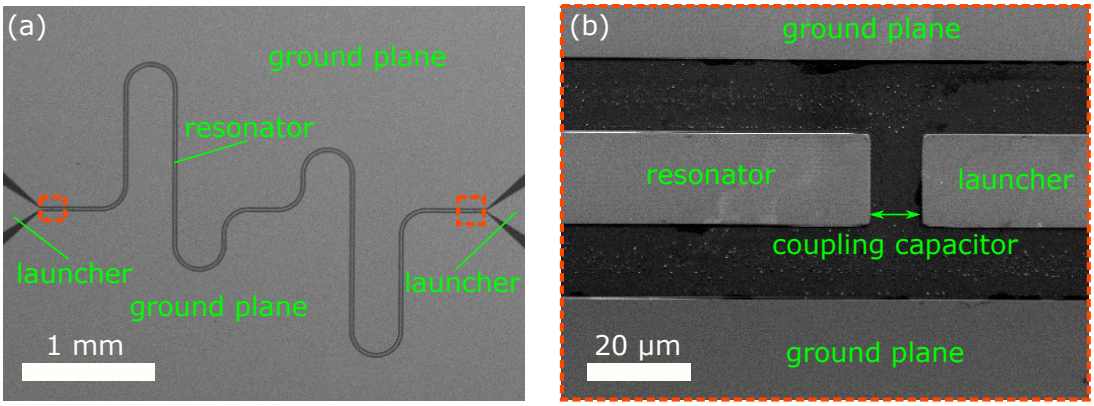

Figure 4.10.: Scanning electron micrograph of resonator (a) and close-up view of coupling capacitor (b). Pictures taken by T. Huber

Contrary to the quarter wave resonator, a half wave resonator is directly integrated into the microwave signal path. A segment of length l of the inner conductor of a transmission line is "separated" from its surroundings by two coupling capacitors C_k (see Fig. 4.10). The boundary conditions for the standing wave electric field are now similar to a standing sound wave in a tube with two open ends. Alternatively, the resonator can be described as a Fabry-Pérot cavity. The standing wave has a voltage antinode/current node at the coupling capacitors and a voltage node/current antinode in the middle of the resonator. Their wavelength is given by $\lambda_n = 2l/n$. The fundamental resonance frequency in a half wave resonator then reads

$$\omega_n = 2\pi \cdot \frac{v_\mathrm{ph}}{\lambda_n} = 2\pi \cdot \frac{c}{\sqrt{\epsilon_\mathrm{eff}}} \frac{n}{2l} \,. \tag{4.74}$$

4.5.2. Lumped elements approach

As in the case of quarter wave resonators, half wave resonators can be described in a lumped elements RLC model around the resonance (see Fig. 4.11). R_L represents the (real valued) load impedance given by the microwave generator and detector. It is chosen to be equal to the characteristic impedance Z_0 of cablings and waveguides where the signal is conveyed. The coupling to and from the resonator is maintained by coupling capacitors of capacitance C_k, the

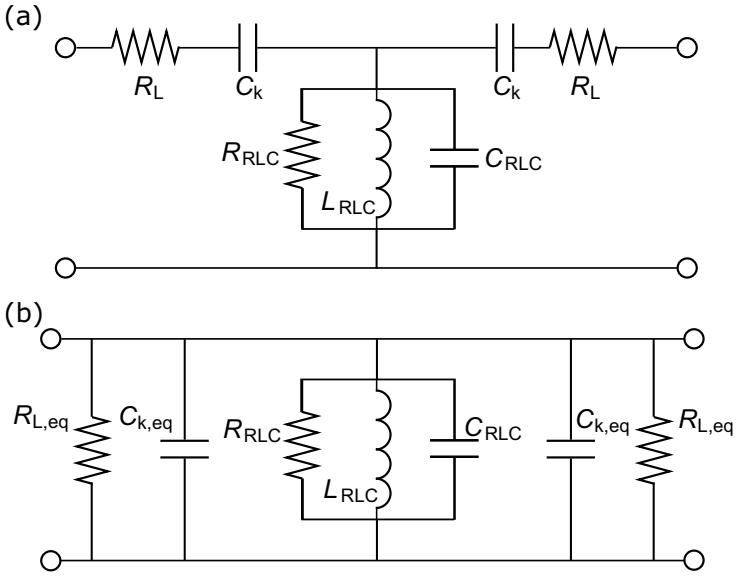

Figure 4.11.: Lumped elements (a) and Norton-equivalent circuit (b) representation of a CPW half wave resonator. Microwaves are generated and detected with devices with load impedances of R_{L} and coupled in and out of the waveguide resonator by coupling capacitors C_{k}. The resonator itself is modelled by R_{RLC}, L_{RLC}, and C_{RLC}. In the Norton-equivalent circuit, the series connection of R_{L} and C_{k} are transformed into a parallel connection of resistor $R_{\mathrm{L,eq}}$ and capacitor $C_{\mathrm{k,eq}}$. Adapted from [Göppl et al., 2008].

in- and output impedances are $Z_{\mathrm{in/out}} = R_{\mathrm{L}} + (i\omega C_{\mathrm{k}})^{-1}$. The resonant behaviour of the CPW resonator is represented by a parallel RLC circuit of R_{RLC}, L_{RLC}, and C_{RLC}.

As in the case of quarter wave resonators, relations between the lumped elements and waveguide capacitance and inductance can be given [Göppl et al., 2008]. It follows that

$$C_{\mathrm{RLC}} = \frac{l}{2} C_{\mathrm{CPW}} \,, \tag{4.75}$$

and

$$L_{\mathrm{RLC}} = \frac{2l}{\pi^2} L_{\mathrm{CPW}} \,. \tag{4.76}$$

The resonance frequency deduced from the lumped elements model

$$\omega_{\mathrm{r}} = \frac{1}{\sqrt{L_{\mathrm{RLC}} C_{\mathrm{RLC}}}} = 2\pi \frac{1}{2l\sqrt{L_{\mathrm{CPW}} C_{\mathrm{CPW}}}} \tag{4.77}$$

is again consistent with the one deduced from the transmission line model (setting $v_{\mathrm{ph}} = c/\epsilon_{\mathrm{eff}} = 1/\sqrt{L_{\mathrm{CPW}} C_{\mathrm{CPW}}}$ in Eq. 4.74).

According to *Norton's theorem* of circuit theory, a linear electrical network consisting of a voltage source and a series impedance can be replaced by an equivalent current source along

with the same impedance in parallel to the source. The series connection of R_L and C_k can thus be transformed to an equivalent resistance $R_\mathrm{L,eq}$ and an equivalent capacitance $C_\mathrm{k,eq}$ in parallel. These equivalent quantities have to be chosen in a way, that the in- and output impedances remain as $Z_\mathrm{in/out} = R_\mathrm{L} + (i\omega C_\mathrm{k})^{-1}$. This can be accomplished by [Göppl et al., 2008]

$$R_\mathrm{L,eq} = \frac{1 + \omega^2 C_\mathrm{k}^2 R_\mathrm{L}^2}{\omega^2 C_\mathrm{k}^2 R_\mathrm{L}}\,, \tag{4.78}$$

$$C_\mathrm{k,eq} = \frac{C_\mathrm{k}}{1 + \omega^2 C_\mathrm{k}^2 R_\mathrm{L}^2}\,. \tag{4.79}$$

In the parameter range of this thesis ($\omega \approx 2\pi \cdot 5\,\mathrm{GHz}$, $R_\mathrm{L} \approx 50\,\Omega$, $C_\mathrm{k} \approx 1 - 10\,\mathrm{fF}$), Eqs. 4.78 and 4.79 can be simplified to

$$R_{L,\mathrm{eq}} \approx \frac{1}{\omega^2 C_\mathrm{k}^2 R_\mathrm{L}}\,, \tag{4.80}$$

$$C_{k,\mathrm{eq}} \approx C_\mathrm{k}\,. \tag{4.81}$$

The fundamental resonance frequency in this representation is then

$$\omega_\mathrm{r} = \frac{2\pi}{2l(L_\mathrm{k} + L_\mathrm{g})(C_\mathrm{CPW} + 2C_\mathrm{k})} \approx \frac{\pi}{l(L_\mathrm{k} + L_\mathrm{g})C_\mathrm{CPW}}\,, \tag{4.82}$$

with again $L_\mathrm{CPW} = L_\mathrm{k} + L_\mathrm{g}$ and $C_\mathrm{k} \ll C_\mathrm{CPW}$.

Concerning the loading of the resonator, the same concepts as in Sect. 4.4.3 can be applied. For a parallel RLC circuit, the total quality factor is given by $Q_\mathrm{L} = R/Z_0$. From the Norton-equivalent circuit of Fig. 4.11 (b), it is easily obtained that

$$\frac{1}{Q_\mathrm{L}} = Z_0 \left(\frac{1}{R_\mathrm{RLC}} + \frac{2}{R_\mathrm{L,eq}} \right)\,. \tag{4.83}$$

The two contributions can then be identified with the internal and coupling quality factor

$$Q_\mathrm{i} = \frac{R_\mathrm{RLC}}{Z_0} \tag{4.84}$$

$$Q_\mathrm{c} = \frac{R_\mathrm{L,eq}}{2Z_0}\,. \tag{4.85}$$

and be converted to the according linewidths

$$\kappa_\mathrm{i} = \omega_\mathrm{r} \frac{Z_0}{R_\mathrm{RLC}} = \frac{1}{R_\mathrm{RLC} C_\mathrm{RLC}} \tag{4.86}$$

$$\kappa_\mathrm{c} = \omega_\mathrm{r} \frac{2Z_0}{R_\mathrm{L,eq}} = 2R_\mathrm{L}(\omega C_\mathrm{k})^2 \frac{1}{C_\mathrm{RLC}}\,, \tag{4.87}$$

where the definition of the characteristic impedance for lossless waveguides (Eq. 4.8) and the approximation for the Norton-equivalent resistance Eq. 4.80 were applied.

4.5.3. Transmission function

The transmission function of a half wave resonator around its resonance is [Petersan and Anlage, 1998]

$$S_{21}(\omega) = \frac{Q_\mathrm{L}/Q_\mathrm{c}}{1 + 2iQ_\mathrm{L}\delta\omega} + re^{i\phi}\,, \tag{4.88}$$

with $\delta\omega = (\omega - \omega_\mathrm{r})/\omega_\mathrm{r}$ the normalized frequency deviation as before. Here, non-ideal coupling was already accounted for by the addition of a complex shift $re^{i\phi}$. Causing *Fano lineshapes* [Fano, 1961], this shift alters the overall appearance of the peak, which will be explained in more depth in Sect. 6.1.1.

For half wave resonators it is more difficult to break down the total quality factor into an internal and a coupling quality factor from a fit to the data. The reason is that without calibration, no reference background level can be specified. More precisely, the data implies an unknown amplitude a originating from attenuation, loss, and gain in the signal path. This amplitude masks, e.g., the transmission at resonance $|S_{21}(\omega = \omega_\mathrm{r})| = a \cdot Q_\mathrm{L}/Q_\mathrm{c}$ (here ignoring the complex shift $\rightarrow r = 0$) [Probst et al., 2015]. This is why experimental data is usually fitted to the function

$$S_{21}(\omega) = \frac{r_\mathrm{bg}}{1 + 2iQ_\mathrm{L}\delta\omega} + re^{i\phi}\,, \tag{4.89}$$

where r_bg accounts for the unknown background and coupling amplitude.

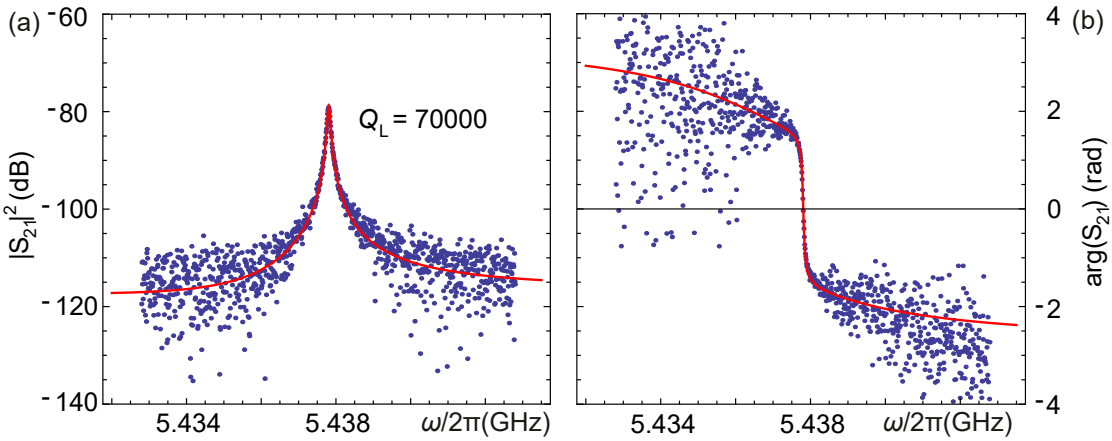

Figure 4.12.: Power transmission (a) and phase (b) of a Nb half wave resonator at base temperature of the dilution refrigerator. The data shows a peak in the transmission and a phase shift of π at resonance and was fitted to Eq. 4.89.

Fig. 4.12 shows recorded data of a half wave resonator made of Nb at the base temperature of the dilution refrigerator. There is a clear peak in the transmitted power and a phase shift of π, that can be described by Eq. 4.89. A loaded quality factor of $Q_\mathrm{L} = 70000$ emerges, which is a typical value for Nb CPW resonators at cryogenic temperatures [Göppl et al., 2008]. Note that in this particular measurement, one of the cables in the cryostat was broken. This is indicated by the overall low transmission and large noise away from resonance.

5

Characterization of Molybdenum/Rhenium alloys

Regarding the integration of a CNT into complex device structures, different approaches can be pursued. One is to directly grow the CNT on-chip in a last step, after having fabricated all other circuit elements. These have to consist of a metal that withstands the carbon nanotube growth process. For most superconductors, the aggressive mixture of CH_4 and H_2 at high temperatures is highly detrimental. In the past, an alloy of molybdenum and rhenium has shown remarkable results in respect of transition temperature [Testardi et al., 1971, Gavaler et al., 1972, Postnikov et al., 1977], making transparent contacts to CNTs [Schneider et al., 2012, Stiller et al., 2013, Schmid et al., 2015], and sustaining high frequency characteristics [Singh et al., 2014b].

In this chapter, thin films composed of a MoRe alloy are investigated by means of dc, XPS, and high frequency experiments [Götz et al., 2016]. With the objective of building high frequency nanotube hybrid devices, special emphasis is put on the examination of CPW resonator devices and the impact of the CNT growth process on device parameters. The work of this chapter was done in cooperation with K. Götz and has already partially been presented in his Ph.D. thesis [Götz, 2018] and published in [Götz et al., 2016].

5.1. Thin film deposition

For the deposition of a MoRe metal film on a substrate of either SiO_2 or Al_2O_3 a co-sputter process in a UHV sputtering system was established (see Fig. 5.1 (a)). The sputter chamber has two sputter targets facing the sample holder under the same angle and is pumped to a base pressure of typically 10^{-7} to $10^{-8}\,\mathrm{mbar}$. The distance between the sputter targets is $15\,\mathrm{cm}$, while the sample holder is located $13.5\,\mathrm{cm}$ above the target plane. To ignite the plasmas for the dc and rf process, argon gas is injected via a mass flow controller into the chamber. When a pressure of $10^{-1}\,\mathrm{mbar}$ is reached, first a rf drive is applied.

After ignition of the argon plasma the pressure can be adjusted and kept constant at a value $7 \cdot 10^{-3}\,\mathrm{mbar}$ throughout the process. The rf-output is tuned to sustain plasma stability at the molybdenum electrode. Following the stabilisation of the rf plasma, the plasma at the rhenium electrode is ignited and controlled using a dc power supply.

Sputter rates are read out by a deposition controller. They can be altered for the individual materials by the applied dc and rf power (see Fig. 5.1 (b)), but are kept constant during individual thin film growth processes. Material deposition commences by simultaneously opening both shutters of the sputter targets.

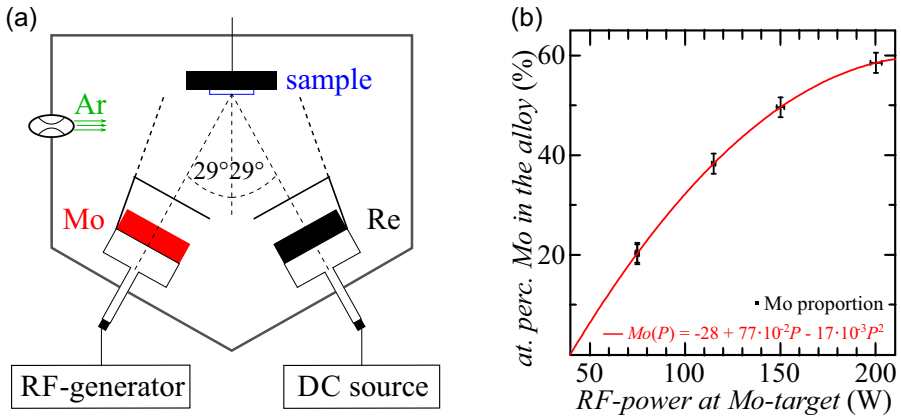

Figure 5.1.: Schematic of the sputtering chamber and the MoRe co-sputter process (a). The rates of the individual materials are adjustable by the applied sputter powers. The relative molybdenum atomic percentage in the bulk is shown as function of the applied rf power P_{Mo} at the Mo target (b). Adapted from [Götz et al., 2016].

5.2. X-ray photoelectron spectroscopy

Alloy compositions are stable because of the constant chamber pressure during deposition and are in the following regulated only by varying the applied rf power P_{Mo} at the molybdenum electrode. To obtain these compositions, *X-ray photoelectron spectroscopy* (XPS) has been performed on the films by K. Götz [Götz et al., 2016]. Under irradiation by a monochromatic X-ray source photo-electrons are emitted by surfaces of the films. Their kinetic energies and intensities are then detected spectroscopically. Because of the energies being element-specific, conclusions can be drawn about the atomic concentrations at the surface of the investigated films.

In Fig. 5.2 (a) XPS spectra of a co-sputtered MoRe ($P_{\mathrm{Mo}} = 75\,\mathrm{W}$) film are plotted. The peaks are characteristic to the orbitals from which the photo-electrons are emitted. From the black curve it can be seen that MoRe surfaces are constituted of a large amount of oxygen and carbon. A probable source for this contamination is the exposure to air between deposition and spectroscopy. The red curve shows the bulk spectrum, where approximately $5\,\mathrm{nm}$ of the film have been removed beforehand by *in-situ* Ar-sputtering in the XPS UHV chamber. A strong suppression of the oxygen and carbon peak is apparent.

The chemical composition as function of depth is displayed in Fig. 5.2 (b). It has been determined using the method of area sensitivity factors [Moulder et al., 1992] on the Mo3d-, Re4f-, C1s-, and O1s-peaks for each etching step. The MoRe alloy ratio is then obtained by normalising to the sum of the contributions of both co-sputtered metals. For the exemplary device a ratio of $\mathrm{Mo_{20}Re_{80}}$ results.

In the following the influence of the carbon nanotube growth process is investigated. Samples containing MoRe thin films have been exposed to a methane-hydrogen atmosphere in a CVD furnace at $900\,^{\circ}\mathrm{C}$ (as described in Sect. 2.2.1) for different amounts of time.

Fig. 5.3 (a) shows the XPS spectra of a film sputtered at $P_{\mathrm{Mo}} = 75\,\mathrm{W}$ after exposure to the

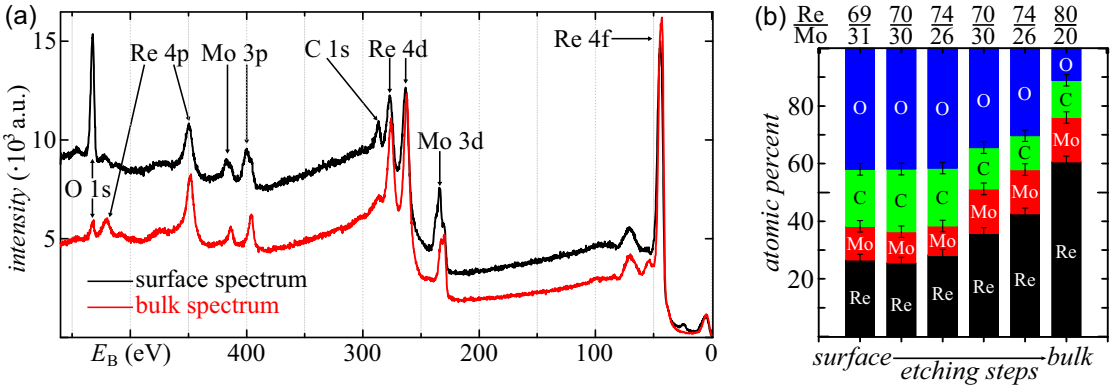

Figure 5.2.: XPS spectra of a pristine MoRe film on Si/SiO_2 are shown for surface (black) and bulk (red) (a). The applied rf power was $P_{Mo} = 75\,W$. For the bulk spectrum, $5\,nm$ of the film has been removed by in-situ argon-ion sputtering. Peaks correspond to orbitals of the photo-emitted electrons and allow conclusions about the material composition. Atomic percentages for the different materials can be computed with the help of area sensitivity factors to give depth profiles for individual etching steps from surface to $\sim 5\,nm$ depth (b). Adapted from [Götz et al., 2016].

CVD process for $30\,min$, again for surface and bulk. Considering peak heights and areas, it is evident that the carbon peak is strongly enhanced, even in the "bulk" (i.e. at $5\,nm$ depth), while the oxygen peak is reduced in comparison to the pristine sample of Fig. 5.2. Using the area sensitivity factor, percentages of 26% carbon, 22% molybdenum, 49% rhenium, and neglectable amounts of oxygen are given (see Fig. 5.3 (b)). The high percentage of carbon in the bulk suggests diffusion of carbon during the CVD process into the metal film. Furthermore, the resulting alloy ratio of $Mo_{31}Re_{69}$ implies structural changes during CVD, as the same sputter parameters as for the pristine film have been used.

5.3. Critical temperature and current density in the dc regime

In order to characterise MoRe alloys regarding superconducting qualities and dc transport, thin films were patterned into Hall bar structures by reactive ion etching (see Fig. 5.4 (a)). Selected samples have undergone the CVD process for different exposure times. The films used have been pre-examined by XPS or grown in the same deposition step as these.

Low temperature dc measurements (performed by K. Götz [Götz et al., 2016]) show that the *residual resistance ratios* RRR, defined as the ratio of the resistance at room temperature to the resistance just above the superconducting transition temperature, for all $Mo_{20}Re_{80}$ films are in the range $0.8 \lesssim RRR \lesssim 1$. Cooldowns of Hall bars made of $Mo_{20}Re_{80}$ show (see Fig. 5.4 (b)), that critical temperatures of $8\,K \leq T_c \leq 9\,K$ are sustained for CVD exposure times as large as $20\,min$. Only at $30\,min$ of exposure the critical temperature drops below $4\,K$. Samples with an alloy composition of $Mo_{58}Re_{42}$ have also been investigated. These show a high initial critical temperature of $T_c \geq 10\,K$ that, however, drops to half its value already after $10\,min$ of CVD

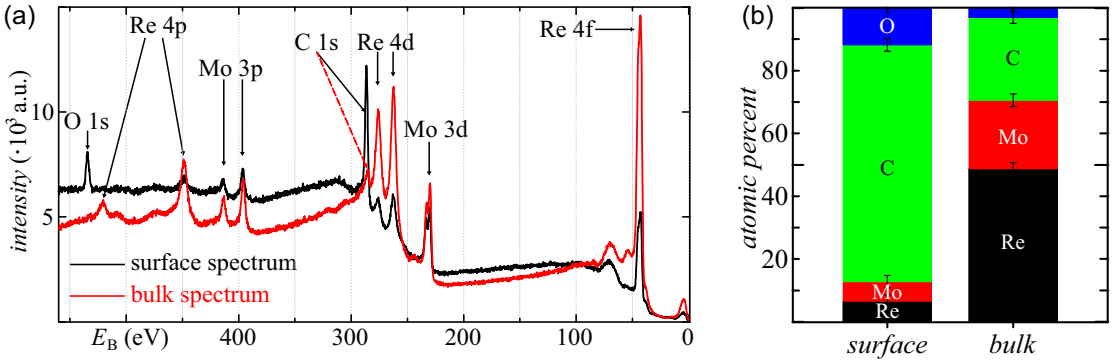

Figure 5.3.: (a) XPS spectra for a CVD exposed (30 minute) MoRe film for surface and bulk again at $P_{\mathrm{Mo}} = 75\,\mathrm{watt}$. (b) Atomic composition of the film for surface and bulk. The carbon proportion is enlarged in comparison to the pristine film. Adapted from [Götz et al., 2016].

exposure. This indicates that films with these alloy ratios are more harmed by the hot CH_4/H_2 flow.

Fig. 5.4 (c) shows the critical temperature in dependence of an applied magnetic field perpendicular to a pristine and a CVD exposed film. The data is fit to the empirical equation $B_c(T) = B_{c0} \cdot \left(1 - (T/T_{c0})^2\right)$ [Tinkham, 2004], where T_{c0} is the zero-field critical temperature and B_{c0} is the critical field at $T = 0$. Extrapolation of the fit gives values of $B_{c0} = 7.3\,\mathrm{T}$ and $T_{c0} = 8.3\,\mathrm{K}$ for the pristine sample. A strong reduction of critical temperature and magnetic field to $T_{c0} = 3.9\,\mathrm{K}$ and $B_{c0} = 3.6\,\mathrm{T}$ can be observed after $30\,\mathrm{min}$ of CVD exposure, as expected.

Additionally, critical current measurements have been performed. Fig. 5.4 (d) shows the critical current of a $Mo_{20}Re_{80}$ Hall bar, with $10\,\mathrm{min}$ CVD exposure time and $T_c = 9.2\,\mathrm{K}$. Over a temperature range of up to $5\,\mathrm{K}$ it maintains a critical current of $I_c \gtrsim 80\,\mathrm{mA}$, respectively a critical current density of $j_c \gtrsim 2.7 \cdot 10^5 \mathrm{A/mm^2}$. These high values of j_c are consistent with previous reports on suspended $Mo_{50}Re_{50}$-nanostructures after a high temperature annealing step [Aziz et al., 2014].

The results of this section show that the $Mo_{20}Re_{80}$ alloy could be a suitable material choice for integrating carbon nanotubes into superconducting device structures and possibly even growing them on-chip in a last fabrication step.

5.4. High frequency characterization

Superconducting quarter wave resonators have been fabricated in order to determine the high frequency properties of the MoRe thin films and investigate their potential application in cavity quantum electrodynamics and optomechanics experiments.

Films of $Mo_{20}Re_{80}$ with thicknesses of $t = 150\,\mathrm{nm}$ were grown on either Si/SiO_2 or Al_2O_3 substrates and patterned by optical lithography and RIE into quarter wave resonator structures as described in Sect. 4.4. In dilution refrigerator experiments transmission data can be recorded

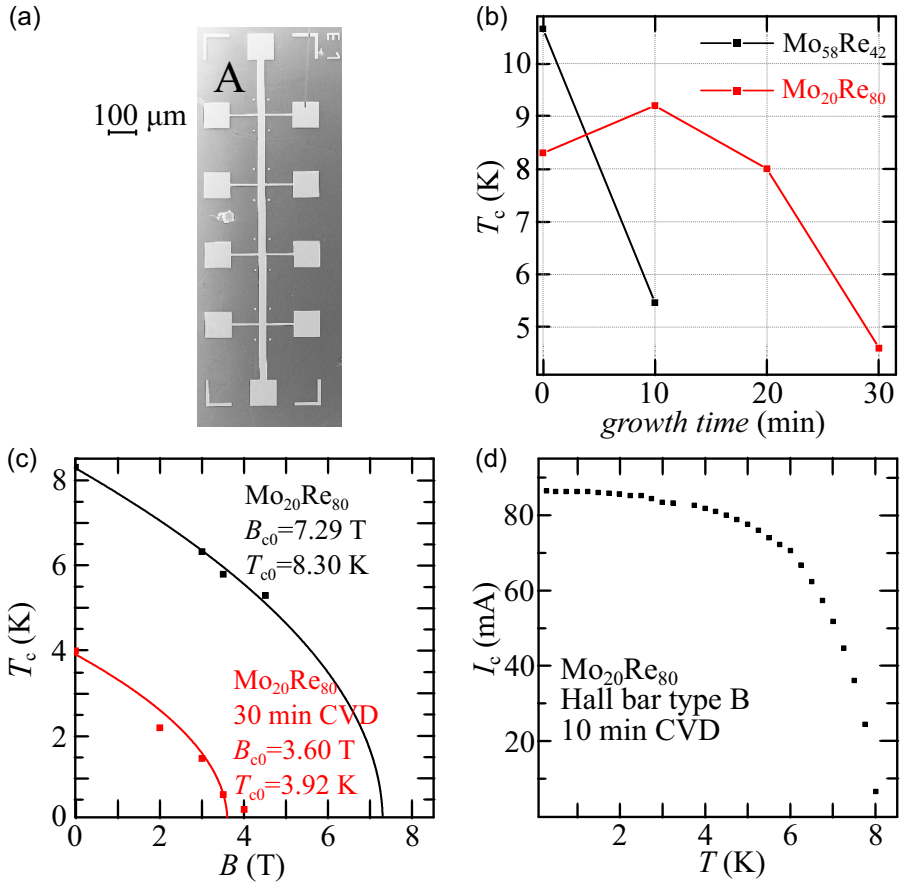

Figure 5.4.: (a) SEM micrograph of a Hall bar structure device used for dc characterisation. The Hall bar width for device type A is $w = 28\,\mu\mathrm{m}$ and the film thickness $t = 150\,\mathrm{nm}$, for device type B $w = 5\,\mu\mathrm{m}$ and $t = 60\,\mathrm{nm}$. (b) Critical temperature T_c in dependence of exposure time to the CVD process for two different alloy compositions. (c) Measured critical temperature T_c as function of the applied perpendicular magnetic field B for a pristine and a CVD exposed device. (d) Measured critical current I_c through a type B Hall bar as function of temperature. Adapted from [Götz et al., 2016].

and resonance frequencies and individual quality factors can be determined using Eq. 4.73. Exemplary measurements are shown in Fig. 5.5. From a fit to the data, an internal quality factor $Q_\mathrm{i} \simeq 23600$ and a coupling quality factor $Q_\mathrm{c} \simeq 10800$ are obtained for a pristine device at $T = 100\,\mathrm{mK}$ (Fig. 5.5 (a)). For a similarly fabricated device, that has been exposed to the CVD growth process for $30\,\mathrm{min}$, still all three resonances can be identified. Internal quality factors are in the range of $Q_\mathrm{i} \simeq 5000$ (Fig. 5.5 (b)).

According to Tinkham [Tinkham, 2004] and Cardwell/Ginley [Ginley and Cardwell, 2002], the appropriate limit for alloy superconductors is the local dirty limit, as their short mean free path assures that $\xi \approx l \ll \lambda_\mathrm{eff}$ (with again the coherence length ξ, the mean free path l, and the

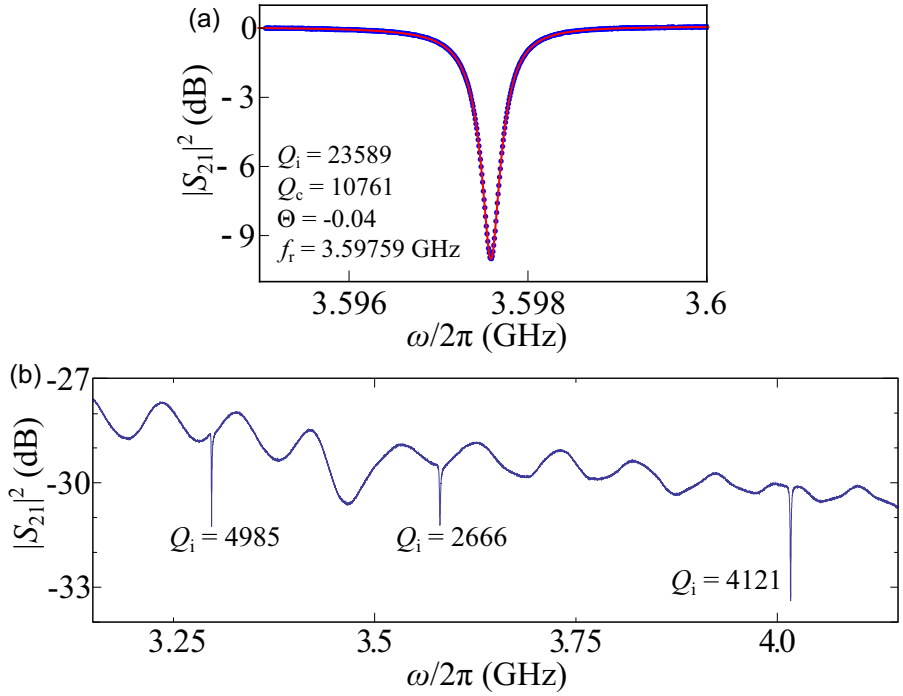

Figure 5.5.: Transmission spectra $|S_{21}|^2$ for different MoRe resonator devices. (a) Detail measurement of a single resonance of a pristine device at $T = 100\,\mathrm{mK}$. A background has been subtracted. From the fit (red), the resonance frequency and quality factors can be determined. (b) Three resonances of a device after 30 min exposure to the CVD process at $T = 15\,\mathrm{mK}$. The resonances can still be identified in the uncalibrated data. Adapted from [Götz et al., 2016].

effective penetration depth λ_{eff}). For dirty and local superconductors, Lemberger [Lemberger et al., 2007] and Watanabe [Watanabe et al., 1994] give an expression for the penetration depth consistent with BCS theory,

$$\lambda_{\mathrm{eff}}(T=0) = \frac{\pi\mu_0\Delta_0}{\hbar\rho(T_c)} \rightarrow \lambda_{\mathrm{eff}} \approx 1.05\cdot 10^{-3}\sqrt{\frac{\rho(T_c)}{T_c}}\,\mathrm{m}\,, \tag{5.1}$$

where $\rho(T_c)$ is the residual resistivity close to the critical temperature. With this, penetration depths $\lambda_{\mathrm{eff}} = 345\,\mathrm{nm}$ for the pristine film and $\lambda_{\mathrm{eff}} = 443\,\mathrm{nm}$ for the CVD exposed film can be estimated. Because film thicknesses for resonator devices were kept constant as $t = 150\,\mathrm{nm}$, all films are considered thin. These limits have also been used in previous studies by other groups [Singh et al., 2014b].

5.4.1. Temperature dependence of resonant behaviour according to Mattis-Bardeen theory

In Sect. 4.4.2, it was shown that the resonance frequency and the internal quality factor are strongly temperature dependent. Fig. 5.6 shows the temperature dependence of ω_r for a pris-

tine resonator on compensation-doped Si covered by $500\,\mathrm{nm}$ thermal SiO_2 and $10\,\mathrm{nm}$ ALD-deposited Al_2O_3 (device 1) and a resonator that has undergone $10\,\mathrm{min}$ of the CNT growth process (device 2). The resonance frequency clearly decreases with rising temperature ($T \gtrsim 0.8\,\mathrm{K}$ for device 1, $T \gtrsim 0.4\,\mathrm{K}$ for device 2). This can be explained by a decrease in the superfluid density of the superconducting film. A related rise in quasiparticle density leads to a higher dissipation of the signal in the resonator and thus to a reduction of the internal quality factor [Mattis and Bardeen, 1958, Singh et al., 2014b, Götz et al., 2016] (see Fig. 5.7).

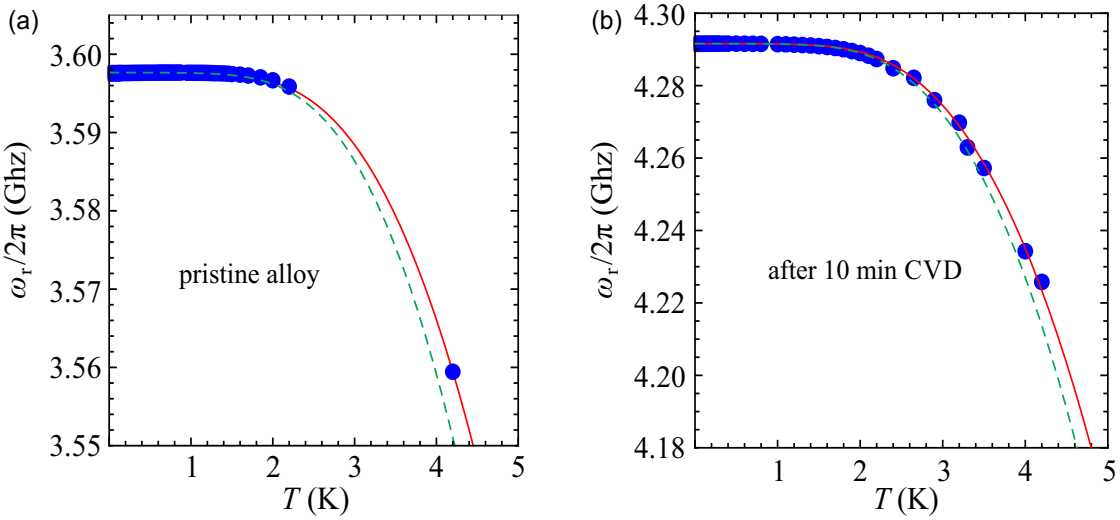

Figure 5.6.: Temperature dependence of resonance frequency for devices 1 (a) and 2 (b). The figure includes a theoretical model (dashed green) using parameters from dc experiments and a fit with the kinetic inductance fraction α_k as a single fit parameter (solid red). Adapted from [Götz et al., 2016].

Using Eq. 4.64, the temperature dependence can be expressed by

$$\frac{\delta\omega_r}{\omega_{r0}} = -\frac{\alpha_k}{2}\frac{\delta L_s}{L_{s0}} = \frac{\alpha_k}{2}\frac{\delta\sigma_2}{\sigma_2}\,, \tag{5.2}$$

where in the last step the dirty local limit for thin films was used: Eq. 4.50 gives the relation between L_s and σ_2. The kinetic inductance fraction α_k can be calculated as described in Sect. 4.3.5: with only T_c and σ_n as experimentally determinable parameters, the temperature dependence of $\delta\sigma_2/\sigma_2$ and so $\delta\omega_r/\omega_{r0}$ can be modelled.

First, for device 1, $T_c = 8.31\,\mathrm{K}$ and $\sigma_n = 1.1 \cdot 10^6\,\mathrm{S/m}$, and for device 2, $T_c = 7.92\,\mathrm{K}$ and $\sigma_n = 0.94 \cdot 10^6\,\mathrm{S/m}$ are obtained by dc experiments explained in the previous section. As also $\hbar\omega, k_B T < 2\Delta$, Eqs. 4.46 and 4.47 can be used to approximate the complex conductivity, with a temperature dependent BCS energy gap $\Delta(T) = \Delta_0\sqrt{\cos\left[\pi/2 \cdot (T/T_c)^2\right]}$ (Eq. 4.41) and $\Delta_0 = 1.764\,k_B T_c$ (Eq. 4.40). This results in temperature dependent expressions $\sigma_1(T)$ and $\sigma_2(T)$ for both devices.

Then, in the case of thin films of thickness t in the local limit the surface inductance can be calculated as $L_s = 1/(\sigma_2 \omega t)$ (Eq. 4.50 and the following paragraph). Obtained values for the

surface inductance ($T \approx 0$, $\omega \approx \omega_\mathrm{r}$), giving $L_\mathrm{s} = 1.03\,\mathrm{pH/m}$ (device 1) and $L_\mathrm{s} = 1.27\,\mathrm{pH/m}$ (device 2), are in reasonable agreement with other publications [Singh et al., 2014b].

Using a geometrical factor $g(s, w, t)$ (Eq. 4.54) that considers the waveguide geometry leads to values for the kinetic inductance of $L_\mathrm{k} = 1.36 \cdot 10^{-7}\,\mathrm{H/m}$ (device 1) and $L_\mathrm{k} = 1.68 \cdot 10^{-7}\,\mathrm{H/m}$ (device 2). For both devices, a geometric inductance (given by the waveguide geometry) can be calculated using Eq. 4.18 as $L_\mathrm{g} = 4.24 \cdot 10^{-7}\,\mathrm{H/m}$. From these parameters follows a kinetic inductance fraction $\alpha_\mathrm{k} = L_\mathrm{k}/(L_\mathrm{k} + L_\mathrm{g})$ (Eq. 4.58); theoretical values $\alpha_\mathrm{k,th} = 0.243$ (device 1) and $\alpha_\mathrm{k,th} = 0.284$ (device 2) are obtained.

Now, all parameters and functions of above equation 5.2 are known; the corresponding resonance frequency temperature dependence is plotted in Fig. 5.6 as a dashed green line. For both devices, these are in reasonable agreement with fit curves (solid red) using α_k as a free parameter. In this case, $\alpha_\mathrm{k,fit} = 0.199$ (device1) and $\alpha_\mathrm{k,fit} = 0.249$ are obtained.

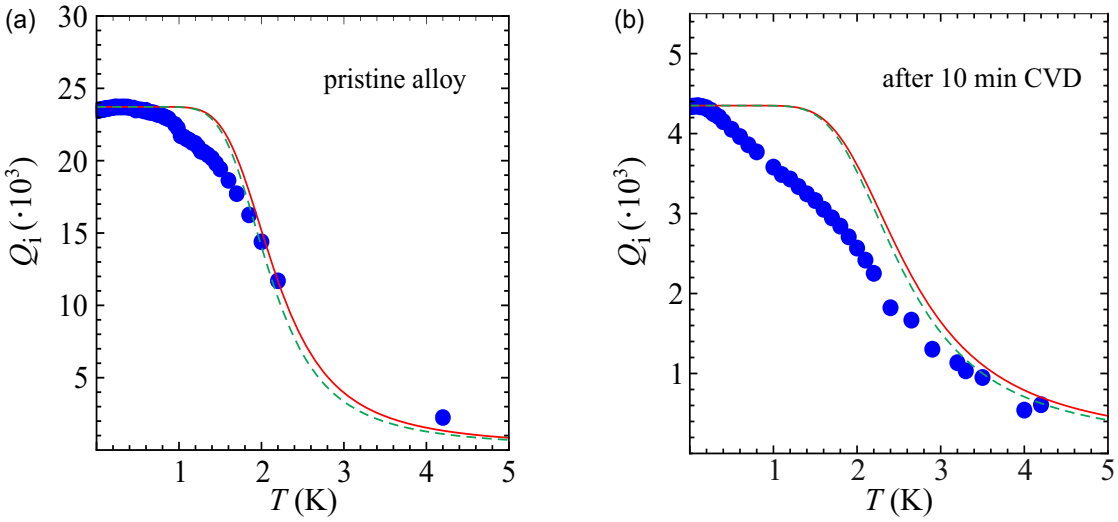

Figure 5.7.: Temperature dependence of internal quality factor for devices 1 (a) and 2 (b). The Figure includes a theoretical model (dashed green) using parameters from dc experiments and a fit with the kinetic inductance fraction α_k obtained from the fits in Fig. 5.6 (solid red). Adapted from [Götz et al., 2016].

Proceeding in the same manner, the temperature dependence of the internal quality factor can be modelled. In the dirty local thin film limit, Eq. 4.70 transforms to

$$\delta\left(\frac{1}{Q_\mathrm{i}}\right) = \alpha_\mathrm{k}\frac{\delta R_\mathrm{s}}{\omega L_\mathrm{s}} = \alpha_\mathrm{k}\frac{\delta\sigma_1}{\sigma_2}\,. \tag{5.3}$$

In Fig. 5.7 the expected temperature dependence of Q_i is plotted, using for the kinetic inductance fraction the theoretical (green) and fit values (red) obtained from the resonance frequency fit. An overall consistency to the data can be recognised, while significant deviation exists.

Another MoRe resonator device with a CVD exposure time of 30 min has also been high frequency characterised due to its resonance frequency and internal quality factor temperature

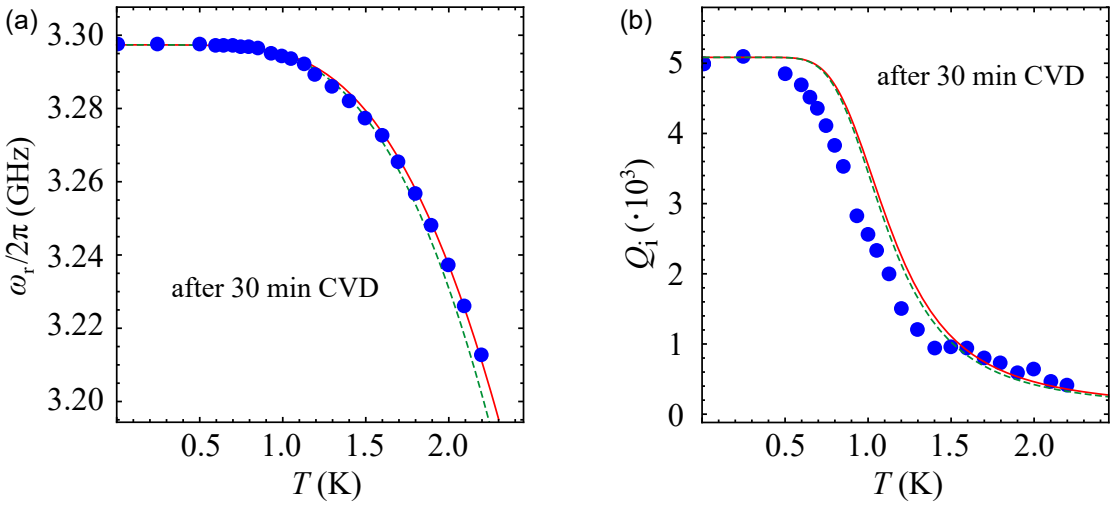

Figure 5.8.: Temperature dependence of resonance frequency (a) and internal quality factor (b) of MoRe device after being exposed to the CNT growth process for 30 min. Dashed green lines again correspond to a theoretical model, red solid line in (a) is a fit with the kinetic inductance fraction as free parameter. The obtained value has then been used as fixed parameter in (b). Theoretical modelling and fit procedure are performed as described in the main text. Adapted from [Blien et al., 2016].

dependence; see Fig. 5.8. In the same manner as above, a theoretical kinetic inductance fraction $\alpha_{\mathrm{k,th}} = 0.399$ was calculated using a critical temperature of $T_\mathrm{c} = 4\,\mathrm{K}$ and a normal state conductivity $\sigma_\mathrm{n} = 1.11 \cdot 10^6\,\mathrm{S/m}$ obtained with dc experiments. A theoretical model curve for the temperature dependence of resonance frequency and internal quality factor is plotted in Fig. 5.8 as dashed green line. As above, also a fit has been performed to the data of Fig 5.8 (a) with α_k as free parameter (red solid line). Here, $\alpha_{\mathrm{k,fit}} = 0.361$ has been obtained. As before, this value has been used as fixed parameter for the corresponding curve (red solid line) in Fig. 5.8 (b). In comparison with device 1 and 2, the normal state conductivity is in the same range as for the pristine device, but the critical temperature was reduced much and the kinetic inductance fraction has increased. Clearly, the deterioration of superconducting properties is proportional to the CVD exposure time.

5.4.2. Deviations form Mattis-Bardeen: two-level systems in substrate

Mattis-Bardeen theory predicts a saturation of the resonance frequency and internal quality factor with decreasing temperature for $T \ll T_\mathrm{c}$. In our devices, however, non-monotonic behaviour of ω_r and Q_i is observed: for $T \lesssim 0.5\,\mathrm{K}$ the resonance frequency and quality factor start to decrease with falling temperature. This is consistent with coupling to *two-level systems* (TLS) in the substrate that contribute to dissipation and dispersion simultaneously [Phillips, 1987, Pappas et al., 2011, Götz et al., 2016].

TLS are commonly present in amorphous materials [Phillips, 1972, Anderson et al., 1972]

as broad spectrum tunneling states; examples are tunneling atoms, dangling bonds, or trapped charges in the material. TLS are microscopically modelled as polar molecules, e.g. OH^- [Pappas et al., 2011], that carry electric dipole moments $\vec{D}$ that can couple to the electric field $\vec{E}$ generated by the resonator. In this way, they contribute to the dielectric function as [Pappas et al., 2011]

$$\epsilon_{\mathrm{TLS}}(\omega, T) = \epsilon'_{\mathrm{TLS}} - i\epsilon''_{\mathrm{TLS}} = \frac{Pd^2}{3\hbar} \int_0^{\varepsilon_{\max}} \chi_{\mathrm{res}}(\omega, T) d\varepsilon \,, \tag{5.4}$$

where P is the TLS density of states, $d = |\vec{D}|$ is the dipole moment, and χ_{res} is the resonant susceptibility, which is here integrated over energy ε. The real and imaginary part of the TLS related dielectric function are responsible for the resonance frequency and internal quality factor shift of the CPW resonator in this temperature regime.

The resonant susceptibility can be decomposed into three factors [Pappas et al., 2011]: the first one is a weighting function $\tanh(\varepsilon/2k_{\mathrm{B}}T)$, giving the probability difference of ground and excited state. The second one is the single-pole response of a TLS in the ground state under the *rotating wave approximation* (RWA). The third one is a power saturation term: it is close to 1 for weak driving, but limits the contribution of the resonant TLS for higher power. These undergo Rabi oscillations causing reduced response to χ_{res}. Carrying out the integral in Eq. 5.4 then gives real and imaginary part of ϵ_{TLS}.

The influence of the TLS on the resonance frequency is given by the real part of ϵ_{TLS} and can be modelled by [Phillips, 1987, Pappas et al., 2011, Pozar, 2011]

$$\frac{\delta\omega_{\mathrm{r}}}{\omega_0} = -\frac{F}{2}\frac{\delta\epsilon'_{\mathrm{TLS}}}{\epsilon} = \frac{F\vartheta}{\pi}\left[\mathrm{Re}\Psi\left(\frac{1}{2} + \frac{1}{2\pi i}\frac{\hbar\omega_{\mathrm{r}}(T)}{k_{\mathrm{B}}T}\right) - \ln\left(\frac{1}{2\pi}\frac{\hbar\omega_{\mathrm{r}}(T)}{k_{\mathrm{B}}T}\right)\right] . \tag{5.5}$$

Here, F, ϑ, and ϵ are the filling factor, loss tangent, and (full) dielectric permittivity of the substrate, and Ψ is the digamma function.

For off-resonant TLS, the real part of the RWA contribution decays as $(\omega_\varepsilon - \omega)^{-1}$, where $\omega_\varepsilon = \varepsilon/\hbar$ is the excitation frequency for a TLS; this leads to a logarithmic convergence of the integration in 5.4. In other words, off-resonant TLS have significant contribution to the resonance frequency shift. As the TLS in an amorphous material possess a broad spectral range of energy splittings, they can be seen as unsaturated. In this way, ϵ' is almost power independent and 5.5 applies to high and low power excitation [Pappas et al., 2011].

Fig. 5.9 displays the low temperature behaviour of ω_{r} for device 1 and 2 with a fit to Eq. 5.5 with $F\vartheta$ and ω_0 as free parameters. For very low temperatures $T < 100\,\mathrm{mK}$, the data points do not follow the upturn of the fit curve but stay constant. This indicates temperature saturation effects in the cryostat that are however difficult to determine from these measurements. The fit results in $F\vartheta = 3.968 \cdot 10^{-5}$ for the pristine device, which is comparable to niobium CPW resonators on sapphire [Gao et al., 2008]. From this parameter product a TLS-related low-temperature and low-power internal quality factor can be estimated as

$$Q_{\mathrm{i,TLS}} = \frac{1}{F\vartheta} \,. \tag{5.6}$$

For device 1 this provides $Q_{\mathrm{i,TLS}} \approx 25000$, as expected slightly exceeding the experimentally determined value of $Q_{\mathrm{i}}(20\,\mathrm{mK}) \approx 23500$. For device 2, $F\vartheta = 4.087 \cdot 10^{-5}$ respectively

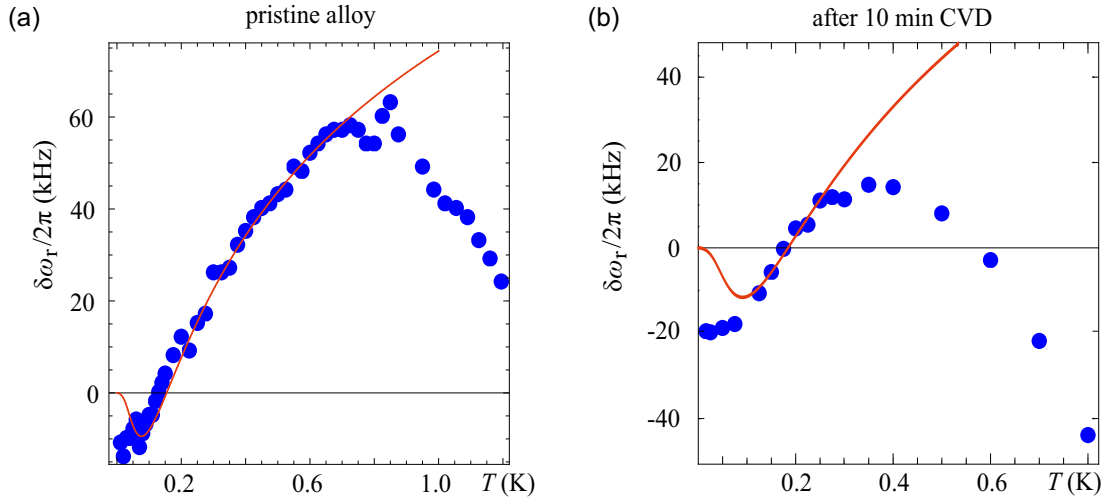

Figure 5.9.: Low-temperature resonance frequency temperature dependence for devices 1 (a) and 2 (b). The deviation from the Mattis-Bardeen model can be explained by interaction with two-level systems in the substrate. The figure includes a fit to the TLS model (red). Adapted from [Götz et al., 2016].

$Q_{\mathrm{i,TLS}} \approx 24500$ is obtained, comparable to the value of device 1. The fact that $Q_{\mathrm{i,TLS}}$ originates from two-level systems in the substrate explains why its value is not dependent on the level of metal degradation.

Similarly, for the internal quality factor the following TLS-related temperature dependence can be given [Phillips, 1987, Pappas et al., 2011]

$$\delta\left(\frac{1}{Q_\mathrm{i}}\right) = F\frac{\delta\epsilon''_{\mathrm{TLS}}}{\epsilon} = F\vartheta_{\mathrm{eff}}\tanh\left(\frac{\hbar\omega_\mathrm{r}(T)}{2k_\mathrm{B}T}\right) + \frac{1}{Q_{\mathrm{other}}}\,. \tag{5.7}$$

The imaginary part of the RWA contribution of the susceptibility has a Lorentzian lineshape $(\omega_\varepsilon - \omega)^{-2}$: only TLS close to the excitation frequency have significant contribution to the loss and the contribution is power dependent. Therefore, ϑ_{eff} represents an effective, reduced loss tangent that considers that two-level systems are partially saturated by a strong drive and can no longer contribute to energy dissipation. Q_{other} describes other absorption channels, that are not associated with TLS.

As can be seen in Fig. 5.10, the fit for device 1 and the measured data show conformity, with fit parameters of $F\vartheta_{\mathrm{eff}} = 5.677 \cdot 10^{-7}$ and $Q_{\mathrm{other}} = 23800$. Only few data points show the decrease with falling temperature for device 2. A fit to these gives $F\vartheta_{\mathrm{eff}} = 1.634 \cdot 10^{-6}$ and $Q_{\mathrm{other}} = 4370$. Apparently, the behaviour is not sufficiently described by the two-level system model.

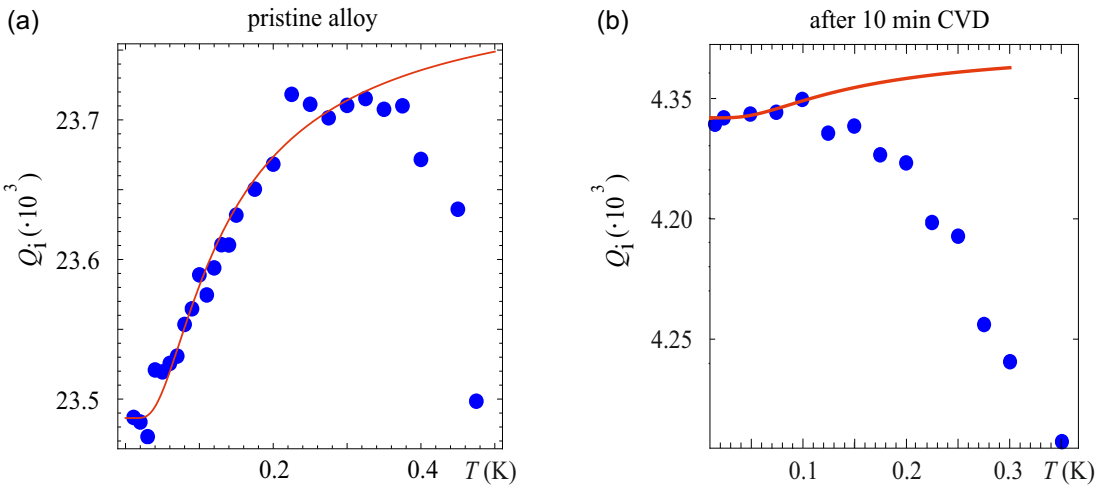

Figure 5.10.: Low-temperature internal quality factor temperature dependence for devices 1 (a) and 2 (b). The figure includes a fit to the TLS model (red). Adapted from [Götz et al., 2016].

6

Coupling a carbon nanotube to a microwave resonator

A chip that combines a half wave CPW resonator and a suspended carbon nanotube quantum dot needs complex electrode structures. As much time was spent into design and fabrication of such a device, the first half of this chapter serves to show the obstacles that have to be faced and the progress of development. The work presented was done in collaboration with two master students, A. Albang and N. Hüttner. The chapter finishes with experimental results proving the presence of a capacitively coupled cavity/quantum dot system.

Initially, the method of choice to produce such a combined device was to use overgrowth on CPW resonators made of MoRe. As then the fork transfer technique was implemented and began to show first results [Blien et al., 2018], the superconductor was switched to Nb as it produces much larger quality factors. This is why only device fabrication suitable for the fork transfer is introduced in this chapter. However, on the way to a working hybrid device it turned out that the quality factor[1] can be diminished by unforeseen influences. In particular, the additional fine electrode structure that is required for the transfer process has dramatic effects on the resonant microwave field, which will be shown below.

6.1. Resonator fabrication and quality factor optimisation

In the following, the fabrication of resonator and corresponding electrode structures of the final chip design is explained in general. For the detailed parameters, see [Hüttner, 2019]. The following steps are performed:

1. Cleaning of the substrate ($500\,\mu\mathrm{m}$ compensation doped Si with $500\,\mathrm{nm}$ thermally grown SiO_2) with acetone, propanol, and plasma ashing.
2. In UHV sputter systems, Nb is deposited on the chips to form a thin film.
3. Resonator and electrode coarse structure are defined by optical lithography and subsequently etched with RIE.
4. The thin gate finger is defined by EBL.
5. Metal (Ti and Au) is evaporated by electron beam and thermal evaporation on the chip. To improve the contact to the Nb, in-situ pre-sputtering with an Ar-plasma prior to the evaporation is advisable. The evaporation is followed by a lift-off in warm acetone.

[1] This always refers to the total quality factor in this chapter.

6. To electrically isolate the gate finger, a layer of 200 nm PMMA is spun onto the sample and cross-linked by EBL overexposure in the respective regions. Steps 4 & 5 are repeated for the fabrication of the lead electrodes and the dc gate connection to bias the cavity resonator.

7. In a final step, using optical lithography and an anisotropic etching step as described in Sect. 2.2.2, the deep-etched areas for the fork transfer are produced.

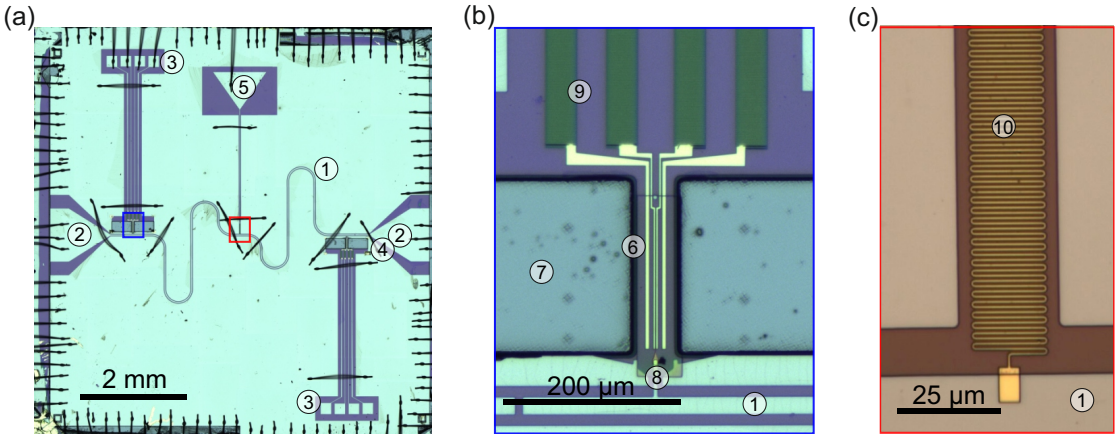

Figure 6.1.: Optical micrographs of the cavity resonator with additional structures needed for the fork transfer process. (a) shows the whole surface of the chip, including the cavity resonator (1), its launcher bond pads (2), the dc bond pads (3) leading to the coupling or transfer area (4), and the dc bond pad leading to the cavity centre conductor (5). Dark lines are bond wires for electrical connection or potential equalisation. In (b), the coupling area is magnified (blue rectangle). The transfer electrodes (6) are located between the deep-etched areas (7). A thin gate finger (8) is connected to the cavity centre conductor. Small meanders (9) serve as rf blocks and connect the transfer electrodes to their bond pads. (c) shows another zoom near the cavity centre (red rectangle). Here, a similarly structured meander (10) connects the CPW central conductor to the dc gate bond pad (5) from (a), so that an additional dc voltage can be applied to the gate finger. (a) and (b) adapted from [Blien et al., 2020].

In this way, samples as in Fig. 6.1 are produced. The half wave resonator (1) is seen in Fig. 6.1 (a) as a meander with its launcher bond pads (2) on the left and right side of the chip. In the same fabrication step, the dc bond pads later connected to the leads (3) and to the cavity centre conductor (5) are formed. Two transfer regions (4) are located near the coupling capacitors of the CPW resonator, where the electric field of the resonator is maximal. Only one of them is electrically connected; the other one is fabricated as surplus. If CNT transfer has failed multiple times, or the dc electrodes of one structure have been affected in another way, the second transfer area can be used. A further magnification of one of the coupling regions in Fig. 6.1 (b) reveals the electrode fine structure. A thin and long gate finger (8) is connected directly to the resonator centre conductor extending over the length of a protrusion between the two deep-etched areas

(7). The gate finger is electrically isolated via using cross-linked PMMA from the lead and cutting electrodes (6). Between these and their corresponding bond pads (3), thin meanders (9) are formed, that serve as rf blocks to conserve the rf signal in the cavity. In Fig. 6.1 (c), an optical micrograph of the meander (10) connecting the cavity centre conductor with the dc gate bond pad (5) is shown as an example. The connection is established at the voltage antinode of the fundamental mode (at half the length of the CPW resonator) to minimally disturb the resonance. In this way, an additional dc gate voltage can be applied to the gate finger (8).

The usual approach in device fabrication was then to first finalise the structuring of the CPW resonator and test it in the 4K stick to identify resonance frequency ω_r and quality factor Q_L. From these, the low temperature ω_r and Q_L can be estimated. A carbon nanotube can then be transferred using the fork transfer method (see Sect. 2.2.2).

6.1.1. Parasitic electromagnetic environment

As can be seen in Fig. 6.1, the ground planes of the coplanar waveguide have to be modified to integrate additional structure, i.e. the dc contacts, into the device. These interruptions in the ground plane can be seen as effective discontinuities, which change the on-chip current and potential distribution. Additionally, mode conversion to the slotline mode takes place at discontinuities [Simons, 2001]. Together with transmission in the normal conducting metal of the PCB and sample holder and through the vacuum of the sample holder, this leads to parasitic parallel circuit paths between the ports and the resonator [Hornibrook et al., 2012b]. This can be seen in the lumped elements representation of Fig. 6.2 (red path).

Here, another effect is also illustrated: the large overlap of the gate finger and the lead electrodes establishes an additional *dissipative coupling* to ground (due to the contacts being made of Au/Ti). This is accounted for by a capacitance C_elec and a resistance R_elec (blue path).

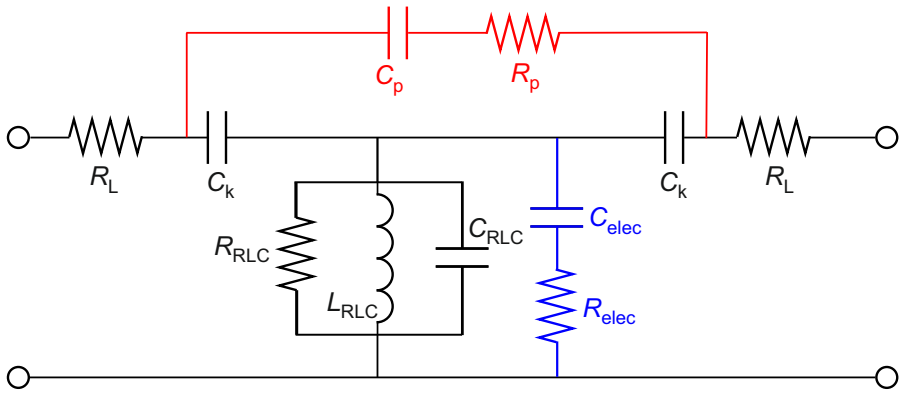

Figure 6.2.: Lumped elements model of a CPW half wave resonator with parasitic coupling. The parasitic paths are accounted for with parasitic capacitances C_p and C_elec and dissipative elements R_p and R_elec. The parallel path is drawn in red, the additional path to ground in blue. Adapted from [Hornibrook et al., 2012b].

Parasitic paths manifest themselves as Fano lineshapes [Fano, 1961] in the resonator trans-

mission spectra. Examples are shown in the next section. These lineshapes arise from coherent coupling of the single frequency mode of the resonator (a Lorentzian) with a continuum of states given by a parallel circuit path that has a flat frequency response [Miroshnichenko et al., 2010]. The interference of these can be destructive, leading to the asymmetric lineshape. The reason for this destructive interference is that the phase of the discrete resonance changes drastically (by π) around resonance. Through this, the discrete state interferes with the continuum of states with opposite phase on the left and right side of the resonance [Fano, 1961]. The original resonance frequency is then located between minimum and maximum of the Fano lineshape. Note that parasitic parallel paths do not necessarily represent loss mechanisms unless they are dissipative. This is however always the case in practical implementations due to resistive losses in normal metals and dissipation in dielectric materials in the vicinity of the resonator [Hornibrook et al., 2012b].

6.1.2. Quality factor optimisation

The unwanted coupling to dissipative elements leads to a substantial suppression of the quality factor of microwave resonators. A key challenge in fabrication of hybrid quantum devices is therefore to minimize this coupling and maintain high quality factors. This section shows the evolution of the device geometry for a Nb resonator of length $l \approx 10.5\,\mathrm{mm}$ corresponding to a resonance frequency of $\omega_{\mathrm{cav}} \approx 2\pi \cdot 6\,\mathrm{GHz}$. This was largely done by trial and error: individual modifications of the resonator geometry were implemented stepwise and several devices with the same geometry were tested to guarantee reproducibility. Here, the four most general modifications are presented on exemplary devices at $T = 4\,\mathrm{K}$. For more information see [Hüttner, 2019].

In [Hornibrook et al., 2012b], simulations show that discontinuities in transmission line geometries cause enhanced current densities and electric field in the normal conducting metal and dielectric, leading to parasitic dissipative signal paths. Although not further elaborated, the sample enclosure can contribute to these paths. Different enclosures have been simulated in [Hornibrook et al., 2012a]. Several measures for improvement are presented [Hornibrook et al., 2012b, Hornibrook et al., 2012a]: to confine these electric fields and currents, the application of non-tapered transmission lines and adding of tightly spaced vias to ground[2] on the PCB are discussed. Additionally, numerous bond wires can be used to connect the microwave resonator to the PCB, ensuring potential equalisation. These features have been implemented in our setup: the PCB is conductor-backed, has vias to ground and uses transmission lines of constant width reducing discontinuities; see Fig. 6.3. Additionally, a multitude of bond wires is used to connect the CPW chip to the PCB and to overbond on-chip structures in order to further extend potential equalisation; see Fig. 6.1 (a). Despite having integrated these features, even plain resonators without additional discontinuities in the ground planes showed Fano resonances, see Figs. 6.5 (a), with quality factors $Q \leq 4000$ at $T = 4\,\mathrm{K}$. Further improvement to reduce parasitic coupling can be surely accomplished here by simulating PCB and sample enclosure with a commercially available simulation software.

In a next step, resonators with gaps in the ground planes but without additional lead and

[2] "Ground" here denotes the metal covered back side of the PCB.

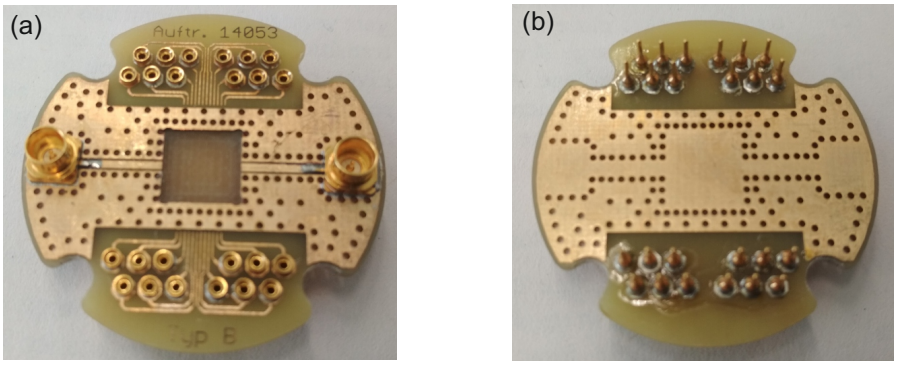

Figure 6.3.: Front (a) and rear (b) of the PCB. Visible are the non-tapered transmission lines and numerous vias connecting the ground plane to the backside of the PCB.

transfer electrodes were fabricated. To suppress the evolution of unwanted modes and equalise the electric potential on opposing ground planes, the gaps were bonded over with Al wires (as in Fig. 6.1 (a)). The connection to bias the resonator with a dc gate voltage was made with a thin gold meander. It is directly connected to the centre $\frac{l}{2}$ of the cavity and a bond pad as shown in Fig. 6.1 (c). This connection at the exact antinode of the electric field of the cavity serves to minimally disturb the resonance. The thin meander works as an effective rf block creating a large inductance and thus a maximal impedance mismatch to the resonator connection [Frey et al., 2012, Hao et al., 2014]. Therefore, high frequency signals cannot leave the cavity through this port but are reflected back. Tests in the 4K stick (see Fig. 6.5 (b)) and the dilution refrigerator showed, that the integration of these steps did not particularly influence the quality factor of the resonator.

Finally, the dc lead and transfer electrodes were included in the structure. Early test resonators with a superconducting gate finger (width $5\,\mu\mathrm{m}$), that extends partly under the inner lead electrodes (width $4\,\mu\mathrm{m}$, electrically isolated from the gate by a Al_2O_3 layer), produced no resonances at all. By cutting the connection between gate finger and cavity (see Fig. 6.4) using a *focused ion beam* (FIB), however, resonant behaviour could be re-established (see Fig. 6.5 (c)) with quality factors of about $Q \approx 1500$.

This shows that, in the model of Fig. 6.2, C_{elec} and R_{elec} were large enough to completely suppress the resonant behaviour of the cavity. Having identified the crucial problem, special emphasis has been placed on reducing this coupling of the cavity mode into the dc electrodes, by modifying the structure as follows:

1. The gate finger has been made of normal conducting metal (Au and Ti) and was reduced to a width of $100\,\mathrm{nm}$ and a height of $60\,\mathrm{nm}$, so that it fits into the gap of $1\,\mu\mathrm{m}$ between the lead electrodes. It was again protected with $200\,\mathrm{nm}$ PMMA.

2. The source and drain electrodes have been reduced to $2\,\mu\mathrm{m}$ width. For the outer transfer electrodes, a width of $4\,\mu\mathrm{m}$ has been maintained.

3. Meander structures, like for the dc gate connection, have been integrated to the all four

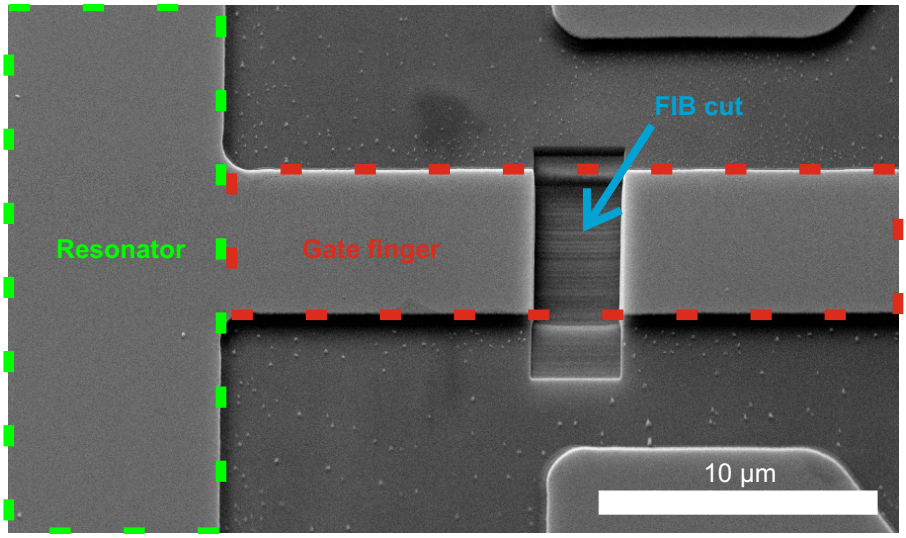

Figure 6.4.: SEM micrograph of a device where the connection between resonator and gate finger has been cut using a FIB. Picture taken by N. Hüttner.

dc electrodes between transfer area and bond pads to conserve the resonator mode in the cavity (see Fig. 6.1 (b)).

These final modifications lead to devices as shown in Fig. 6.1 that featured resonances with quality factors of $Q \approx 350$ (see Fig. 6.5 (d)). Devices fabricated in this manner are suitable for transferring a carbon nanotube into the coupling region. Thus, the fabrication of hybrid quantum or optomechanical devices becomes feasible.

The generally low quality factor of $Q = 350$ can be explained by the modified structure of the cavity resonators. A high dissipation in the normal conducting leads is the most obvious reason, although it cannot be excluded that the cavity mode leaks into the surrounding electronics. Therefore, to further increase the quality factor in future devices, it will be advisable to either cut the connection of cavity and gate finger of the unneeded coupling region or to fabricate only a single coupling region from the beginning. First tests of subsequent cutting of the gate finger have shown positive results (see [Hüttner, 2019]). Here, quality factors of $Q = 2000$ have been obtained. While a further reduction of the width of the source and drain electrodes seems to have negative impact on the fork transfer, shortening the overlap of gate and lead electrodes also could suppress the coupling of the cavity mode. For this task, smaller forks are necessary. Towards this, first steps have been taken in our work group by R. Graaf. In his master thesis [Graaf, 2019], he dealt with the customised fabrication of quartz forks by etching them out of Si/SiO_2 wafers.

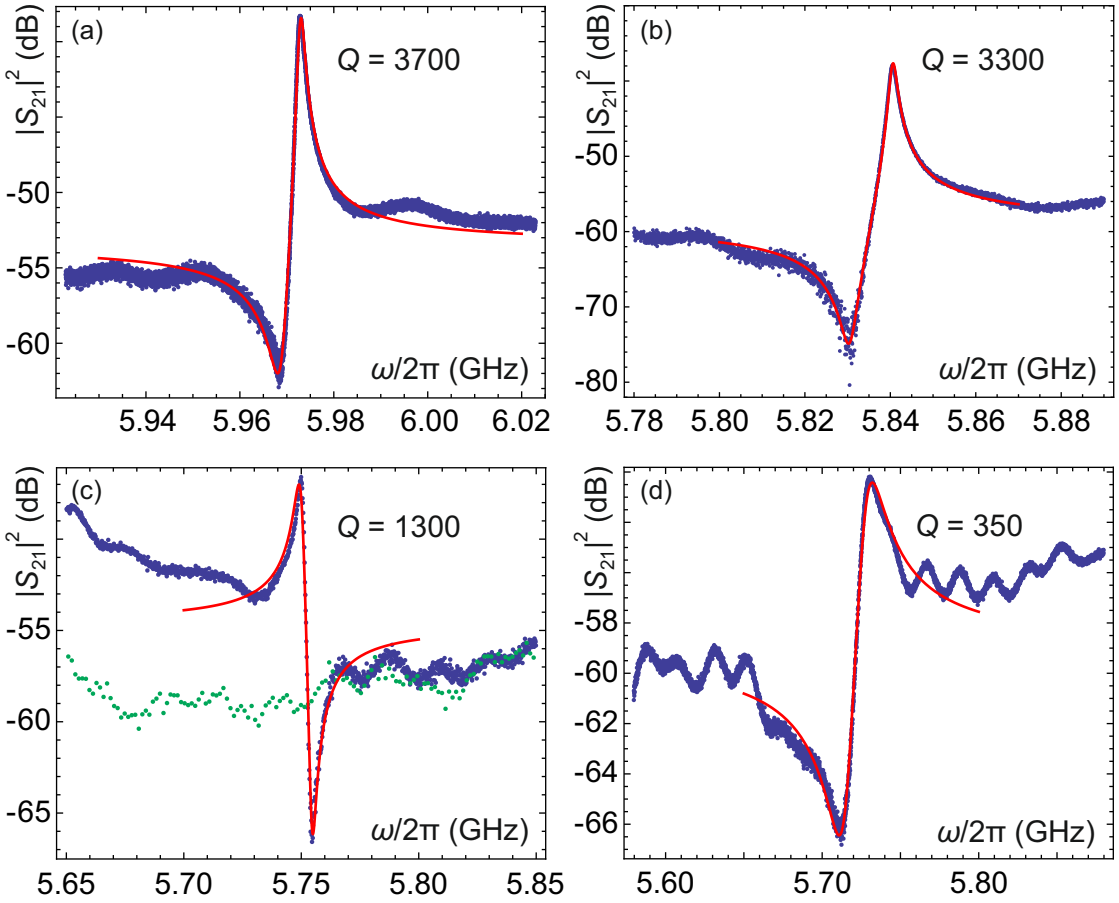

Figure 6.5.: Evolution of the resonant behaviour with device geometry at $T = 4\,\mathrm{K}$ and generator power $P = -20\,\mathrm{dBm}$. (a) shows the resonance of a plain resonator without additional structure. (b) Next, a device with gaps in the ground planes and a thin gold meander for biasing the resonator with a dc gate voltage was fabricated. Its behaviour is similar to the plain resonator. (c) A device geometry where the dc electrodes had been included at first showed no resonances (green). However, by cutting the connection between resonator and gate finger, a resonance could again be observed (blue). (d) Having included modifications in the coupling area (see main text), a device (suitable for coupling to a suspended CNT) with a finite but low quality factor could be fabricated. Red lines show fits to the data using Eq. 4.88.

6.2. Experimental demonstration of the coupling between cavity and nanotube quantum dot

A carbon nanotube was transferred to the device shown in Fig. 6.1 with according transmission characteristics in Fig. 6.5 (d). After cool down to the base temperature of our dilution refrigerator, the cavity resonator showed a transmission behaviour as in Fig. 6.6. The red line is a fit to Eq. 4.89, yielding a resonance frequency of $\omega_{\mathrm{cav}} = 2\pi \cdot 5.74\,\mathrm{GHz}$ and a quality factor of $Q = 497$ (and therefore a cavity decay rate of $\kappa_{\mathrm{cav}} = \omega_{\mathrm{cav}}/Q = 2\pi \cdot 11.6\,\mathrm{MHz}$). The overall small increase of the quality factor compared to the resonance at $T = 4\,\mathrm{K}$ (from earlier measurements, an increase by a factor ~ 10 was expected) shows that the quality factor is not limited by internal dissipation in the superconductor but to a large extent by geometry and dissipation in the normal conducting leads. As explained in the last section, the parasitic and electrode capacitances lead to the broadened Fano resonance in Fig. 6.6 (a) and the peculiar shape in phase of Fig. 6.6 (b). However, these capacitances shall be ignored in calculations henceforth.

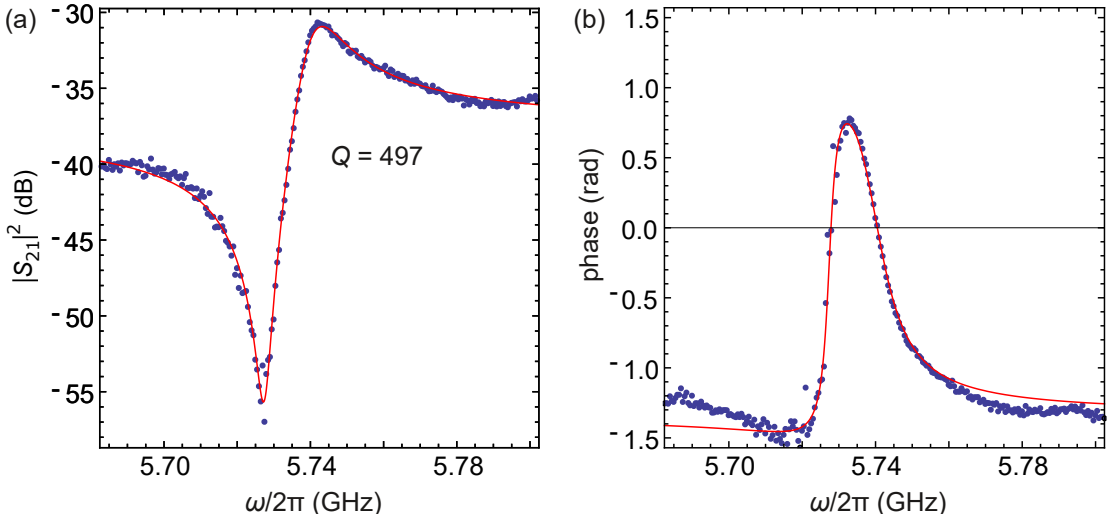

Figure 6.6.: Resonator transmission (a) and (corrected) phase (b). The red line shows a fit to Eq. 4.89, reproducing the Fano resonance and peculiar phase lineshape. From the fit, a resonance frequency $\omega_{\mathrm{cav}} = 2\pi \cdot 5.74\,\mathrm{GHz}$ and quality factor $Q = 497$ is obtained.

Fig. 6.7 displays a schematic and circuit representation of the combined cavity/carbon nanotube quantum dot system. Indexed with "CPW" are parameters belonging to the coplanar waveguide[3]; the coupling capacitors are denoted as C_{k} and the capacitance of the gate finger to the CNT as C_{g}. As has been seen in Sect. 4.5.2, the cavity can be modelled as a lumped elements resonator with a total capacitance

$$C_{\mathrm{tot}} = \frac{C_{\mathrm{CPW}}}{2} + 2C_{\mathrm{k}} + C_{\mathrm{g}}\,. \tag{6.1}$$

[3]The parameters here are given as total values, not per unit length as in Sect. 4.2.

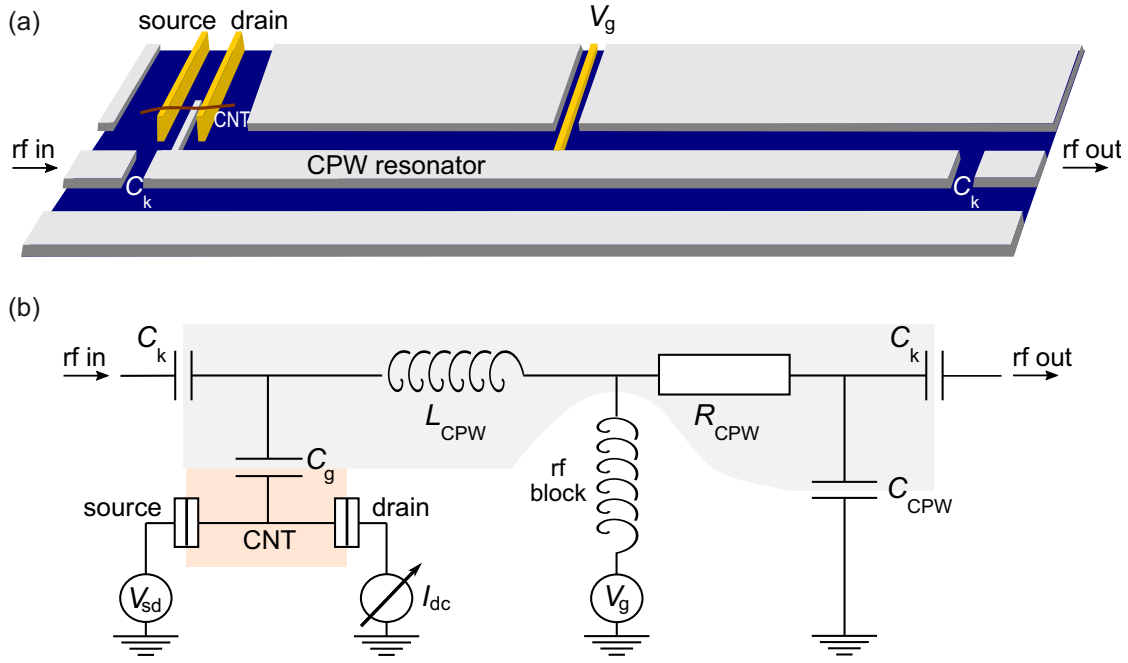

Figure 6.7.: Schematic (a) and circuit (b) representation of the resonator/quantum dot hybrid device. The carbon nanotube (brown) is capacitively (C_g) coupled to the CPW resonator (R_CPW, L_CPW, C_CPW). Microwave transmission can be measured by coupling a signal in and out of the cavity via coupling capacitors (C_k). The centre conductor of the CPW can be additionally biased with a dc gate voltage V_g to tune the electrostatic potential of the QD. Adapted from [Blien et al., 2020].

The coupling between cavity resonator and carbon nanotube is then mediated via the change in the gate capacitance C_g, respectively, the change in quantum capacitance of the CNT (see Sect. 2.3.5). This in turn is dependent on the parameters of the quantum dot, which can be controlled via gate voltage V_g and bias voltage V_sd. Therefore, a shift in resonance frequency (or phase) of the cavity can be interpreted as a shift in quantum capacitance of the CNT quantum dot. This is called dispersive coupling.

6.2.1. First tests for electronic coupling

To investigate interaction between the two subsystems, the quantum dot behaviour of the CNT has been utilised. In the case of finite coupling, the electric field of the driven microwave cavity should have an effect on the non-linear conductance of the quantum dot. Fig. 6.8 shows the experimental results: a larger power circulating in the cavity leads to a broadening of the Coulomb resonances. Similar results on the coupling of a microwave resonator to a AlGaAs quantum dot are shown in [Frey et al., 2011].

In Fig. 6.8 (a), the stability diagram of the vicinity of the investigated Coulomb diamond is plotted. The dashed green line marks the trace over the Coulomb oscillation that is used to

study the influence of the cavity power. The bias voltage for this trace was fixed at $V_{\rm sd} = 2\,\mathrm{mV}$ and the gate voltage was swept in a range $-1.48\,\mathrm{V} \leq V_{\rm g} \leq -1.41\,\mathrm{V}$. While measuring the current I, a signal was injected into the microwave cavity fixed in frequency at $\omega_{\rm gen} = \omega_{\rm cav} = 2\pi \cdot 5.74\,\mathrm{GHz}$ and generator power $P_{\rm gen}$. The signal generator was here directly connected to the cryostat high frequency input line (see Fig. 3.3 (a) for a schematic setup). In this way, the signal passes a set of attenuators with total attenuation of $53\,\mathrm{dB}$ before reaching the cavity. After each repetition of sweeping $V_{\rm g}$, $P_{\rm gen}$ was increased by $1\,\mathrm{dBm}$, covering a range $-27\,\mathrm{dBm} \leq P_{\rm gen} \leq +20\,\mathrm{dBm}$ (see Fig. 6.8 (b)). Above $P_{\rm gen} = +5\,\mathrm{dBm}$, a broadening of the Coulomb oscillation emerges. This is due to an additional voltage $\delta V_{\rm ac}$ on the gate electrode that corresponds to the circulating power in the cavity. As this voltage is oscillating at a rate $\omega_{\rm cav} = 2\pi \cdot 5.74\,\mathrm{GHz}$, the dc amplifier used to record the current measures a time-averaged contribution to I. This leads to a decrease in current on the peak of the Coulomb oscillation and an increase on its flanks. Linecuts (see Fig. 6.8 (c)) show that a larger generator power $P_{\rm gen}$ leads to a larger broadening of the Coulomb oscillation. Below a power of $P_{\rm gen} = +3\,\mathrm{dBm}$, the resonator mode has no effect on the conductance. Repeating the measurement on a second Coulomb oscillation on the electron conduction side (see Sect. C.1) has shown similar broadening behaviour.

Following [Frey et al., 2011], a second test for coupling was performed: the conductance of the quantum dot was investigated, while sweeping the frequency of the signal injected into the cavity. In Fig. 6.9 (a), the bias voltage was kept a constant value of again $V_{\rm sd} = 2\,\mathrm{mV}$. The gate voltage was set to $V_{\rm g} = -1.443\,\mathrm{V}$, and thus on the flank of the Coulomb oscillation of Fig. 6.8 (c) for low power. Keeping the generator power at $P_{\rm gen} = +12\,\mathrm{dBm}$, the frequency is swept in a range $2\pi \cdot 4\,\mathrm{GHz} \leq \omega_{\rm gen} \leq 2\pi \cdot 6\,\mathrm{GHz}$, while, again, the current is measured. Away from cavity resonance, the current is comparable with the measurement of Fig. 6.8, at $\omega_{\rm gen} \approx \omega_{\rm cav}$, however, a large peak emerges. This can be explained in the following way: the power is not large enough to significantly broaden the Coulomb resonance for off-resonant driving ($\omega_{\rm gen} \neq \omega_{\rm cav}$). In the vicinity of $\omega_{\rm cav}$, however, the power in the cavity leads to a large enough $\delta V_{\rm ac}$ to increase the current as explained above and for Fig. 6.8. According to [Frey et al., 2011], for low enough powers, this should directly reflect the cavity transmission (along with respective resonance frequency and quality factor). In principle, this technique is similar to the detection mechanism of nanomechanics of CNTs as presented in Sect. 2.4.3 and [Hüttel et al., 2009]. Here also, $I(\omega_{\rm gen}) \sim \mathrm{d}I^2/\mathrm{d}V_{\rm g}^2$ and for low enough $\mathrm{d}V_{\rm g}$ (or equally $P_{\rm gen}$), the quality factor is reflected in the frequency dependence of the current. Therefore, the measurement was repeated on the Peak of the Coulomb oscillation ($V_{\rm g} = -1.445\,\mathrm{V}$) for a generator power of $P_{\rm gen} = +5\,\mathrm{dBm}$ (see Fig. 6.9 (b)). A Lorentzian fit gives a resonance frequency and quality factor of

$$\omega_{\rm cav} = 2\pi \cdot 5.739\,\mathrm{GHz}\,, \text{ and } Q = 390\,.$$

While the resonance frequency agrees nicely with the one obtained from the fit of the cavity transmission in Fig. 6.6, the quality factor is in the same order of magnitude, but slightly lower due to the high generator power.

A second measurement of this kind was performed on the electron conduction side (on the Coulomb oscillation of Fig. C.1). Here, the power on the generator was increased after each frequency sweep by $\Delta P_{\rm gen} = 5\,\mathrm{dBm}$; the bias was $V_{\rm sd} = 1\,\mathrm{mV}$ and the gate voltage $V_{\rm g} = -0.273\mathrm{V}$, on the flank of the Coulomb oscillation. The microwave resonance again appears in

the current through the CNT, sweeping the frequency over a range $5.67\,\mathrm{GHz} \leq \omega \leq 5.81\,\mathrm{GHz}$ as is shown in Fig. 6.9 (a). With increasing power, the broadening of the resonance in the current is evident. A linecut at $P_{\mathrm{gen}} = -2\,\mathrm{dBm}$ (see Fig. 6.10 (b)) reveals a Lorentzian with

$$\omega_{\mathrm{cav}} = 2\pi \cdot 5.739\,\mathrm{GHz}\,, \text{ and } Q = 800\,,$$

again consistent with earlier resonator characterization.

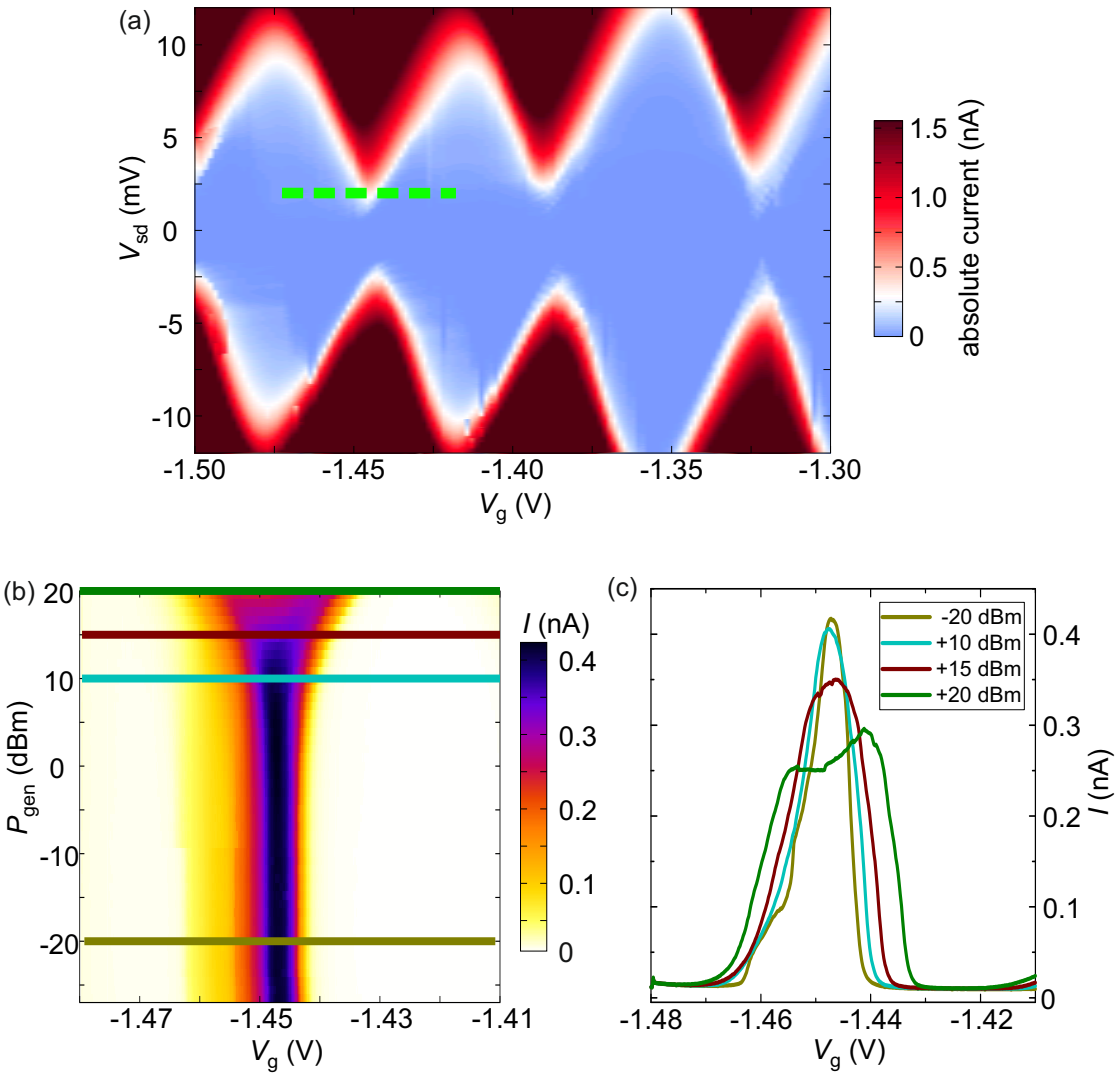

Figure 6.8.: Coulomb resonance broadening with increasing intracavity power. (a) shows the stability diagram around the respective Coulomb resonance. The green dotted line indicates the gate sweep $-1.48\,\mathrm{V} \leq V_\mathrm{g} \leq -1.41\,\mathrm{V}$ that has been performed in (b). For a fixed bias $V_\mathrm{sd} = 2\,\mathrm{mV}$ and generator frequency $\omega_\mathrm{gen} = \omega_\mathrm{cav} = 2\pi \cdot 5.74\,\mathrm{GHz}$, the current was measured while ramping up the generator power. A broadening of the Coulomb peak with increasing power is apparent. For clarity, linecuts at different generator powers are displayed in (c).

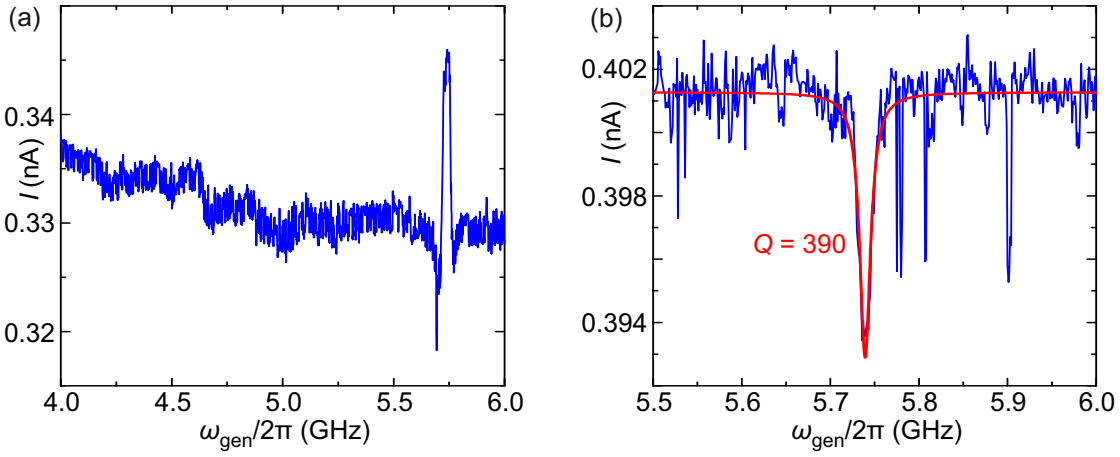

Figure 6.9.: Cavity resonance in the current through the carbon nanotube. (a) Gate and bias voltage are kept constant at $V_\mathrm{g} = -1.443\,\mathrm{V}$ and $V_\mathrm{sd} = 2\,\mathrm{mV}$ and the frequency of the cavity input signal is swept over a range $2\pi \cdot 4\,\mathrm{GHz} \leq \omega_\mathrm{gen} \leq 2\pi \cdot 6\,\mathrm{GHz}$ at constant generator power $P_\mathrm{gen} = +12\,\mathrm{dBm}$. Away from resonance the current through the CNT is nearly constant, while at cavity resonance a large peak emerges. The detection mechanism is similar to the one presented in [Hüttel et al., 2009]. (b) Detailed measurement of the resonance at slightly different gate voltage setting of $-1.445\,\mathrm{V}$ for lower drive power $P_\mathrm{gen} = +5\,\mathrm{dBm}$. A Lorentzian fit gives a quality factor of $Q = 390$.

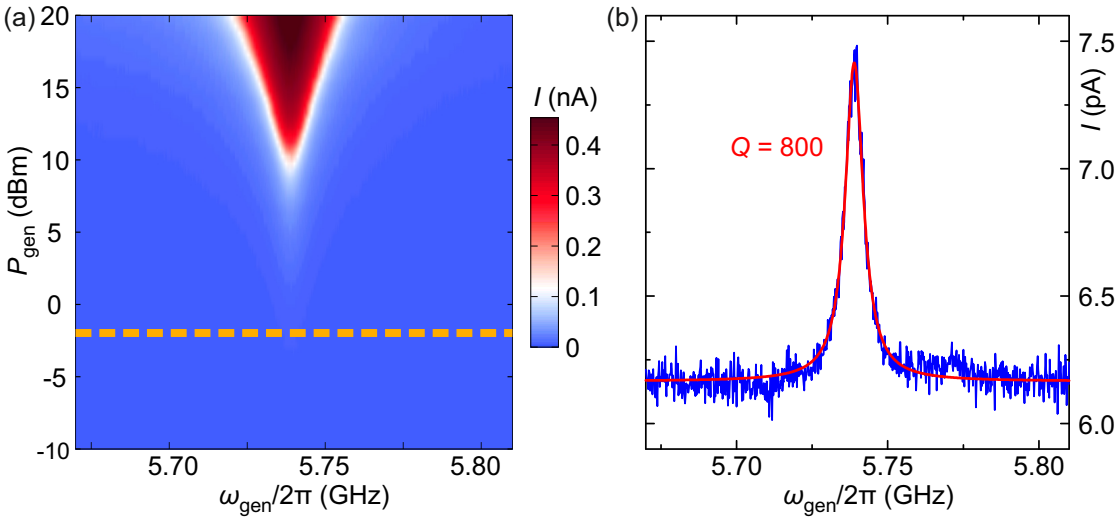

Figure 6.10.: Cavity resonance in nanotube current on electron conduction side. Gate and bias voltage settings are $V_\mathrm{g} = -0.273\,\mathrm{V}$ and $V_\mathrm{sd} = 1\,\mathrm{mV}$. The cavity input frequency was swept over a range $5.67\,\mathrm{GHz} \leq \omega \leq 5.81\,\mathrm{GHz}$. (a) Broadening of microwave with increasing generator power. (b) A linecut at $P_\mathrm{gen} = -2\,\mathrm{dBm}$ (orange dotted line in (a)) reveals a quality factor of $Q = 800$.

6.2.2. Quantum dot spectroscopy with a CPW resonator

So far, the Coulomb oscillation broadening and the microwave resonance in the nanotube current gave first hints that a coupling between CNT and microwave cavity has been established. This shall now be investigated in greater detail. For that, dc transport spectroscopy of the nanotube quantum dot behaviour is recorded, while simultaneously measuring the transmission characteristics of the cavity at its resonance frequency. Its drive power is chosen low enough (from measurements of the last subsection) to prevent significant broadening of the Coulomb oscillations.

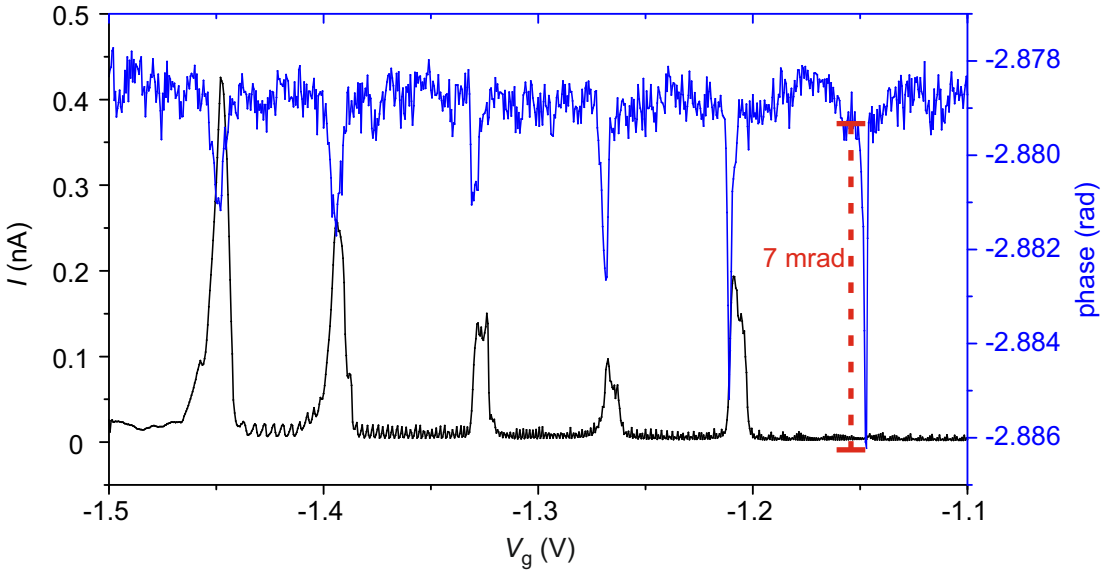

Figure 6.11.: Current through CNT and resonator phase while sweeping the gate voltage. The cavity was excited with a generator power of $P_{\mathrm{gen}} = -10\,\mathrm{dBm}$ at its resonance frequency. Characteristic Coulomb oscillations show up in the current. Sharp dips in the resonator phase emerge, slightly shifted to smaller gate voltages compared to the current oscillations. A bias of $V_{\mathrm{sd}} = 2\,\mathrm{mV}$ was applied.

Fig. 6.11 displays the dc current through the nanotube, as well as the phase of the cavity response at $\omega \approx \omega_{\mathrm{cav}}$ (where the phase is steepest), while sweeping the gate voltage in a range $-1.5\,\mathrm{V} \leq V_{\mathrm{g}} \leq -1.1\,\mathrm{V}$ and an applied bias of $V_{\mathrm{sd}} = 2\,\mathrm{mV}$. The resonator phase shows significant dips at almost the same gate voltages where Coulomb oscillations emerge in the current. Here, a phase noise $< 1\,\mathrm{mrad}$ can be maintained, while the dips are up to $7\,\mathrm{mrad}$ in depth, which is comparable to values obtained in the work of M. Delbecq [Delbecq et al., 2011, Delbecq, 2013]. The same behaviour (although weaker) is observed for the resonator amplitude (see Fig. 6.13 (c) for this). The observation of the Coulomb oscillations in the resonator phase again shows that the two systems are coupled [Delbecq et al., 2011]. The interaction is mediated in the form of dipole coupling between the charge states of the quantum dot and the electric field of the microwave cavity [Frey et al., 2012].

Given the phase shifts in Fig. 6.11, the quantum capacitance of the carbon nanotube QD at the Coulomb oscillations can be estimated. The fit function of Fig. 6.6 is used to translate the phase shift into a frequency shift $\Delta\omega$. Applying Thomson's formula results in

$$\Delta C = \left(\left(\frac{\omega_{\mathrm{cav}}}{\omega_{\mathrm{cav}} - \Delta\omega} \right)^2 - 1 \right) \cdot C_{\mathrm{tot}} \,. \tag{6.2}$$

For the rightmost phase dip, e.g., the phase changes by $\sim 7\,\mathrm{mrad}$, corresponding to a frequency shift of $\Delta\omega \approx 17.8\,\mathrm{kHz}$. To a good approximation, the total capacitance is equal to half the waveguide capacitance, $C_{\mathrm{tot}} \approx C_{\mathrm{CPW}}/2 = 0.875\,\mathrm{pF}$ (see Eq. 6.1), giving

$$\Delta C \approx 5.4\,\mathrm{aF}\,.$$

Although comparable to previously reported values [Delbecq, 2013], this number hast to faced with caution. Deducing a frequency shift from a measurement of the phase at a single frequency assumes purely dispersive coupling. However, also dissipative coupling may play a significant role. Here, the resonance of the cavity broadens when coupling to the quantum dot conductance. Energy stored in the cavity is dissipated in resistive circuit elements, here the carbon nanotube and normal conducting leads. The phase function then becomes less steep and its overall shape changes, masking the effects of dispersive coupling.

Therefore, transmission spectra covering the full resonance were taken over the gate range of a single Coulomb oscillation. Then, for each gate voltage a fit to Eq. 4.89 can be applied. In this way, the changes in resonance frequency and bandwidth can be traced, as depicted in Fig. 6.12. While the resonance frequency shifts (a), as expected, also the bandwidth gets significantly larger (b), signifying the co-existence of dispersive and dissipative coupling. Here, zero bias was applied to the lead electrodes. Applying Eq. 6.2 to the resonance frequency shift (see Fig. 6.12 (c)) provides a maximum capacitance change of

$$\Delta C \approx 11.4\,\mathrm{aF}\,,$$

which is about the double value obtained from the phase shifts of Fig. 6.11. Changes in inductance have been neglected in all calculations. Note that the value for the capacitance change from the resonance frequency shift is significantly larger than the value for the gate capacitance found from dc spectroscopy (see Sect. 2.3.3), $C_{\mathrm{g}}^{\mathrm{CB}} = 2.6\,\mathrm{aF}$. This is due to an altered response of the carbon nanotube to the microwave field in the vicinity of the SET events. As has been shown [Duty et al., 2005, Shevchenko et al., 2015], an *effective capacitance* can be expressed as

$$C_{\mathrm{eff}} = \frac{\partial \langle q_{\mathrm{g}} \rangle}{\partial V_{\mathrm{g}}} \,. \tag{6.3}$$

Here, $\langle q_{\mathrm{g}} \rangle = C_{\mathrm{g}}(V_{\mathrm{g}} - V_{\mathrm{CNT}})$ is the charge on the gate electrode [Steele et al., 2009]. Using Eqs. 2.32 and 2.33 for V_{CNT} in the equation above leads to

$$C_{\mathrm{eff}} = \frac{(C_{\mathrm{s}} + C_{\mathrm{d}})C_{\mathrm{g}}}{C_{\Sigma}} + e\frac{\partial \langle N \rangle}{\partial V_{\mathrm{g}}} \frac{C_{\mathrm{g}}}{C_{\Sigma}} \,. \tag{6.4}$$

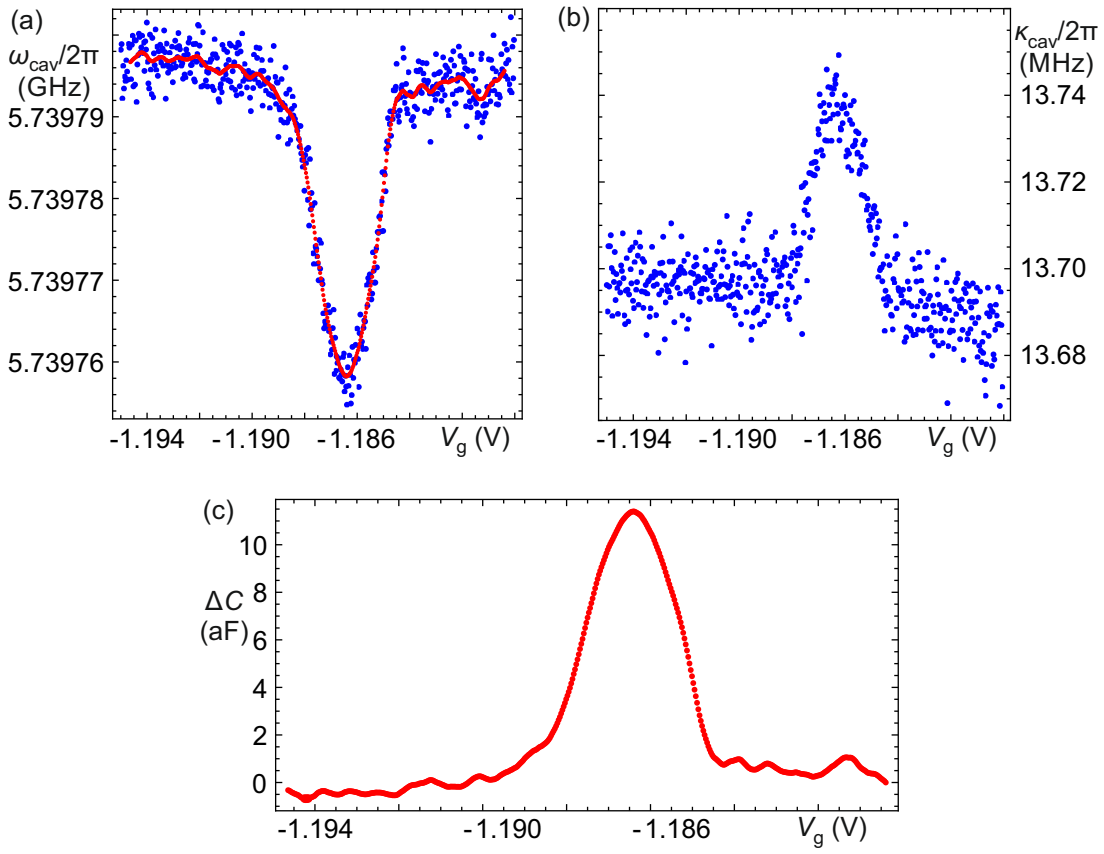

Figure 6.12.: Cavity resonance frequency (a) and bandwidth (b) over a single Coulomb oscillation. The data has been extracted from transmission measurements for each gate voltage and a subsequent fit to Eq. 4.89. A sliding average (red points) has been applied to the data points of (a). From this, a capacitance shift can be calculated (c). Data recorded by N. Hüttner.

This effective capacitance is then a *parallel circuit* of a geometric capacitance (being itself a series circuit of gate and lead capacitances) and the CNT quantum capacitance of Sect. 2.3.5 scaled by the gate conversion factor $\alpha_g = C_g/C_\Sigma$. This is an important result as it shows that single electron effects have to be considered in the cavity-nanotube coupling.

The cavity phase and amplitude response can also be used to record stability diagrams of the quantum dot. Fig. 6.13 shows differential conductance through the CNT, as well as resonator phase and amplitude at $\omega = \omega_{cav}$ over the same gate voltage range. The cavity was driven with a generator power of $P_{gen} = -4\,\mathrm{dBm}$. Typical Coulomb oscillations show up in the differential conductance (a), with faint edges in the small bias regime. For higher bias sharp ridges indicate current driven vibrations of the nanotube as explained in earlier chapters (see Sect. 2.4.2). Interestingly, the resonator phase (b) behaves very differently. Here, the most pronounced features appear in the low bias regime. An asymmetric coupling manifests itself as the emergence of a single edge of the Coulomb diamonds, while the other edge cannot be observed in the phase sig-

nal. The same effect leads to a shift in phase dips to lower frequencies compared to the current peaks in Fig. 6.11. While so far no similar effects were reported, a probable cause for this is a difference in coupling strength to the source and drain charge transitions. This can be induced by the presence of asymmetric tunnel barriers. The resonator phase is then more sensitive to the charge transition of the contact with the smaller tunnel barrier; for a qualitative discussion of this effect, see Sect. C.2. Here, due to the sharper transition, the change in average charge carrier number on the QD with gate voltage $\partial \langle N \rangle / \partial V_{\mathrm{g}}$, and so the quantum capacitance of the QD (see Sect. 2.3.5), is larger. This situation is similar to electromechanical backaction of CNTs around charge transitions; see Sect. 2.4.4 and [Meerwaldt et al., 2012]. There, larger $\partial \langle N \rangle / \partial V_{\mathrm{g}}$ also correspond to larger mechanical frequency shifts. In Fig. 6.13 (b), for higher bias, the coupling becomes weaker due to the broadening of the charge transitions. The sharp edges of current driven vibration are also absent. Although much weaker, in the resonator amplitude (c) similar behaviour can be perceived. A second stability diagram for the hole conduction side is shown in Sect. C.3.

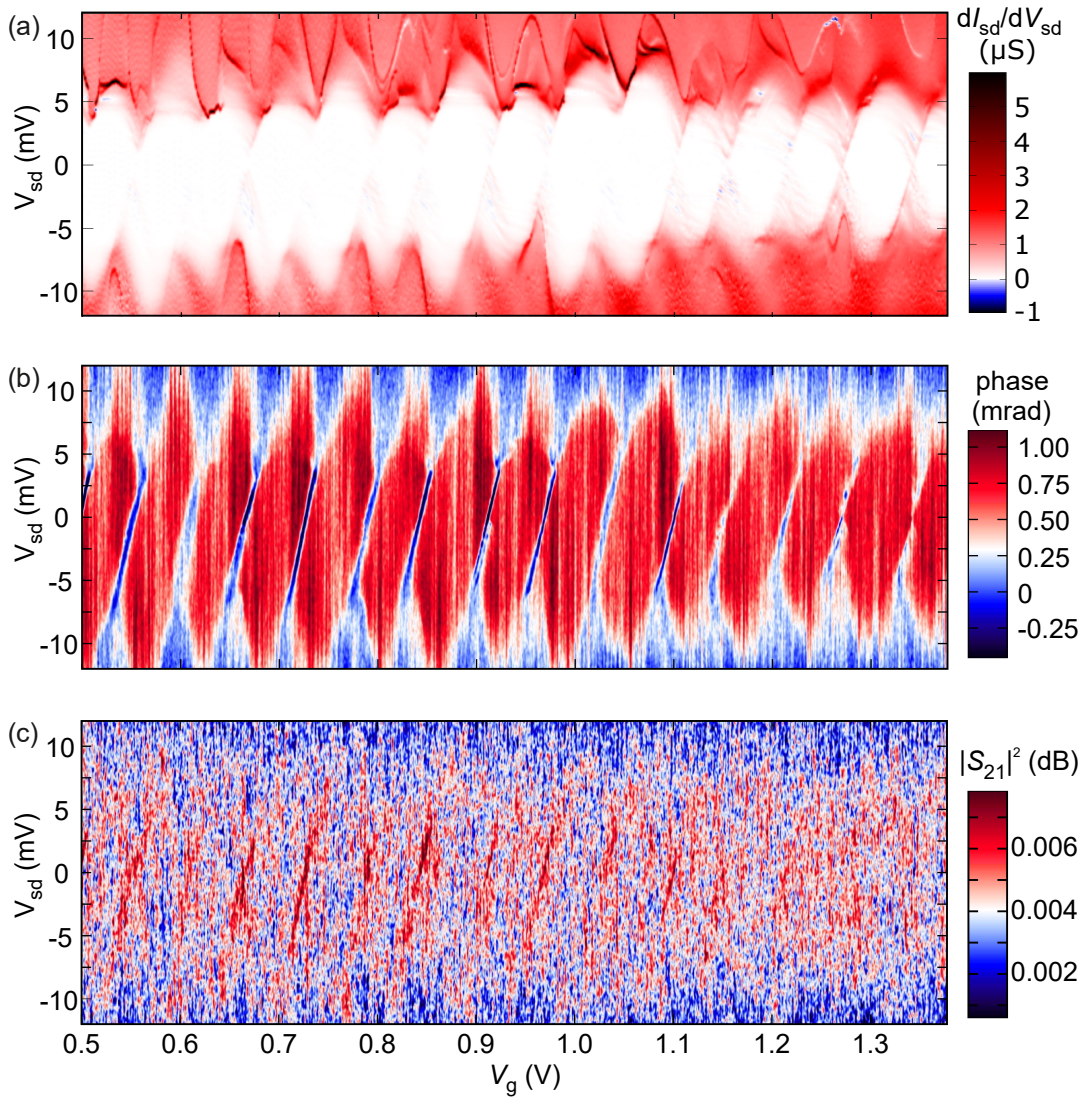

Figure 6.13.: Stability diagrams in the differential conductance (a) and cavity phase (b) and amplitude (c). The conductance has been numerically differentiated. Post processing has been implemented in the form of low-pass filtering (all diagrams) and background subtraction ((b) and (c)). In the conductance, Coulomb diamonds and the onset of current driven vibration can be observed. In the phase and amplitude diagram, only a single edge of the diamonds is visible.

7

Optomechanics

In this central chapter of the thesis, a dispersive optomechanical system consisting of a coplanar microwave cavity capacitively coupled to a vibrating carbon nanotube is presented. The mechanism responsible for the finite interaction between the two subsystems was so far unexplored in published literature. A theoretical model based on insights acquired in previous chapters, that also provide valuable information for future sophisticated device preparation.

The first part of this chapter covers the theory behind the research field of optomechanics. A mathematical treatment is derived, with which the diverse applications of optomechanical setups and different parameter regimes can be described and distinguished. The model, that is demonstrated here, is generic, but derivations are made exclusively for the parameter range of our experiment. This entire section is a brief synopsis of [Aspelmeyer et al., 2014]. See this article for a more comprehensive presentation.

In the second part, the main results of this thesis are presented. Here, a standard optomechanical experiment - *optomechanically induced transparency* (OMIT) - is introduced, enabling us to quantify the optomechanical coupling strength. It is revealed that a mechanism is needed to explain the scale of this coupling, that is orders of magnitude larger than that emerging from intuitive considerations; this mechanism turns out to be the effective capacitance introduced in the previous chapter. For a lookup of the optomechanical device parameters, it is referred to Tab. A.1.

The chapter finishes with a short outlook on future experiments benefiting from this enhanced coupling. Although not yet completely understood, first data of experiments preparing motion manipulation and sideband cooling is shown.

7.1. Optomechanics - Theory

In Fig. 7.1, the prototypical optomechanical system is depicted. It consists of a laser of frequency ω_{L} that drives an optical cavity (ω_{cav}, κ_{cav}), where one of the mirrors forms a mechanical oscillator (ω_{m}, κ_{m}). The fundamental mechanism that couples the mechanics to the light field is given by the concept of radiation pressure. A single photon with wave number k transfers a momentum $\Delta p = 2\hbar k$ onto a mirror from which the photon is reflected. As generally this is a very small value, an optical cavity is used to enhance the interaction. Then, the force on the mirror is proportional to the power P circulating in the cavity and so to the number of photons. At the same time, when the mirror vibrates, the cavity resonance frequency ω_{cav} is periodically modulated at rate ω_{m}. In this way, an interaction between optical field and mechanics emerges. There are many different systems concerning size and mass that can be described by this model:

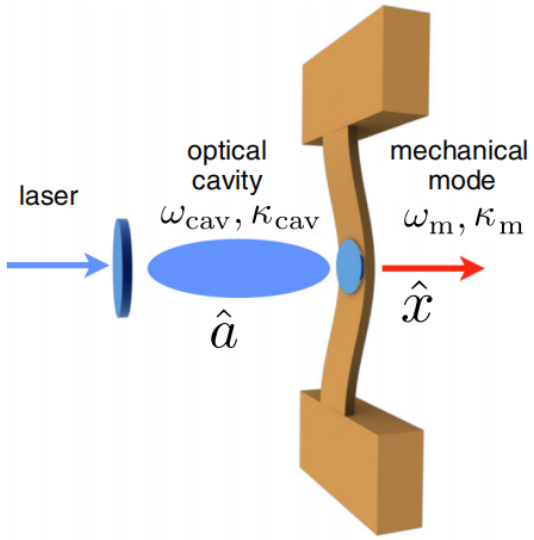

Figure 7.1.: The prototypical optomechanical system. Optical cavity and mechanical resonator are described as quantum harmonic oscillators with resonance frequencies ω_{cav}, ω_{m} and linewidths κ_{cav}, κ_{m}. Adapted from [Aspelmeyer et al., 2014].

from macroscopic mirrors [Braginsky and Manukin, 1967] to microtoroids [Weis et al., 2010] coupled to optical waveguides or micromechanical membranes integrated in superconducting microwave circuits [Teufel et al., 2011], down to collective motion of cold atoms in an optical cavity [Stamper-Kurn, 2014].

Disregarding the interaction for a moment, such a system can be mathematically modelled as two quantum harmonic oscillators. The unperturbed Hamiltonian is then given by

$$\hat{H} = \hbar\omega_{\mathrm{cav}}\hat{a}^\dagger\hat{a} + \hbar\omega_{\mathrm{m}}\hat{b}^\dagger\hat{b}\,, \tag{7.1}$$

with the corresponding counting operators $\hat{a}^\dagger\hat{a}$, $\hat{b}^\dagger\hat{b}$ for the optical/mechanical field. The description in this chapter is mostly formulated in the operator picture of quantum mechanics. However, in the case of large phonon/photon numbers, it can be treated classically by replacing the operators with their expectation value $\hat{a} \to \langle\hat{a}\rangle$.

7.1.1. Interaction Hamiltonian

The fact that the mechanical resonator forms one end mirror of the optical resonator leads to a dispersive coupling: the cavity resonance frequency is changed by the displacement of the mechanical resonator

$$\omega_{\mathrm{cav}}(x) \approx \omega_{\mathrm{cav}} + x\frac{\partial\omega_{\mathrm{cav}}}{\partial x} + \dots\,. \tag{7.2}$$

Keeping only terms of linear order and defining $G = -\frac{\partial\omega_{\mathrm{cav}}}{\partial x}$, one obtains

$$\hbar\omega_{\mathrm{cav}}(x)\hat{a}^\dagger\hat{a} = \hbar(\omega_{\mathrm{cav}} - G\hat{x})\hat{a}^\dagger\hat{a} \tag{7.3}$$

with $\hat{x} = x_{\mathrm{zpf}}\,(\hat{b} + \hat{b}^\dagger)$. The interaction Hamiltonian is then

$$\hat{H}_{\mathrm{int}} = -\hbar g_0 \hat{a}^\dagger \hat{a}(\hat{b} + \hat{b}^\dagger) \tag{7.4}$$

Here, the *single-photon optomechanical coupling strength* $g_0 = G x_{\mathrm{zpf}}$ was used. It characterises the interaction between a single photon and a single phonon and is a measure of how much the cavity resonance frequency changes due to the vacuum fluctuations of the mechanics. Including the interaction as an extra term in Eq. 7.1 gives the Hamiltonian

$$\hat{H} = \hbar\omega_{\mathrm{cav}}\hat{a}^\dagger\hat{a} + \hbar\omega_{\mathrm{m}}\hat{b}^\dagger\hat{b} - \hbar g_0 \hat{a}^\dagger\hat{a}(\hat{b} + \hat{b}^\dagger)\,, \tag{7.5}$$

that describes a vibrational mode coupled to a radiation mode and was first derived by C. K. Law [Law, 1994].

The motion $x(t) = x_0 \cdot \sin(\omega_{\mathrm{m}} t)$ of the mechanical oscillator modulates the cavity resonance frequency leading to sidebands in the cavity transmission at $\omega_{\mathrm{cav}} \pm \omega_{\mathrm{m}}$. At the same time, the interaction part of the Hamiltonian also yields a force on the mechanical resonator generated by the light field. This is called the *radiation pressure force*

$$\hat{F}_{\mathrm{rad}} = -\frac{d\hat{H}_{\mathrm{int}}}{d\hat{x}} = \hbar G \hat{a}^\dagger\hat{a} = \hbar\frac{g_0}{x_{\mathrm{zpf}}}\hat{a}^\dagger\hat{a}\,, \tag{7.6}$$

and can be visualised in the model of Fig. 7.1 as the momentum transfer of the photons to the vibrating mirror per cavity round trip.

In the derivation above, certain terms have been omitted; the Hamiltonian describes a closed system. These include in particular driving (generated by the external laser) and loss associated with outcoupling (signal leaking out of the cavity $\sim \sqrt{\kappa_{\mathrm{c}}}$) or other processes as e.g. dissipation ($\sim \kappa_{\mathrm{i}}$). Usually, a rotating frame transformation is then adapted to the full optomechanical Hamiltonian, where the reference frame is rotating at the laser frequency ω_{L}. This leads to a more convenient representation, because the driving term is then time independent. It is achieved by a unitary transformation with the operator $\hat{U} = \exp\left(i\omega_{\mathrm{L}}\hat{a}^\dagger\hat{a}t\right)$ as $\hat{H}' = \hat{U}\hat{H}\hat{U}^\dagger + i\hbar\hat{U}\partial\hat{U}^\dagger/\partial t$. Applying this to the short form of Eq. 7.5 leads to

$$\hat{H} = -\hbar\Delta\hat{a}^\dagger\hat{a} + \hbar\omega_{\mathrm{m}}\hat{b}^\dagger\hat{b} - \hbar g_0\hat{a}^\dagger\hat{a}\left(\hat{b} + \hat{b}^\dagger\right)\,, \tag{7.7}$$

where $\Delta = \omega_{\mathrm{L}} - \omega_{\mathrm{cav}}$ is the laser detuning. Eq. 7.7 is used as a basis for most optomechanical effects in the dispersive regime.

7.1.2. Linearised approximation

The Hamiltonian shows that the interaction is a non-linear process due to involving three operators[1]. To obtain the *linearised approximate description of optomechanics*, the cavity mode shall be expressed as a classical coherent field with small quantum fluctuations

$$\hat{a} = \bar{\alpha} + \delta\hat{a}\,, \tag{7.8}$$

[1] This is similar to *three-wave mixing* from non-linear optics.

with the average amplitude $\langle \hat{a} \rangle = \bar{\alpha}$. In this way $\bar{\alpha} = \sqrt{n_{\mathrm{cav}}}$ holds, where n_{cav} is the average number of cavity photons. This leads to a modified interaction Hamiltonian

$$\hat{H}_{\mathrm{int}}^{\mathrm{lin}} = -\hbar g_0 \left(\bar{\alpha} + \delta\hat{a}\right)^\dagger \left(\bar{\alpha} + \delta\hat{a}\right) \left(\hat{b} + \hat{b}^\dagger\right). \tag{7.9}$$

Expanding Eq. 7.9 in powers of $\bar{\alpha}$ leads to a term $\sim \bar{\alpha}^2$, which only gives a constant radiation pressure force and can be omitted after a displacement shift. The term $\sim \delta\hat{a}^\dagger\delta\hat{a}$ is smaller than the remaining terms by a factor of $|\bar{\alpha}|$ and is also omitted. This gives a Hamiltonian in the rotating frame

$$\hat{H}^{\mathrm{lin}} = -\hbar\Delta\delta\hat{a}^\dagger\delta\hat{a} + \hbar\omega_{\mathrm{m}}\hat{b}^\dagger\hat{b} - \hbar g\left(\delta\hat{a}^\dagger + \delta\hat{a}\right)\left(\hat{b} + \hat{b}^\dagger\right), \tag{7.10}$$

containing the *optomechanical coupling strength*

$$g = g_0\sqrt{n_{\mathrm{cav}}}\,. \tag{7.11}$$

Although being quadratic in operators, Eq. 7.10 is referred to as *linearised*, because it leads to linear equations of motion (see Sect. 7.1.4). In most experiments, g_0 is fixed by the device geometry or experimental setup and is typically a small value. An advantage of the linearised interaction is then, that the coupling strength can be tuned with the laser power (in the boundaries of the setup). The linearised description is generally valid for $g_0 \ll \kappa_{\mathrm{cav}}$, which is the case in most experiments and all realisations accomplished in this thesis.

7.1.3. Parameter regimes

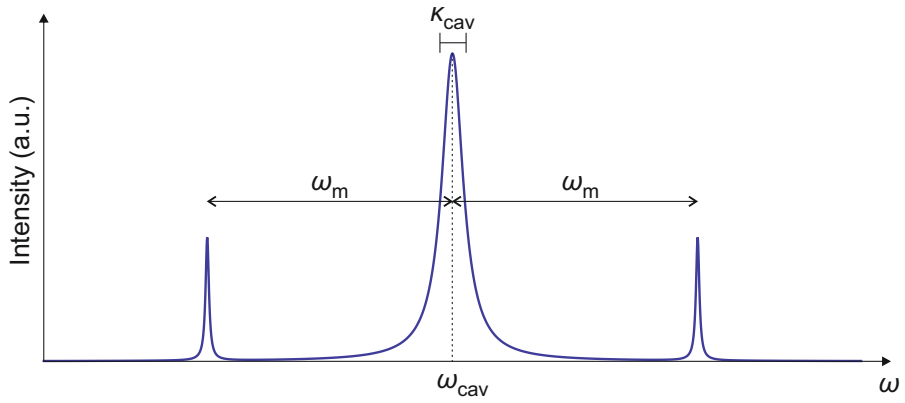

Figure 7.2.: Transmission spectrum of an arbitrary optomechanical system in the resolved sideband regime $\omega_{\mathrm{m}} \gg \kappa_{\mathrm{cav}}$. The motional sidebands at $\omega = \omega_{\mathrm{cav}} \pm \omega_{\mathrm{m}}$ can be discerned from the central cavity mode.

The first distinction can be made concerning the motional sidebands explained in the previous section. The optical linewidth κ_{cav} has to be compared to the mechanical resonance frequency ω_{m} (see Fig. 7.2):

- *Resolved sideband regime*: Here, $\omega_{\mathrm{m}} \gg \kappa_{\mathrm{cav}}$ holds. In this regime, the motional sidebands (at $\omega_{\mathrm{cav}} \pm \omega_{\mathrm{m}}$) can be distinguished from the cavity resonance. This is a necessary condition for mechanical ground state cooling and is also called the *good cavity limit*.
- *Unresolved sideband regime*: In the opposite case, $\omega_{\mathrm{m}} \ll \kappa_{\mathrm{cav}}$, the sidebands lie within the central cavity peak. This is also called *bad cavity limit*.

The experiments demonstrated within this thesis all took place in the resolved sideband regime. It will also be presupposed for the rest of this section.

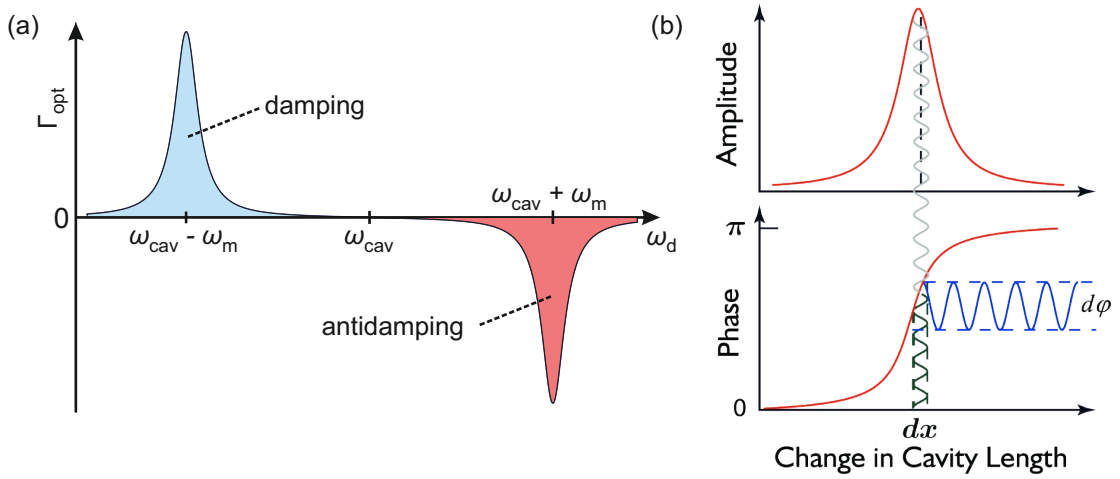

Figure 7.3.: Phenomena and applications in the different regimes concerning the laser detuning Δ. (a) Pumping the system at the red-detuned sideband ($\Delta = -\omega_{\mathrm{m}}$) leads to additional damping of the mechanical resonator (at rate $\Gamma_{\mathrm{opt}} > 0$), while pumping at the blue-detuned sideband ($\Delta = +\omega_{\mathrm{m}}$) leads to antidamping (at rate $\Gamma_{\mathrm{opt}} < 0$). (b) In the case of resonant driving, the motion of the mechanical oscillator causes an interferometric phase shift. (b) adapted from [Aspelmeyer et al., 2014].

Three regimes arise from the particular choice of laser detuning Δ in Eq. 7.10 (see Fig. 7.3):

- $\Delta = -\omega_{\mathrm{m}}$ (*red-detuned regime*): A RWA cancels the off-resonant terms, reducing the interaction Hamiltonian to

$$\hat{H}_{\mathrm{int}}^{\mathrm{lin}} = -\hbar g \left(\delta \hat{a}^{\dagger} \hat{b} + \delta \hat{a} \hat{b}^{\dagger} \right) . \tag{7.12}$$

  In terms of quantum optics, this is equal to a *beam splitter* interaction: a photon can only enter the cavity by annihilating a vibrational phonon. State exchange between the mechanical oscillator and the driven cavity can occur and optomechanical cooling is possible.

- $\Delta = +\omega_{\mathrm{m}}$ (*blue-detuned regime*): Here, a RWA leads to

$$\hat{H}_{\mathrm{int}}^{\mathrm{lin}} = -\hbar g \left(\delta \hat{a}^{\dagger} \hat{b}^{\dagger} + \delta \hat{a} \hat{b} \right) , \tag{7.13}$$

representing a *two-mode squeezing* or *parametric amplification* interaction. In this regime, phonons can only enter the cavity by simultaneously creating a phonon. Thus, this is an amplification process for the vibration. In the case of low intrinsic dissipation, this can lead to dynamical instability evoking self-sustained oscillations [Massel et al., 2011].

- $\Delta = 0$: For resonant driving, no terms can be neglected. The interaction Hamiltonian then reads
$$-\hbar g \left(\delta\hat{a}^\dagger + \delta\hat{a}\right)\left(\hat{b} + \hat{b}^\dagger\right) . \tag{7.14}$$
In this case, the cavity is used as an interferometer. The phase of the optical mode experiences a shift that is proportional to the mechanical position $\hat{x} \sim \hat{b} + \hat{b}^\dagger$. This is the relevant case for optomechanical displacement detection [Regal et al., 2008].

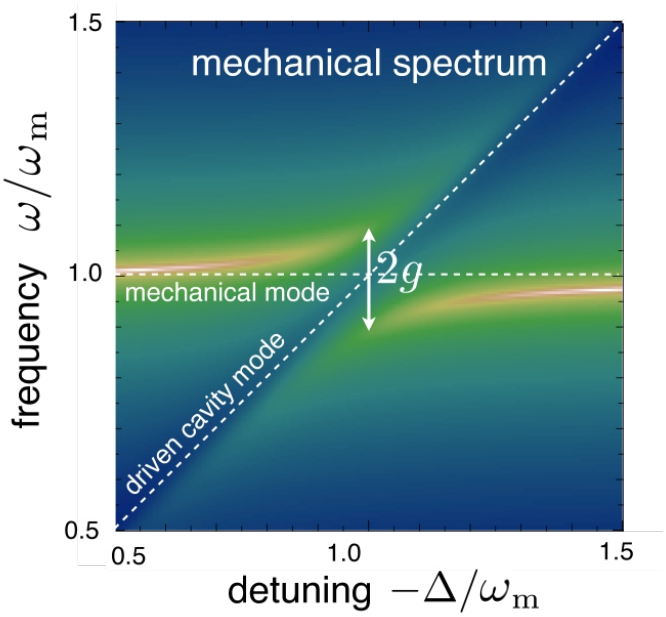

Figure 7.4.: Avoided crossing of hybridised optomechanical modes. At resonant driving ($\Delta = -\omega_\mathrm{m}$), the normal mode splitting is of size $2g$. Adapted from [Aspelmeyer et al., 2014].

Another distinction can be made regarding the optomechanical coupling strengths g/g_0:

- $g \geq \kappa_\mathrm{cav}, \kappa_\mathrm{m}$ (*strong coupling regime*): In the case of red-detuned driving, mechanical and optical field hybridise to form new eigenmodes (see Fig. 7.4). The avoided crossing between them is also called *optomechanical normal mode splitting*. At resonance, $\Delta = -\omega_\mathrm{m}$, the modes are symmetric and antisymmetric superpositions of light and mechanics with a splitting of $2g$.
- $g_0 \geq \kappa_\mathrm{cav}, \kappa_\mathrm{m}$ (*ultrastrong coupling regime*): Here, the optomechanical Hamiltonian cannot be linearised and its full interaction part $\hat{H}_\mathrm{int} = -\hbar g_0 \hat{a}^\dagger\hat{a}\left(\hat{b} + \hat{b}^\dagger\right)$ has to be taken into account, leading to non-linear quantum effects.

7.1.4. Input-output formalism - Equations of motion

Input-output theory serves to give a quantum mechanical description of the transmission of a driven cavity; the discussion here follows [Aspelmeyer et al., 2014]. It includes noise terms (previously ignored in the Hamiltonian) that enter through any kind of coupling into the cavity. The theory uses Heisenberg equations of motion with the Hamiltonian of Eq. 7.7 (disregarding coupling) to describe the dynamics of the field amplitude $\hat{a}$ in the cavity

$$\dot{\hat{a}} = -\frac{\kappa_{\mathrm{cav}}}{2}\hat{a} + i\Delta\hat{a} + \sqrt{\kappa_{\mathrm{c}}}\hat{a}_{\mathrm{in}} + \sqrt{\kappa_{\mathrm{i}}}\hat{f}_{\mathrm{in}}\,, \tag{7.15}$$

with $\kappa_{\mathrm{cav}} = \kappa_{\mathrm{c}} + \kappa_{\mathrm{i}}$. Photon channels of the cavity are ascribed to either input coupling (rate κ_{c}) or any other loss process (rate κ_{i}). The input field $\hat{a}_{\mathrm{in}}$, a stochastic quantum field, is in the simplest case the sum of a coherent laser drive and the fluctuating vacuum electric field that couples to the cavity (and thus also time dependent). Then,

$$P_{\mathrm{in}} = \hbar\omega_{\mathrm{L}} \left\langle \hat{a}_{\mathrm{in}}^{\dagger}\hat{a}_{\mathrm{in}} \right\rangle \tag{7.16}$$

is the power on the cavity input and $\left\langle \hat{a}_{\mathrm{in}}^{\dagger}\hat{a}_{\mathrm{in}} \right\rangle$ is the incident *rate* of photons (for $\omega_{\mathrm{L}} \approx \omega_{\mathrm{cav}}$). The noise amplitude is given by $\hat{f}_{\mathrm{in}}$ and experiences the same type of normalisation as the driving amplitude $\hat{a}_{\mathrm{in}}$.

Focusing on the classical average quantities and ignoring other noise ($\hat{f}_{\mathrm{in}} = 0$), the steady-state solution of Eq. 7.15 is

$$\langle\hat{a}\rangle = \frac{\sqrt{\kappa_{\mathrm{c}}}\,\langle\hat{a}_{\mathrm{in}}\rangle}{\kappa_{\mathrm{cav}}/2 - i\Delta}\,. \tag{7.17}$$

Then, the average number of photons circulating in the cavity can be easily obtained by

$$n_{\mathrm{cav}} = |\langle\hat{a}\rangle|^2 = \frac{\kappa_{\mathrm{c}}}{\Delta^2 + (\kappa_{\mathrm{cav}}/2)^2}\frac{P_{\mathrm{in}}}{\hbar\omega_{\mathrm{L}}}\,. \tag{7.18}$$

In the presence of a second mirror - e.g. the half wave CPW geometry implemented in this thesis - an additional term $\sqrt{\kappa_{\mathrm{c}}^{(2)}}\hat{a}_{\mathrm{in}}^{(2)}$ can be included in Eq. 7.15. This is however redundant, if only transmission through one mirror is measured (while reflected signal on the other mirror is neglected). The effects of the second mirror can then be lumped into the decay rate κ_{i}.

Now including the coupling, equations of motion for optical and mechanical field amplitudes can be stated as

$$\dot{\hat{a}} = -\frac{\kappa_{\mathrm{cav}}}{2}\hat{a} + i(\Delta + G\hat{x})\hat{a} + \sqrt{\kappa_{\mathrm{c}}}\hat{a}_{\mathrm{in}} + \sqrt{\kappa_{\mathrm{i}}}\hat{f}_{\mathrm{in}}\,, \tag{7.19}$$

and

$$\dot{\hat{b}} = \left(-i\omega_{\mathrm{m}} - \frac{\kappa_{\mathrm{m}}}{2}\right)\hat{b} + ig_0\hat{a}^{\dagger}\hat{a} + \sqrt{\kappa_{\mathrm{m}}}\hat{b}_{\mathrm{in}}\,. \tag{7.20}$$

These have the form of *quantum Langevin equations* and describe how optical and mechanical field evolve, including all fluctuation effects.

In the limit of large phonon/photon numbers (semiclassical limit), the averaged versions of these equations can be used. For light field amplitude $\alpha(t) = \langle\hat{a}(t)\rangle$, drive amplitude $\alpha_{\mathrm{in}}(t)$,

and oscillator position $x(t) = \langle \hat{x}(t) \rangle = 2x_{\mathrm{zpf}} \mathrm{Re}\left(\left\langle \hat{b} \right\rangle\right)$ follows

$$\dot{\alpha} = -\frac{\kappa_{\mathrm{cav}}}{2}\alpha + i(\Delta + G\hat{x})\alpha + \sqrt{\kappa_{\mathrm{c}}}\alpha_{\mathrm{in}}(t)\,, \tag{7.21}$$

and

$$m\ddot{x} = -m\omega_{\mathrm{m}}^2 x - m\kappa_{\mathrm{m}}\dot{x} + \hbar G|\alpha|^2\,. \tag{7.22}$$

Noise can in principle be included (in semiclassical terms), but is disregarded here.

The above equations are nonlinear coupled differential equations, which cannot be solved analytically. Therefore, it is convenient to proceed with the "linearised" Hamiltonian of Eq. 7.10. It is quadratic in operators, leading to linear equations of motion

$$\delta\dot{\hat{a}} = \left(i\Delta - \frac{\kappa_{\mathrm{cav}}}{2}\right)\delta\hat{a} + ig\left(\hat{b} + \hat{b}^\dagger\right) + \sqrt{\kappa_{\mathrm{c}}}\delta\hat{a}_{\mathrm{in}}(t) + \sqrt{\kappa_{\mathrm{i}}}\hat{f}_{\mathrm{in}}(t)\,, \tag{7.23}$$

$$\delta\dot{\hat{a}}^\dagger = \left(-i\Delta - \frac{\kappa_{\mathrm{cav}}}{2}\right)\delta\hat{a}^\dagger - ig\left(\hat{b}^\dagger + \hat{b}\right) + \sqrt{\kappa_{\mathrm{c}}}\delta\hat{a}_{\mathrm{in}}^\dagger(t) + \sqrt{\kappa_{\mathrm{i}}}\hat{f}_{\mathrm{in}}^\dagger(t)\,, \tag{7.24}$$

$$\dot{\hat{b}} = \left(-i\omega_{\mathrm{m}} - \frac{\kappa_{\mathrm{m}}}{2}\right)\hat{b} + ig\left(\delta\hat{a} + \delta\hat{a}^\dagger\right) + \sqrt{\kappa_{\mathrm{m}}}\hat{b}_{\mathrm{in}}(t)\,. \tag{7.25}$$

These equations govern the dynamics of the system, can be solved numerically[2] and are able to fully describe phenomena that accord to the linearised regime.

The classical linearised equations of motion ignoring damping that follow from Eqs. 7.23, 7.24, and 7.25 are then

$$\delta\dot{a} = \left(i\Delta - \frac{\kappa_{\mathrm{cav}}}{2}\right)\delta a + iG\bar{\alpha}x + \sqrt{\kappa_{\mathrm{c}}}\alpha_{\mathrm{in}}(t)\,, \tag{7.26}$$

$$\delta\dot{a}^* = \left(-i\Delta - \frac{\kappa_{\mathrm{cav}}}{2}\right)\delta a^* - iG\bar{\alpha}x^* + \sqrt{\kappa_{\mathrm{c}}}\alpha_{\mathrm{in}}^*(t)\,, \tag{7.27}$$

$$m\ddot{x} = -m\omega_{\mathrm{m}}^2 x - m\kappa_{\mathrm{m}}\dot{x} + \hbar G\bar{\alpha}(\delta a + \delta a^*)\,. \tag{7.28}$$

7.1.5. Microwave optomechanics

In the microwave domain, the same theoretical description as derived in the last sections can be applied. The generic system is depicted in Fig. 7.5. It consists of a resonant LC circuit that is coupled to an external mw drive. The capacitance consists of two parallel plates, with one of them being able to oscillate. In this way, the total capacitance of the circuit $C(x)$ is deflection dependent and the capacitive shift $\partial C/\partial x$ is translated to a resonance frequency shift $\partial\omega_{\mathrm{cav}}/\partial x$. Thus, the standard optomechanical radiation pressure interaction is obtained and the formalism presented above applies. Typically, cavity resonance frequencies lie in the GHz-range and mechanical oscillators consist of nanomechanical resonators implemented in the circuit, such as nanobeams [Rocheleau et al., 2009] or drum resonators [Teufel et al., 2011].

The resonance frequency of LC circuits is given by the Thomson formula $\omega_{\mathrm{cav}} = 1/\sqrt{LC}$. The optomechanical (single-photon) coupling strength can then be expressed as

$$g_0 = \frac{\partial\omega_{\mathrm{cav}}}{\partial x}x_{\mathrm{zpf}} = \frac{\omega_{\mathrm{cav}}}{2C}\frac{\partial C}{\partial x}x_{\mathrm{zpf}}\,. \tag{7.29}$$

[2] This is usually done by Fourier transforming the operators into the frequency domain, $\hat{a}(\omega) = \int_{-\infty}^{+\infty} dt e^{i\omega t}\hat{a}(t)$

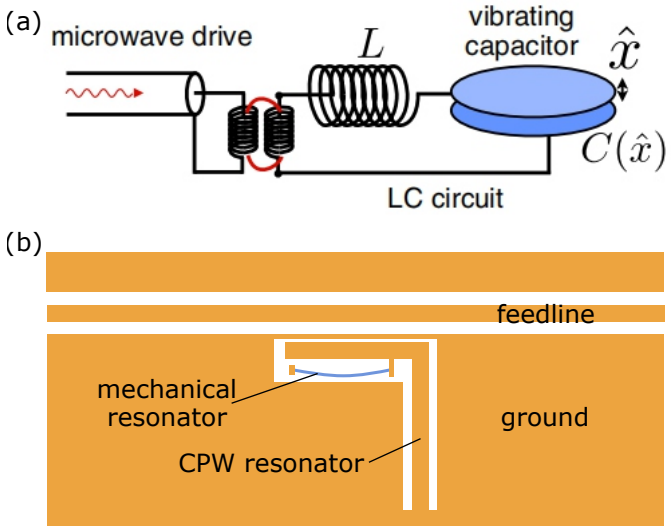

Figure 7.5.: Prototypical optomechanical systems in the microwave regime. (a) A mw drive is coupled (here inductively) to an LC resonator. The interaction is mediated by the vibrating capacitor $C(\hat{x})$. (b) The capacitance of a quarter wave resonator is modified via a mechanically resonating beam. When vibrating, the capacitance between CPW resonator and ground is altered. Adapted from [Aspelmeyer et al., 2014] and [Teufel et al., 2008].

7.2. Quantum capacitance enhanced optomechanics

The system investigated in this thesis consists of a CPW cavity and carbon nanotube that is mechanically active. It is shown schematically and as circuit model in Fig. 6.7. Considering the fact that $\omega_{\mathrm{m}} \gg \kappa_{\mathrm{cav}}$, the system is in the sideband-resolved regime. The purpose of this section is to quantify, experimentally and theoretically, the optomechanical coupling strength. It is mediated via the change in capacitance between the vibrating CNT and the gate finger that is connected to the cavity. The question arises: how large can such a coupling be? Is the (single-photon) strong coupling regime feasible?

7.2.1. Geometric coupling

According to Eq. 7.29, the single-photon coupling strength g_0 can be expressed in terms of the cavity resonance frequency ω_{cav}, the total capacitance C_{tot}, the zero-point fluctuation amplitude x_{zpf} of the mechanics, and the change in total capacitance with displacement $\partial C_{\mathrm{tot}}/\partial x$. The first two parameters are set by the geometry of the waveguide and the third can be calculated using $x_{\mathrm{zpf}} = \sqrt{\hbar/2m\omega_{\mathrm{m}}}$ of Sect. 2.4 and is dependent on the mass and mechanical resonance frequency of the CNT.

The total capacitance consists of a parallel circuit of the equivalent waveguide capacitance C_{RLC}, the coupling capacitors C_{k}, and the capacitance between gate and carbon nanotube C_{g} (as in Eq. 6.1). The equivalent waveguide capacitance can be calculated from the device geometry

using conformal mapping (Eqs. 4.20 and 4.25, see Sect. B.3) as $C_{\mathrm{RLC}} = C_{\mathrm{CPW}}/2 = 0.875\,\mathrm{pF}$. Coupling capacitors can be estimated by finite element modelling and are typically in the range of fF [Göppl et al., 2008]. In Sect. 2.3.3, the gate capacitance was estimated to be $C_{\mathrm{g}}^{\mathrm{CB}} = 2.6\,\mathrm{aF}$. Therefore, by far the largest capacitance is C_{RLC}, so that $C_{\mathrm{tot}} \approx C_{\mathrm{RLC}}$ is given. Additionally, since only C_{g} is dependent on the CNT vibration, $\partial C_{\mathrm{tot}}/\partial x = \partial C_{\mathrm{g}}/\partial x$ holds. With these assumptions, Eq. 7.29 can be approximated by

$$g_0 \approx \frac{\omega_{\mathrm{cav}}}{2C_{\mathrm{RLC}}} \frac{\partial C_{\mathrm{g}}}{\partial x} x_{\mathrm{zpf}} \,. \tag{7.30}$$

The problem is then reduced to estimating $\partial C_{\mathrm{g}}/\partial x$, which shall be discussed in the following.

Recapitulating the wire-over plane model (Eq. 2.26), where the nanotube is considered as conductive wire (radius R, length L) over an infinite metallic plane (gate electrode at distance d), the total gate capacitance is given by[3]

$$C_{\mathrm{g}}(x) = \frac{2\pi\epsilon_0\epsilon_{\mathrm{r}} L}{\operatorname{arcosh}\left(\frac{d-x}{R}\right)} \,. \tag{7.31}$$

In the above equation, the nanotube motion was approximated as a change of distance to the gate electrode that is constant along the space coordinate along the nanotube axis. The derivative with respect to x is accordingly

$$\frac{\partial C_{\mathrm{g}}(x)}{\partial x} = \frac{2\pi\epsilon_0\epsilon_{\mathrm{r}} L}{R\sqrt{\left(\frac{d-x}{R}\right)^2 - 1}\left(\operatorname{arcosh}\left(\frac{d-x}{R}\right)\right)^2} \,. \tag{7.32}$$

Now the parameters of our optomechanical setup (see Tab.A.1) shall be used to estimate the coupling strength:

- $d = 450\,\mathrm{nm}$ is given by the device geometry; in detail, the cross section is given by $200\,\mathrm{nm}$ cross-linked PMMA and $250\,\mathrm{nm}$ vacuum.
- $\epsilon_{\mathrm{r}} = 2$ can be approximated by taking the average of the same PMMA/vacuum structure (with a typical dielectric constant for PMMA $\epsilon_{\mathrm{r}}^{\mathrm{PMMA}} \sim 3$ [Brydson, 1999]).
- $L_{\mathrm{eff}} = 143\,\mathrm{nm}$ comes from the identification of the gate capacitance from Coulomb blockade measurements with the wire-over-plane capacitance at zero deflection $C_{\mathrm{g}}^{\mathrm{CB}} = C_{\mathrm{g}}(0)$. This is the effective length of the CNT that interacts with the gate electrode[4]
- $m = (2\pi RL\rho_{\mathrm{graphene}})/2 = 4.8 \cdot 10^{-21}\,\mathrm{kg}$ is the effective vibrating mass of the CNT. It is assumed to be half its total mass.
- $R = 2\,\mathrm{nm}$ is assumed to be a typical value of SWCNTs[5]

[3] Note that the coordinate system has changed in comparison to Eq. 2.26, $z \to x$

[4] The gate electrode is also not an infinite plane, but has a finite width of $100\,\mathrm{nm}$, making this approximation reasonable.

[5] Eq. 7.32 is not particularly dependent on the CNT radius; see the discussion of error sources at the end of Sect. 7.2.3.

This gives a value of $\partial C_\mathrm{g}(0)/\partial x = 0.95\,\mathrm{pF/m}$. Together with device parameters taken from Tab. A.1, a geometric single-photon coupling of

$$g_0^* = 2\pi \cdot 2.9\,\mathrm{mHz}$$

emerges. In comparison to the cavity decay rate $\kappa_\mathrm{cav} = 2\pi \cdot 12\,\mathrm{MHz}$, this is a tiny number. Even with large photon numbers $n_\mathrm{cav} \approx 10^9$, the optomechanical coupling $g^* = g_0^*\sqrt{n_\mathrm{cav}} \lesssim 100\,\mathrm{Hz}$ remains small, making strong coupling seem impossible.

7.2.2. Optomechanically induced transparency

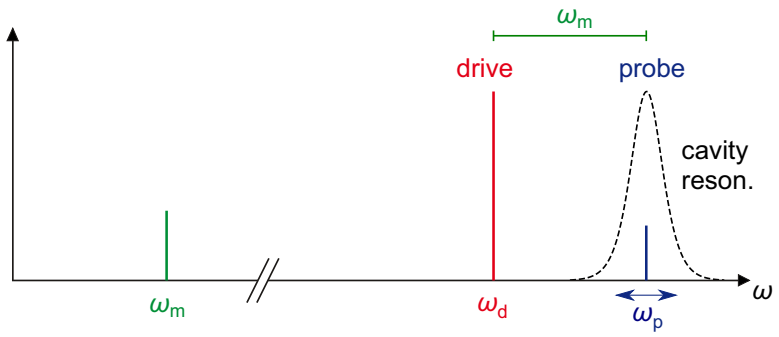

Figure 7.6.: Frequency scheme of OMIT experiment. A small field probes the cavity around its resonance frequency ω_cav, while at the same time, a large pump or drive tone is applied at $\omega_\mathrm{d} = \omega_\mathrm{cav} - \omega_\mathrm{m}$. Adapted from [Blien et al., 2020].

In order to measure the optomechanical coupling strength, an *optomechanically induced transparency* (OMIT) type experiment [Weis et al., 2010] was performed. The frequency "scheme" is shown in Fig. 7.6; for the measurement setup, see Fig. 3.3 (a). If not stated otherwise, no bias was applied to the carbon nanotube during any optomechanics experiment ($V_\mathrm{sd} = 0$).

A strong drive tone pumps the cavity on the red-detuned sideband ($\omega_\mathrm{d} = \omega_\mathrm{cav} - \omega_\mathrm{m}$), while simultaneously the cavity is probed around ω_cav with a weak field (ω_p), generated and detected by a VNA. Drive and probe field interfere to create a beat at their frequency difference in the cavity. When the resonance condition $\omega_\mathrm{p} - \omega_\mathrm{d} = \omega_\mathrm{m}$ is fulfilled, the beat coherently drives the mechanical resonator. The vibration can in turn *optomechanically upconvert* a photon from the drive field to a photon of frequency ω_cav by absorption of a phonon in the mechanical resonator. This process corresponds to *anti-Stokes scattering* in Raman physics (see also Sect. 7.3). Also, the system has to be in the resolved sideband regime to sufficiently suppress the inverse process, i.e., Stokes scattering. The upconverted photon interferes destructively with the probe field, giving rise to a sharp dip in the cavity transmission (see Fig. 7.7). As expected, the OMIT dip shifts in frequency when detuning ω_d. The overall shape of the dip (width and depth) is dependent on the optomechanical coupling strength g. Note that for the particular experiment of Fig. 7.7, a large probe signal was applied, leading to strong mechanical driving and asymmetrically shaped OMIT dips [Shevchuk et al., 2015].

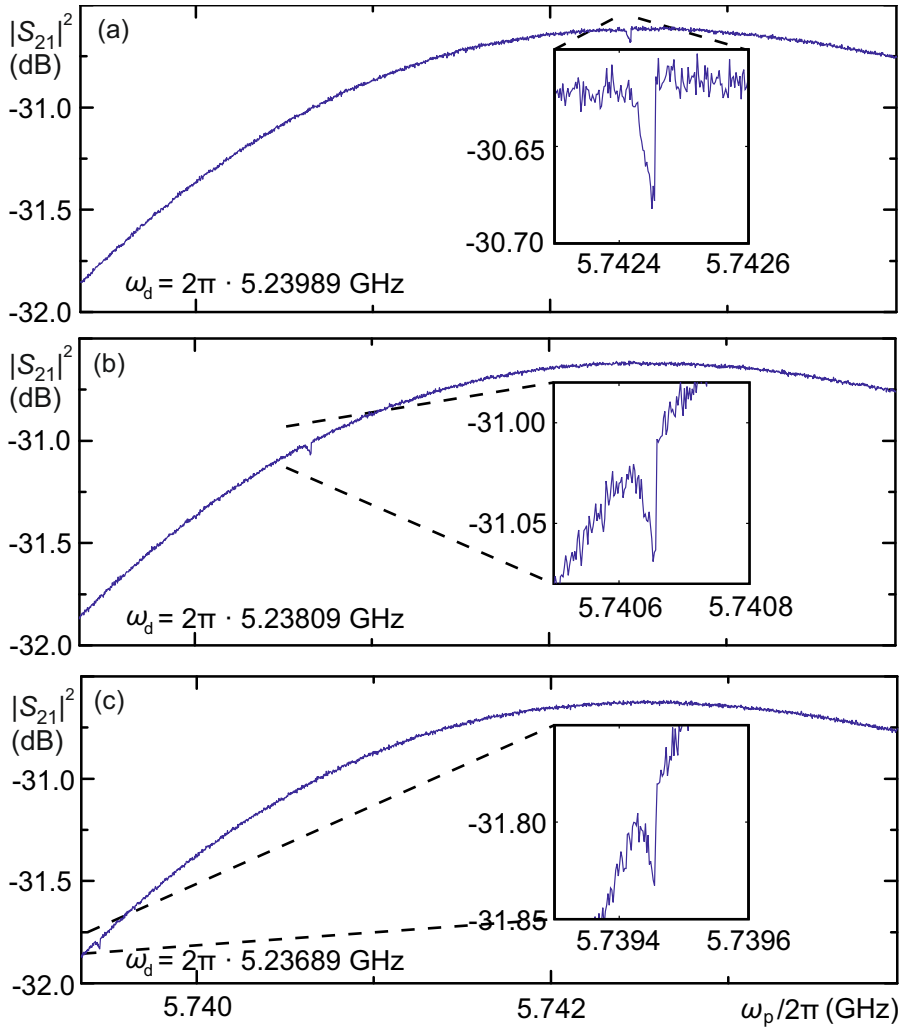

Figure 7.7.: OMIT feature for three different choices of ω_d. Drive and probe power were set to $P_\mathrm{d} = +20\,\mathrm{dBm}$, respectively $P_\mathrm{p} = 0\,\mathrm{dBm}$. In (a), the resonance condition $\omega_\mathrm{d} = \omega_\mathrm{cav} - \omega_\mathrm{m}$ was satisfied, while in (b), (c) ω_d was slightly detuned. The gate voltage was fixed at $V_\mathrm{g} = -1.855\,\mathrm{V}$, with no bias applied ($V_\mathrm{sd} = 0$). Adapted from [Blien et al., 2020].

Solving the equations of motion for OMIT - fit procedure

To quantify the coupling, we adapt the mathematical model of Weis *et al.* [Weis et al., 2010]. In the remainder of this section, the total cavity dissipation rate shall be expressed by its internal dissipation rate κ_i and the ones referring to in- and output coupling κ_in, κ_out as

$$\kappa_\mathrm{cav} = \kappa_\mathrm{i} + \kappa_\mathrm{in} + \kappa_\mathrm{out}\,. \tag{7.33}$$

The linearised classical equations of motion Eqs. 7.26, 7.27, and 7.28 with a probe field

$$\alpha_\mathrm{in}(t) = \alpha_\mathrm{p} e^{-i\Omega t} \tag{7.34}$$

in a frame rotating with the drive frequency ω_d are taken as a starting point. Here,

$$\Omega = \omega_\mathrm{p} - \omega_\mathrm{d} \tag{7.35}$$

is the detuning between probe and drive frequency. Then, the ansatz

$$\delta a(t) = A^- e^{-i\Omega t} + A^+ e^{+i\Omega t} \tag{7.36}$$
$$\delta a^*(t) = (A^+)^* e^{-i\Omega t} + (A^-)^* e^{+i\Omega t} \tag{7.37}$$
$$x(t) = X e^{-i\Omega t} + X^* e^{+i\Omega t} \tag{7.38}$$

is used, leading to six equations when sorted by rotation terms. However, only the ones containing A^- are important

$$(-i(\Delta+\Omega) + \frac{\kappa_\mathrm{cav}}{2})A^- = +iG\bar{\alpha}X + \sqrt{\kappa_\mathrm{in}}\alpha_\mathrm{p} \tag{7.39}$$
$$(+i(\Delta-\Omega) + \frac{\kappa_\mathrm{cav}}{2})(A^+)^* = -iG\bar{\alpha}X^* \tag{7.40}$$
$$m(\omega_\mathrm{m}^2 - \Omega^2 - i\kappa_\mathrm{m}\Omega)X = +\hbar G\bar{\alpha}(A^- + (A^+)^*)\,, \tag{7.41}$$

because these denote the transmission on the upper sideband[6] $\omega_\mathrm{d} + \Omega$. As earlier, the detuning $\Delta = \omega_\mathrm{d} - \omega_\mathrm{cav}$ was used. In the red-detuned regime, as it is the case here, $\Delta = -\omega_\mathrm{m}$.

The inverse of the first factor in the last equation is called the bare *mechanical susceptibility* $\chi_\mathrm{m} = \left[m(\omega_\mathrm{m}^2 - \Omega^2 - i\kappa_\mathrm{m}\Omega)\right]^{-1}$ connecting the external force to the response of the coordinate, while the right side in the last equation gives an optomechanical correction to the mechanical susceptibility; see also Sect. 7.3.

As the off-resonant lower sideband is strongly suppressed in the resolved sideband regime, $A^+ \approx 0$ holds. Additionally, the mechanical susceptibility can be linearised as $m(\omega_\mathrm{m}^2 - \Omega^2 - i\kappa_\mathrm{m}\Omega) \approx m\omega_\mathrm{m}(2(\omega_\mathrm{m} - \Omega) - i\kappa_\mathrm{m})$ for small $\omega_\mathrm{m} - \Omega$. Then Eqs. 7.39 and 7.41 simplify to

$$(-i(\Delta+\Omega) + \frac{\kappa_\mathrm{cav}}{2})A^- = +iG\bar{\alpha}X + \sqrt{\kappa_\mathrm{in}}\alpha_\mathrm{p} \tag{7.42}$$
$$m\omega_\mathrm{m}(2(\omega_\mathrm{m} - \Omega) - i\kappa_\mathrm{m})X = +\hbar G\bar{\alpha}A^-\,. \tag{7.43}$$

[6] Transforming Eq. 7.36 back from the rotating frame, yields $A^- e^{-i(\omega_\mathrm{d}+\Omega)t} + A^+ e^{-i(\omega_\mathrm{d}-\Omega)t}$. Hence, A^- is the amplitude of the upper sideband (coinciding with the cavity resonance) and A^+ is the amplitude of the lower sideband seen from the drive frequency ω_d.

Using $g = Gx_{\mathrm{zpf}}\bar{\alpha}$ and $x_{\mathrm{zpf}} = \sqrt{\hbar/(2m\omega_{\mathrm{m}})}$, and defining $\Delta_{\mathrm{p}} = \omega_{\mathrm{p}} - (\omega_{\mathrm{d}} + \omega_{\mathrm{m}}) = \Omega - \omega_{\mathrm{m}}$, the intracavity amplitude can be expressed as

$$A^{-}(\Delta_{\mathrm{p}}, g) = \frac{1}{-i\Delta_{\mathrm{p}} + \kappa_{\mathrm{cav}}/2 + \frac{g^2}{-i\Delta_{\mathrm{p}}+\kappa_{\mathrm{m}}/2}} \sqrt{\kappa_{\mathrm{in}}}\alpha_{\mathrm{p}}\,. \tag{7.44}$$

When the drive frequency deviates from the motional sideband condition $\omega_{\mathrm{d}} = \omega_{\mathrm{cav}} - \omega_{\mathrm{m}}$, this can be accounted for by a modified parameter $\Delta'_{\mathrm{p}} = \omega_{\mathrm{p}} - \omega_{\mathrm{cav}}$ in the above equation [Weis et al., 2010]. The influence of the crosstalk side channel, leading to the Fano lineshape of the cavity transmission, also needs to be considered. As in Eq. 4.89, it can be included in the calculation by adding a complex shift $re^{i\phi}$

$$A_{\mathrm{Fano}}(\Delta_{\mathrm{p}}, \Delta'_{\mathrm{p}}, g) = \left(\frac{1}{-i\Delta'_{\mathrm{p}} + \kappa_{\mathrm{cav}}/2 + \frac{g^2}{-i\Delta_{\mathrm{p}}+\kappa_{\mathrm{m}}/2}} + re^{i\phi} \right) \sqrt{\kappa_{\mathrm{in}}}\alpha_{\mathrm{p}}\,. \tag{7.45}$$

Now, the signal amplitude transmitted through the cavity is

$$s_{\mathrm{out}}(\Delta_{\mathrm{p}}, \Delta'_{\mathrm{p}}, g) = \sqrt{\kappa_{\mathrm{out}}} A_{\mathrm{Fano}} = \left(\frac{1}{-i\Delta'_{\mathrm{p}} + \kappa_{\mathrm{cav}}/2 + \frac{g^2}{-i\Delta_{\mathrm{p}}+\kappa_{\mathrm{m}}/2}} + re^{i\phi} \right) \sqrt{\kappa_{\mathrm{in}}\kappa_{\mathrm{out}}}\alpha_{\mathrm{p}}\,. \tag{7.46}$$

The above equation can be used to reproduce OMIT traces and obtain the optomechanical coupling strength g. For this, the parameters ω_{cav}, κ_{cav}, r, and ϕ are predetermined from cavity transmission measurements (see Fig. 6.6) and treated as constant. The drive frequency ω_{d} is also fixed. Therefore, the only parameters determining the fit are the mechanical parameters ω_{m} and κ_{m}, the coupling strength g, and the transmission amplitude $\sqrt{\kappa_{\mathrm{in}}\kappa_{\mathrm{out}}}\alpha_{\mathrm{p}}$. The power transmission $|S_{21}|^2$ recorded by the VNA can then be fitted by applying $|s_{\mathrm{out}}|^2$ with said free parameters.

Fig. 7.8 shows OMIT dips that have been fitted with Eq. 7.46. In (a), a large probe tone was applied causing strong mechanical driving and hence nonlinear response of the mechanical system and an asymmetric lineshape of the dip. Therefore, the fit only gives a qualitative agreement; however, strongly driven optomechanical systems are the basis for prospective experiments and analysis in the Duffing regime and beyond [Shevchuk et al., 2015]. A decrease in probe power to $P_{\mathrm{p}} = -20\,\mathrm{dBm}$ and an increase in drive power to $P_{\mathrm{d}} = +25\,\mathrm{dBm}$ results in a symmetric OMIT feature (b). An optomechanical coupling strength of $g = 20.8\,\mathrm{kHz}$ could be extracted. Furthermore, the fit gives a mechanical linewidth of $\kappa_{\mathrm{m}} = 2\pi \cdot 5.1\,\mathrm{kHz}$ and a resonance frequency $\omega_{\mathrm{m}} = 2\pi \cdot 502.5\,\mathrm{MHz}$. Compared to the dc detection method of Sect. 2.4.3, ω_{m} is of similar size, while the linewidth is much smaller. This is due to much stronger driving in the dc method, which can be identified again by the asymmetric mechanical lineshape. Note that the mechanical resonance frequencies in Fig. 7.8 (a) and (b) differ because of different gate voltage settings.

Cavity photon number calibration

To determine the single-photon coupling strength g_0, the average number of photons circulating in the cavity has to be known. In principle, this can be calculated easily by using Eq. 7.18. In

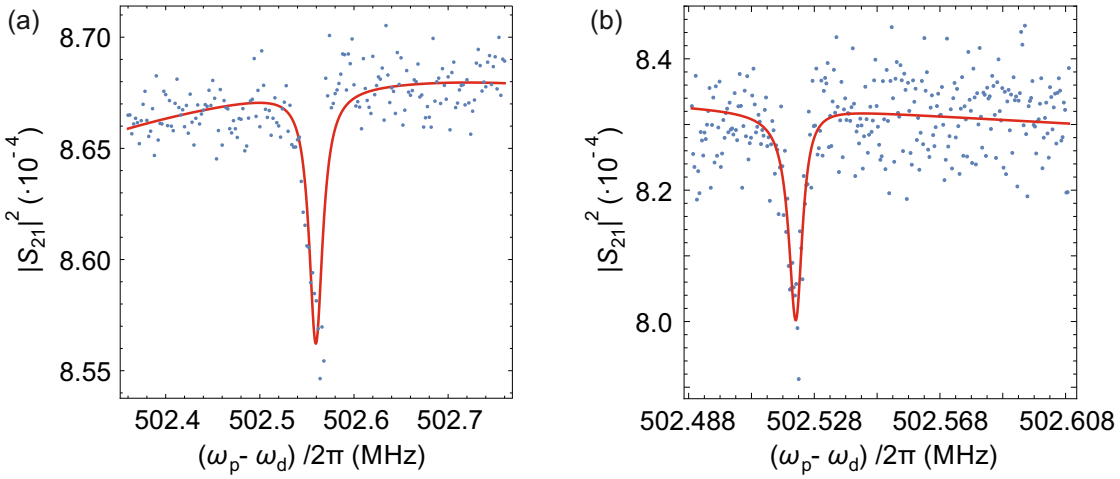

Figure 7.8.: OMIT data evaluation. (a) shows the same trace as the inset in Fig. 7.7 (a) along with a fit to Eq. 7.46. Given the asymmetry of the dip due to a strong probe tone, the fit is only a rough approximation. In (b) a weaker probe ($P_\mathrm{p} = -20\,\mathrm{dBm}$) and slightly stronger drive tone ($P_\mathrm{d} = +25\,\mathrm{dBm}$) were applied, resulting in a symmetric dip. Also, the gate voltage was set to $V_\mathrm{g} = -1.18901\,\mathrm{V}$. The fit in (b) gives an optomechanical coupling of $g = 20.8\,\mathrm{kHz}$. (a) adapted from [Blien et al., 2020].

practice, however, two problems arise. First, the coupling decay rate κ_c is unknown for our system. While it could still be estimated using Eq. 4.87 and finite element modelling for C_k or by comparison to plain resonators with the same C_k assuming overcoupled behaviour, the second issue is more severe. The power incident on the cavity P_in has to be determined from the generator power and the loss along the signal path. This is however difficult, due to an imprecise knowledge of attenuation mediated by the high frequency cabling, the attenuators along the signal path and the bond wires connecting the device to the PCB. Room temperature calibration to account for losses is inaccurate for low temperatures and excludes bond wires.

Therefore, another way to determine n_cav was explored. It is known from the device scheme of Fig. 6.7 (a) that the centre conductor also acts as dc gate for the CNT. As has been shown already in Sect. 6.2.1, the Coulomb oscillations broaden with rising intracavity power. This is due to the additional voltage δV_ac on the gate electrode that shifts the Coulomb oscillation, causing a broadening of the time-averaged dc current. The cavity can be modelled classically with a sinusoidal ac gate voltage on top of the dc voltage in a dc current measurement

$$I_\mathrm{driven}(V_\mathrm{g}, P_\mathrm{gen}) = \frac{1}{2\pi}\int_0^{2\pi} I\left(V_\mathrm{g} + \delta V_\mathrm{ac}(P_\mathrm{gen})\cdot\sin(\phi)\right)\mathrm{d}\phi\,. \tag{7.47}$$

Here, $\delta V_\mathrm{ac}(P_\mathrm{gen})$ is the unknown dependence of ac voltage amplitude on the generator power. Both V_g and δV_ac are applied via the same gate electrode and therefore affect the quantum dot with the same gate lever arm.

Fig. 7.9 (a) shows Coulomb oscillation broadening for the sideband drive at $\omega_\mathrm{d} = \omega_\mathrm{cav} - \omega_\mathrm{m}$ for varying generator powers $0\,\mathrm{dBm} \leq P_\mathrm{gen} \leq +25\mathrm{dBm}$. Note that the broadening is much

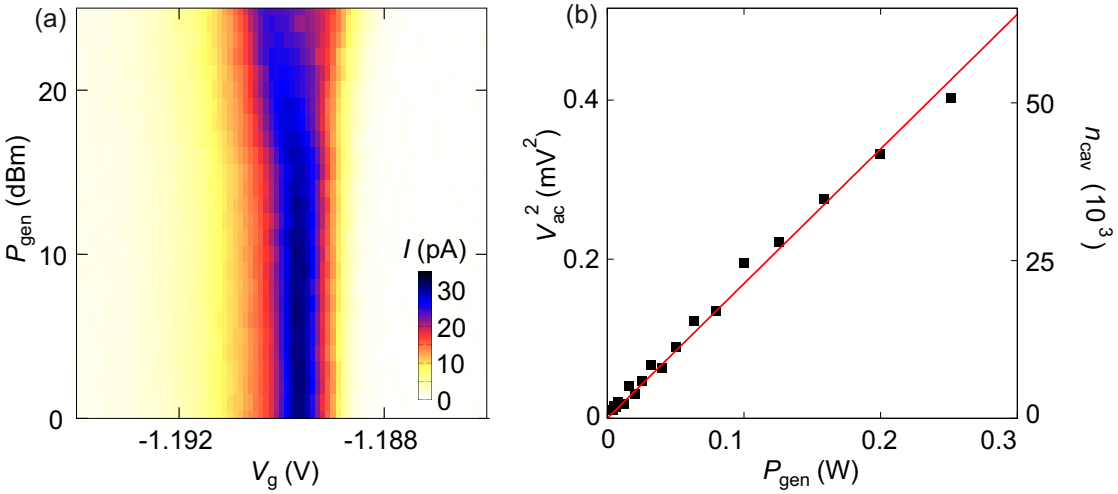

Figure 7.9.: Determination of the number of photons in the cavity from Coulomb oscillation broadening. (a) In dc measurements of the QD current, the Coulomb peak broadens with rising generator power P_{gen}. (b) From this, the additional voltage component δV_{ac} can be calculated, leading with lumped elements modelling of the cavity to n_{cav}. Adapted from [Blien et al., 2020].

less distinct than for resonant driving as in Fig. 6.8, which is expected from the filtering behaviour of a cavity. For a generator power of $P_{\mathrm{gen}} = -10\,\mathrm{dBm}$, the function $I(V_{\mathrm{g}})$ is determined by interpolation of the data points and setting $\delta V_{\mathrm{ac}}(-10\,\mathrm{dBm}) \approx 0$, so that $I(V_{\mathrm{g}}) \coloneqq I_{\mathrm{driven}}(V_{\mathrm{g}}, -10\,\mathrm{dBm})$. Then, δV_{ac} can be obtained for each P_{gen} by fitting the respective current trace to Eq. 7.47. The result is depicted in Fig. 7.9 (b).

The number of photons n_{cav} can then be calculated from the energy stored in the resonator

$$E = \frac{1}{2} C_{\mathrm{CPW}} \left(\frac{\delta V_{\mathrm{ac}}}{\sqrt{2}} \right)^2 = n_{\mathrm{cav}} \hbar \omega_{\mathrm{d}} \tag{7.48}$$

where the factor $1/\sqrt{2}$ comes from the non-homogenous voltage distribution along the cavity waveguide, for a time when the energy is completely stored in the electric field of the capacitor C_{CPW}.

Alternatively, the lumped elements model for a half wave resonator can be used (see Sect. 4.5.2). The energy stored in the cavity is $E = 1/2 C_{\mathrm{RLC}} V_{\mathrm{rms}}^2 + 1/2 L_{\mathrm{RLC}} I_{\mathrm{rms}}^2$, with the effective amplitudes denoted by rms and $V_{\mathrm{rms}} = \delta V_{\mathrm{ac}}/\sqrt{2}$. Then, with $I_{\mathrm{rms}} = V_{\mathrm{rms}}/Z_0$

$$E = \frac{1}{2} C_{\mathrm{RLC}} \delta V_{\mathrm{ac}}^2 \,, \tag{7.49}$$

which is equal to Eq. 7.48, as $C_{\mathrm{RLC}} = C_{\mathrm{CPW}}/2$.

In Fig. 7.9 (b), the expected linear dependence of squared amplitude δV_{ac} and corresponding cavity photon number n_{cav} on the generator power P_{gen} is shown. For the trace in Fig. 7.8 (b), a generator power of $P_{\mathrm{gen}} = +25\,\mathrm{dBm}$ was applied, which gives $n_{\mathrm{cav}} = 67500$.

Now the single-photon coupling strength can be calculated. It is

$$g_0 = 80.1\,\mathrm{Hz}\,,$$

four orders of magnitude larger than the value estimated from geometric coupling in Sect. 7.2.1 ($g_0^* = 2\pi \cdot 2.9\,\mathrm{mHz}$). In the following, the mechanism that generates such an enhanced coupling is discussed.

7.2.3. Quantum capacitance enhanced optomechanical coupling

In the determination of the coupling using Eq. 7.29, the change of capacitance with displacement $\partial C_\mathrm{g}/\partial x$ is the most important parameter. So far, a geometric capacitance between carbon nanotube and gate electrode has been considered. However, a characteristic of our carbon nanotube - coplanar waveguide resonator system fundamentally different to other optomechanical systems is the formation of a quantum dot in the CNT. The validity of the metallic wire-over-plane model can be questioned, as electronic behaviour is completely dominated by single-electron effects. In the following, a model is derived that includes these effects into a theory of *quantum capacitance enhanced optomechanics*. Here, a full separation of time scales is assumed, meaning $\omega_\mathrm{m} \ll \omega_\mathrm{cav} \ll \Gamma_\mathrm{broad}$, where Γ_broad is the lifetime broadening of the QD states as in Sect. 2.3.4.

In the wire-over-plane model, the carbon nanotube was considered a conductive (metallic) wire that charges continuously with applied gate voltage. However, a quantum dot shows a step-like charging originating in the SET behaviour. As has been shown in Sect. 6.2.2, an effective capacitance C_eff is defined that considers the electronic nature of the CNT and its influence on the effective charge on the gate electrode. This gives rise to an altered capacitive response of the cavity on the CNT motion. In the following, the first term (geometric part) of Eq. 6.4 with $\alpha_\mathrm{g} = C_\mathrm{g}/C_\Sigma$

$$C_\mathrm{eff} = \frac{(C_\mathrm{s} + C_\mathrm{d})C_\mathrm{g}}{C_\Sigma} + e\frac{\partial \langle N \rangle}{\partial V_\mathrm{g}}\alpha_\mathrm{g}$$

is considered small (as has been shown in the wire-over-plane calculation). This leads to

$$C_\mathrm{eff} \approx e\alpha_\mathrm{g}\frac{\partial \langle N \rangle}{\partial V_\mathrm{g}}\,, \tag{7.50}$$

where $\langle N \rangle$ is the number of charge carriers on the CNT quantum dot; it is averaged over SET processes with rates faster than cavity and mechanical resonance frequency $\Gamma_\mathrm{broad} > \omega_\mathrm{cav},\, \omega_\mathrm{m}$.

Now, this capacitance is assumed to be the deflection dependent part of the total capacitance in Eq. 7.29, such that

$$g_0 \approx \frac{\omega_\mathrm{cav}}{2C_\mathrm{RLC}}\frac{\partial C_\mathrm{eff}}{\partial x}x_\mathrm{zpf}\,. \tag{7.51}$$

Any change in gate capacitance δC_g by the CNT motion leads to a change in position of the Coulomb oscillation with respect to the gate voltage. Thus, δC_g can be translated into an effective gate voltage modulation $\delta V_\mathrm{g}^\mathrm{eff}$ as

$$C_\mathrm{g}\delta V_\mathrm{g}^\mathrm{eff} = V_\mathrm{g}\delta C_\mathrm{g}\,, \tag{7.52}$$

with C_g being the static, geometric capacitance at zero deflection. The change of capacitance with deflection is now expanded

$$\frac{\partial C_\mathrm{eff}}{\partial x} = \frac{\partial C_\mathrm{eff}}{\partial V_\mathrm{g}^\mathrm{eff}} \frac{\partial V_\mathrm{g}^\mathrm{eff}}{\partial x} = \frac{\partial C_\mathrm{eff}}{\partial V_\mathrm{g}^\mathrm{eff}} \frac{V_\mathrm{g}}{C_\mathrm{g}} \frac{\partial C_\mathrm{g}}{\partial x} \,. \tag{7.53}$$

Inserting Eq. 7.50, under the implicit assumption that a variation of the effective gate voltage $\delta V_\mathrm{g}^\mathrm{eff}$ acts on the system in the same way as a variation of the actual gate voltage δV_g, leads then to

$$\frac{\partial C_\mathrm{eff}}{\partial x} = e\alpha_\mathrm{g} \frac{\partial^2 \langle N \rangle}{\partial V_\mathrm{g}^2} \frac{V_\mathrm{g}}{C_\mathrm{g}} \frac{\partial C_\mathrm{g}}{\partial x} = \eta \frac{\partial C_\mathrm{g}}{\partial x} \,. \tag{7.54}$$

Here, η is the amplification factor of the gate coupling.

As explained above, the lifetime broadened regime is used to describe the QD states. From Eq. 2.16, $\mu = e\alpha_\mathrm{g} V_\mathrm{g}$, and with V_g0 as the Coulomb oscillation position, $\langle N \rangle \, (V_\mathrm{g})$ can be written as

$$\langle N \rangle = N_0 + \int_{-\infty}^{V_\mathrm{g}} \frac{1}{2\pi} \frac{\hbar\Gamma_\mathrm{broad}}{e\alpha_\mathrm{g}(V_\mathrm{g}' - V_\mathrm{g0})^2 + \left(\frac{\hbar\Gamma_\mathrm{broad}}{2}\right)^2} \mathrm{d}V_\mathrm{g}' \,. \tag{7.55}$$

Using this in Eq. 7.54 leads to an expression for g_0 that strongly reflects the quantum dot characteristics of the CNT. The coupling g_0 can be adjusted via the applied gate voltage in the vicinity of a Coulomb oscillation. From device data, the amplification factor η in Eq. 7.54 is found to reach values of $\eta \sim 10^4$ [Blien et al., 2020].

Gate voltage dependence of the coupling and comparison to the model

In order to experimentally determine the dependence of the optomechanical coupling on the QD characteristics, Fig. 7.10 (a) presents OMIT measurements for varying gate voltage. V_g is here stepped over the same Coulomb oscillation[7] as in Fig. 7.9, while for every gate voltage value an OMIT trace was recorded.

The first thing that catches the eye is the shift to lower frequencies of the OMIT dip. Comparing the gate voltage range with Fig. 7.9, it can be deduced that the frequency shift is maximum near the Coulomb peak centre. This circumstance can easily be explained by the electrostatic softening of the mechanical mode in the vicinity of the charge degeneracy point as in Sect. 2.4.4. The mechanical resonance frequency shifts due to the interaction of the CNT vibration with single electron tunneling; this is a well known feature, see also [Steele et al., 2009, Meerwaldt et al., 2012].

More interestingly, the OMIT dip feature is very pronounced on the edges of the Coulomb oscillation, while on its centre and on the outer edges, the coupling vanishes. Fitting each trace to Eq. 7.46 yields the gate-dependent coupling $g(V_\mathrm{g})$. The result is depicted in Fig. 7.10 (b) (along with $g_0(V_\mathrm{g})$), proving that the enhancement of the optomechanical coupling must be intrinsically related to Coulomb blockade.

In Fig. 7.11 (a)-(c), the theoretical model of the coupling according to the last section is depicted. In (a), the charge on the quantum dot averaged over tunneling events is shown. It

[7] Note that there was a slight drift in gate voltage over measurement time.

resembles a step function that decreases with rising V_g, because the gate voltage settings correspond to the hole conduction side of the CNT. Its sharpness is given for zero bias by the lifetime broadening Γ_broad. The effective capacitance, depicted in (b), then becomes a Lorentzian and is proportional to the conductance of the QD[8]. Note that the effective capacitance can be identified with the capacitance shift of Fig. 6.12 (c): both curves agree nicely in shape and magnitude. As the methods used to obtain these curves are distinct - one using a mechanical signal, the other one the cavity resonance frequency shift - the validity of the model of quantum capacitance enhanced coupling is confirmed. Taking the second derivative then leads to the optomechanical coupling as shown in (c). The functional dependence has been fitted to the data points of Fig. 7.10 (b) that have been overlaid here. The free parameters were the Coulomb oscillation position V_g0, the broadening Γ_broad, and an additional scaling factor a, resulting in $V_\mathrm{g0} = -1.8841\,\mathrm{V}$, $\hbar\Gamma_\mathrm{broad} = 0.673\,\mathrm{meV}$, and $a = g_0^\mathrm{exp}/g_0^\mathrm{th} = 5.77$. From this, it can be seen that the separation of time scales is valid: the broadening corresponds to a frequency of $166\,\mathrm{GHz}$, orders of magnitude larger than optical or mechanical resonance frequency. With the introduction of the scaling factor, the theory curve quantitatively reproduces the experimental gate voltage dependence $g_0(V_\mathrm{g})$. This is a convincing agreement considering the uncertainties of input parameters; for a discussion of these uncertainties, see the end of this section.

The situations leading to the three most distinctive points in the coupling of Fig. 7.11 (c) are illustrated in Fig. 7.11 (d)-(f). Away from the Coulomb oscillation, the charge on the QD is constant, and the optomechanical coupling has only geometric contributions that are negligible in magnitude (d). On the flank of a conductance peak, the modulation of C_eff by a small change in deflection δx ($\sim \delta C_\mathrm{g}$) is intense (e). At the centre of the resonance, the charge is able to adapt to the deflection, but the derivative $\partial C_\mathrm{eff}/\partial V_\mathrm{g}$ and with it the coupling $g_0 \sim |\partial C_\mathrm{eff}/\partial x|$ is approximately zero.

[8] This has already been shown in Sect. 2.3.5.

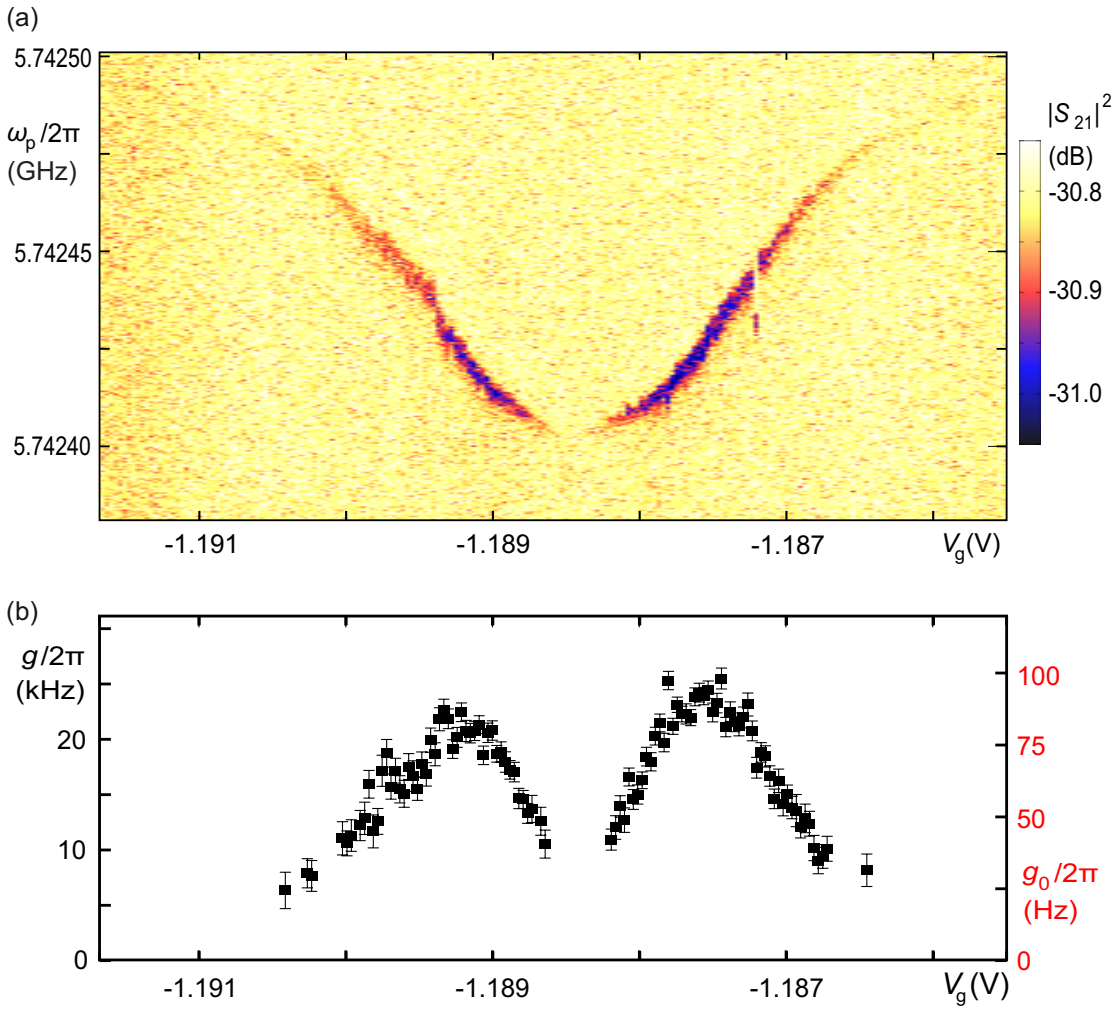

Figure 7.10.: Gate dependency of optomechanical coupling. In (a), OMIT traces for varying gate voltages in the vicinity of a Coulomb oscillation are shown. In some regions, the dip is faint, while in others it is more pronounced. Fits to Eq. 7.46 yield the coupling strengths g and g_0, which are depicted over the same gate voltage range in (b). Adapted from [Blien et al., 2020].

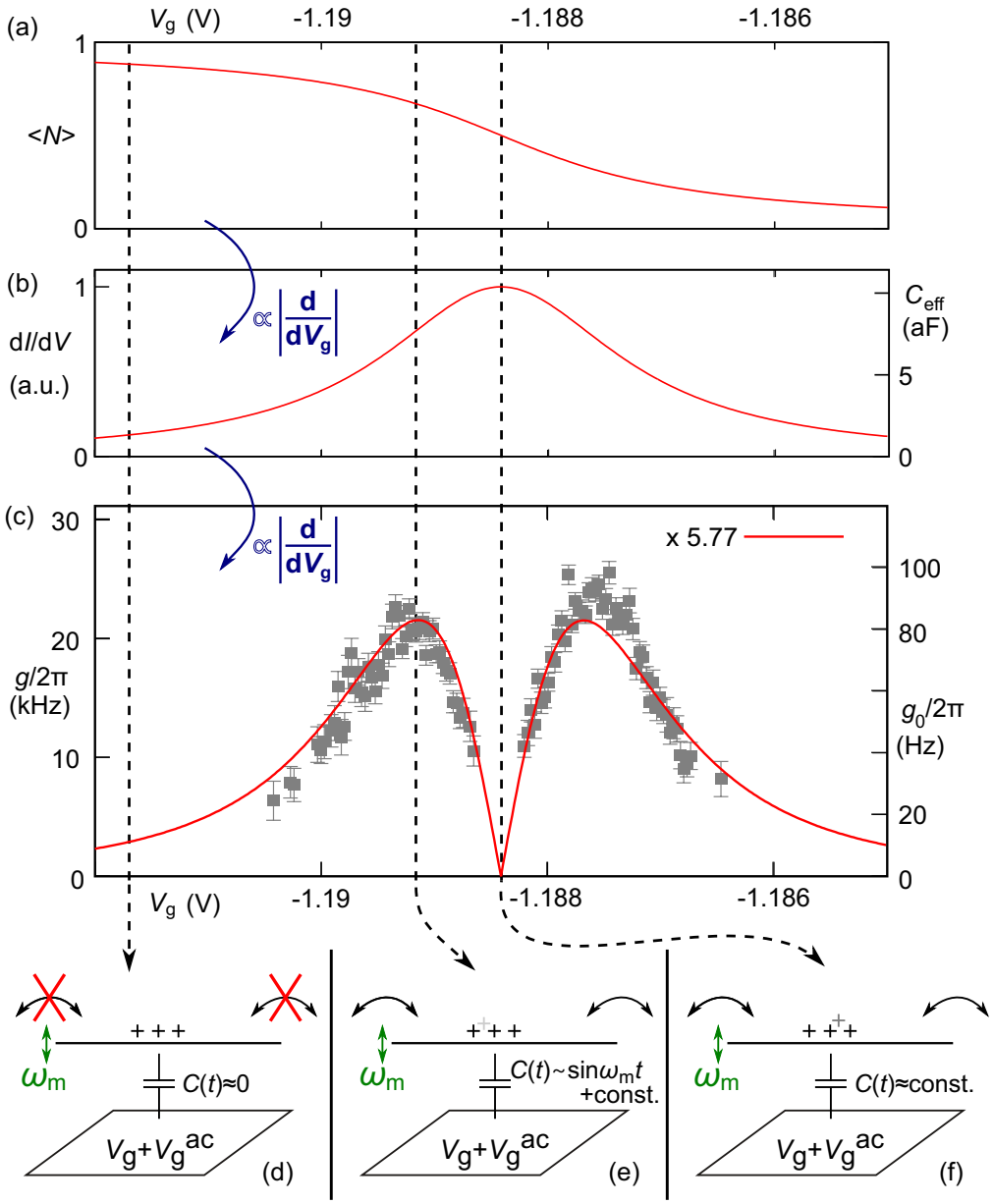

Figure 7.11.: Quantum capacitance enhanced optomechanical coupling mechanism. Red solid lines correspond to the model presented in the main text; the Coulomb oscillation centre $V_g^* = -1.18841$, the line width $\hbar\Gamma_{\mathrm{broad}} = 0.673\,\mathrm{meV}$, and a pre-scaling factor $a = 5.77$ have been obtained by fitting the optomechanical coupling strength $g(V_g)$. (a) Time-averaged dot occupation $\langle N\rangle\,(V_g)$ for the gate voltage range of one Coulomb oscillation. (b) Corresponding conductance $\mathrm{d}I/\mathrm{d}V$ and resulting effective capacitance C_{eff}. (c) Quantum capacitance enhanced optomechanical coupling g and corresponding single-photon coupling g_0. Overlaid data points to which the fit was performed are the same as in Fig. 7.10 (b). (d)-(f) Schemata for the system situations corresponding to gate voltages indicated with the dashed lines in (a)-(c). Adapted from [Blien et al., 2020].

Discussion of error sources

In the following, the error sources and approximations, that enter the calculation for the quantum capacitance enhancement, shall be stated and discussed [Blien et al., 2020].

First of all, the parameters in the calculation for the coupling strength for which an approximative value was used are considered error sources. From Eq. 7.51,

$$g_0 = e\alpha_\mathrm{g}\frac{\omega_\mathrm{cav}}{2C_\mathrm{RLC}}\frac{\partial^2\langle N\rangle}{\partial V_\mathrm{g}^2}\frac{V_\mathrm{g}}{C_\mathrm{g}}\frac{\partial C_\mathrm{g}}{\partial x}x_\mathrm{zpf}\,,$$

Eq. 7.32,

$$\frac{\partial C_\mathrm{g}(x)}{\partial x} = \frac{2\pi\epsilon_0\epsilon_\mathrm{r}L}{R\sqrt{\left(\frac{d-x}{R}\right)^2-1}\left(\operatorname{arcosh}\left(\frac{d-x}{R}\right)\right)^2}\,,$$

and

$$x_\mathrm{zpf} = \sqrt{\frac{\hbar}{2m\omega_\mathrm{m}}}$$

the mass of the CNT m, its length L and radius R, and the dielectric constant of the gate oxide ϵ_r, can be identified. Parts of the discussion were already stated in Sect. 7.2.1, but shall be repeated here.

The length of the nanotube, entering the calculation for its total mass and thus the zero-point motion amplitude, is approximated by the contact separation ($l = 1\,\mu\mathrm{m}$). In the case that the CNT is not aligned perpendicular to the leads, it can be larger. This can for example happen when the CNTs grow not in a right angle from tine to tine on the quartz tuning fork. The effective mass of the CNT vibrational resonator is then estimated to be half its total mass, $m = (2\pi RL\rho_\mathrm{graphene})/2$; it is reflected in the zero-point motion amplitude of the carbon nanotube, $x_\mathrm{zpf} \sim 1/\sqrt{m}$. As can be deduced from above equations, an error in the effective mass/nanotube length is thus reflected in the coupling strength g_0 as a deviation on the order of the square root of this error.

The radius is assumed to take on a typical value of $R = 2\,\mathrm{nm}$; it also affects the nanotube mass and the geometric coupling strength $\partial C_\mathrm{g}/\partial x$. While the radius could in reality be significantly smaller or larger, the optomechanical coupling is however not very dependent on it: in a realistic range of $0.5\,\mathrm{nm} \leq R \leq 5\,\mathrm{nm}$, the gate coupling $\partial C_\mathrm{g}/\partial x$ only changes by a factor of 2. The single-photon coupling g_0 is even less dependent on R.

The space between CNT and gate electrode was simplified as a single material with a relative dielectric constant $\epsilon_r = 2$ and thickness $d = 450\,\mathrm{nm}$. It actually consists of $250\,\mathrm{nm}$ vacuum and $200\,\mathrm{nm}$ cross-linked PMMA. The dielectric constant used here is an average value of the dielectric constants of these two materials. An error in the relative dielectric constant leads to an error in the coupling strength on the same order of magnitude.

Aside from the estimated values of parameters, there are also other error sources. The wire-over-plane model that is used for calculating the geometric capacitance assumes a thin, long rod above an infinite conducting plane. The width of the gate electrode along the CNT axis is, however, approximately only $100\,\mathrm{nm}$. As the electronic length of the CNT is also in the same range, $L_\mathrm{eff} = 143\,\mathrm{nm}$, the wire-over-plane model is a reasonable approximation concerning the above assumption, but may lead to additional deviations between model and experimental value.

Furthermore, the experimentally determinable value is the optomechanical coupling strength g while the model parameter is the single-photon coupling strength g_0. To translate between these two, the number of cavity photons n_{cav} has to be known accurately. Here, it was determined via the Coulomb resonance broadening as presented in Sect. 7.2.2. While this approach is justified, errors in the determination of n_{cav} enter the deduction of g_0 via its square root.

7.3. Radiation pressure cooling and thermal vibration detection

In this section, a brief outlook on ongoing and planned experiments shall be given. The optomechanical coupling can be used to actively manipulate the motion of the vibrational resonator via *dynamical backaction*. Mechanical amplifiers [Singh et al., 2014a] or ground state cooling of the nanomechanical motion [Teufel et al., 2011] are possible. In this section, the focus lies on the optomechanical cooling and motion detection of the nanoresonator: theory is provided following [Aspelmeyer et al., 2014] and first experimental data is presented and discussed.

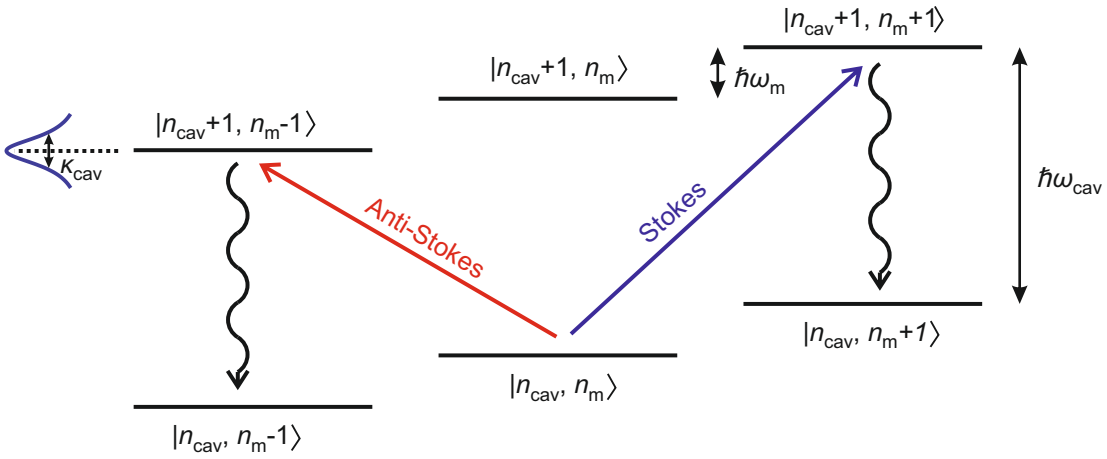

Figure 7.12.: Schematic energy level diagram for illustration of backaction effects. Red detuned pumping leads to Anti-Stokes processes reducing the phonon occupation of the mechanical resonator. Blue detuned pumping leads via Stokes processes to the coherent driving of the mechanical resonator. Adapted from [Schliesser et al., 2008].

Backaction cooling or heating can be understood as Anti-Stokes or Stokes scattering processes known from Raman physics. A schematic energy level diagram is depicted in Fig. 7.13. When pumping the cavity on the red/blue detuned sideband, a photon of energy $\hbar(\omega_{\mathrm{cav}} \pm \omega_{\mathrm{m}})$ can only enter the cavity by annihilation/creation of a phonon. The photon is then shifted upwards/downwards in energy to $\hbar\omega_{\mathrm{cav}}$. The cavity occupation is raised by one, while lowering/raising the mechanical resonator occupation by one quantum ($|n_{\mathrm{cav}}+1, n_{\mathrm{m}} \pm 1\rangle$). With a large density of states at the cavity resonance, the excited photon mode then decays and returns to its initial state. However, the mechanical resonator has now a phonon occupation with one

quantum less/more than before ($|n_{\mathrm{cav}}, n_{\mathrm{m}} \pm 1\rangle$). Repeating this process leads to cooling/heating of the mechanical mode.

From Fig. 7.13 it is also clear why the resolved sideband regime is important in this context. In the unresolved case ($\omega_{\mathrm{m}} \ll \kappa_{\mathrm{cav}}$), the energy levels overlap and there is a non-negligible probability that when pumping with, e.g., a red-detuned drive, also the upper level $|n_{\mathrm{cav}}+1, n_{\mathrm{m}}+1\rangle$ is addressed. The decay to $|n_{\mathrm{cav}}, n_{\mathrm{m}}+1\rangle$ then competes with the desired Anti-Stokes process, reducing cooling.

7.3.1. Theory

To quantify these processes, a model is derived from a classical approach [Aspelmeyer et al., 2014, Teufel et al., 2008]. Here, the origin of backaction effects is the radiation pressure F_{rad} coming from the momentum transfer of the photons onto the mirror. As explained in the beginning of this chapter, the mechanical motion modulates the cavity resonance frequency at rate ω_{m}. For a fixed-frequency optical drive signal, the power that enters the cavity, and therefore the radiation pressure, will also oscillate at ω_{m}. Yet, this force lags the mechanical motion by a time $\tau = \kappa_{\mathrm{cav}}^{-1}$ introduced by the final cavity decay rate. It is this retarded nature of the radiation pressure (hence the term *dynamical backaction* [Braginsky and Manukin, 1967]) that causes F_{rad} to yield components oscillating both in and out of phase with the mechanics. The in phase component then leads to an extra contribution to the restoring force in the equation of motion, while the out of phase component leads to extra damping.

The mechanical susceptibility describes the response of the mechanics to an external force

$$\chi_{\mathrm{m}} = \frac{x(\omega)}{F_{\mathrm{ext}}}\,. \tag{7.56}$$

In absence of optomechanical coupling, it takes the form $\chi_{\mathrm{m}}^{-1}(\omega) = m[(\omega_{\mathrm{m}}^2 - \omega^2) - i\kappa_{\mathrm{m}}\omega]$ (see Sect. 7.2.2). The radiation pressure force, however, modifies the original susceptibility

$$\chi_{\mathrm{m,eff}}^{-1}(\omega) = \chi_{\mathrm{m}}^{-1}(\omega) + \Sigma(\omega)\,. \tag{7.57}$$

This additional term is found by proceeding from the solutions of the linearised classical equations of motion as presented in Sect. 7.2.2. The field amplitude A (Eqs. 7.36 and 7.37) can then be expressed in terms of X and plugged into Eq. 7.38. With $g = Gx_{\mathrm{zpf}}\bar{\alpha}$ and $x_{\mathrm{zpf}} = \sqrt{\hbar/(2m\omega_{\mathrm{m}})}$ as before, this yields the modification of the response

$$\Sigma(\Omega) = 2m\omega_{\mathrm{m}}g^2\left(\frac{1}{(\Delta+\Omega)+i\kappa_{\mathrm{cav}}/2} + \frac{1}{(\Delta-\Omega)-i\kappa_{\mathrm{cav}}/2}\right), \tag{7.58}$$

with $\Delta = \omega_{\mathrm{d}} - \omega_{\mathrm{cav}}$ and $\Omega = \omega_{\mathrm{p}} - \omega_{\mathrm{d}}$ being again the optical detunings.

The radiation pressure contribution is rearranged to

$$\Sigma(\Omega) = m\Omega[2\delta\omega_{\mathrm{m}}(\Omega) - i\Gamma_{\mathrm{opt}}(\Omega)]\,, \tag{7.59}$$

as then the real and imaginary terms can be attributed to the terms of the original susceptibility, which leads to

$$\chi_{\mathrm{m,eff}}^{-1}(\Omega) = m\left[\omega_{\mathrm{m}}^2 + 2\Omega\delta\omega_{\mathrm{m}}(\Omega) - \Omega^2 - i\Omega(\kappa_{\mathrm{m}} + \Gamma_{\mathrm{opt}}(\Omega))\right]. \tag{7.60}$$

The real and imaginary part of the full expression, Eq. 7.60, then give the frequency dependent mechanical resonance frequency shift $\delta\omega_{\mathrm{m}}(\Omega)$ caused by the optical field and optomechanical damping rate $\Gamma_{\mathrm{opt}}(\Omega)$. The explicit expressions are

$$\delta\omega_{\mathrm{m}}(\Omega) = g^2\frac{\omega_{\mathrm{m}}}{\Omega}\left[\frac{\Delta+\Omega}{(\Delta+\Omega)^2+\kappa_{\mathrm{cav}}^2/4}+\frac{\Delta-\Omega}{(\Delta-\Omega)^2+\kappa_{\mathrm{cav}}^2/4}\right] \tag{7.61}$$

$$\Gamma_{\mathrm{opt}}(\Omega) = \Gamma_{\mathrm{opt}}^{+}(\Omega)-\Gamma_{\mathrm{opt}}^{-}(\Omega) = g^2\frac{\omega_{\mathrm{m}}}{\Omega}\left[\frac{\kappa_{\mathrm{cav}}}{(\Delta+\Omega)^2+\kappa_{\mathrm{cav}}^2/4}-\frac{\kappa_{\mathrm{cav}}}{(\Delta-\Omega)^2+\kappa_{\mathrm{cav}}^2/4}\right] \tag{7.62}$$

and provide an exact solution in the linearised regime also valid for strong coupling $g > \kappa_{\mathrm{cav}}$ [Aspelmeyer et al., 2014].

The frequency shift $\delta\omega_{\mathrm{m}}$ due to the radiation field is called *optical spring effect*. Eq. 7.61 shows that depending on the detuning, spring softening or hardening can occur. For $\Omega = \omega_{\mathrm{m}}$ and the parameters of this thesis (see Tab. A.1), the optical spring effect corresponds to maximum frequency shifts $\delta\omega_{\mathrm{m}} \approx 40\,\mathrm{Hz}$. On the red sideband ($\Delta = -\omega_{\mathrm{m}}$), however, where the experiments of this thesis have taken place, the shift can be calculated to be $< 1\,\mathrm{Hz}$. Thus, a detection of the shift was not experimentally pursued.

The optomechanical damping rate Γ_{opt} leads to a modified mechanical dissipation rate

$$\kappa_{\mathrm{eff}} = \kappa_{\mathrm{m}} + \Gamma_{\mathrm{opt}}\,. \tag{7.63}$$

From Eq. 7.62 it can be concluded that Γ_{opt} can be positive or negative, dependent on the detuning. In this way, it can increase or decrease the full mechanical linewidth κ_{eff} and thus lead to extra damping or antidamping (amplification). When $\Gamma_{\mathrm{opt}} \leq -\kappa_{\mathrm{m}}$, the effective linewidth becomes negative and mechanical instability sets in. The function of Eq. 7.62 has already been plotted in Fig. 7.3 (a), when discussing the parameter regimes of optomechanics.

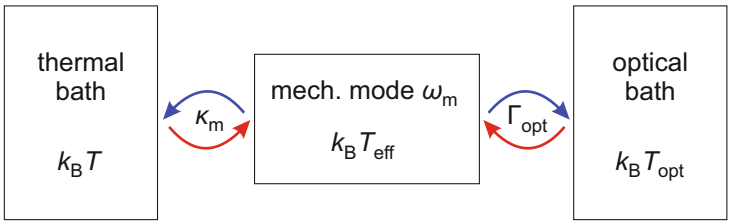

Figure 7.13.: Sideband cooling via an "optical bath". The mechanical resonator is coupled to a conventional thermal bath of temperature T and an "optical bath" of temperature T_{opt} with respective absorption and emission rates, resulting in a mechanical mode temperature T_{eff}. Adapted from [Hertzberg, 2009].

The mechanical resonator is coupled to its environment, which can be seen as a thermal bath of temperature T. In equilibrium, an average phonon number of $n_{\mathrm{m,th}} = k_{\mathrm{B}}T/\hbar\omega_{\mathrm{m}}$ is present and energy is transferred at rate κ_{m}. The optical field can now be thought of as an optical bath $k_{\mathrm{B}}T_{\mathrm{opt}} = \hbar\omega_{\mathrm{m}}n_{\mathrm{m,opt}}$ with rate Γ_{opt} (see Fig. 7.13). The mechanical resonator emits energy

to its environment at rate $\kappa_{\rm eff} n_{\rm m} \hbar\omega_{\rm m} = (\kappa_{\rm m} n_{\rm m,th} + \Gamma_{\rm opt} n_{\rm m,opt}) \cdot \hbar\omega_{\rm m}$, which yields the rate equation [Marquardt et al., 2007]

$$n_{m,\rm eff} = \frac{\Gamma_{\rm opt} n_{m,\rm opt} + \kappa_{\rm m} n_{m,\rm th}}{\Gamma_{\rm opt} + \kappa_{\rm m}} \,. \tag{7.64}$$

Here, $n_{\rm m,eff}$ is the effective average phonon number. The mechanical resonator coupled to the optical field will thus achieve a mode temperature of $T_{\rm eff} = n_{\rm m,eff}\hbar\omega_{\rm m}/k_{\rm B}$.

A brief discussion of radiation pressure cooling in the parameter range of this thesis shall end this section. In the resolved sideband regime ($\omega_{\rm m} \gg \kappa_{\rm cav}$), Marquardt *et al.* have found an expression for the "optical" phonon number from quantum noise analysis [Marquardt et al., 2007]

$$n_{\rm m,opt} = \left(\frac{\kappa_{\rm cav}}{4\omega_{\rm m}}\right)^2 \,. \tag{7.65}$$

In the same regime, from Eq. 7.62 with $\Delta = -\omega_{\rm m}$ and $\Omega = \omega_{\rm m}$ follows

$$\Gamma_{\rm opt} = \frac{4g^2}{\kappa_{\rm cav}} \,. \tag{7.66}$$

With the parameters taken from Tab. A.1, this results in $n_{m,\rm th} = 0.414$ for $T = 10\,\rm mK$, $\Gamma_{\rm opt} = 2\pi \cdot 211\,\rm Hz$, and $n_{\rm m,opt} = 3.33 \cdot 10^{-5}$. Using Eq. 7.64, optomechanical cooling leads in this parameter range to an effective phonon number $n_{\rm m,eff} = 0.398$, respectively a mode temperature of $T_{\rm eff} = 9.59\,\rm mK$. This is a small effect. However, for the calculation a $\kappa_{\rm m} = 5.1\,\rm kHz$ obtained with the OMIT method was used. The intrinsic $\kappa_{\rm m}$ might be much smaller and even comparable to $\Gamma_{\rm opt}$. Also, $\Gamma_{\rm opt}$ scales linearly with g^2 and therefore with $n_{\rm cav}$, which can in principle be easily increased with the intracavity power. Furthermore, this approach can also be used to detect the thermal motion, that with $n_{\rm m,th} = 0.414 < 1$ at $T = 10\,\rm mK$ should already be in its ground state.

7.3.2. Two-tone spectroscopy

In this section, first experimental results towards thermal motion detection are presented. The two-tone spectroscopy technique that has been used is schematically depicted in Fig. 7.14. The CNT is excited via an antenna drive ($\omega_{\rm A}$) around $\omega_{\rm m}$ as in the dc detection method (see Sect. 2.4.3). At the same time, the cavity is driven around the red sideband ($\omega_{\rm cav} - \omega_{\rm m}$) in such a way that $\omega_{\rm A} + \omega_{\rm d} = \omega_{\rm cav}$ always holds. The photons of the drive field are optomechanically upconverted to photons of frequency $\omega_{\rm cav}$ by absorption of a phonon in the CNT resonator. Due to the filter characteristics of the cavity, this Anti-Stokes scattering is strongly enhanced, while the scattering to $\omega_{\rm cav} - 2\omega_{\rm m}$, the Stokes process, is suppressed. Transitions happen at rates $\Gamma^{\pm}_{\rm opt}$ of Eq. 7.62. The noise spectrum of the upconverted photons is read out with a spectrum analyser. When the nanotube is only thermally vibrating, the microwave noise spectral density S is proportional to the displacement spectral density S_x and, due to the equipartition theorem, to the mode temperature [Teufel et al., 2011].

Fig. 7.15 displays output spectra for high (a, $P_{\rm A} = -30\,\rm dBm$) and low (b, $P_{\rm A} = -60\,\rm dBm$) antenna drive power[9]. For both measurements, the gate voltage was tuned in such a way that

[9] $P_{\rm A}$ is the output power of the frequency generator that drives the antenna.

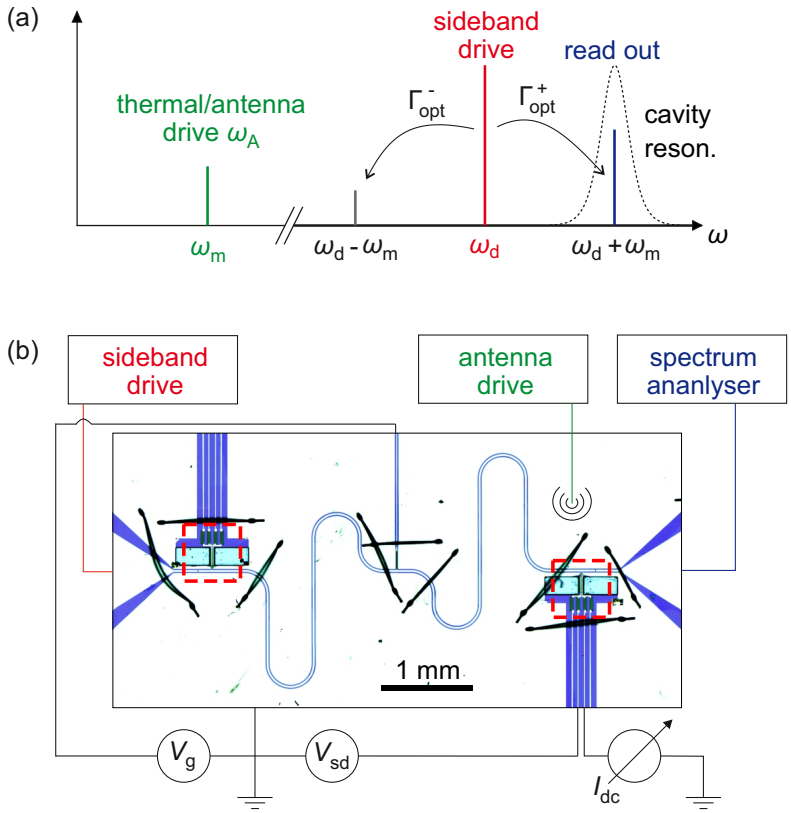

Figure 7.14.: Frequency (a) and setup (b) scheme of two-tone spectroscopy. Sideband photons are injected on the cavity input. Through optomechanical interaction with the thermal or driven motion of the mechanical resonator, they are scattered upwards in energy (to $\hbar\omega_{\mathrm{cav}}$). Detection follows on the cavity output with a spectrum analyser. Adapted from [Teufel et al., 2011] and [Blien et al., 2020].

the optomechanical coupling constant g is maximal and the drive power was $P_{\mathrm{d}} = +20\,\mathrm{dBm}$ (corresponding to $n_{\mathrm{cav}} = 2.1 \cdot 10^4$). Note that the choice of antenna power in (a) was considered a low power for the dc detection method, as here the mechanical peak was already on the verge of detectability; see Fig. 2.19. A Lorentzian was fitted to the data of (b)

$$S(\omega) = S_{\mathrm{noise}} + P_{\mathrm{up}} \cdot \frac{\kappa_{\mathrm{eff}}}{(\kappa_{\mathrm{eff}}/2)^2 + (\omega - \omega_{\mathrm{m}})^2} \,.$$

From the fit, a resonance frequency $\omega_{\mathrm{m}} = 502.54\,\mathrm{MHz}$ and a linewidth $\kappa_{\mathrm{eff}} = 7.43\,\mathrm{kHz}$ could be extracted. As $\Gamma_{\mathrm{opt}} = 65\,\mathrm{Hz} \approx 0$ for this drive power, $\kappa_{\mathrm{eff}} \approx \kappa_{\mathrm{m}}$. Thus, the linewidth is comparable to the one obtained from the OMIT fit in Sect. 7.2.2, Fig. 7.8 (b) with $Q_{\mathrm{m}} \approx 68000$. The upconverted power is $P_{\mathrm{up}} = 2.1\,\mathrm{fW}$ and the background noise density $S_{\mathrm{noise}} = 61.5\,\mathrm{fW/Hz}$. This noise can be attributed to the direct mixing of the antenna drive with the sideband signal in non-linear elements of the electronic circuit, such as, e.g., the amplifiers. Due to the stronger antenna drive in (a), the noise density is much larger.

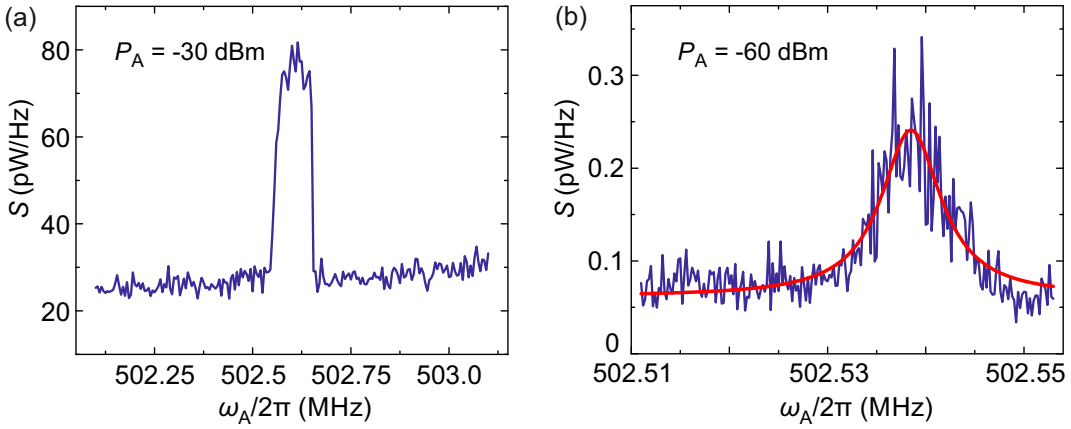

Figure 7.15.: Upconverted signal for antenna powers $P_\mathrm{A} = -30\,\mathrm{dBm}$ (a) and $P_\mathrm{A} = -60\,\mathrm{dBm}$ (b). The peak in (a) shows non-linear behaviour, whereas in (b), a Lorentzian can be fitted to extract parameters (see main text).

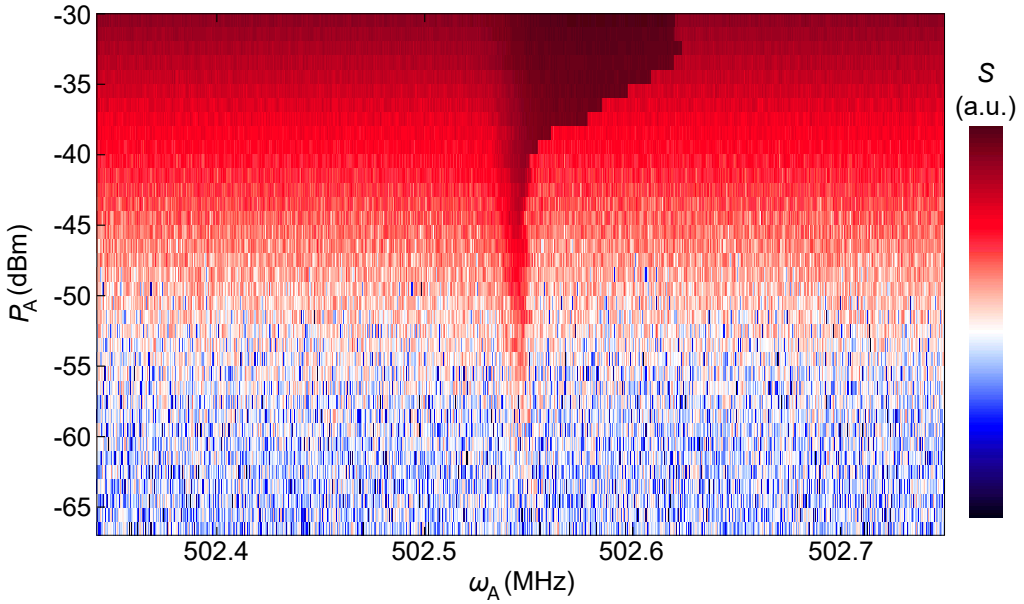

Figure 7.16.: Detectability of mechanics in dependence of antenna power P_A. A two-tone spectroscopy as described before but with varying antenna power has been used. The detected mechanical signal is nonlinear in a range $-30\,\mathrm{dBm} \lesssim P_\mathrm{A} \lesssim -45\,\mathrm{dBm}$ and linear in a range $-45\,\mathrm{dBm} \lesssim P_\mathrm{A} \lesssim -60\,\mathrm{dBm}$. Below a power of $P_\mathrm{A} \approx -60\,\mathrm{dBm}$, the signal is no longer observable with the setup of this thesis.

The objective was to detect the thermal vibration of the nanotube. To do so, the antenna power was decreased further and further, while trying to maintain a detectable output signal; see 7.16.

Note in Fig. 7.15 (b), the lowest possible power that produced a signal was used. Heating up the device to temperatures up to 1 K led to no improvement. Thermal vibrations of the CNT could not be detected with the setup used in this thesis.

The combined system was also tested for optomechanical downconversion. Here, the drive frequency is blue detuned from the cavity resonance $\omega_\mathrm{d} = \omega_\mathrm{cav} + \omega_\mathrm{m}$. A photon enters the cavity by generating a phonon in the nanotube resonator, leading to amplification of the motion. Although not as reproducible as with upconversion, Fig. 7.17 shows downconversion peaks for different antenna drive powers. A large and linearly rising background probably masks part of the signal. As the antenna power is decreased, the peak sharpens but is barely visible for $P_\mathrm{A} = -40\,\mathrm{dBm}$. It should in principle be easier to detect a mechanical signal with optomechanical

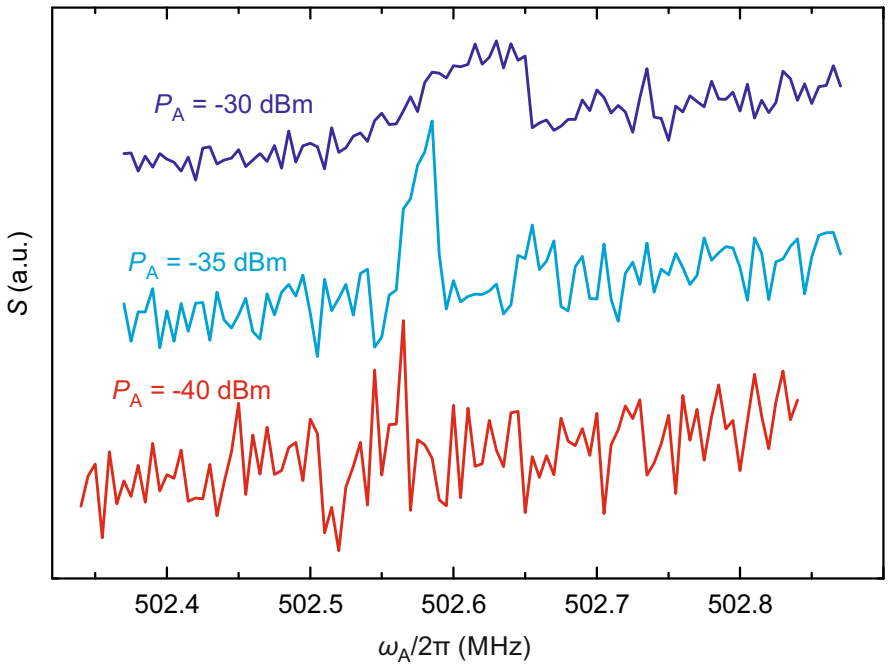

Figure 7.17.: Downconverted power spectrum for different antenna powers. The drive power was set to $P_\mathrm{d} = +20\,\mathrm{dBm}$ and the measurement bandwidth was 5 Hz. The mechanics is reflected in a peak at $\omega_\mathrm{A} \approx 502.55\,\mathrm{MHz}$ that becomes sharper with decreasing antenna power.

downconversion without the use of an antenna: the mechanical signal is enhanced evoking sharp peaks that are large in amplitude, as e.g. in [Singh et al., 2014a]. However, the (negative) optomechanical damping rate, and therefore $n_{m,\mathrm{eff}}$, is small in our case ($\Gamma_\mathrm{opt} = -4g^2/\kappa_\mathrm{cav} \approx -2\pi \cdot 65\,\mathrm{Hz}$, see previous section). This and the large background noise could be reasons why no signal could be detected even for high drive powers, when switching off the antenna drive.

Red sideband upconversion was further examined for its gate voltage dependence as has been done for the OMIT experiment (see Sect. 7.2.3). In Fig. 7.18, this is shown for the voltage range of the Coulomb oscillation that was used throughout this thesis (upconversion at an adjacent Coulomb oscillation is shown in Sect. C.4 displaying similar behaviour). In (a), a low antenna

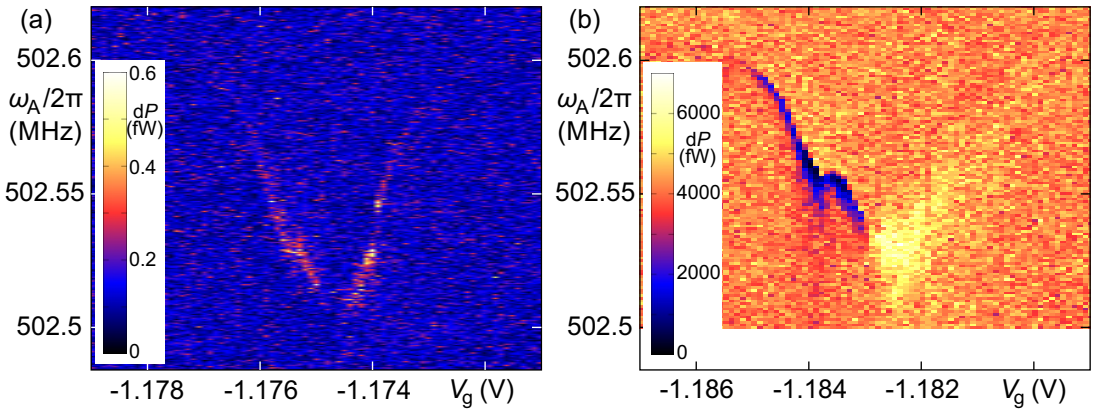

Figure 7.18.: Gate voltage dependence of upconverted signal over one Coulomb oscillation. (a) shows the noise spectrum for zero bias and an antenna power of $P_\mathrm{A} = -55\,\mathrm{dBm}$. At the flanks of the Coulomb peak, the upconverted signal is most prominent. In (b), a larger power $P_\mathrm{A} = -30\,\mathrm{dBm}$ and additionally a bias voltage $V_\mathrm{sd} = 0.5\,\mathrm{mV}$ was applied. The upconverted signal transforms into dips for parts of the gate voltage range. In both measurements, the drive power was $P_\mathrm{d} = +20\,\mathrm{dBm}$. Note again the difference in the gate voltage range due to drifts over measurement time Adapted from [Blien et al., 2020].

power of $P_\mathrm{A} = -55\,\mathrm{dBm}$ was applied. The upconverted signal shows in principle the same behaviour as the OMIT feature of Sect. 7.2.3, with the decrease of the mechanical resonance frequency due to backaction of the single electron tunneling on the mechanics and the enhanced optomechanical coupling on the flanks of the Coulomb peak. In (b), the antenna power was set to a higher level of $P_\mathrm{A} = -30\,\mathrm{dBm}$. This leads to a larger background signal, that for the left half of the Coulomb peak ($V_\mathrm{g} \leq -1.183\,\mathrm{V}$) leads to destructive interference (dips in the signal) emerging from a phase shift of the upconverted photons. Additionally, a bias voltage of $V_\mathrm{sd} = 0.5\,\mathrm{mV}$ has been applied to the CNT, resulting in a broadening of the overall feature along the gate axis due to broadening of the Coulomb oscillation. The upconversion peaks on the right half ($V_\mathrm{g} \approx -1.182\,\mathrm{V}$) are also broader in linewidth. The features in (b) show that further measurements and analysis would be highly worthwhile. For example, a finite dc bias could be used to study the impact of a current on the mechanics, allowing for the investigation of energy transfer.

7.3.3. Future improvements and compromises

This final chapter reflects about how to improve both the device and the measurement system concerning optomechanical motion manipulation and detection of thermally driven mechanics.

First, the single-photon coupling strength g_0 will be discussed considering Eq. 7.51

$$g_0 \approx \frac{\omega_{\mathrm{cav}}}{2C_{\mathrm{RLC}}} \frac{\partial C_{\mathrm{eff}}}{\partial x} x_{\mathrm{zpf}}$$

and Eq. 7.54

$$\frac{\partial C_{\mathrm{eff}}}{\partial x} = e\alpha_{\mathrm{g}} \frac{\partial^2 \langle N \rangle}{\partial V_{\mathrm{g}}^2} \frac{V_{\mathrm{g}}}{C_{\mathrm{g}}} \frac{\partial C_{\mathrm{g}}}{\partial x} = \eta \frac{\partial C_{\mathrm{g}}}{\partial x} \ :$$

- Decreasing C_{CPW}, respectively C_{RLC}, directly increases g_0, but also the cavity frequency ω_{cav}. The benefit of larger coupling will probably overcome the drawback of generally larger losses in cables and rf elements at higher frequencies. Furthermore, quarter wave resonators [Li et al., 2013] could be used as these have only half the waveguide capacitance as half wave resonators for the same ω_{cav}. Alternatively, it is possible to employ high impedance resonators [Stockklauser et al., 2017]. These might not have ideal waveguide characteristics (due to a differing characteristic impedance Z_0) but can come with the comfort of smaller capacitance C_{CPW}. Generally, adapting the waveguide geometry and modelling its electromagnetic design with commercially available software might be an easy to implement improvement.

- In addition to the point above, also varying the inductive part of the resonator might be beneficial. For instance, the implementation of a SQUID into the resonator geometry makes for a frequency- and impedance-tunable cavity [Stockklauser et al., 2017] with adjustable coupling strength and sideband resolution up to a certain extent.

- Increasing $\partial^2 \langle N \rangle / \partial V_{\mathrm{g}}^2$ increases $\partial C_{\mathrm{eff}} / \partial x$. Selecting sharper Coulomb oscillations increases the coupling; however, the tunnel rate Γ_{broad} has to remain much larger than ω_{cav}, so that the separation of time scales is a good approximation. In addition, with sharper Coulomb oscillations keeping a constant working point is more difficult (e.g. due to fluctuating or drifting gate voltage).

- Increasing V_{g} should in principle also increase the gate coupling. Usually, however, Coulomb oscillations tend to broaden at larger $|V_{\mathrm{g}}|$, decreasing $\partial^2 \langle N \rangle / \partial V_{\mathrm{g}}^2$. This is because with larger gate voltage, the quantum dot spatially expands resulting in smaller tunnel barriers.

- Increasing $\alpha_{\mathrm{g}}(\partial C_{\mathrm{g}}/\partial x)/C_{\mathrm{g}} = (\partial C_{\mathrm{g}}/\partial x)/C_{\Sigma}$ can be accomplished by decreasing the CNT-to-gate distance, which remains an issue of fabrication. The nanotube length L does not affect this quotient much.

- Increasing x_{zpf} increases g_0. In the case of a beam resonator (Eq. 2.24), this could be obtained by making the lead contact distance larger, leading to longer nanotubes. The mass m of the nanotube increases slower with its length than its resonance frequency ω_{m}

decreases, so that $x_{\mathrm{zpf}} = \sqrt{\hbar/2m\omega_{\mathrm{m}}}$ would increase. However, in the case of a string resonator(Eq. 2.25) x_{zpf} is independent of the CNT length. In any event, $\omega_{\mathrm{m}} \gg \kappa_{\mathrm{cav}}$ has to be fulfilled to remain in the sideband resolved regime.

- Similarly, if it was possible to prevent or reduce the fabrication based built-in tension of the nanotube, ω_{m} could be decreased. The same device geometry but with enhanced x_{zpf} would then be feasible.

The optomechanical coupling strength g can additionally be boosted by raising the number of photons n_{cav} in the cavity. Regarding Eq. 7.18

$$n_{\mathrm{cav}} = |\langle \hat{a} \rangle|^2 = \frac{\kappa_{\mathrm{c}}}{\Delta^2 + (\kappa_{\mathrm{cav}}/2)^2} \frac{P_{\mathrm{in}}}{\hbar\omega_{\mathrm{L}}} ,$$

there are several ways:

- A first and obvious way is to increase the power on the cavity input P_{in}. While the maximum range of the generators used in this thesis has been exploited, it is still possible to decrease the attenuation along the signal input path by rearranging the attenuators. However, larger field amplitudes leads again to Coulomb resonance broadening and therefore smaller g_0, as explained above.

- As with sideband driving $\Delta = -\omega_{\mathrm{m}}$ holds, it would be again convenient to reduce ω_{m}. Since then the drive frequency shifts closer to the cavity resonance, n_{cav} is increased automatically.

- Decreasing the internal decay rate κ_{i} of course increases n_{cav}, because less power is dissipated or lost in the cavity. This could for example be accomplished by making shorter contacts with less overlap with the gate electrode. This diminishes signal outcoupling by decreasing C_{elec}. Then, smaller forks for a more directed nanotube transfer would be beneficial. Another option would be to increase the lead electrode spacing, so the distance to the gate electrode becomes larger. This has however additional effects on ω_{m} as discussed before.

- Regarding the first factor of above equation, for a given κ_{i}, a larger coupling rate κ_{c} decreases the pump power necessary to achieve a certain n_{cav}. In fact, κ_{c} can be adjusted with the geometry of the coupling capacitors and has an optimum value[10] of $\sqrt{4\Delta^2 + \kappa_{\mathrm{i}}^2}$. However, this is not an experimentally favourable value as with red sideband driving ($\Delta = -\omega_{\mathrm{m}}$), the optimum would be $\kappa_{\mathrm{c}} \approx 2\omega_{\mathrm{m}}$, strongly violating the resolved sideband condition.

Concerning the last point, it is better to additionally consider Eq. 7.66

$$\Gamma_{\mathrm{opt}} = \frac{4g^2}{\kappa_{\mathrm{cav}}} = 4g_0^2 \frac{n_{\mathrm{cav}}}{\kappa_{\mathrm{cav}}} .$$

[10] In the case of resonant driving $\Delta = 0$, this corresponds to the critically coupled regime $\kappa_{\mathrm{c}} = \kappa_{\mathrm{i}}$ of Sect. 4.4.3.

For a given n_{cav}, a smaller κ_{cav} (or κ_{c} accordingly) improves the cooling power, but also increases the drive power necessary to obtain that n_{cav}. The drive power can however be controlled by the microwave sources during the experiment.

From the last two paragraphs it seems favourable to decrease ω_{m}. In practice however, this is not always the case. When ω_{m} becomes comparable to κ_{cav}, Eq. 7.66 does not hold anymore. From the full equation (Eq. 7.62), it is obvious that $\Gamma_{\mathrm{opt}}^{+}$ then becomes comparable to $\Gamma_{\mathrm{opt}}^{-}$, diminishing the cooling rate. In the level diagram of Fig. 7.12, sideband suppression is decreased, as neighbouring states start to overlap favouring unwanted transitions.

The lower phonon limit that can be reached by radiation pressure cooling is given by Eq. 7.65. Again, it can be concluded that a larger ω_{m} and smaller κ_{cav} are beneficial, as they lead to smaller theoretical occupation numbers.

Clearly, changing individual parameters can have effects on others, as discussed above. The most promising adjustments concerning sideband cooling for the system of this thesis would be to rearrange the attenuators in the signal input path, increasing n_{cav}, and alter the lead contact geometry, decreasing κ_{i}.

Additionally to the parameter optimisation, provisions concerning measurement system improvement can be implemented:

- Regarding thermal vibration detection, the use of Josephson parametric amplifiers located near the device would be beneficial, as they are able to decrease the noise by several orders of magnitude accounting for quantum limited detection [Teufel et al., 2011].
- For similar reason, low temperature high-frequency amplifiers with smaller bandwidth and therefore lower noise temperature could be installed.
- The voltage potential of the dc gate could be stabilised by using gate oxides that are not susceptible for accumulating charges. Also, using low-drift and low-noise voltage sources can improve this circumstance [Moser et al., 2014].
- The phase stability of the setup could be further enhanced by the implementation of phase-stabilised cables, vibration damping of the cryostat mounting, and an optimised stabilisation of device temperature inside the cryostat.

8

Conclusion and Outlook

The work presented in this thesis illustrates a first step in the direction of optomechanical experiments making use of single electron effects. For this purpose, a particular cavity has been designed and developed: a superconducting microwave coplanar waveguide resonator with a nanotube fork transfer compatible electrode structure accounts for the "optical" part of the system. The quantum dot nature of the mechanical part, a carbon nanotube, leads to an inherently present quantum capacitance altering the coupling between the two subsystems. It is enhanced by orders of magnitudes compared to the pure geometric coupling. On the other hand, via a gate voltage the interaction is also tunable, from a maximum value to vanishing coupling. A theoretical model was presented which is able to explain these features. Data was acquired using an optomechanically induced transparency experiment [Weis et al., 2010]. The overall well agreement between model and data shows its validity [Blien et al., 2020]. Error sources, leading to deviations, have been discussed within this scope.

Starting from the build-up of the microwave measurement setup in a dilution refrigerator environment, the project presented within this thesis yielded first results with the demonstration of superconducting coplanar waveguide resonators. In particular, an alloy of rhenium and molybdenum has been extensively investigated in regard to high frequency characteristics [Götz et al., 2016]. The suitability of this alloy in CPW devices combined with an on-chip carbon nanotube overgrowth technique has been shown [Blien et al., 2016].

For reasons of fabrication optimisation and predictability, a CNT fork transfer technique was implemented [Blien et al., 2018] allowing to separate the growth process from the electrode chip. With this it became possible to use niobium coplanar resonators increasing the "optical" quality factor.

Having undergone much structural refinement, a hybrid nanotube-cavity device that displayed coupling of clean CNT electronics to the cavity mode as presented in Sect. 6.2.1 could be fabricated. Using a dc detection technique [Hüttel et al., 2009], the mechanical activity of the CNT could be proven and its resonance frequency could be identified. Here, the mechanical frequency was unexpectedly large, however bringing the combined device in the so called good cavity regime ($\kappa_{\mathrm{cav}} \ll \omega_{\mathrm{m}}$). With this, optomechanical experiments in the dispersive coupling regime as presented in Sect. 7.2 and 7.3 could be followed [Blien et al., 2020].

Parallel to the time consuming device optimisation a theoretical description of the optomechanical interaction enhancement has been established prior to the experiment. It is based on the effective capacitance of single electron devices [Duty et al., 2005], optomechanical parameter description in the microwave domain [Aspelmeyer et al., 2014], and the model of the conduc-

tance of a quantum dot in the lifetime broadened regime [Meerwaldt et al., 2012]. First estimations using earlier CNT and cavity experimental data revealed a coupling enhancement of $10^4 - 10^5$, which could later be experimentally proven [Blien et al., 2020].

Future and planned development comprises the subsequent measures. On the cavity side, the refinement of the coplanar waveguide concerning quality factor optimisation and nanotube transfer structure. Here, the help of electromagnetic simulation software and finite element modelling is of particular interest. Then, setup optimisation which can be accomplished already by rearranging the attenuators of the high frequency input. Larger cavity amplitudes increase the optomechanical coupling. In a next step, better amplifiers might be used to reduce measurement noise. Moreover, adjustments in the CVD parameters of the carbon nanotube growth process could lead to individual SWCNTs with cleaner electronic structure and larger mechanical quality factors. Also, customized forks could lead to better control in the growth process and a refined cavity structure. For still more sophisticated device parameter optimisation it is referred to Sect. 7.3.3, where this topic is explained in greater detail.

With these improvements, interesting experiments are at hand. Large enough couplings ($g > \kappa_{\mathrm{cav}}, \kappa_{\mathrm{m}}$) will bring the system into the strong coupling regime. Here, mechanical and cavity mode hybridise leading to optomechanical normal mode splitting in their energy spectra. Carbon nanotubes have reached quality factors of up to five million [Moser et al., 2014], allowing for a mechanical linewidth decrease of at least one order of magnitude ($\kappa_{\mathrm{m}} \sim 500\,\mathrm{Hz}$). Further, the cavity resonator used in this experiment had an unusually small Q factor. Earlier devices showed up to $Q \sim 10^5$ corresponding to $\kappa_{\mathrm{cav}} \sim 57\,\mathrm{kHz}$. The coupling parameter presented in this thesis already reaches $g \sim 25\,\mathrm{kHz}$, however with a moderate photon number of $n_{\mathrm{cav}} = 67500$. Increasing n_{cav} by a factor 10-100 should be easily accomplishable by revising the measurement setup. The strong coupling regime will therefore be feasible in the near future.

Two-tone spectroscopy, as presented in Sect. 7.3, might be able to resolve the thermal vibration of the carbon nanotube in the absence of resonant driving. In a next step, motion manipulation could be pursued: depending on the detuning, the vibration of the CNT can be further cooled or coherently driven. Ground state cooling and the detection of zero point fluctuations could be realised [Teufel et al., 2011]. On the other hand, coherent driving can lead to self-induced oscillations or mechanical lasing [Wen et al., 2019].

A closely related implementation is the analysis of the influence of dc current on the vibration mode. This is also directly available as it is easy to apply a bias voltage in this particular device structure. Studying the energy flow allows for the revelation of cooling or heating of the vibration by (single) electrons. Further, the impact of higher order transport processes - such as cotunneling or the Kondo effect - on the vibration could be taken into account [Götz et al., 2018].

Abovementioned ideas all make use of the resolved sideband or good cavity regime. But also in the bad cavity regime, where $\omega_{\mathrm{m}} < \kappa_{\mathrm{cav}}$, interesting approaches arise. The vibration detection could be handled in single-shot or realtime measurements due to a large "optical" bandwidth. Time-resolved mechanical frequency spectra and the decay of vibration could be captured; see [Barnard et al., 2019] for an optical implementation. Also, a larger number of motional sidebands may be covered in the cavity linewidth. Then, one resonant photon is able to create more

than one phonon before decaying, leading to larger motional amplification [Aspelmeyer et al., 2014]. This regime can be reached with long carbon nanotubes ($\omega_{\mathrm{m}} \sim 2\pi \cdot 10\,\mathrm{MHz}$) and large external couplings of the microwave resonator ($\kappa_{\mathrm{cav}} \sim 2\pi \cdot 100\,\mathrm{MHz}$).

A complementing field could be optomechanics in the dissipative coupling regime [Aspelmeyer et al., 2014]. Here, the interaction originates in the position dependency of the cavity dissipation rate $\kappa_{\mathrm{cav}}(x)$, leading to a different interaction Hamiltonian. Many of the above described experiments and effects are modified, e.g. it is no longer a necessity to be in the good cavity regime to achieve ground state cooling [Elste et al., 2009]. In a dissipatively coupled optomechanical setup, the microwave signal of the cavity has to be conducted through the carbon nanotube. As has been shown in the Master thesis of P. Brunner [Brunner, 2016], so called impedance matching devices or stub tuners are a suitable starting point for these kind of experiments.

Technological applications could adopt the controllable coupling strength. Its gate voltage dependence allows for easily switching the interaction with microwaves on and off.

The fact that carbon nanotubes as mechanical resonators couple to different electromagnetic frequency ranges - optical light as well as microwaves - makes quantum switchboards or transducers realisable [Fan et al., 2018]. Here, quantum mechanical states can be transferred in the frequency domain. This is of particular interest as microwave photons are used in quantum logic but the corresponding quantum states are not easily transmitted at these frequencies, due to attenuation and thermal noise at room temperature. The conversion to optical frequencies reduces decoherence and dissipation. Therefore, optical photons are ideal carriers of information in quantum communication. This makes a transducer, that coherently translates between quantum operation and communication, necessary and attractive.

In addition, mechanical resonators can also be used for storing quantum information in optical communication networks. Pulsed optical driving schemes have been used to write and retrieve the information from a mechanical excitation, that is able to preserve quantum states due to a long decay time [Fiore et al., 2011]. This can also be done (continuously driven) in the microwave domain with a voltage based switching of the coupling of the quantum logic to the mechanical storage. Again, the transducer characteristics then allow for the state transfer to the optical communication domain.

A

Device Parameters

The following table A.1 presents an overview of names, symbols, and values of the important optomechanical device parameters. Where applicable, the origin is stated as the section number where the quantity has been introduced and according data have been presented. If the quantity is derived from other parameters, the used formula is given.

Parameter	Origin	Symbol	Value
"Optical" cavity			
Resonance frequency	Sect. 6.2	ω_{cav}	$2\pi \cdot 5.74005\,\mathrm{GHz}$
Linewidth	ω_{cav}/Q	κ_{cav}	$2\pi \cdot 11.6\,\mathrm{MHz}$
Quality factor	Sect. 6.2	Q_{c}	497
Capacitance	Sect. 7.2.1	C_{RLC}	875 fF
Mechanical resonator			
Resonance frequency	Sec. 2.4.3	ω_{m}	$2\pi \cdot 502.5\,\mathrm{MHz}$
Line width	Sec. 2.4.3	κ_{m}	$\sim 2\pi \cdot 50\,\mathrm{kHz}$
Quality factor	$\omega_{\mathrm{m}}/\kappa_{\mathrm{m}}$	Q_{m}	$\sim 10^4$
Thermal occ. (10 mK)	$k_{\mathrm{B}}T/\hbar\omega_{\mathrm{m}}$	n_{m}	0.41
Nanotube length	Lead contact distance	L	$1\,\mu\mathrm{m}$
Effective electronic length	Sect. 7.2.1	L_{eff}	143 nm
Nanotube radius	Estimation	R	2 nm
Effective mass	$2\pi RL\rho_{\mathrm{graphene}}/2$	m	$4.8 \cdot 10^{-21}\,\mathrm{kg}$
Coupling			
Zero-point motion amplitude	$\sqrt{\hbar/2m\omega_{\mathrm{m}}}$	x_{zpf}	1.9 pm
Distance to gate / ground	Device parameter	d	450 nm
Dielectric constant	$(\epsilon_{\mathrm{r}}^{\mathrm{vacuum}} + \epsilon_{\mathrm{r}}^{\mathrm{PMMA}})/2$	ϵ_{r}	2
Geometric capacitance to gate / ground	Sect. 7.2.1	C_{g}	2.6 aF
Geometric gate coupling	Sect. 7.2.1	$\partial C_{\mathrm{g}}/\partial x$	$0.95\,\frac{\mathrm{pF}}{\mathrm{m}}$
Optomechanical parameters ($n_{\mathrm{cav}} = 67500$)			(for optimal V_{g})
Side band resolution	$\omega_{\mathrm{m}}/\kappa_{\mathrm{cav}}$		43.5
Geometric single-photon coupling	Sect. 7.2.1	g_0	$2\pi \cdot 2.9\,\mathrm{mHz}$
Max. quantum capacitance enh. single-photon coupling	Sect. 7.2.3	g_0	$2\pi \cdot 95\,\mathrm{Hz}$
Optomechanical coupling	$g_0\sqrt{n_{\mathrm{cav}}}$	g	$2\pi \cdot 24.7\,\mathrm{kHz}$
Cavity pull-in parameter	g_0/x_{zpf}	G	$2\pi \cdot 51\,\frac{\mathrm{Hz}}{\mathrm{pm}}$
Dispersive coupling	$g_0/\kappa_{\mathrm{cav}}$	$\tilde{A}$	$8.2 \cdot 10^{-6}$
Maximal sideband cooling rate	$4n_{\mathrm{cav}}g_0^2/\kappa_{\mathrm{cav}}$	Γ_{opt}	$2\pi \cdot 211\,\mathrm{Hz}$
Cooperativity	$\Gamma_{\mathrm{opt}}/\kappa_{\mathrm{m}}$	C	$4.2 \cdot 10^{-3}$
Cooling power	$\Gamma_{\mathrm{opt}}\hbar\omega_{\mathrm{m}}$	$\dot{Q}$	$4.4 \cdot 10^{-22}\,\mathrm{W}$

Table A.1.: Overview of the parameters of the optomechanical system

B

Additional calculations of CPW device parameters

B.1. Effective permittivity ϵ_{eff} of Si/SiO_2-substrate

Using Eqs. 4.19 and 4.25,

$$\epsilon'_{\text{eff}} = 1 + \frac{\epsilon_{r1} - 1}{2} \frac{K(k_1)}{K(k'_1)} \frac{K(k'_0)}{K(k_0)} + \frac{\epsilon_{r2} - \epsilon_{r1}}{2} \frac{K(k_2)}{K(k'_2)} \frac{K(k'_0)}{K(k_0)} ,$$

and the definitions of $K(k_i)$, k_i, and k'_i (Eqs. 4.13-4.16), the effective permittivity of a double-layer substrate can be calculated. Our metal films are deposited on a Si substrate ($h_1 = 500\,\mu\text{m}$, $\epsilon_{r1} = 11.7$) that is capped with a layer of SiO_2 ($h_2 = 500\,\text{nm}$, $\epsilon_{r2} = 3.78$) on top. With a waveguide central conductor width $s = 20\,\mu\text{m}$ and a gap width $w = 12\,\mu\text{m}$, an effective permittivity of

$$\epsilon'_{\text{eff}} = 6.35$$

can be calculated.

B.2. Characteristic waveguide impedance Z_0

With the effective permittivity of our substrate and device geometry, the waveguide characteristic impedance can be determined with the help of Eq. 4.26,

$$Z_0 = \frac{1}{4\epsilon_0 c \sqrt{\epsilon'_{\text{eff}}}} \frac{K(k'_0)}{K(k_0)} = 50.4\,\Omega\,.$$

which is close to the characteristic impedance of $Z_0 = 50\,\Omega$ of the surrounding electronics and cabling.

B.3. Waveguide Capacitance

Furthermore, the waveguide capacitance (per unit length) can be calculated with Eq. 4.20,

$$C_{\text{CPW}} = 4\epsilon_0 \epsilon'_{\text{eff}} \frac{K(k_0)}{K(k'_0)} = 167\,\text{pF/m}\,.$$

With a resonator length of $l = 10.5\,\text{mm}$ follows a total waveguide capacitance of

$$C_{\text{CPW}} = 1.75\,\text{pF}\,.$$

C

Additional data of resonator/quantum dot coupling experiments

C.1. Coulomb resonance broadening with intracavity power on electron conduction side

The Coulomb resonance broadening with increasing intracavity power, as already presented in Fig. 6.9, has been repeated for a gate voltage range on the electron conduction side; see Fig. C.1. Again, the cavity was driven on resonance, the current through the CNT was measured while sweeping the gate voltage. After every sweep, the cavity input power has been increased. The same reasoning as in 6.2.1 holds: increasing power inside the cavity leads to an additional contribution δV_{ac} to the gate voltage, effectively broadening the resonance.

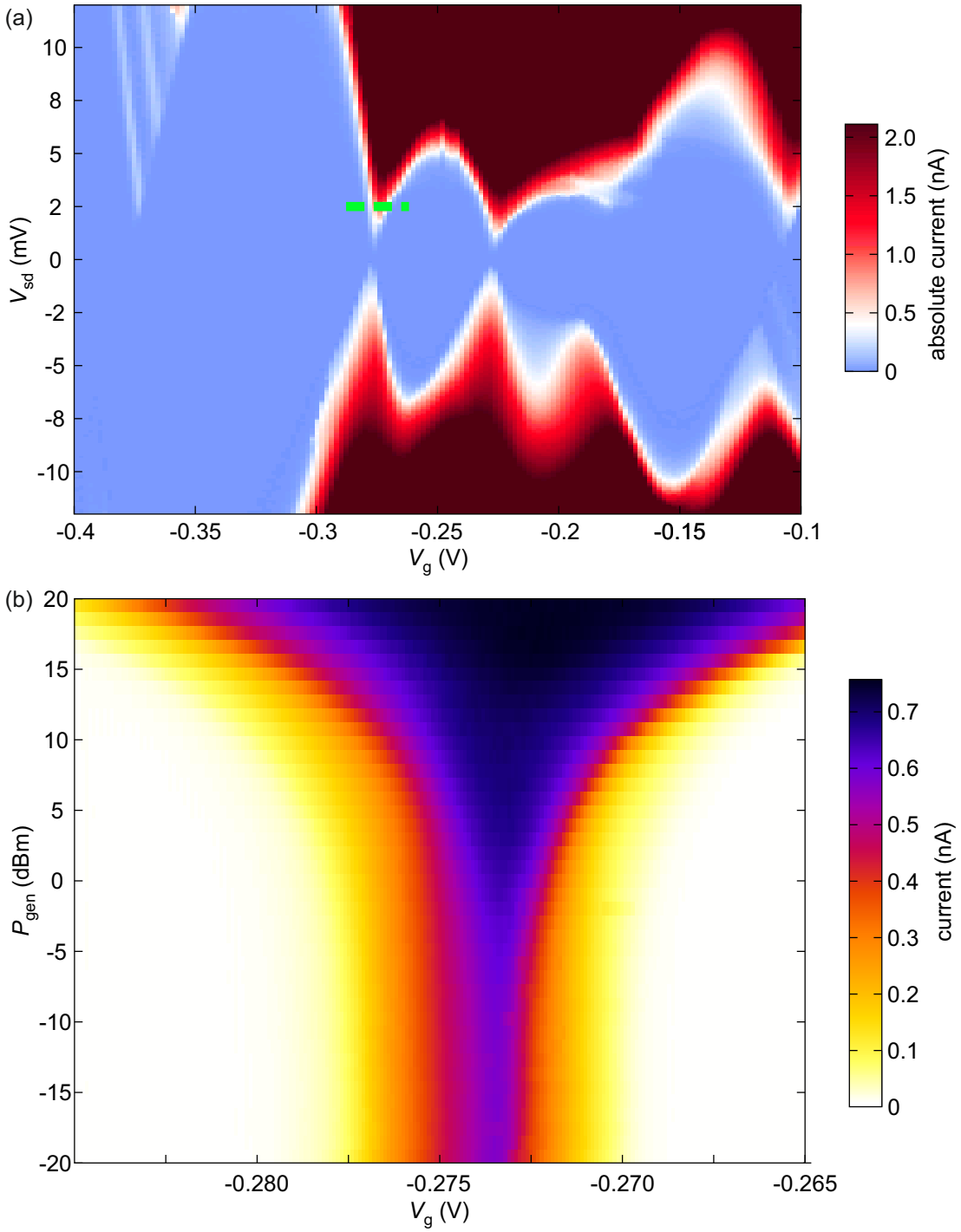

Figure C.1.: Coulomb resonance broadening on electron conduction side. (a) Corresponding stability diagram and Coulomb resonance in the carbon nanotube current. (b) Broadening of the Coulomb resonance (green dashed line in (a)) with rising intracavity power fixed at cavity resonance ω_{cav}.

C.2. Asymmetric lead coupling

Here, it is shown why the resonator phase and amplitude experience only seem to respond at a single slope of the Coulomb diamonds in the case of asymmetric lead coupling; see also [Meerwaldt et al., 2012] for a similar discussion about the intensity of CNT electromechanical backaction. As has been shown in Sect. 2.3.4, the tunnel rates can be modelled with (Eqs. 2.13 and 2.14)

$$\Gamma_s^+ = a_s \int_{-\infty}^{\mu_\mathrm{s}} \mathrm{DOS}(\mu)\,\mathrm{d}\mu \quad , \quad \Gamma_d^+ = a_d \int_{-\infty}^{\mu_\mathrm{d}} \mathrm{DOS}(\mu)\,\mathrm{d}\mu$$

and

$$\Gamma_s^- = a_s \int_{\mu_\mathrm{s}}^{\infty} \mathrm{DOS}(\mu)\,\mathrm{d}\mu \quad , \quad \Gamma_d^- = a_d \int_{\mu_\mathrm{d}}^{\infty} \mathrm{DOS}(\mu)\,\mathrm{d}\mu\,.$$

The average number of charges on the QD is then (Eq. 2.15)

$$\langle N \rangle = N_0 + \frac{\Gamma^+}{\Gamma^+ + \Gamma^-}\,,$$

where $\Gamma^\pm = \Gamma_s^\pm + \Gamma_d^\pm$.

As distinct from the simplified model in Sect. 2.3.4, now the tunnel rates shall be asymmetric. This is done by considering different prefactors $a_\mathrm{s} \neq a_\mathrm{d}$. Additionally, a bias voltage V_sd shall be applied so that $\mu_\mathrm{s} = \mu_\mathrm{d} + eV_\mathrm{sd}$. Applying the lifetime broadened regime, the density of states on the QD can be modelled as (Eq. 2.11)

$$\mathrm{DOS}(\mu) = \frac{1}{2\pi} \frac{\hbar\Gamma_\mathrm{broad}}{(\mu - \mu_\mathrm{CNT})^2 + \left(\frac{\hbar\Gamma_\mathrm{broad}}{2}\right)^2}\,.$$

Then the average charge on the QD can be calculated qualitatively as

$$\begin{aligned}
&\langle N \rangle \sim \Gamma_\mathrm{s}^+ + \Gamma_\mathrm{d}^+ = \\
&= a_\mathrm{s} \int_{-\infty}^{\mu + eV_\mathrm{sd}/2} \frac{1}{2\pi} \frac{\hbar\Gamma_\mathrm{broad}}{(\mu' - \mu_\mathrm{CNT})^2 + \left(\frac{\hbar\Gamma_\mathrm{broad}}{2}\right)^2} \mathrm{d}\mu' \\
&+ a_\mathrm{d} \int_{-\infty}^{\mu - eV_\mathrm{sd}/2} \frac{1}{2\pi} \frac{\hbar\Gamma_\mathrm{broad}}{(\mu' - \mu_\mathrm{CNT})^2 + \left(\frac{\hbar\Gamma_\mathrm{broad}}{2}\right)^2} \mathrm{d}\mu' \\
&= \frac{a_\mathrm{s} + a_\mathrm{d}}{2} + \frac{a_\mathrm{s}}{\pi} \cdot \arctan\left(\frac{2(\mu - \mu_\mathrm{CNT}) + eV_\mathrm{sd}}{\hbar\Gamma_\mathrm{broad}}\right) + \frac{a_\mathrm{d}}{\pi} \cdot \arctan\left(\frac{2(\mu - \mu_\mathrm{CNT}) - eV_\mathrm{sd}}{\hbar\Gamma_\mathrm{broad}}\right)\,.
\end{aligned}$$

For asymmetric tunnel rates characterised by prefactors $a_\mathrm{d} = 5a_\mathrm{s}$, the average charge and its first derivative with respect to V_g in dependence of the gate voltage are depicted in Fig. C.2 for a specific bias voltage according to the formula above. As can be seen in the inset of (b), V_gl and V_gr denote the gate voltages corresponding to the left and right edge of the Coulomb diamond; they depend on the applied gate bias voltage V_sd and the gate conversion factor α_g. For $V_\mathrm{g} = V_\mathrm{gl}$, the QD level of the CNT is aligned with the Fermi edge of the source electrode;

see inset of (a). Tunneling is allowed, but due to the unequal tunnel rates, tunneling onto the QD is suppressed, as tunneling off the QD is enhanced. Therefore, for $V_{\mathrm{gl}} \lesssim V_{\mathrm{g}} \lesssim V_{\mathrm{gr}}$ the average number of charges on the quantum dot is $N_0 + \delta$ with $\delta < 0.5$; see Fig. C.2 (a). For $V_{\mathrm{g}} > V_{\mathrm{gr}}$ the average number of charges is fixed again at $\langle N \rangle = N_0 + 1$. The transition at V_{gr} is steeper than at V_{gl}, leading to a larger $\partial \langle N \rangle / \partial V_{\mathrm{g}}$. As the phase shift of the cavity is proportional to this value, it is larger for the gate voltage corresponding to the alignment of the QD level and lead chemical potential with smaller tunnel barrier, i.e. larger tunnel rate.

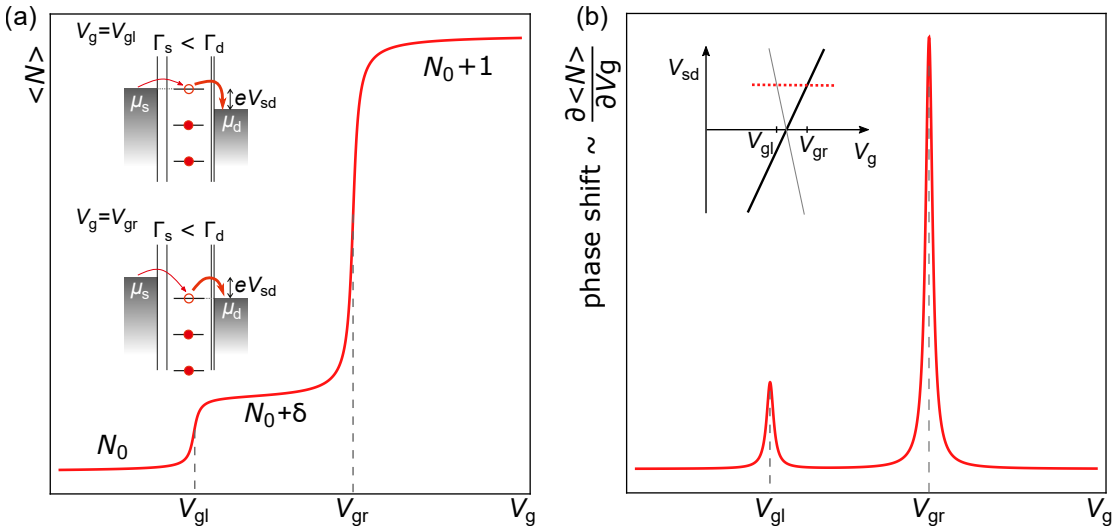

Figure C.2.: Average charge (a) and first derivative (b) in dependence of gate voltage for asymmetric tunnel rates with $a_{\mathrm{d}} = 5a_{\mathrm{s}}$. In the inset of (a), the QD ladder diagrams corresponding to the gate voltages V_{gl} and V_{gl} is shown; the inset of (b) displays the phase shift trace in the corresponding Coulomb diamond. The phase shift ($\sim \partial \langle N \rangle / \partial V_{\mathrm{g}}$) is larger for the Coulomb diamond edge corresponding to the larger tunnel barrier.

C.3. Stability diagram in cavity phase on hole conduction side

In Fig. C.3, the stability diagram of the CNT quantum dot for a lower gate voltage range but otherwise same parameters (bias voltage, generator power) as in Fig. 6.13 is shown. Again, only single edges of the Coulomb diamonds are visible due to asymmetric tunnel barriers as explained in Sect. C.2. Here however, the skew of this single line changes over the presented gate voltage range from one direction (green arrows) to the other (yellow arrows). Due to symmetry considerations, this could be attributed to the transition from hole conduction to electron conduction regime. Correspondingly, the bandgap would be situated in a gate voltage range $-0.58\,\mathrm{V} \leq V_{\mathrm{g}} \leq -0.38\,\mathrm{V}$ which would imply a small bandgap carbon nanotube.

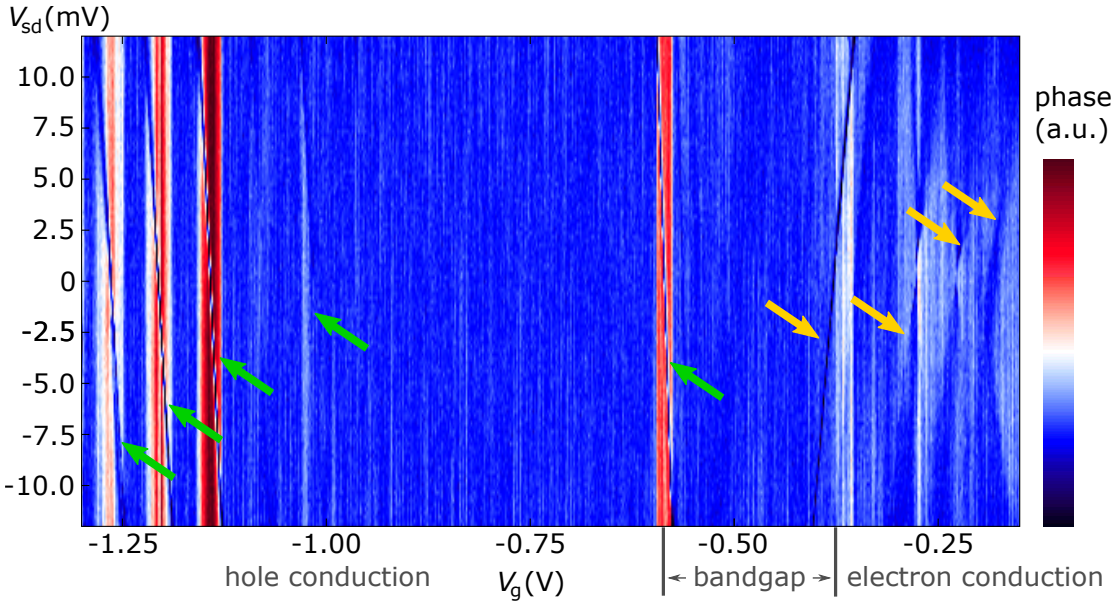

Figure C.3.: Stability diagram in the cavity phase. Only single edges of the Coulomb diamonds are visible because of asymmetric lead coupling. For gate voltages $V_g \leq -0.58\,\mathrm{V}$, these edges are skewed to one direction (green arrows), while for gate voltage $V_g \geq -0.38\,\mathrm{V}$, they are skewed to the other direction (yellow arrows). A background has been subtracted.

C.4. Two-tone spectroscopy at different Coulomb oscillation

Fig. C.4 displays a two-tone spectroscopy experiment with a red sideband drive($P_d = +20\,\mathrm{dBm}$) as presented in 7.3. Here, the gate voltage range was $-1.13\,\mathrm{V} \leq V_g \leq -1.124\,\mathrm{V}$ corresponding to the subsequent Coulomb oscillation as in Fig. 7.18. Here, the generator that drives the antenna was set to a moderate power of $P_A = -45\,\mathrm{dBm}$. The overall same behaviour as in Fig. 7.18 with electrostatic frequency softening and similar gate voltage dependence of optomechanical coupling is found.

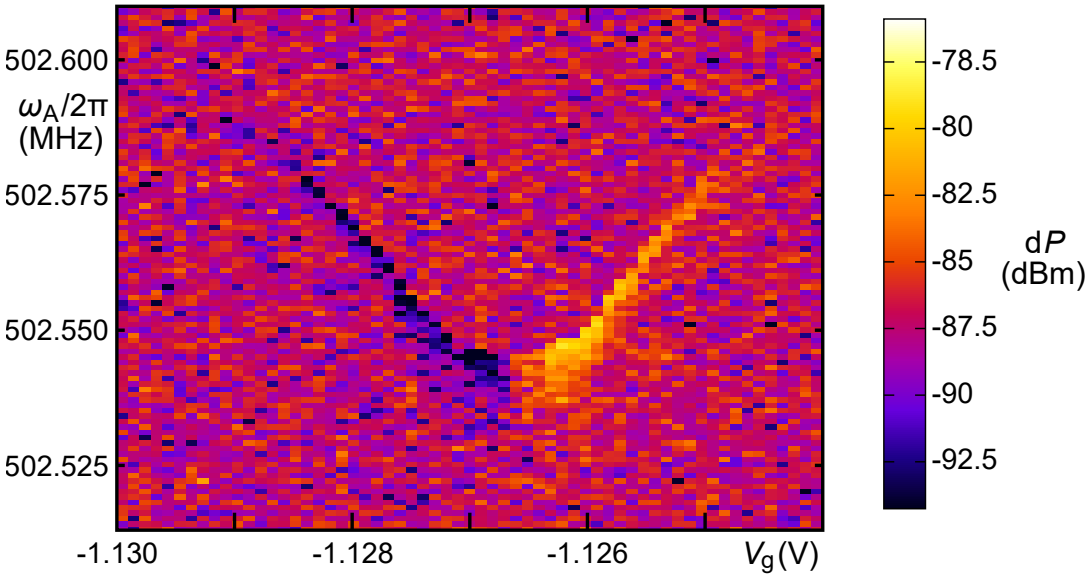

Figure C.4.: Gate voltage dependence of red sideband upconversion experiment as presented in Fig. 7.18, but at subsequent Coulomb oscillation. An antenna power of $P_{\mathrm{A}} = -45\,\mathrm{dBm}$ was applied. Adapted from [Blien et al., 2020].

Bibliography

[Anderson et al., 1972] P. W. Anderson, B. I. Halperin, and c. M. Varma. *Anomalous low-temperature thermal properties of glasses and spin glasses*. Philosophical Magazine **25**(1), 1–9 (1972), doi:10.1080/14786437208229210.

[Ares et al., 2016] N. Ares, T. Pei, A. Mavalankar, M. Mergenthaler, J. H. Warner, G. A. D. Briggs, and E. A. Laird. *Resonant Optomechanics with a Vibrating Carbon Nanotube and a Radio-Frequency Cavity*. Physical Review Letters **117**(17) (2016), doi:10.1103/physrevlett.117.170801.

[Aspelmeyer et al., 2014] M. Aspelmeyer, T. J. Kippenberg, and F. Marquardt. *Cavity optomechanics*. Reviews of Modern Physics **86**(4), 1391–1452 (2014), doi:10.1103/revmodphys.86.1391.

[Aziz et al., 2014] M. Aziz, D. C. Hudson, and S. Russo. *Molybdenum-rhenium superconducting suspended nanostructures*. Applied Physics Letters **104**(23), 233102 (2014), doi:10.1063/1.4883115.

[Bandaru, 2007] P. R. Bandaru. *Electrical Properties and Applications of Carbon Nanotube Structures*. Journal of Nanoscience and Nanotechnology **7**(4), 1239–1267 (2007), doi:10.1166/jnn.2007.307.

[Bardeen et al., 1957] J. Bardeen, L. N. Cooper, and J. R. Schrieffer. *Theory of Superconductivity*. Physical Review **108**(5), 1175–1204 (1957), doi:10.1103/physrev.108.1175.

[Barnard et al., 2019] A. W. Barnard, M. Zhang, G. S. Wiederhecker, M. Lipson, and P. L. McEuen. *Real-time vibrations of a carbon nanotube*. Nature **566**(7742), 89–93 (2019), doi:10.1038/s41586-018-0861-0.

[Beenakker, 1991] C. W. J. Beenakker. *Theory of Coulomb-blockade oscillations in the conductance of a quantum dot*. Physical Review B **44**(4), 1646–1656 (1991), doi:10.1103/physrevb.44.1646.

[Bethune et al., 1993] D. S. Bethune, C. H. Kiang, M. S. de Vries, G. Gorman, R. Savoy, J. Vazquez, and R. Beyers. *Cobalt-catalysed growth of carbon nanotubes with single-atomic-layer walls*. Nature **363**(6430), 605–607 (1993), doi:10.1038/363605a0.

[Blais et al., 2004] A. Blais, R.-S. Huang, A. Wallraff, S. M. Girvin, and R. J. Schoelkopf. *Cavity quantum electrodynamics for superconducting electrical circuits: An architecture for quantum computation*. Physical Review A **69**(6) (2004), doi:10.1103/physreva.69.062320.

[Blien et al., 2016] S. Blien, K. J. G. Götz, P. L. Stiller, T. Mayer, T. Huber, O. Vavra, and A. K. Hüttel. *Towards carbon nanotube growth into superconducting microwave resonator geometries*. physica status solidi (b) **253**(12), 2385–2390 (2016), doi:10.1002/pssb.201600217.

[Blien et al., 2018] S. Blien, P. Steger, A. Albang, N. Paradiso, and A. K. Hüttel. *Quartz Tuning-Fork Based Carbon Nanotube Transfer into Quantum Device Geometries*. physica status solidi (b) **255**(12), 1800118 (2018), doi:10.1002/pssb.201800118.

[Blien et al., 2020] S. Blien, P. Steger, N. Hüttner, R. Graaf, and A. K. Hüttel. *Quantum capacitance mediated carbon nanotube optomechanics*. Nature Communications **11**(1) (2020), doi:10.1038/s41467-020-15433-3.

[Braginsky and Manukin, 1967] V. B. Braginsky and A. B. Manukin. *Ponderomotive effects of electromagnetic radiation*. Sov. Phys. JETP **25**(4), 653–655 (1967).

[Braginsky et al., 2001] V. B. Braginsky, S. E. Strigin, and S. P. Vyatchanin. *Parametric oscillatory instability in Fabry–Perot interferometer*. Physics Letters A **287**(5-6), 331–338 (2001), doi:10.1016/s0375-9601(01)00510-2.

[Brunner, 2016] P. Brunner (2016). Reflection measurements on superconducting stub tuners for nanotube integration. mathesis, Universität Regensburg.

[Brydson, 1999] J. A. Brydson. *Plastics Materials*. Butterworth-Heinemann, 7th edition (1999).

[Cao et al., 2005] J. Cao, Q. Wang, and H. Dai. *Electron transport in very clean, as-grown suspended carbon nanotubes*. Nature Materials **4**(10), 745–749 (2005), doi:10.1038/nmat1478.

[Castellanos-Gomez et al., 2014] A. Castellanos-Gomez, M. Buscema, R. Molenaar, V. Singh, L. Janssen, H. S. J. van der Zant, and G. A. Steele. *Deterministic transfer of two-dimensional materials by all-dry viscoelastic stamping*. 2D Materials **1**(1), 011002 (2014), doi:10.1088/2053-1583/1/1/011002.

[Chaimool and Akkaraekthali, 2012] S. Chaimool and P. Akkaraekthali (2012). CPW-Fed Antennas for WiFi and WiMAX. In *Advanced Transmission Techniques in WiMAX*. InTech.

[Charlier et al., 2007] J.-C. Charlier, X. Blase, and S. Roche. *Electronic and transport properties of nanotubes*. Reviews of Modern Physics **79**(2), 677–732 (2007), doi:10.1103/revmodphys.79.677.

[Clarke, 2007] B. Clarke. *Microwave Measurements*, chapter 18: Measurement of the dielectric properties of materials at RF and microwave frequencies, page 412. The Institution of Engineering and Technology, London, United Kingdom (2007).

[Cleland, 2003] A. N. Cleland. *Foundations of Nanomechanics*. Springer Berlin Heidelberg (2003).

[Clerk and Marquardt, 2014] A. A. Clerk and F. Marquardt. *Cavity Optomechanics*, chapter 2: Basic Theory of Cavity Optomechanics, pages 5–24. Springer-Verlag Berlin Heidelberg, first edition (2014).

[Collin, 2001] R. E. Collin. *Foundations for Microwave Engineering*. Wiley-IEEE Press, 2nd edition (2001).

[Day et al., 2003] P. K. Day, H. G. LeDuc, B. A. Mazin, A. Vayonakis, and J. Zmuidzinas. *A broadband superconducting detector suitable for use in large arrays*. Nature **425**(6960), 817–821 (2003), doi:10.1038/nature02037.

[Delbecq, 2013] M. Delbecq. *Coupling quantum dot circuits to microwave cavities*. phdthesis, Université Pierre et Marie Curie (2013).

[Delbecq et al., 2011] M. R. Delbecq, V. Schmitt, F. D. Parmentier, N. Roch, J. J. Viennot, G. Fève, B. Huard, C. Mora, A. Cottet, and T. Kontos. *Coupling a Quantum Dot, Fermionic Leads, and a Microwave Cavity on a Chip*. Physical Review Letters **107**(25) (2011), doi:10.1103/physrevlett.107.256804.

[Deng et al., 2013] C. Deng, M. Otto, and A. Lupascu. *An analysis method for transmission measurements of superconducting resonators with applications to quantum-regime dielectric-loss measurements*. Journal of Applied Physics **114**(5), 054504 (2013), doi:10.1063/1.4817512.

[Duty et al., 2005] T. Duty, G. Johansson, K. Bladh, D. Gunnarsson, C. Wilson, and P. Delsing. *Observation of Quantum Capacitance in the Cooper-Pair Transistor*. Physical Review Letters **95**(20) (2005), doi:10.1103/physrevlett.95.206807.

[Eichler et al., 2012] A. Eichler, M. del Álamo Ruiz, J. A. Plaza, and A. Bachtold. *Strong Coupling between Mechanical Modes in a Nanotube Resonator*. Physical Review Letters **109**(2) (2012), doi:10.1103/physrevlett.109.025503.

[Eichler et al., 2013] A. Eichler, J. Moser, M. I. Dykman, and A. Bachtold. *Symmetry breaking in a mechanical resonator made from a carbon nanotube*. Nature Communications **4**(1) (2013), doi:10.1038/ncomms3843.

[Elste et al., 2009] F. Elste, S. M. Girvin, and A. A. Clerk. *Quantum Noise Interference and Backaction Cooling in Cavity Nanomechanics*. Physical Review Letters **102**(20) (2009), doi:10.1103/physrevlett.102.207209.

[Fan et al., 2018] L. Fan, C.-L. Zou, R. Cheng, X. Guo, X. Han, Z. Gong, S. Wang, and H. X. Tang. *Superconducting cavity electro-optics: A platform for coherent photon conversion between superconducting and photonic circuits*. Science Advances **4**(8), eaar4994 (2018), doi:10.1126/sciadv.aar4994.

[Fano, 1961] U. Fano. *Effects of Configuration Interaction on Intensities and Phase Shifts*. Physical Review **124**(6), 1866–1878 (1961), doi:10.1103/physrev.124.1866.

[Fiore et al., 2011] V. Fiore, Y. Yang, M. C. Kuzyk, R. Barbour, L. Tian, and H. Wang. *Storing Optical Information as a Mechanical Excitation in a Silica Optomechanical Resonator*. Physical Review Letters **107**(13) (2011), doi:10.1103/physrevlett.107.133601.

[Frey et al., 2011] T. Frey, P. J. Leek, M. Beck, K. Ensslin, A. Wallraff, and T. Ihn. *Characterization of a microwave frequency resonator via a nearby quantum dot*. Applied Physics Letters **98**(26), 262105 (2011), doi:10.1063/1.3604784.

[Frey et al., 2012] T. Frey, P. J. Leek, M. Beck, A. Blais, T. Ihn, K. Ensslin, and A. Wallraff. *Dipole Coupling of a Double Quantum Dot to a Microwave Resonator*. Physical Review Letters **108**(4) (2012), doi:10.1103/physrevlett.108.046807.

[Gao, 2008] J. Gao. *The physics of superconducting microwave resonators*. phdthesis, California Institue of Technology (2008).

[Gao et al., 2008] J. Gao, M. Daal, A. Vayonakis, S. Kumar, J. Zmuidzinas, B. Sadoulet, B. A. Mazin, P. K. Day, and H. G. Leduc. *Experimental evidence for a surface distribution of two-level systems in superconducting lithographed microwave resonators*. Applied Physics Letters **92**(15), 152505 (2008), doi:10.1063/1.2906373.

[Gavaler et al., 1972] J. R. Gavaler, M. A. Janocko, and C. K. Jones. *A-15 structure Mo–Re superconductor*. Applied Physics Letters **21**(4), 179–180 (1972), doi:10.1063/1.1654334.

[Gevorgian et al., 1995] S. Gevorgian, L. J. P. Linner, and E. L. Kollberg. *CAD models for shielded multilayered CPW*. IEEE Transactions on Microwave Theory and Techniques **43**(4), 772–779 (1995), doi:10.1109/22.375223.

[Ginley and Cardwell, 2002] D. Ginley and D. Cardwell. *Handbook of Superconducting Materials*. Taylor Francis (2002).

[Glazman and Shekhter, 1989] L. I. Glazman and R. I. Shekhter. *Coulomb oscillations of the conductance in a laterally confined heterostructure*. Journal of Physics: Condensed Matter **1**(33), 5811–5815 (1989), doi:10.1088/0953-8984/1/33/027.

[Glover and Tinkham, 1957] R. E. Glover and M. Tinkham. *Conductivity of Superconducting Films for Photon Energies between 0.3 and 40 kT_c*. Physical Review **108**(2), 243–256 (1957), doi:10.1103/physrev.108.243.

[Göppl et al., 2008] M. Göppl, A. Fragner, M. Baur, R. Bianchetti, S. Filipp, J. M. Fink, P. J. Leek, G. Puebla, L. Steffen, and A. Wallraff. *Coplanar waveguide resonators for circuit quantum electrodynamics*. Journal of Applied Physics **104**(11), 113904 (2008), doi:10.1063/1.3010859.

[Graaf, 2019] R. Graaf (2019). Development of fork fabrication for carbon nanotube transfer. mathesis, Universität Regensburg.

[Gramich et al., 2015] J. Gramich, A. Baumgartner, M. Muoth, C. Hierold, and C. Schönenberger. *Fork stamping of pristine carbon nanotubes onto ferromagnetic contacts for spin-valve devices*. physica status solidi (b) **252**(11), 2496–2502 (2015), doi:10.1002/pssb.201552213.

[Götz, 2018] K. Götz. *Carbon Nanotube quantum dots: Transport, mechanical charge detection, and fabrication development*. phdthesis, Universität Regensburg (2018).

[Götz et al., 2016] K. J. G. Götz, S. Blien, P. L. Stiller, O. Vavra, T. Mayer, T. Huber, T. N. G. Meier, M. Kronseder, C. Strunk, and A. K. Hüttel. *Co-sputtered MoRe thin films for carbon nanotube growth-compatible superconducting coplanar resonators*. Nanotechnology **27**(13), 135202 (2016), doi:10.1088/0957-4484/27/13/135202.

[Götz et al., 2018] K. J. G. Götz, D. R. Schmid, F. J. Schupp, P. L. Stiller, C. Strunk, and A. K. Hüttel. *Nanomechanical Characterization of the Kondo Charge Dynamics in a Carbon Nanotube*. Physical Review Letters **120**(24) (2018), doi:10.1103/physrevlett.120.246802.

[Hanson et al., 2007] R. Hanson, L. P. Kouwenhoven, J. R. Petta, S. Tarucha, and L. M. K. Vandersypen. *Spins in few-electron quantum dots*. Reviews of Modern Physics **79**(4), 1217–1265 (2007), doi:10.1103/revmodphys.79.1217.

[Hao et al., 2014] Y. Hao, F. Rouxinol, and M. D. LaHaye. *Development of a broadband reflective T-filter for voltage biasing high-Q superconducting microwave cavities*. Applied Physics Letters **105**(22), 222603 (2014), doi:10.1063/1.4903777.

[Hein, 1999] M. Hein. *High-Temperature-Superconductor Thin Films at Microwave Frequencies*. Springer Berlin Heidelberg, 1st edition (1999).

[Hertzberg, 2009] J. B. Hertzberg. *Back-Action Evading Measurements of Nanomechanical Motion Approaching Quantum Limits*. phdthesis, University of Maryland (2009).

[Hornibrook et al., 2012a] J. M. Hornibrook, E. E. Mitchell, C. J. Lewis, and D. J. Reilly. *Parasitic Losses in Nb Superconducting Resonators*. Physics Procedia **36**, 187–192 (2012), doi:10.1016/j.phpro.2012.06.069.

[Hornibrook et al., 2012b] J. M. Hornibrook, E. E. Mitchell, and D. J. Reilly. *Superconducting Resonators with Parasitic Electromagnetic Environments*. arXiv:1203.4442 (2012).

[Hüttel et al., 2008] A. K. Hüttel, M. Poot, B. Witkamp, and H. S. J. van der Zant. *Nanoelectromechanics of suspended carbon nanotubes*. New Journal of Physics **10**(9), 095003 (2008), doi:10.1088/1367-2630/10/9/095003.

[Hüttel et al., 2009] A. K. Hüttel, G. A. Steele, B. Witkamp, M. Poot, L. P. Kouwenhoven, and H. S. J. van der Zant. *Carbon Nanotubes as Ultrahigh Quality Factor Mechanical Resonators*. Nano Letters **9**(7), 2547–2552 (2009), doi:10.1021/nl900612h.

[Hüttner, 2019] N. Hüttner (2019). Superconducting Resonators for coupling to carbon nanotubes. mathesis, Universität Regensburg.

[Huh et al., 2005] Y. Huh, M. L. H. Green, Y. H. Kim, J. Y. Lee, and C. J. Lee. *Control of carbon nanotube growth using cobalt nanoparticles as catalyst*. Applied Surface Science **249**(1-4), 145–150 (2005), doi:10.1016/j.apsusc.2004.11.059.

[Iijima and Ichihashi, 1993] S. Iijima and T. Ichihashi. *Single-shell carbon nanotubes of 1-nm diameter*. Nature **363**(6430), 603–605 (1993), doi:10.1038/363603a0.

[Ilani et al., 2006] S. Ilani, L. A. K. Donev, M. Kindermann, and P. L. McEuen. *Measurement of the quantum capacitance of interacting electrons in carbon nanotubes*. Nature Physics **2**(10), 687–691 (2006), doi:10.1038/nphys412.

[John et al., 2004] D. L. John, L. C. Castro, and D. L. Pulfrey. *Quantum capacitance in nanoscale device modeling*. Journal of Applied Physics **96**(9), 5180–5184 (2004), doi:10.1063/1.1803614.

[Kautz, 1978] R. L. Kautz. *Picosecond pulses on superconducting striplines*. Journal of Applied Physics **49**(1), 308–314 (1978), doi:10.1063/1.324387.

[Kepler, 1619] J. Kepler. *De Cometis Libelli Tres* (1619).

[Khalil et al., 2012] M. S. Khalil, M. J. A. Stoutimore, F. C. Wellstood, and K. D. Osborn. *An analysis method for asymmetric resonator transmission applied to superconducting devices*. Journal of Applied Physics **111**(5), 054510 (2012), doi:10.1063/1.3692073.

[Kong et al., 1998] J. Kong, A. M. Cassell, and H. Dai. *Chemical vapor deposition of methane for single-walled carbon nanotubes*. Chemical Physics Letters **292**(4-6), 567–574 (1998), doi:10.1016/s0009-2614(98)00745-3.

[Kouwenhoven et al., 1997] L. P. Kouwenhoven, C. M. Marcus, P. L. McEuen, S. Tarucha, R. M. Westervelt, and N. S. Wingreen (1997). Electron Transport in Quantum Dots. In *Mesoscopic Electron Transport*, pages 105–214. Springer Netherlands.

[Krause et al., 2012] A. G. Krause, M. Winger, T. D. Blasius, Q. Lin, and O. Painter. *A high-resolution microchip optomechanical accelerometer*. Nature Photonics **6**(11), 768–772 (2012), doi:10.1038/nphoton.2012.245.

[Laird et al., 2015] E. A. Laird, F. Kuemmeth, G. A. Steele, K. Grove-Rasmussen, J. Nygård, K. Flensberg, and L. P. Kouwenhoven. *Quantum transport in carbon nanotubes*. Reviews of Modern Physics **87**(3), 703–764 (2015), doi:10.1103/revmodphys.87.703.

[Lassagne et al., 2009] B. Lassagne, Y. Tarakanov, J. Kinaret, D. Garcia-Sanchez, and A. Bachtold. *Coupling Mechanics to Charge Transport in Carbon Nanotube Mechanical Resonators*. Science **325**(5944), 1107–1110 (2009), doi:10.1126/science.1174290.

[Law, 1994] C. K. Law. *Effective Hamiltonian for the radiation in a cavity with a moving mirror and a time-varying dielectric medium*. Physical Review A **49**(1), 433–437 (1994), doi:10.1103/physreva.49.433.

[Lebedew, 1901] P. Lebedew. *Untersuchungen über die Druckkräfte des Lichtes*. Annalen der Physik **311**(11), 433–458 (1901), doi:10.1002/andp.19013111102.

[Lemberger et al., 2007] T. R. Lemberger, I. Hetel, J. W. Knepper, and F. Y. Yang. *Penetration depth study of very thin superconducting Nb films*. Physical Review B **76**(9) (2007), doi:10.1103/physrevb.76.094515.

[Li et al., 2013] H. Li, Y. Wang, L. Wei, P. Zhou, Q. Wei, C. Cao, Y. Fang, Y. Yu, and P. Wu. *Experimental demonstrations of high-Q superconducting coplanar waveguide resonators*. Chinese Science Bulletin **58**(20), 2413–2417 (2013), doi:10.1007/s11434-013-5882-3.

[London and London, 1935] F. London and H. London. *The electromagnetic equations of the supraconductor*. Proceedings of the Royal Society of London. Series A - Mathematical and Physical Sciences **149**(866), 71–88 (1935), doi:10.1098/rspa.1935.0048.

[Lu, 1997] J. P. Lu. *Elastic properties of carbon nanotubes and nanoropes*. Physical Review Letters **79**(7), 1297–1300 (1997), doi:10.1103/physrevlett.79.1297.

[Luryi, 1988] S. Luryi. *Quantum capacitance devices*. Applied Physics Letters **52**(6), 501–503 (1988), doi:10.1063/1.99649.

[Margańska et al., 2019] M. Margańska, D. Schmid, A. Dirnaichner, P. Stiller, C. Strunk, M. Grifoni, and A. Hüttel. *Shaping Electron Wave Functions in a Carbon Nanotube with a Parallel Magnetic Field*. Physical Review Letters **122**(8) (2019), doi:10.1103/physrevlett.122.086802.

[Marquardt et al., 2007] F. Marquardt, J. P. Chen, A. A. Clerk, and S. M. Girvin. *Quantum Theory of Cavity-Assisted Sideband Cooling of Mechanical Motion*. Physical Review Letters **99**(9) (2007), doi:10.1103/physrevlett.99.093902.

[Massel et al., 2011] F. Massel, T. T. Heikkilä, J.-M. Pirkkalainen, S. U. Cho, H. Saloniemi, P. J. Hakonen, and M. A. Sillanpää. *Microwave amplification with nanomechanical resonators*. Nature **480**(7377), 351–354 (2011), doi:10.1038/nature10628.

[Mattis and Bardeen, 1958] D. C. Mattis and J. Bardeen. *Theory of the Anomalous Skin Effect in Normal and Superconducting Metals*. Physical Review **111**(2), 412–417 (1958), doi:10.1103/physrev.111.412.

[Mazin, 2004] B. A. Mazin. *Microwave kinetic inductance detectors*. phdthesis, California Institute of Technology (2004).

[Meerwaldt et al., 2012] H. B. Meerwaldt, G. Labadze, B. H. Schneider, A. Taspinar, Y. M. Blanter, H. S. J. van der Zant, and G. A. Steele. *Probing the charge of a quantum dot with a nanomechanical resonator*. Physical Review B **86**(11) (2012), doi:10.1103/physrevb.86.115454.

[Megrant et al., 2012] A. Megrant, C. Neill, R. Barends, B. Chiaro, Y. Chen, L. Feigl, J. Kelly, E. Lucero, M. Mariantoni, P. J. J. O'Malley, D. Sank, A. Vainsencher, J. Wenner, T. C. White,

Y. Yin, J. Zhao, C. J. Palmstrøm, J. M. Martinis, and A. N. Cleland. *Planar superconducting resonators with internal quality factors above one million*. Applied Physics Letters **100**(11), 113510 (2012), doi:10.1063/1.3693409.

[Miroshnichenko et al., 2010] A. E. Miroshnichenko, S. Flach, and Y. S. Kivshar. *Fano resonances in nanoscale structures*. Reviews of Modern Physics **82**(3), 2257–2298 (2010), doi:10.1103/revmodphys.82.2257.

[Moser et al., 2014] J. Moser, A. Eichler, J. Güttinger, M. I. Dykman, and A. Bachtold. *Nanotube mechanical resonators with quality factors of up to 5 million*. Nature Nanotechnology **9**(12), 1007–1011 (2014), doi:10.1038/nnano.2014.234.

[Moulder et al., 1992] J. F. Moulder, W. F. Sickle, P. E. Sobol, and K. D. Bomben. *Handbook of X-ray Photoelectron Spectroscopy*. Perkin-Elmer Corporation, Physical Electronics Division, 2nd edition (1992).

[Nichols and Hull, 1903] E. F. Nichols and G. F. Hull. *The Pressure Due to Radiation*. Proceedings of the American Academy of Arts and Sciences **38**(20), 559 (1903), doi:10.2307/20021808.

[Pappas et al., 2011] D. P. Pappas, M. R. Vissers, D. S. Wisbey, J. S. Kline, and J. Gao. *Two Level System Loss in Superconducting Microwave Resonators*. IEEE Transactions on Applied Superconductivity **21**(3), 871–874 (2011), doi:10.1109/tasc.2010.2097578.

[Pei et al., 2012] F. Pei, E. A. Laird, G. A. Steele, and L. P. Kouwenhoven. *Valley–spin blockade and spin resonance in carbon nanotubes*. Nature Nanotechnology **7**(10), 630–634 (2012), doi:10.1038/nnano.2012.160.

[Petersan and Anlage, 1998] P. J. Petersan and S. M. Anlage. *Measurement of resonant frequency and quality factor of microwave resonators: Comparison of methods*. Journal of Applied Physics **84**(6), 3392–3402 (1998), doi:10.1063/1.368498.

[Phillips, 1972] W. A. Phillips. *Tunneling states in amorphous solids*. Journal of Low Temperature Physics **7**(3-4), 351–360 (1972), doi:10.1007/bf00660072.

[Phillips, 1987] W. A. Phillips. *Two-level states in glasses*. Reports on Progress in Physics **50**(12), 1657–1708 (1987), doi:10.1088/0034-4885/50/12/003.

[Pippard, 1953] A. B. Pippard. *An experimental and theoretical study of the relation between magnetic field and current in a superconductor*. Proceedings of the Royal Society of London. Series A. Mathematical and Physical Sciences **216**(1127), 547–568 (1953), doi:10.1098/rspa.1953.0040.

[Poot and van der Zant, 2012] M. Poot and H. S. J. van der Zant. *Mechanical systems in the quantum regime*. Physics Reports **511**(5), 273–335 (2012), doi:10.1016/j.physrep.2011.12.004.

[Postnikov et al., 1977] V. S. Postnikov, V. V. Postnikov, and V. S. Zheleznyi. *Superconductivity in Mo-Re system alloy films produced by electron beam evaporation in high vacuum*. Physica Status Solidi (a) **39**(1), K21–K23 (1977), doi:10.1002/pssa.2210390148.

[Pozar, 2011] D. M. Pozar. *Microwave Engineering*. John Wiley & Sons, 4th edition (2011).

[Pöpel, 1989] R. Pöpel. *Surface impedance and reflectivity of superconductors*. Journal of Applied Physics **66**(12), 5950–5957 (1989), doi:10.1063/1.343622.

[Probst et al., 2015] S. Probst, F. B. Song, P. A. Bushev, A. V. Ustinov, and M. Weides. *Efficient and robust analysis of complex scattering data under noise in microwave resonators*. Review of Scientific Instruments **86**(2), 024706 (2015), doi:10.1063/1.4907935.

[Radushkevich and Lukyanovich, 1952] L. V. Radushkevich and V. M. Lukyanovich. *About the structure of carbon formed by thermal decomposition of carbon monoxide on iron substrate*. J. Phys. Chem. (Moscow) **26**, 88–95 (1952).

[Ranjan et al., 2015] V. Ranjan, G. Puebla-Hellmann, M. Jung, T. Hasler, A. Nunnenkamp, M. Muoth, C. Hierold, A. Wallraff, and C. Schönenberger. *Clean carbon nanotubes coupled to superconducting impedance-matching circuits*. Nature Communications **6**(1) (2015), doi:10.1038/ncomms8165.

[Regal et al., 2008] C. A. Regal, J. D. Teufel, and K. W. Lehnert. *Measuring nanomechanical motion with a microwave cavity interferometer*. Nature Physics **4**(7), 555–560 (2008), doi:10.1038/nphys974.

[Rocheleau et al., 2009] T. Rocheleau, T. Ndukum, C. Macklin, J. B. Hertzberg, A. A. Clerk, and K. C. Schwab. *Preparation and detection of a mechanical resonator near the ground state of motion*. Nature **463**(7277), 72–75 (2009), doi:10.1038/nature08681.

[Saito et al., 1998] R. Saito, G. Dresselhaus, and M. S. Dresselhaus. *Physical Properties of Carbon Nanotubes*. Published by imperial college press and distributed by world scientific publishing co. (1998).

[Sazonova et al., 2004] V. Sazonova, Y. Yaish, H. Üstünel, D. Roundy, T. A. Arias, and P. L. McEuen. *A tunable carbon nanotube electromechanical oscillator*. Nature **431**(7006), 284–287 (2004), doi:10.1038/nature02905.

[Schliesser et al., 2008] A. Schliesser, R. Rivière, G. Anetsberger, O. Arcizet, and T. J. Kippenberg. *Resolved-sideband cooling of a micromechanical oscillator*. Nature Physics **4**(5), 415–419 (2008), doi:10.1038/nphys939.

[Schmid et al., 2012] D. R. Schmid, P. L. Stiller, C. Strunk, and A. K. Hüttel. *Magnetic damping of a carbon nanotube nano-electromechanical resonator*. New Journal of Physics **14**(8), 083024 (2012), doi:10.1088/1367-2630/14/8/083024.

[Schmid et al., 2015] D. R. Schmid, S. Smirnov, M. Margańska, A. Dirnaichner, P. L. Stiller, M. Grifoni, A. K. Hüttel, and C. Strunk. *Broken SU(4) symmetry in a Kondo-correlated carbon nanotube*. Physical Review B **91**(15) (2015), doi:10.1103/physrevb.91.155435.

[Schneider et al., 2012] B. H. Schneider, S. Etaki, H. S. J. van der Zant, and G. A. Steele. *Coupling carbon nanotube mechanics to a superconducting circuit*. Scientific Reports **2**(1) (2012), doi:10.1038/srep00599.

[Shevchenko et al., 2015] S. N. Shevchenko, D. G. Rubanov, and F. Nori. *Delayed-response quantum back action in nanoelectromechanical systems*. Physical Review B **91**(16) (2015), doi:10.1103/physrevb.91.165422.

[Shevchuk et al., 2015] O. Shevchuk, V. Singh, G. A. Steele, and Y. M. Blanter. *Optomechanical response of a nonlinear mechanical resonator*. Physical Review B **92**(19) (2015), doi:10.1103/physrevb.92.195415.

[Simons, 2001] R. N. Simons. *Coplanar Waveguide Circuits, Components, and Systems*. John Wiley & Sons, 1st edition (2001).

[Singh et al., 2014a] V. Singh, S. J. Bosman, B. H. Schneider, Y. M. Blanter, A. Castellanos-Gomez, and G. A. Steele. *Optomechanical coupling between a multilayer graphene mechanical resonator and a superconducting microwave cavity*. Nature Nanotechnology **9**(10), 820–824 (2014), doi:10.1038/nnano.2014.168.

[Singh et al., 2014b] V. Singh, B. H. Schneider, S. J. Bosman, E. P. J. Merkx, and G. A. Steele. *Molybdenum-rhenium alloy based high-Q superconducting microwave resonators*. Applied Physics Letters **105**(22), 222601 (2014), doi:10.1063/1.4903042.

[Stamper-Kurn, 2014] D. M. Stamper-Kurn. *Cavity Optomechanics*, chapter 13: Cavity Optomechanics with Cold Atoms, pages 283–325. Springer-Verlag Berlin Heidelberg, first edition (2014).

[Staring et al., 1991] A. A. M. Staring, J. G. Williamson, H. van Houten, C. W. J. Beenakker, L. P. Kouwenhoven, and C. T. Foxon. *Coulomb-blockade oscillations in a quantum dot*. Physica B: Condensed Matter **175**(1-3), 226–230 (1991), doi:10.1016/0921-4526(91)90717-s.

[Steele et al., 2009] G. A. Steele, A. K. Huttel, B. Witkamp, M. Poot, H. B. Meerwaldt, L. P. Kouwenhoven, and H. S. J. van der Zant. *Strong Coupling Between Single-Electron Tunneling and Nanomechanical Motion*. Science **325**(5944), 1103–1107 (2009), doi:10.1126/science.1176076.

[Steger, 2019] P. Steger (2019). Fabrication of a carbon nanotube mechanical resonator using a quartz tuning fork based transfer method. mathesis, Universität Regensburg.

[Stiller et al., 2013] P. L. Stiller, S. Kugler, D. R. Schmid, C. Strunk, and A. K. Hüttel. *Negative frequency tuning of a carbon nanotube nano-electromechanical resonator under tension*. physica status solidi (b) **250**(12), 2518–2522 (2013), doi:10.1002/pssb.201300073.

[Stockklauser et al., 2017] A. Stockklauser, P. Scarlino, J. Koski, S. Gasparinetti, C. Andersen, C. Reichl, W. Wegscheider, T. Ihn, K. Ensslin, and A. Wallraff. *Strong Coupling Cavity QED with Gate-Defined Double Quantum Dots Enabled by a High Impedance Resonator*. Physical Review X **7**(1) (2017), doi:10.1103/physrevx.7.011030.

[Tans et al., 1997] S. J. Tans, M. H. Devoret, H. Dai, A. Thess, R. E. Smalley, L. J. Geerligs, and C. Dekker. *Individual single-wall carbon nanotubes as quantum wires*. Nature **386**(6624), 474–477 (1997), doi:10.1038/386474a0.

[Tavernarakis et al., 2018] A. Tavernarakis, A. Stavrinadis, A. Nowak, I. Tsioutsios, A. Bachtold, and P. Verlot. *Optomechanics with a hybrid carbon nanotube resonator*. Nature Communications **9**(1) (2018), doi:10.1038/s41467-018-03097-z.

[Testardi et al., 1971] L. R. Testardi, J. J. Hauser, and M. H. Read. *Enhanced superconducting T_c and structural transformation in Mo-Re alloys*. Solid State Communications **9**(21), 1829–1831 (1971), doi:10.1016/0038-1098(71)90100-1.

[Teufel et al., 2008] J. D. Teufel, J. W. Harlow, C. A. Regal, and K. W. Lehnert. *Dynamical Backaction of Microwave Fields on a Nanomechanical Oscillator*. Physical Review Letters **101**(19) (2008), doi:10.1103/physrevlett.101.197203.

[Teufel et al., 2009] J. D. Teufel, T. Donner, M. A. Castellanos-Beltran, J. W. Harlow, and K. W. Lehnert. *Nanomechanical motion measured with an imprecision below that at the standard quantum limit*. Nature Nanotechnology **4**(12), 820–823 (2009), doi:10.1038/nnano.2009.343.

[Teufel et al., 2011] J. D. Teufel, T. Donner, D. Li, J. W. Harlow, M. S. Allman, K. Cicak, A. J. Sirois, J. D. Whittaker, K. W. Lehnert, and R. W. Simmonds. *Sideband cooling of micromechanical motion to the quantum ground state*. Nature **475**(7356), 359–363 (2011), doi:10.1038/nature10261.

[Tinkham, 2004] M. Tinkham. *Introduction to Superconductivity*. Dover Publications Inc., 2nd edition (2004).

[Turneaure et al., 1991] J. P. Turneaure, J. Halbritter, and H. A. Schwettman. *The surface impedance of superconductors and normal conductors: The Mattis-Bardeen theory*. Journal of Superconductivity **4**(5), 341–355 (1991), doi:10.1007/bf00618215.

[Usmani et al., 2007] O. Usmani, Y. M. Blanter, and Y. V. Nazarov. *Strong feedback and current noise in nanoelectromechanical systems*. Physical Review B **75**(19) (2007), doi:10.1103/physrevb.75.195312.

[Veyres and Hanna, 1980] C. Veyres and V. F. Hanna. *Extension of the application of conformal mapping techniques to coplanar lines with finite dimensions*. International Journal of Electronics **48**(1), 47–56 (1980), doi:10.1080/00207218008901066.

[Vladimir B. Braginsky, 1995] F. Y. K. Vladimir B. Braginsky. *Quantum Measurement*. Cambridge University Press (1995).

[Waissman et al., 2013] J. Waissman, M. Honig, S. Pecker, A. Benyamini, A. Hamo, and S. Ilani. *Realization of pristine and locally tunable one-dimensional electron systems in carbon nanotubes*. Nature Nanotechnology **8**(8), 569–574 (2013), doi:10.1038/nnano.2013.143.

[Walsh and Tomaselli, 1990] P. J. Walsh and V. P. Tomaselli. *Theory of microwave surface impedance in superconductors and normal metals*. American Journal of Physics **58**(7), 644–650 (1990), doi:10.1119/1.16425.

[Watanabe et al., 1994] K. Watanabe, K. Yoshida, T. Aoki, and S. Kohjiro. *Kinetic Inductance of Superconducting Coplanar Waveguides*. Japanese Journal of Applied Physics **33**(Part 1, No. 10), 5708–5712 (1994), doi:10.1143/jjap.33.5708.

[Weis et al., 2010] S. Weis, R. Rivière, S. Deléglise, E. Gavartin, O. Arcizet, A. Schliesser, and T. J. Kippenberg. *Optomechanically Induced Transparency*. Science **330**(6010), 1520–1523 (2010), doi:10.1126/science.1195596.

[Wen, 1969] C. P. Wen. *Coplanar Waveguide: A Surface Strip Transmission Line Suitable for Nonreciprocal Gyromagnetic Device Applications*. IEEE Transactions on Microwave Theory and Techniques **17**(12), 1087–1090 (1969), doi:10.1109/tmtt.1969.1127105.

[Wen et al., 2019] Y. Wen, N. Ares, F. J. Schupp, T. Pei, G. A. D. Briggs, and E. A. Laird. *A coherent nanomechanical oscillator driven by single-electron tunnelling*. Nature Physics **16**(1), 75–82 (2019), doi:10.1038/s41567-019-0683-5.

[Wu et al., 2010] C. C. Wu, C. H. Liu, and Z. Zhong. *One-Step Direct Transfer of Pristine Single-Walled Carbon Nanotubes for Functional Nanoelectronics*. Nano Letters **10**(3), 1032–1036 (2010), doi:10.1021/nl904260k.

[Yuli V. Nazarov, 2009] Y. M. B. Yuli V. Nazarov. *Quantum Transport*. Cambridge University Pr. (2009).

Curriculum Vitae

Stefan Blien, geboren am 30. Juli 1986 in Straubing.

1993 – 1997	Grundschule Ulrich Schmidl in Straubing
1997 – 2006	Ludwigsgymnasium in Straubing
2006	Abitur
2006 – 2013	Universität Regensburg, Studium der Physik
2008	Vordiplom
2012 – 2013	Diplomarbeit am Lehrstuhl "Physik der Mikro- und Nanostrukturen", Prof. Dr. Dieter Weiss, Universität Regensburg "Untersuchung von kristallographisch geätzten Graphen-Antidotgittern"
2013	Diplom
2013 – 2019	Wissenschaftlicher Mitarbeiter in der Gruppe "Nanotube transport and nanomechanics", Universität Regensburg

Scientific contributions

Conferences

- Winter school of the Johannes-Kepler-Universität Linz;
  Mauterndorf, 21.02. – 26.02.2016;
  Poster "Co-sputtered MoRe as carbon nanotube growth-compatible superconductor"

- Frühjahrstagung der Deutschen Physikalischen Gesellschaft;
  Regensburg, 06.03. – 11.03.2016;
  Talk "Co-sputtered Mo/Re superconducting coplanar resonators compatible with carbon nanotube growth"

- Frühjahrstagung der Deutschen Physikalischen Gesellschaft;
  Dresden, 19.03. – 24.03.2017;
  Poster "Rhenium-molybdenum coplanar superconducting electronics compatible with carbon nanotube growth"
  Poster "Towards GHz reflection on a suspended carbon nanotube"

- Winter school of the Johannes-Kepler-Universität Linz;
  Mauterndorf, 26.02. – 02.03.2018;
  Poster "Carbon nanotube transfer into superconducting resonator geometries"

- Frühjahrstagung der Deutschen Physikalischen Gesellschaft;
  Berlin, 11.03. – 16.03.2018;
  Poster "Coupling suspended carbon nanotubes to superconducting resonators"

- ElecMol International Conference on Molecular Electronics;
  Paris, 17.12. – 20.12.2018;
  Talk "Single electron optomechanics with a carbon nanotube resonator"

- Frühjahrstagung der Deutschen Physikalischen Gesellschaft;
  Regensburg, 31.03. – 05.04.2019;
  Talk "Optomechanics of a suspended carbon nanotube quantum dot coupled to a coplanar microwave resonator, part 2: experiment"

Internal Workshops

- GRK 1570 *Electronic Properties of Carbon Based Nanostructures*;
  St. Oswald, 21.09. – 23.09.2016;
  Talk "Optomechanics with carbon nanotubes"

- GRK 1570 *Electronic Properties of Carbon Based Nanostructures*;
  Rattenberg, 18.09. – 20.09.2017;
  Talk "Carbon Nanotube Transfer into Superconducting Resonator Geometries"

- GRK 1570 *Electronic Properties of Carbon Based Nanostructures*;
  Regensburg, 26.09.2018;
  Talk "Coupling a suspended carbon nanotube quantum dot to a microwave resonator"

Publications

- F. Oberhuber, S. Blien, S. Heydrich, F. Yaghobian, T. Korn, C. Schüller, C. Strunk, D. Weiss, and J. Eroms: *Weak localization and Raman study of anisotropically etched graphene antidots*; Applied Physics Letters **103**(14):143111, sep 2013

- K. J. G. Götz, S. Blien, P. L. Stiller, O. Vavra, T. Mayer, T. Huber, T. N. G. Meier, M. Kronseder, Ch. Strunk, and A. K. Hüttel: *Co-sputtered MoRe thin films for carbon nanotube growth-compatible superconducting coplanar resonators*; Nanotechnology **27**(13):135202, feb 2016

- S. Blien, K. J. G. Götz, P. L. Stiller, T. Mayer, T. Huber, O. Vavra, and A. K. Hüttel: *Towards carbon nanotube growth into superconducting microwave resonator geometries*; Physica Status Solidi (b) **253**(12):2385–2390, sep 2016

- F. Oberhuber, S. Blien, F. Schupp, D. Weiss, and J. Eroms: *Anisotropic etching of graphene in inert and oxygen atmospheres*; Physica Status Solidi (a) **214**(2):1600459, nov 2016

- S. Blien, P. Steger, A. Albang, N. Paradiso, and A. K. Hüttel: *Quartz tuning-fork based carbon nanotube transfer into quantum device geometries*; Physica Status Solidi (b) **255**(12):1800118, jun 2018

- S. Blien, P. Steger, N. Hüttner, R. Graaf, and A. K. Hüttel: *Quantum capacitance mediated carbon nanotube optomechanics*; Nature Communications **11**(1):1636, apr 2020

nature COMMUNICATIONS

ARTICLE

https://doi.org/10.1038/s41467-020-15433-3 OPEN

Quantum capacitance mediated carbon nanotube optomechanics

Stefan Blien[1], Patrick Steger[1], Niklas Hüttner[1], Richard Graaf[1] & Andreas K. Hüttel[1,2]✉

Cavity optomechanics allows the characterization of a vibration mode, its cooling and quantum manipulation using electromagnetic fields. Regarding nanomechanical as well as electronic properties, single wall carbon nanotubes are a prototypical experimental system. At cryogenic temperatures, as high quality factor vibrational resonators, they display strong interaction between motion and single-electron tunneling. Here, we demonstrate large optomechanical coupling of a suspended carbon nanotube quantum dot and a microwave cavity, amplified by several orders of magnitude via the nonlinearity of Coulomb blockade. From an optomechanically induced transparency (OMIT) experiment, we obtain a single photon coupling of up to $g_0 = 2\pi \cdot 95$ Hz. This indicates that normal mode splitting and full optomechanical control of the carbon nanotube vibration in the quantum limit is reachable in the near future. Mechanical manipulation and characterization via the microwave field can be complemented by the manifold physics of quantum-confined single electron devices.

[1] Institute for Experimental and Applied Physics, University of Regensburg, 93040 Regensburg, Germany. [2] Present address: Department of Applied Physics, Aalto University, Puumiehenkuja 2, 02150 Espoo, Finland. ✉email: andreas.huettel@ur.de

The technically challenging integration of suspended single-wall cabon nanotubes into complex qantum devices has recently made significant advances[1–6], as has also the integration of nanotube quantum dots into coplanar microwave cavities[7–9]. Both regarding their nanomechanical[10,11] as well as their electronic properties[12,13], carbon nanotubes are a prototypical experimental system. However, small vibrational deflection and length have made their optomechanical coupling to microwave fields[14] so far impossible.

In this work, we demonstrate large optomechanical coupling of a suspended carbon nanotube quantum dot and a microwave cavity. The nanotube is deposited onto source and drain electrodes close to the coplanar waveguide cavity; a finger-like extension of the cavity center conductor, passing below the suspended nanotube, serves as capacitively coupling gate. We find that the optomechanical coupling of the transversal nanotube vibration and the cavity mode is amplified by several orders of magnitude via the inherent nonlinearity of Coulomb blockade. With this, full optomechanical control of the carbon nanotube vibration in the quantum limit[15] is reachable in the near future. A unique experimental system becomes accessible, where the nanomechanically active part directly incorporates a quantum-confined electron system[16].

Results

Device precharacterization. Our device, depicted in Fig. 1a, combines a half-wavelength coplanar microwave cavity with a suspended carbon nanotube quantum dot. Near the coupling capacitor, the center conductor of the niobium-based cavity is connected to a thin gate electrode, buried between source and drain contacts of the carbon nanotube, see the sketch of Fig. 1b. At the cavity center, i.e., the location of the voltage node of its fundamental mode, a bias connection allows additional application of a dc voltage V_g to the gate. The device is mounted at the base temperature stage ($T \simeq 10$ mK) of a dilution refrigerator; for details see Supplementary Note 4 and Supplementary Fig. 4.

At cryogenic temperatures, electronic transport through the carbon nanotube is dominated by Coulomb blockade, with the typical behavior of a small band gap nanotube[12]. Near the electronic band gap, sharp Coulomb oscillations of conductance can be resolved; measurements are shown in Fig. 1c and Supplementary Fig. 3. A well-known method to detect the transversal vibration resonance of a suspended nanotube quantum dot is to apply a rf signal and measure the time-averaged dc current[17–19]. On resonance, the oscillating geometric capacitance, effectively broadening the Coulomb oscillations, leads to an easily recognizable change in current. This was used to identify the transversal vibration resonances of the device; Fig. 1d plots the resonance frequencies over a wide gate voltage range. Two coupled vibration modes are observed (see also Supplementary Note 5), one of which clearly displays electrostatic softening[20,21]. At low gate voltages, $|V_g| \leq 1.2$ V, where subsequent experiments are carried out, the resonance which we will utilize in the following is at $\omega_m \simeq 2\pi \cdot 502.5$ MHz, with typical quality factors around or exceeding $Q_m \sim 10^4$ observed in time-averaged dc current detection[17].

The combined suspended nanotube—cavity device forms a dispersively coupled optomechanical system[14]. The cavity has a resonance frequency of $\omega_c = 2\pi \cdot 5.74$ GHz with a decay rate of $\kappa_c = 2\pi \cdot 11.6$ MHz, dominated by internal losses. Nevertheless, due to the large mechanical resonance frequency ω_m of the carbon nanotube, the coupled system is far in the resolved sideband regime $\omega_m \gg \kappa_c$, the most promising parameter region for a large number of optomechanical protocols including ground state cooling and quantum control.

Optomechanically induced transparency (OMIT). To probe for optomechanical coupling, we perform an OMIT type experiment[22], cf. Fig. 2a, b: a strong, red-detuned drive field ($\omega_d \simeq \omega_c - \omega_m$) pumps the microwave cavity; the transmission of a weak, superimposed probe signal ω_p near ω_c is detected. A distinct, sharp OMIT absorption feature within the transmission

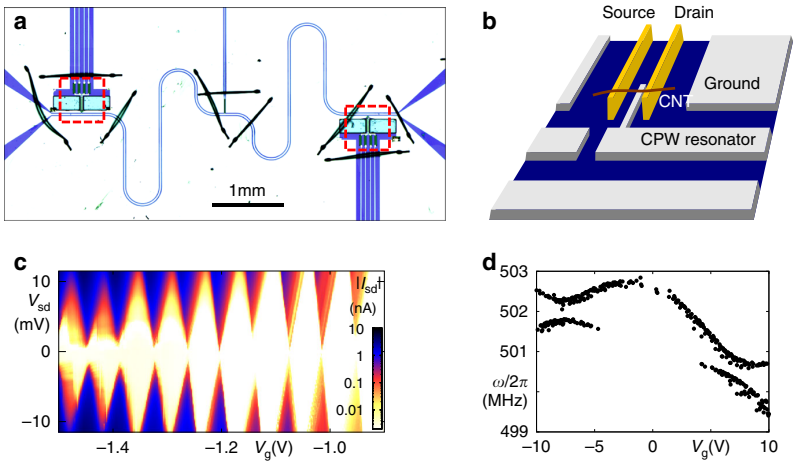

Fig. 1 Integrating a suspended carbon nanotube into a microwave cavity. a Optical micrograph showing a niobium-based $\lambda/2$ coplanar waveguide cavity for transmission measurement, with carbon nanotube deposition areas and dc contact structures (see the red dashed squares) near the coupling capacitors. For fabrication redundancy, two deposition areas exist on the device, but only one is used here. Bond wires visible as dark lines connect different segments of the ground plane to avoid spurious resonances. **b** Simplified sketch of the nanotube deposition area, including source and drain electrodes, a carbon nanotube deposited on them, and the buried gate connected to the cavity center conductor. **c** dc transport characterization of the carbon nanotube at $T_{base} \simeq 10$ mK. The plot of the absolute value of currrent $|I|$ as function of gate voltage V_g and bias voltage V_{sd} displays the typical diamond-shaped Coulomb blockade regions of suppressed conductance[12,40,41]. **d** Using rf excitation with an antenna and dc measurement[17,18], two transversal vibration modes can be traced across a large gate voltage range; the figure plots the detected resonance frequencies. The corresponding raw data as well as a fit can be found in Supplementary Figs. 6 and 7.

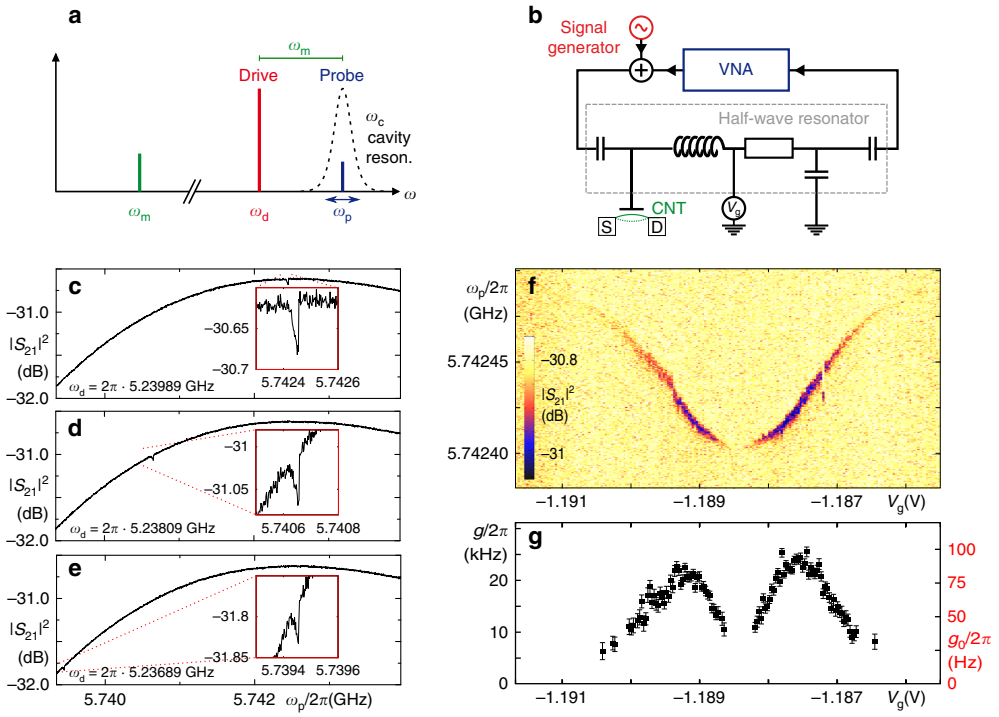

Fig. 2 Optomechanically induced transparency (OMIT) in the Coulomb blockade regime. a Frequency scheme and **b** detection setup of an OMIT measurement. A strong drive signal at $\omega_d = \omega_c - \omega_m$ pumps the microwave cavity; the cavity transmission near the cavity resonance ω_c is characterized using a superimposed weak probe signal ω_p from a vector network analyzer (VNA). Device parameters are: $\omega_c \simeq 2\pi \cdot 5.74$ GHz, $\kappa_c = 2\pi \cdot 11.6$ MHz, $\omega_m \simeq 2\pi \cdot 502.5$ MHz. **c**–**e** Probe signal power transmission $|S_{21}(\omega_p)|^2$ for three different choices of cavity drive frequency ω_d, at $\omega_d = \omega_c - \omega_m$ (**c**) and slightly detuned (**d**, **e**). The gate voltage $V_g = -1.1855$ V is fixed on the flank of a sharp Coulomb oscillation of conductance; $V_{sd} = 0$. **f** Probe signal transmission as in **c**–**e**, now for a fixed cavity drive frequency $\omega_d = 2\pi \cdot 5.23989$ GHz and varied gate voltage V_g across a Coulomb oscillation. The depth of the OMIT feature allows the evaluation of the optomechanical coupling $g(V_g)$ at each gate voltage value. **g** Optomechanical coupling $g(V_g)$ (left axis) and corresponding single photon coupling $g_0(V_g) = g(V_g)/\sqrt{n_c}$ (right axis), extracted from the data of **f**; $n_c = 67{,}500$. Error bars indicate the standard error of the fit result.

resonance of the cavity becomes visible in the measurements of Fig. 2c–e. It occurs due to destructive interference of the probe field with optomechanically upconverted photons of the drive field, when the two-photon resonance condition $\omega_p - \omega_d = \omega_m$ is fulfilled[22], and shifts in frequency as expected when ω_d is detuned from the precise red sideband condition, see Fig. 2d, e. Fitting the OMIT feature allows to extract the optomechanical coupling parameter $g = \sqrt{n_c}(\partial\omega_c/\partial x)x_{zpf}$, describing the cavity detuning per displacement of the mechanical harmonic oscillator[14,22], see Supplementary Note 9 for details. Surprisingly, from Fig. 2c, one obtains a single-photon coupling on the order of $g_0 = g/\sqrt{n_c} \sim 2\pi \cdot 100$ Hz.

Such a value of g_0 strongly exceeds expectations from the device geometry[23]. For a mechanical oscillator dispersively coupled to a coplanar waveguide resonator, the coupling is given by

$$g_0 = \frac{\omega_c}{2C_c}\frac{\partial C_c}{\partial x}x_{zpf}, \qquad (1)$$

where C_c is the total capacitance of the cavity, x is the mechanical displacement, and x_{zpf} the mechanical zero-point fluctuation length scale. Assuming a metallic wire over a metallic plane and inserting device parameters[23], the coupling calculated from the change in geometric gate capacitance $C_g(x)$ becomes $\partial C_g/\partial x \sim 10^{-12}$ F m^{-1}. This leads to $g_0^* = 2\pi \cdot 2.9$ mHz, more than four orders of magnitude smaller than the measured g_0. To explain this discrepancy, we need to focus on the properties of the carbon nanotube as a quantum dot, with a strongly varying quantum capacitance $C_{CNT}(x)$ as the displacement-dependent component of C_c dominating g_0.

Figure 2f depicts OMIT measurements for similar parameters as in Fig. 2c–e, however, we now keep the drive frequency ω_d constant and vary the gate voltage V_g across a Coulomb oscillation of conductance. The mechanical resonance frequency ω_m shifts to lower frequencies in the vicinity of the charge degeneracy point. This electrostatic softening is a well-known characteristic of suspended carbon nanotube quantum dots[18,24]. More interestingly, the resulting gate-dependent coupling $g(V_g)$ (along with $g_0(V_g)$) is plotted in Fig. 2g. It is maximal at the edges of the finite conductance peak, whereas at its center and on the outer edges, the coupling vanishes; the enhancement of g_0 is intrinsically related to Coulomb blockade.

Mechanism of enhanced coupling. Figure 3 explores the nature of this enhanced coupling mechanism. We treat the nanotube as a single quantum dot; see Supplementary Note 3 for a discussion of the validity of this assumption. Further, we assume a full separation of time scales $\omega_m \ll \omega_c \ll \Gamma$, where Γ describes the tunnel rates of the quantum dot. We can then introduce the quantum capacitance[25,26]

$$C_{CNT} = e\frac{C_g}{C_{dot}}\frac{\partial\langle N\rangle}{\partial V_g}, \qquad (2)$$

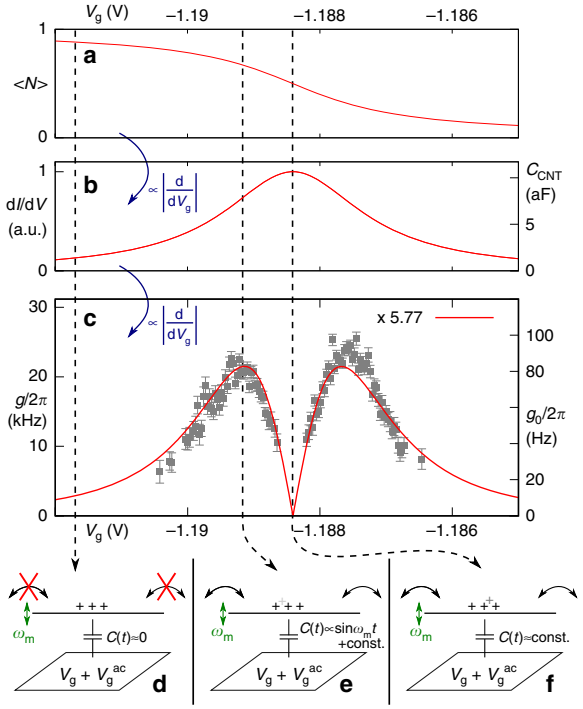

Fig. 3 Coulomb blockade enhanced optomechanical coupling mechanism. Solid lines correspond to the model of a Lorentz-broadened quantum dot level at $k_BT \ll \Gamma$. The Coulomb oscillation center $V_g^* = -1.18841$ V, the line width $\hbar\Gamma = 0.673$ meV, and a scaling prefactor $a = 5.77$ (see text) have been obtained by fitting to the OMIT data $g(V_g)$. **a** Time-averaged charge occupation $\langle N\rangle(V_g)$ of the quantum dot (note that we are in the hole conduction regime). **b** Conductance $dI/dV_{sd}(V_g)$ (left axis) and quantum capacitance C_{CNT} (right axis), cf. Supplementary Fig. 12. **c** Coulomb-blockade enhanced optomechanical coupling $g(V_g)$ (left axis) and single photon coupling $g_0(V_g)$ (right axis). The data points are identical to Fig. 2g; the calculation result has been scaled with 5.77 to fit the data. **d**–**f** Schemata for the situations corresponding to the dashed lines in **a**–**c**, see the text.

where $\langle N\rangle(V_g)$ is the number of charge carriers (here holes) on the quantum dot averaged over the tunneling events, and C_{dot} is the total quantum dot capacitance; see Supplementary Note 12 for a derivation. In a quantum dot, each Coulomb oscillation corresponds to the addition of one electron or hole. The charge occupation $\langle N\rangle(V_g)$ resembles a step function, with the sharpness of the step given for zero bias voltage by lifetime and temperature broadening. This is plotted in Fig. 3a, for the limit of $k_BT \ll \Gamma$. The quantum capacitance $C_{CNT}(V_g)$ becomes a Lorentzian, as plotted in Fig. 3b.

Any motion δx modulates the geometric capacitance $C_g(x)$. It thus shifts the position of the Coulomb oscillations in gate voltage, acting equivalent to an effective modulation of the gate voltage δV_g. With this, the optomechanical coupling g, scaling with $|\partial C_{CNT}/\partial x|$, becomes proportional to the derivative $\partial C_{CNT}/\partial V_g$ and thus the second derivative of $\langle N\rangle(V_g)$, as is illustrated in Fig. 3c. The functional dependence has been fitted to the data points of Fig. 2g, here again shown in the background.

The three key situations depending on the gate voltage are sketched in Fig. 3d–f: away from the conductance peak, the charge on the nanotube is constant, and only geometric capacitances change, see Fig. 3d. On the flank of the conductance resonance, a small change δx ($\propto \delta C_g$) strongly modulates C_{CNT}, see Fig. 3e. At the center of the conductance resonance, the charge adapts to x, but the derivative $\partial C_{CNT}/\partial V_g$ and with it $g \propto |\partial C_{CNT}/\partial x|$ is approximately zero.

The detailed derivation and the full expressions and values for Fig. 3 can be found in the Supplementary Information, Supplementary Note 12, and Supplementary Table 1. The parameter entering the optomechanical coupling in Eq. (1), the derivative of the quantum capacitance $\partial C_{CNT}/\partial x$, is found to be

$$\frac{\partial C_{CNT}}{\partial x} = \eta \frac{\partial C_g}{\partial x} = e \frac{\partial^2 \langle N\rangle}{\partial V_g^2} \frac{V_g}{C_{dot}} \frac{\partial C_g}{\partial x}, \qquad (3)$$

indicating that for significant optomechanical coupling a sharp Coulomb oscillation (i.e., low temperature and low intrinsic line width Γ, leading to large values of $\partial^2\langle N\rangle/\partial V_g^2$) and a large V_g are required. From device data, we obtain an amplification factor $\eta \sim 10^4$. The experimental gate voltage dependence $g_0(V_g)$ is qualitatively reproduced very well. To obtain the quantitative agreement of Fig. 3c, we have introduced an additional scaling prefactor as free fit parameter, resulting in $g_0^{exp}/g_0^{th} = 5.77$. Given the uncertainties of input parameters, this is a good agreement; see Supplementary Note 15 for a discussion of error sources.

Discussion

In literature, many approaches have been pursued to enhance optomechanical coupling[26–35]. Resonant coupling, with $\omega_m = \omega_c$, has been demonstrated successfully for a carbon nanotube quantum dot[26], but does not provide access to the wide set of experimental protocols developed for the usual case of dispersive coupling and the "good cavity limit" $\omega_m \gg \kappa_c$. The mechanism presented here is most closely related to those where a superconducting charge qubit was coherently introduced between mechanical resonator and cavity[27]. However, the impact of single electron tunneling and shot noise on the optomechanical system shall require careful analysis.

Given the sizeable coupling in the good cavity limit $\kappa_c \ll \omega_m$, many experimental techniques for future experiments are at hand. First steps are demonstrated in Fig. 4 in a two-tone spectroscopy experiment: a mechanical drive signal ω_a is applied simultaneously to a cavity pump signal at $\omega_d = \omega_c - \omega_a$; the plotted cavity output power at ω_c clearly shows the optmechanical upconversion (anti-Stokes scattering) at mechanical resonance $\omega_a = \omega_m$. In Fig. 4a, the dc bias across the nanotube is set to zero, and the antenna drive kept at a minimum. In Fig. 4b, both antenna drive and bias voltage have been increased. A background signal independent of device parameters emerges; at the same time, the upconverted signal displays a phase shift and destructive interference with the background for parts of the gate voltage range, meriting further measurements and analysis.

Future improvements of the optomechanical coupling via drive power and device geometry and of the detection sensitivity via the output amplifier chain shall allow detection of the thermal motion of the carbon nanotube and subsequently motion amplitude calibration.

The observation of strong optomechanical coupling and the corresponding normal mode splitting requires a coupling g exceeding both mechanichal linewidth κ_m and cavity line width κ_c. Clean carbon nanotubes have reached mechanical quality factors up to[36] $Q_m \sim 10^6$, allowing for two orders of magnitude improvement and a line width of $\kappa_m \sim 2\pi \cdot 500$ Hz. Regarding microwave resonators we have reached up to $Q_c = 10^5$ in our setup so far, corresponding to $\kappa_c = 2\pi \cdot 57$ kHz. This means that strong coupling should be reachable already at moderate increase of our so far rather low cavity photon number n_c.

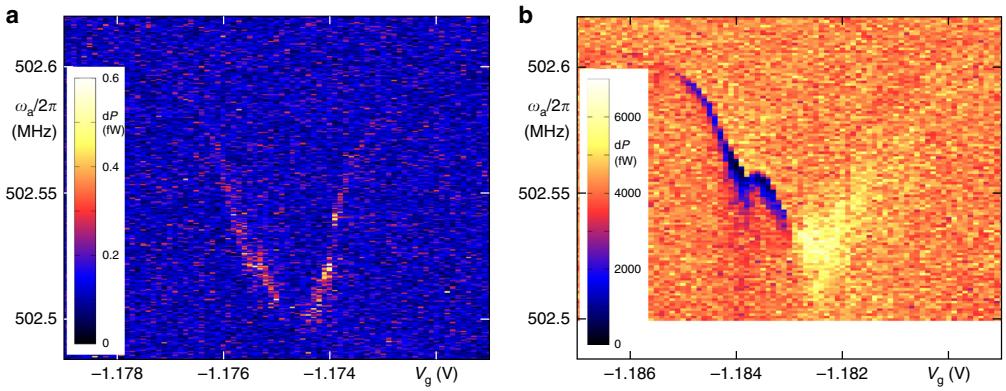

Fig. 4 Two-tone spectroscopy. Via an antenna, the carbon nanotube is driven at ω_a close its mechanical eigenfrequency; the microwave cavity is simultaneously pumped at $\omega_d = \omega_c - \omega_a$. The plots show the power output of the cavity at the upconverted frequency ω_c, with the nanotube acting as nonlinear element. Drive power $P_d = 20$ dBm ($n_c \simeq 2.1 \times 10^4$), measurement bandwidth 5 Hz. **a** Antenna generator power $P_a = -55$ dBm, bias $V_{sd} = 0$; **b** antenna generator power $P_a = -30$ dBm, bias $V_{sd} = 0.5$ mV.

Regarding the cooperativity $C = 0.0042$ of our experiment (cf. Supplementary Table 1), already an improvement of the nanotube Q_m by a factor 100 brings it into the same order of magnitude as the thermal mode occupation $n_m = 0.4$, with significant further and independent room for improvement via the cavity photon number n_c.

With this, a wide range of physical phenomena becomes experimentally accessible, ranging from side-band cooling of the vibration mode and potentially its quantum control[37] all the way to real-time observation of its interaction with single electron tunneling phenomena[38].

Data availability

The datasets generated during and/or analyzed during this study are available from the corresponding author on reasonable request.

Received: 18 July 2019; Accepted: 11 March 2020;
Published online: 02 April 2020

References

1. Wu, C. C., Liu, C. H. & Zhong, Z. One-step direct transfer of pristine single-walled carbon nanotubes for functional nanoelectronics. *Nano Lett.* **10**, 1032–1036 (2010).
2. Pei, F., Laird, E. A., Steele, G. A. & Kouwenhoven, L. P. Valley-spin blockade and spin resonance in carbon nanotubes. *Nat. Nanotechnol.* **7**, 630–634 (2012).
3. Ranjan, V. et al. Clean carbon nanotubes coupled to superconducting impedance-matching circuits. *Nat. Commun.* **6**, 7165 (2015).
4. Gramich, J., Baumgartner, A., Muoth, M., Hierold, C. & Schönenberger, C. Fork stamping of pristine carbon nanotubes onto ferromagnetic contacts for spin-valve devices. *Phys. Stat. Solidi B* **252**, 2496–2502 (2015).
5. Waissman, J. et al. Realization of pristine and locally tunable one-dimensional electron systems in carbon nanotubes. *Nat. Nanotechnol.* **8**, 569–574 (2013).
6. Blien, S., Steger, P., Albang, A., Paradiso, N. & Hüttel, A. K. Quartz tuning-fork based carbon nanotube transfer into quantum device geometries. *Phys. Stat. Solidi B* **255**, 1800118 (2018).
7. Delbecq, M. R. et al. Photon-mediated interaction between distant quantum dot circuits. *Nat. Commun.* **4**, 1400 (2013).
8. Viennot, J. J., Dartiailh, M. C., Cottet, A. & Kontos, T. Coherent coupling of a single spin to microwave cavity photons. *Science* **349**, 408–411 (2015).
9. Cubaynes, T. et al. Highly coherent spin states in carbon nanotubes coupled to cavity photons. *npj Quant. Inf.* **5**, 47 (2019).
10. Witkamp, B., Poot, M. & van der Zant, H. Bending-mode vibration of a suspended nanotube resonator. *Nano Lett.* **6**, 2904-2908 (2006).
11. Sazonova, V. et al. A tunable carbon nanotube electromechanical oscillator. *Nature* **431**, 284–287 (2004).
12. Laird, E. A. et al. Quantum transport in carbon nanotubes. *Rev. Mod. Phys.* **87**, 703–764 (2015).
13. Margańska, M. et al. Shaping electron wave functions in a carbon nanotube with a parallel magnetic field. *Phys. Rev. Lett.* **122**, 086802 (2019).
14. Aspelmeyer, M., Kippenberg, T. J. & Marquardt, F. Cavity optomechanics. *Rev. Mod. Phys.* **86**, 1391–1452 (2014).
15. Poot, M. & van der Zant, H. S. J. Mechanical systems in the quantum regime. *Phys. Rep.* **511**, 273–335 (2012).
16. Weig, E. M. et al. Single-electron-phonon interaction in a suspended quantum dot phonon cavity. *Phys. Rev. Lett.* **92**, 046804 (2004).
17. Hüttel, A. K. et al. Carbon nanotubes as ultrahigh quality factor mechanical resonators. *Nano Lett.* **9**, 2547–2552 (2009).
18. Steele, G. A. et al. Strong coupling between single-electron tunneling and nanomechanical motion. *Science* **325**, 1103–1107 (2009).
19. Götz, K. J. G. et al. Nanomechanical characterization of the Kondo charge dynamics in a carbon nanotube. *Phys. Rev. Lett.* **120**, 246802 (2018).
20. Wu, C. C. & Zhong, Z. Capacitive spring softening in single-walled carbon nanotube nanoelectromechanical resonators. *Nano Lett.* **11**, 1448–1451 (2011).
21. Stiller, P. L., Kugler, S., Schmid, D. R., Strunk, C. & Hüttel, A. K. Negative frequency tuning of a carbon nanotube nano-electromechanical resonator under tension. *Phys. Stat. Solidi B* **250**, 2518–2522 (2013).
22. Weis, S. et al. Optomechanically induced transparency. *Science* **330**, 1520–1523 (2010).
23. Regal, C. A., Teufel, J. D. & Lehnert, K. W. Measuring nanomechanical motion with a microwave cavity interferometer. *Nat. Phys.* **4**, 555–560 (2008).
24. Lassagne, B., Tarakanov, Y., Kinaret, J., Garcia-Sanchez, D. & Bachtold, A. Coupling mechanics to charge transport in carbon nanotube mechanical resonators. *Science* **325**, 1107–1110 (2009).
25. Duty, T. et al. Observation of quantum capacitance in the Cooper-pair transistor. *Phys. Rev. Lett.* **95**, 206807 (2005).
26. Ares, N. et al. Resonant optomechanics with a vibrating carbon nanotube and a radio-frequency cavity. *Phys. Rev. Lett.* **117**, 170801 (2016).
27. Pirkkalainen, J.-M. et al. Hybrid circuit cavity quantum electrodynamics with a micromechanical resonator. *Nature* **494**, 211–215 (2013).
28. Rimberg, A. J., Blencowe, M. P., Armour, A. D. & Nation, P. D. A cavity-Cooper pair transistor scheme for investigating quantum optomechanics in the ultra-strong coupling regime. *New J. Phys.* **16**, 055008 (2014).
29. Heikkilä, T. T., Massel, F., Tuorila, J., Khan, R. & Sillanpää, M. A. Enhancing optomechanical coupling via the Josephson effect. *Phys. Rev. Lett.* **112**, 203603 (2014).
30. Abdi, M., Pernpeintner, M., Gross, R., Huebl, H. & Hartmann, M. J. Quantum state engineering with circuit electromechanical three-body interactions. *Phys. Rev. Lett.* **114**, 173602 (2015).
31. Lecocq, F., Teufel, J. D., Aumentado, J. & Simmonds, R. W. Resolving the vacuum fluctuations of an optomechanical system using an artificial atom. *Nat. Phys.* **11**, 635–639 (2015).
32. Pirkkalainen, J.-M. et al. Cavity optomechanics mediated by a quantum two-level system. *Nat. Commun.* **6**, 6981 (2015).
33. Xue, Z.-Y., Yang, L.-N. & Zhou, J. Circuit electromechanics with single photon strong coupling. *Appl. Phys. Lett.* **107**, 023102 (2015).

34. Santos, J. T., Li, J., Ilves, J., Ockeloen-Korppi, C. F. & Sillanpää, M. Optomechanical measurement of a millimeter-sized mechanical oscillator approaching the quantum ground state. *New J. Phys.* **19**, 103014 (2017).
35. Shevchuk, O., Steele, G. A. & Blanter, Y. M. Strong and tunable couplings in flux-mediated optomechanics. *Phys. Rev. B* **96**, 014508 (2017).
36. Moser, J., Eichler, A., Güttinger, J., Dykman, M. I. & Bachtold, A. Nanotube mechanical resonators with quality factors of up to 5 million. *Nat. Nanotechnol.* **9**, 1007–1011 (2014).
37. O'Connell, A. D. et al. Quantum ground state and single-phonon control of a mechanical resonator. *Nature* **464**, 697–703 (2010).
38. Barnard, A. W., Zhang, M., Wiederhecker, G. S., Lipson, M. & McEuen, P. L. Real-time vibrations of a carbon nanotube. *Nature* **566**, 89–93 (2019).
39. Reinhardt, S. et al. Lab::Measurement—a portable and extensible framework for controlling lab equipment and conducting measurements. *Comput. Phys. Commun.* **234**, 216–222 (2019).
40. Kouwenhoven, L. P. et al. *Electron Transport in Quantum Dots* (Kluwer, 1997).
41. Nazarov, Y. V. & Blanter, Y. M. *Quantum Transport: Introduction to Nanoscience* (Cambridge University Press, Cambridge, 2009).

Acknowledgements

The authors acknowledge funding by the Deutsche Forschungsgemeinschaft via Emmy Noether grant Hu 1808/1, SFB 631, SFB 689, SFB 1277, and GRK 1570. We would like to thank G. Rastelli, F. Marquardt, E. A. Laird, Y. M. Blanter, and D. Weiss for insightful discussions, O. Vavra for experimental help, and Ch. Strunk and D. Weiss for the use of the experimental facilities. The data have been recorded using Lab::Measurement[39].

Author contributions

A.K.H. and S.B. conceived and designed the experiment. P.S. and R.G. developed and performed the nanotube growth and transfer; N.H. and S.B. developed and fabricated the coplanar waveguide device. The low temperature measurements were performed jointly by all authors. Data evaluation and writing of the paper was done jointly by S.B., N.H., and A.K.H. The project was supervised by A.K.H.

Competing interests

The authors declare no competing interests.

Additional information

Supplementary information is available for this paper at https://doi.org/10.1038/s41467-020-15433-3.

Correspondence and requests for materials should be addressed to A.K.Hüt.

Peer review information *Nature Communications* thanks Joel Moser and the other anonymous reviewer(s) for their contribution to the peer review of this work.

Reprints and permission information is available at http://www.nature.com/reprints

Publisher's note Springer Nature remains neutral with regard to jurisdictional claims in published maps and institutional affiliations.

Danksagung

Abschließend möchte ich mich bei all jenen bedanken, die mich im Rahmen dieser Dissertation und darüber hinaus unterstützt und begleitet haben.

Zuallerst gilt mein Dank Dr. Andreas K. Hüttel, für die Möglichkeit an diesem interessanten Thema arbeiten zu können, für die tatkräftige Unterstützung beim Planen, Messen und Auswerten, sowie beim Finden neuer Wege und Ideen. Eine schöne und erfolgreiche Zusammenarbeit war in den letzten Jahren stets selbstverständlich. Danke auch für die mentale Unterstützung und die Überzeugung gegenüber meinem Thema. Viel Erfolg für deine Zukunft, ich hoffe die Mikrowellen-Optomechanik hält noch viele spannende Ergebnisse für dich bereit!

Jessica Siperek möchte ich danken für die vielen Ermutigungen und Ermunterungen meine Dissertation betreffend. Auch in meinem Leben abseits der Uni hilfst du mir stets die Balance zu halten, bist verständnisvoll und stehst hinter meinen Plänen. Danke für die schönste Zeit!

Prof. Dr. Christoph Strunk danke ich für die fachlichen Diskussionen, besonders im Rahmen von zu schreibenden Veröffentlichungen oder zu haltenden Vorträgen. Seinem ganzen Team danke ich für die freundliche Aufnahme und die gegenseitige Unterstützung.

Bei den Doktorandenkollegen Daniel Schmid, Peter Stiller, Alois Dirnaichner und Karl Götz der AG Hüttel möchte ich mich bedanken für die vielen kurzweiligen Stunden zusammen im Büro oder Labor, gefüllt von fachlichem und darüber hinausgehendem Gedankenaustausch.

Dr. Andreas Pfeffer und Dr. Ondrej Vavra gilt mein Dank für die Verbesserung der Messsetups und die Einführung in die do-it-yourself Mentalität im Labor.

Dr. Nicola Paradiso, Patrick Steger und Richard Graaf danke ich für das Instandhalten und Verbessern des Transfersetups.

Großer Dank gebührt Niklas Hüttner und Alexander Albang für die Herstellung der Resonatoren, das methodische Arbeiten und die Entwicklung der Resonator-Hybridgeometrie, was die optomechanischen Experimente dieser Arbeit überhaupt möglich gemacht hat.

Vielen Dank auch an Thomas Huber für die vielen Diskussionen, fürs Korrekturlesen der Dissertation und fürs Helium Nachfüllen, wenn ich mal wieder im Urlaub war. Die Arbeit im gemeinsamen Labor war immer lustig und konstruktiv.

Simon Reinhardt und Dr. Andreas K. Hüttel danke ich für die Hilfe beim Programmieren der Messskripte.

Einen großen Dank auch an Dominik Berndt, der immer bereit war spontan neue optische Masken für uns herzustellen, was mit zum Gelingen dieses Projekts beigetragen hat.

Pascal Brunner und Benedikt Hartmann danke ich für die weiteren Projekte, in die ich über den Rahmen dieser Arbeit hinaus involviert war.

Unseren Technikern Uli Gürster, Thomas Haller, Michael Weigl, Florian Birkner und Conny Linz danke ich für die kompetente Beantwortung technischer Fragen und die Hilfe im Labor und Reinraum.

Danke an die Jungs der Heliumverflüssigungsanlage, Christian Haimerl und Thomas Solleder, für die Bereitstellung von Kaltem.

Vielen Dank natürlich an die Grillgruppe, allen voran Thomas Kuczmik, Robin Huber, Andreas Sandner, Thomas Hupfauer, Peter Stiller und Daniel Schmid. Auch die Feiern waren immer erstklassig. Danke für Organisation und Ausgestaltung.

Florian Oberhuber möchte ich danken für die Einführung in das wissenschaftliche Arbeiten und die Ermutigung zur Promotion.

Prof. Dr. Jascha Repp danke ich sehr für die kurzfristige Übernahme der Zweitkorrektur.

Vielen Dank natürlich an Claudia Moser und Elke Haushalter für die stets freundliche Art und schnelle Hilfe bei Organisatorischem.

Zu guter Letzt möchte ich mich bei meiner Familie und besonders bei meinen Eltern bedanken, die immer Interesse an meiner Arbeit zeigten und mich über all die Jahre in meinen Vorhaben und Zielen unterstützt haben.

Nachträgliche Änderungen

- Titelblatt innen, Rückseite: Der Termin des Kolloquiums wurde hinzugefügt.
- Seite 17: Fig. 2.9: Die Tunnelraten Γ_{d}^{-} und Γ_{d}^{+} wurden gegeneinander ausgetauscht.
- Seite 46: "The phase constant is then given" wurde geändert zu "The phase velocity is then given"
- Seite 50: Eq. 4.29 wurde geändert zu "$\Delta\vec{B} = \frac{1}{\lambda_{\mathrm{L}}^2}\vec{B}$"
- Seite 74: Caption Fig. 5.7: "of resonance frequency" wurde geändert zu "of internal quality factor"
- Seite 76: rabi $\rightarrow$ Rabi
- Seite 82: "between the single frequency mode" wurde geändert zu "of the single frequency mode"
- Seite 86: "from a earlier measurements" wurde geändert zu "from earlier measurements"
- Seite 95: "with the smaller tunnel rate" wurde geändert zu "with the smaller tunnel barrier"
- Seite 111: Caption Fig. 7.8: "$V_{\mathrm{g}} = -1.8901\,\mathrm{V}$" wurde geändert zu "$V_{\mathrm{g}} = -1.18901\,\mathrm{V}$"
- Seite 126: Ein Punkt wurde hinter "highly worthwhile" eingefügt.
- Seite 133: "demandable" wurde geändert zu "necessary"
- Seite 142: "As the phase is shift" wurde geändert zu "As the phase shift"